FINAL REPORT

NASA NAG3-2109

TURBOFAN ACOUSTIC PROPAGATION AND RADIATION

Walter Eversman

Mechanical and Aerospace Engineering
and Engineering Mechanics

University of Missouri-Rolla
Rolla, Missouri 65401

June, 2000

FINAL REPORT

NASA NAG3-2109

TURBOFAN ACOUSTIC PROPAGATION AND RADIATION

Walter Eversman

Mechanical and Aerospace Engineering
and Engineering Mechanics

University of Missouri-Rolla
Rolla, Missouri 65401

June, 2000

TABLE OF CONTENTS

INTRODUCTION

This document describes progress in the development of finite element codes for the prediction of near and far field acoustic radiation from the inlet and aft fan ducts of turbofan engines. The report consists of nine papers which have appeared in archival journals and conference proceedings, or are presently in review for publication. Brief summaries of each paper are given here.

1. Aft Fan Duct Acoustic Radiation. (Journal of Sound and Vibration 1998 213(2), 235- 257)

Details are given of a finite element code which has been developed for the prediction of the radiated acoustic field from the aft fan duct of a turbofan engine. A new technique based on a penalty method is introduced to enforce the condition of continuity of acoustic pressure across the shear layer which bounds the jet.

2. Mapped Infinite Wave Envelope Elements for Acoustic Radiation in a Uniformly Moving Medium. (Journal of Sound and Vibration 1999 224(4), 665-687)

Variable order mapped infinite wave envelope elements are introduced for finite element modeling of acoustic radiation in a uniformly moving medium. The elements are applied to the problem of turbofan inlet radiation, and are shown to provide an effective non-reflecting boundary condition which allows substantial reduction of the FEM mesh in the near field. Results are shown for the acoustic pressure in the near field.

3. A Reflection Free Boundary Condition for Propagation in Uniform Flow Using Mapped Infinite Wave Envelope Elements. (Journal of Computational Acoustics 2000, 8(1), 25-42.)

Variable order mapped infinite wave envelope elements are introduced for finite element modeling of acoustic radiation in a uniformly moving medium. The elements are applied to the problem of turbofan inlet and aft fan duct radiation, and are shown to provide an effective non-reflecting boundary condition which allows substantial reduction of the FEM mesh in the near field. Results are shown for the acoustic pressure in the near field and in the far field.

4. A Numerical Comparison Between Multiple-Scales and FEM Solution for Sound Propagation in Lined Flow Ducts. (AIAA Paper 99-1821, 1999 AIAA Aeroacoustics Conference, Seattle. Provisionally accepted for the Journal of Fluid Mechanics)

An analytical solution based on the method of multiple-scales for acoustic propagation in nonuniform ducts with compressible potential mean flow is compared against a finite element solution. This provides a useful benchmark for the FEM results in cases when scattering of the incident mode does not dominate the transmitted acoustic field. In general this will be true for incident modes which are nearly cut off.

5. Acoustic Propagation at High Frequencies in Ducts. (AIAA Paper 2000-1953, 2000 AIAA Aeroacoustics Conference, Maui, Hawaii)

The problem of acoustic propagation in ducts at high non-dimensional frequencies is examined. It is found that in FEM models using quadratic elements, good solutions for the acoustic potential are achieved using the conventional 10 node per wave length rule of thumb. However, good solutions, via postprocessing, for acoustic pressure require substantially increased mesh density. Cubic and quartic elements are examined and it is found that cubic elements offer are more efficient than quadratic elements for acoustic potential and offer a substantial improvement in acoustic pressure post-processing. Non-dimensional frequencies up to 100 are considered.

6. The Boundary Condition at an Impedance Wall in a Nonuniform Duct with Potential Flow. (Journal of Sound and Vibration, in review)

The acoustic boundary condition at an impedance wall in a nonuniform duct with compressible mean flow is implemented in a weighted residuals finite element formulation. The boundary condition appears to require data which includes the tangential derivative of the tangential mean flow velocity, the normal derivative of the normal component of mean flow velocity, and the derivatives of the mean flow density and the boundary admittance along the boundary. It is shown that it can be substantially simplified to eliminate the tangential derivatives of mean flow properties and to eliminate completely the normal component of mean flow velocity. Implementation of the boundary condition is shown to involve no difficulty.

7. A Reverse Flow Theorem and Acoustic Reciprocity in Compressible Potential Flows. (Journal of Sound and Vibration, in review)

A reverse flow theorem for acoustic propagation in compressible potential flow has been obtained directly from the field equations without recourse to energy conservation arguments. A reciprocity theorem for the scattering matrix for propagation of acoustic modes in a duct with either acoustically rigid walls or acoustically absorbing walls follows. It is found that for a source at a specific end of the duct, suitably scaled reflection matrices in

direct and reverse flow have a reciprocal relationship. Scaled transmission matrices obtained for direct flow and reversed flow with simultaneous switching of source location from one end to the other also have a reciprocal relationship.
Reciprocal relations provide an excellent benchmark for verification of acoustic propagation computations. Numerical verification of the reciprocal relationships is given in a companion paper.

8. Reciprocity and Acoustic Power in One Dimensional Compressible Potential Flows. (Journal of Sound and Vibration, in review)

A reverse flow theorem for one dimensional acoustic propagation in compressible potential flow has been obtained directly from the field equations without recourse to energy conservation arguments. Reciprocity relationships for the scattering coefficients for propagation are derived. It is found that for a source at a specific end of the duct, suitably scaled reflection coefficients in direct and reverse flow have a reciprocal relationship. Scaled transmission coefficients obtained for direct flow and reversed flow with simultaneous switching of source location from one end to the other also have a reciprocal relationship. Reciprocal relations and power conservation arguments are used to show that scaled power reflection and transmission coefficients are invariant to flow reversal and switching of source location from one end of the duct to the other. Numerical verification of the reciprocal relationships is given in a companion paper in which multiple mode propagation and one dimensional propagation are considered.

9. Numerical Experiments on Acoustic Reciprocity in Compressible Potential Flows. (Journal of Sound and Vibration, in review)

A reciprocity theorem for the scattering matrix for propagation of acoustic modes in a duct with acoustically hard walls or with acoustically absorbing walls has been given in a companion publication. It was found that for a source at a specified end of the duct, suitably scaled reflection matrices in direct and reverse flow have a reciprocal relationship. Scaled transmission matrices obtained for direct flow and reversed flow with simultaneous switching of source location from one end to the other also have a reciprocal relationship. A reverse flow theorem for the equivalent one dimensional propagation model, which is a good approximation to the three dimensional model at low frequencies, was also obtained. In this case, using reciprocity and acoustic power conservation arguments it is additionally found that the acoustic power transmission coefficient is the same for a source at either end of the duct for a given flow direction. This result leads to an invariance theorem which relates acoustic power propagated due to sources of equal pressure amplitude at the two ends of the duct. Numerical verification of these reciprocal relationships is given here for propagation in axially symmetric (circular and annular) ducts with multi-modal propagation and at low frequencies when a one dimensional model is appropriate.

Journal of Sound and Vibration (1998) **213**(2), 235–257

AFT FAN DUCT ACOUSTIC RADIATION

W. EVERSMAN

Department of Mechanical and Aerospace Engineering and Engineering Mechanics, University of Missouri-Rolla, Rolla, MO 65401, U.S.A.

AND

D. OKUNBOR

Department of Computer Science, University of Missouri-Rolla, Rolla, MO 65401, U.S.A.

(*Received* 13 *June* 1997, *and in final form* 18 *December* 1997)

A finite element code has been developed for the prediction of the radiated acoustic field from the aft fan duct of a turbofan engine. The acoustic field is modelled based on the assumption that the steady flow in and around the nacelle is irrotational as is the acoustic perturbation. The geometry of the nacelle is axisymmetric and the acoustic source is harmonic and decomposed into its angular harmonics. The steady flow is computed on the acoustic mesh and provides data for the acoustic calculations. The jet is included in the steady flow potential flow model by separating the interior and exterior flow outside the aft fan duct with a thin barrier created by disconnecting the computational domain. The jet and exterior flow are allowed to merge at a defined distance downstream. In the acoustic radiation model continuity of acoustic particle velocity is implicitly satisfied across the shear layer by careful treatment of the surface integral which appears in the finite element method (FEM) formulation. Pressure continuity is enforced by using a penalty constraint on the shear layer. A model for locally reacting acoustic treatment provides a boundary condition on the duct walls. An attempt has been made to limit reflections on the artificial baffle introduced to limit the computational domain, but this is only moderately successful. An old, but reliable frontal solution routine has been updated with considerable impact on computational time. Example calculations are given which show the success achieved in satisfying the complicated interface conditions on the shear layer and the characteristics of the solutions at relatively high frequencies where the refinement of the mesh becomes a limiting consideration for practical computations.

1. INTRODUCTION

In approach and cutback conditions the acoustic field from high by-pass ratio turbofan engines is dominated by tonal noise generated by blade/vane interactions and radiated forward from the nacelle inlet and to the rear from the aft fan duct. In order to meet noise control goals active and passive techniques can be employed to control the source mechanisms and to attenuate acoustic propagation in the inlet and fan exhaust ducts. Methods for the prediction of the effects of various noise control measures on far field acoustic radiation are required in the design process. The investigation reported here is directed toward the development of a robust computational scheme for the prediction of the acoustic field attributed to tonal sources typical of blade/vane interaction in the aft fan duct. It is intended to be coupled to a suitable model of the source mechanism.

The model developed is an extension of computational methods which were developed for inlet radiation [1–4]. The inlet radiation model was based on the assumption of

0022–460X/98/220235 + 23 $25.00/0/sv971480

irrotational acoustic perturbations on an irrotational steady flow. A finite element code was developed which could accurately model the geometric details of an axisymmetric inlet as well as the steady flow field in and around the inlet, including the effect of forward flight. Rapid advances in the capabilities of work stations has made it a realistic goal to accurately predict the acoustic field around realistic geometries at realistic frequencies. Reported here is the development of a similar model for aft radiated noise. The most significant extension is the representation of the important effects of the fan duct jet imbedded in the surrounding flow which includes forward flight effects. The presence of the jet introduces interesting conditions which must be imposed on acoustic propagation across the shear layer which confines it. The methods for achieving these conditions in the context of the finite element method (FEM) are discussed in detail here.

2. FORMULATION OF THE ACOUSTIC RADIATION PROBLEM

The aft radiated acoustic field from a turbofan nacelle is described by a potential formulation as previously introduced for inlet acoustic radiation [1–4]. Figure 1 is a sketch of the important geometrical features of the aft fan duct and centre body. The nacelle has a forward flight Mach number M_0, which at large distances is equivalent to a uniform flow directed away from the fan exhaust duct exit plane. Near the nacelle this velocity field is non-uniform. The exhaust flow, defined at the source plane by Mach number M_j, emerges as a potential flow jet and extends down stream confined by a shear layer separating it from the exterior flow. The shear layer is terminated at a defined length at which point the jet and external flow merge as potential flows. The potential flow merging of the jet and exterior flow at the end of the shear layer produces a localized steady flow anomaly which has not been observed to substantially influence the acoustic radiation. Computations are to be carried out using the FEM in a domain including the interior of the aft fan exhaust duct and an exterior region made finite by invoking a radiation condition at an outer computational boundary and by introducing an artificial baffle oriented to produce a minimal effect on the acoustic radiation field.

The nacelle geometry and the steady flow field are assumed to be axially symmetric. The noise source is assumed to be harmonic in time and is decomposed into its angular modal content, allowing a two-dimensional representation of the acoustic field in an (x, r) plane through the nacelle axis of symmetry. The solution domain is shown in Figure 2. It is the x, r plane in cylindrical co-ordinates. The source plane is designated by C_j. The fan or exit guide vane source is input on this plane by specifying complex amplitudes of incident duct modes (see references [1–4] for details of the implementation of the source boundary

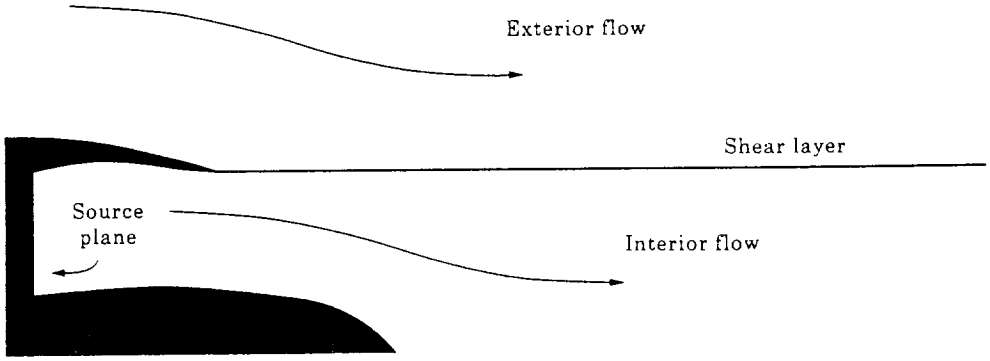

Figure 1. Sketch of the geometry of the aft fan duct, emphasizing the exhaust flow and shear layer.

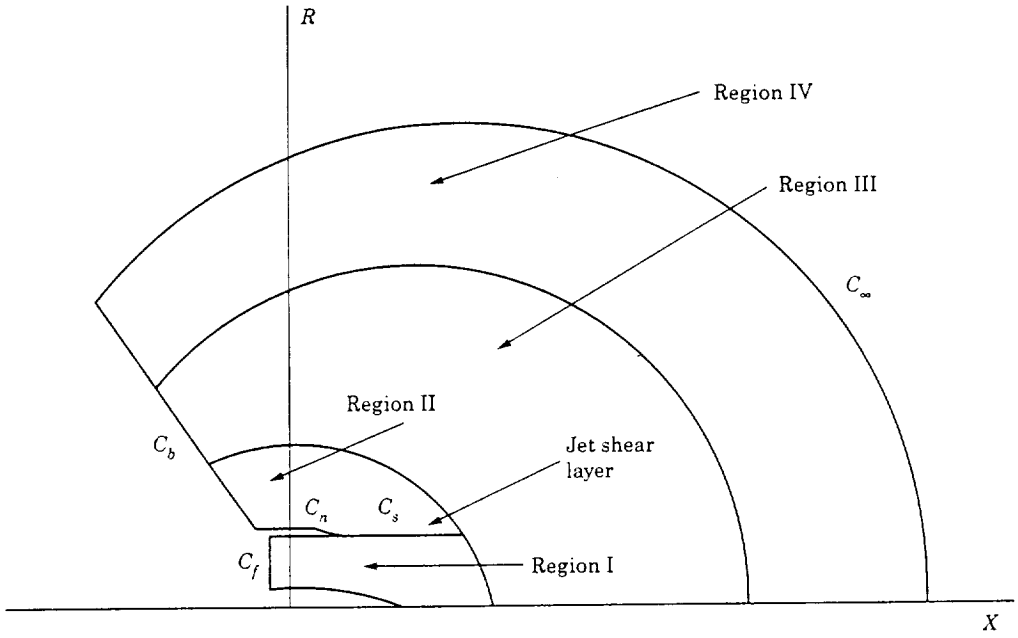

Figure 2. Computational domain showing the boundaries and regions.

condition.). The nacelle outer surface is C_n. The outer boundary of the solution domain C_∞ is a circle which is a constant phase surface for an acoustic source located at the origin. On this boundary a radiation condition is specified. Wave envelope elements [1–4] are used in the far field to reach the outer boundary with minimal cost in mesh refinement. An artificial baffle C_b limits the solution domain well upstream of the fan exit plane and is chosen to be swept in such a way that a minimal effect on the acoustic field is created. This baffle is a ray from the origin and in principle at large distances from the source it should be non-reflecting, although near field effects do lead to reflection. The placement of the baffle must be considered in terms of the likely orientation of the radiated field. The baffle can be eliminated if computational efficiency is not a limiting factor. The shear layer C_s which separates the potential flow jet from the potential exterior flow is a rigid boundary for the calculation of the steady flow field and is a surface across which appropriate continuity conditions must be satisfied in the acoustic calculations.

The starting point for the formulation of both the steady mean flow and the acoustic perturbation consists of the mass and momentum equations and the energy equation in the form of the isentropic equation of state:

$$\frac{\partial \hat{\rho}}{\partial t} + \nabla \cdot (\hat{\rho}\mathbf{V}) = 0, \tag{1}$$

$$\frac{\partial \mathbf{V}}{\partial t} + (\mathbf{V} \cdot \nabla)\mathbf{V} = -\frac{1}{\hat{\rho}} \nabla \hat{p}, \qquad \frac{\hat{p}}{p_0} = \left(\frac{\hat{\rho}}{\rho_0}\right)^{\gamma}, \tag{2, 3}$$

where $\hat{p}$, $\hat{\rho}$ and $\mathbf{V}$ are fluid properties pressure, density and velocity, at this point in dimensional form, and p_0 and ρ_0 are reference values of pressure and density.

A weak form of the field equations begins with equation (1) in which solutions for $\hat{\rho}$ and $\mathbf{V}$ are sought in the class of continuous functions which satisfy the weighted residual relation

$$\iiint_V \left[\nabla W \cdot (\hat{\rho}\mathbf{V}) - W \frac{\partial \hat{\rho}}{\partial t} \right] \mathrm{d}V = \iint_S W \hat{\rho} \mathbf{V} \cdot \mathbf{n} \, \mathrm{d}S \tag{4}$$

for every function $W(\mathbf{x})$ in the class of continuous functions. The surface integral is over the boundaries of the domain of solution and $\mathbf{n}$ is the unit normal out of the domain. In the finite element discretization process which follows, the surface integral must also be interpreted at each subdomain boundary, namely the boundaries of the individual elements. The physical boundaries of the solution domain include the boundaries of the nacelle, including the source plane, the rigid structural boundaries, and absorbing boundaries such as acoustic treatment. Other boundaries are the artificial baffle introduced to limit the solution domain and the outer boundary of the solution domain at which a radiation condition is applied. All of these boundary conditions are introduced through the surface integral. The boundary integral is observed to involve the mass flux normal to the boundary. The integral is therefore in terms of an essential conservation quantity, and this is typical of weak formulations in the framework of the FEM. For boundaries between subdomains (elements) in the FEM discretization at which there is no surface of discontinuity the integral produces no net contribution. This follows because on such boundaries the integrals on either side of the boundary produce contributions equal in magnitude and opposite in sign. In the present problem this applies to all boundaries between elements, although, as will be shown, a careful interpretation of the surface integral must be carried out to establish that it vanishes across the shear layer separating the outer flow field from the jet with a discontinuity in tangential steady flow. In particular, it seems to be necessary to start from the yet to be linearized form of the weighted continuity equation (1), and to carefully linearize it to account for the fact that on the shear layer, which is displaced due to acoustic perturbations, the integral is interpreted to be evaluated on the surface of discontinuity in tangential steady flow velocity with the unit normal defined to reflect this. If the field equation is linearized before the weak formulation is established, an essential contribution to the boundary integral is lost.

3. BOUNDARY CONDITIONS ON THE SHEAR LAYER

Figure 3 shows the idealized interface between the exterior flow and the jet. The surface of discontinuity in tangential velocity is assumed to be displaced from the mean position by

$$\Delta r(x, \theta, t) = \zeta(x, \theta, t), \tag{5}$$

where $\zeta(x, \theta, t)$ is an acoustic perturbation. The normal to the interface is tilted due to the slope of the shear layer approximately by

$$\Delta \mathbf{n}_s = -\frac{\partial \zeta}{\partial x} \mathbf{n}_t, \tag{6}$$

where $\mathbf{n}_s$ can be written in terms of the unit vectors $\mathbf{n}$, $\mathbf{n}_t$, which are normal and tangent to the undisplaced shear layer, in the form

$$\mathbf{n}_s = \mathbf{n} - \frac{\partial \zeta}{\partial x} \mathbf{n}_t. \tag{7}$$

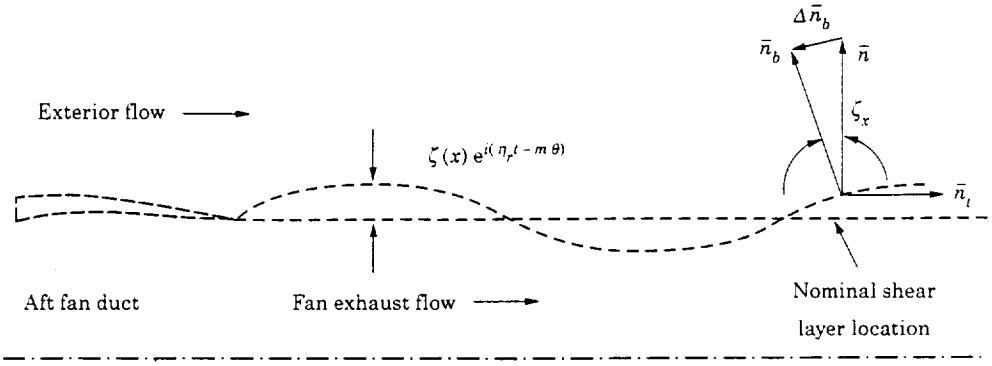

Figure 3. Geometry of the shear layer interface, showing the acoustically displaced boundary between the jet and exterior flow.

The orientation of the unit normals here are consistent with the surface below the shear layer for which the normal out of the fluid is in the direction of the positive normal fluid particle velocity, but a similar argument applies if the surface above the shear layer is considered. The tangential component of the normal to the shear layer is an acoustic perturbation quantity.

The interface conditions across the shear layer can be determined by examining the mass flux and momentum flux at a moving surface of discontinuity. A particularly good explanation is given by Karamcheti [5]. The essential results in the case of a discontinuity in the velocity tangential to the surface of discontinuity are:

$$(\mathbf{V}_u - \mathbf{V}_s)\cdot\mathbf{n}_b = (\mathbf{V}_l - \mathbf{V}_s)\cdot\mathbf{n}_b = 0, \qquad \hat{\rho}_u(\mathbf{V}_u - \mathbf{V}_s)\cdot\mathbf{n}_b - \hat{\rho}_l(\mathbf{V}_l - \mathbf{V}_s)\cdot\mathbf{n}_b = 0, \quad (8, 9)$$

$$\hat{\rho}_u\mathbf{V}_u\cdot\mathbf{n}_b(\mathbf{V}_u - \mathbf{V}_s)\cdot\mathbf{n}_b - \hat{\rho}_l\mathbf{V}_l\cdot\mathbf{n}_b(\mathbf{V}_l - \mathbf{V}_s)\cdot\mathbf{n}_b = \hat{p}_l - \hat{p}_u. \quad (10)$$

Here $\mathbf{V}_u$ and $\mathbf{V}_l$ are the fluid velocity above and below the discontinuity and $\mathbf{V}_s$ is the velocity of an element on the surface of discontinuity. $\hat{\rho}_u$ and $\hat{\rho}_l$ are the fluid densities above and below the discontinuity and $\hat{p}_u$ and $\hat{p}_l$ are the corresponding pressures. Equation (8) follows from the tangential component of the momentum equation and equation (9) from the mass continuity equation. Equation (9) is satisfied automatically due to equation (8). Equation (10) is the component of the momentum equation normal to the discontinuity. With equations (8) and (10) it is determined that

$$\hat{p}_u = \hat{p}_l, \quad (11)$$

which is the condition that pressure be continuous across the shear layer. The linearized version of this would require the acoustic perturbation in pressure to be continuous as well as the pressure of the steady flow.

A linearized version of the surface integral of equation (4) is required for the acoustic analysis which follows. The fluid velocities are replaced by their perturbation forms $\mathbf{V}_u = V_{r_u}\mathbf{n}_t + \mathbf{v}_u$ and $\mathbf{V}_l = V_{r_l}\mathbf{n}_t + \mathbf{v}_l$, where V_{r_u} and V_{r_l} are the mean flow tangential velocities above and below the discontinuity. The densities are replaced by $\hat{\rho}_u = \rho_{r_u} + \rho_u$ and $\hat{\rho}_l = \rho_{r_l} + \rho_l$ with the possibly different mean densities given by ρ_{r_u} and ρ_{r_l}. The acoustic quantities are now ρ_u and ρ_l. It is also important to note that the velocity of an element of the surface of discontinuity is an acoustic quantity and is therefore denoted by $\mathbf{V}_s = \mathbf{v}_s$.

Equation (7), and equation (8) in linearized form, are equivalent to the familiar conditions of continuity of particle displacement,

$$\mathbf{v}_u \cdot \mathbf{n} = \frac{\partial \zeta}{\partial t} + V_{r_u} \frac{\partial \zeta}{\partial x}, \qquad \mathbf{v}_l \cdot \mathbf{n} = \frac{\partial \zeta}{\partial t} + V_{r_l} \frac{\partial \zeta}{\partial x}. \tag{12, 13}$$

The linearized form of the surface integral of equation (4) on the upper and lower surfaces of the shear layer can then be obtained by using equation (7) and equations (12) and (13) (and accounting properly for the evaluation of the integral on the surface above the shear layer):

$$\iint_{S_{s_l}} W(\hat{\rho}\mathbf{V})_l \cdot \mathbf{n}_{h_l} \, \mathrm{d}S = \iint_{S_{s_l}} W \rho_{r_l} \frac{\partial \zeta}{\partial t} \, \mathrm{d}S, \tag{14}$$

$$\iint_{S_{s_u}} W(\hat{\rho}\mathbf{V})_u \cdot \mathbf{n}_{h_u} \, \mathrm{d}S = -\iint_{S_{s_u}} W \rho_{r_u} \frac{\partial \zeta}{\partial t} \, \mathrm{d}S. \tag{15}$$

It is apparent from equations (14) and (15) that along the shear layer the net contribution of the surface integrals will vanish if the steady flow densities above and below the shear layer are the same. If they are different, as in the case of a hot jet in a cold outer medium, there will be a net contribution which is effectively a distributed source on the shear layer with a strength proportional to the difference in the steady flow densities. This is completely consistent with equation (9). It is also consistent with the rigorous analysis given by Myers [6].

4. LINEARIZED WEAK FORMULATION

A linearized weak formulation is obtained by continuing with equation (4) for which the linearization of the boundary integral has been examined. Acoustic propagation and radiation is modelled based on the assumption that the mean flow in and around the nacelle is irrotational and that the acoustic perturbation is also irrotational. The potential formulation makes it possible to introduce mean flow and acoustic perturbation velocity potentials. Acoustic perturbations are assumed on the steady mean flow such that $\hat{\phi} = \phi_r + \phi$, $\hat{\rho} = \rho_r + \rho$ and $\hat{p} = p_r + p$. The acoustic perturbations are assumed to be harmonic in time and in the angular co-ordinate such that $\rho(x, r, \theta, t) = \rho(x, r)\, \mathrm{e}^{\mathrm{i}(\eta_r t - m\theta)}$, $p(x, r, \theta, t) = p(x, r)\, \mathrm{e}^{\mathrm{i}(\eta_r t - m\theta)}$ and $\phi(x, r, \theta, t) = \phi(x, r)\, \mathrm{e}^{\mathrm{i}(\eta_r t - m\theta)}$. The acoustic perturbation in the shear layer position is also assumed to be harmonic in time and the angular co-ordinate yielding $\zeta(x, \theta, t) = \zeta(x)\, \mathrm{e}^{\mathrm{i}(\eta_r t - m\theta)}$. The steady flow density and velocity are ρ_r, $\nabla\phi_r$. In linearized form, the weak formulation of equation (4) becomes [4]

$$\iiint_V \{\nabla W \cdot (\rho_r \nabla\phi + \rho \nabla\phi_r) - \mathrm{i}\eta_r W \rho\} \, \mathrm{d}V = \mathrm{i}\eta_r \iint_{S_s} W(\rho_{r_l} - \rho_{r_u})\zeta \, \mathrm{d}S + \iint_S W(\rho_r \nabla\phi + \rho \nabla\phi_r) \cdot \mathbf{n} \, \mathrm{d}S. \tag{16}$$

The weighting functions are taken as $W(x, r, \theta) = W(x, r)\, \mathrm{e}^{\mathrm{i}m\theta}$. Perturbations are in the form of angular harmonics proportional to $\mathrm{e}^{-\mathrm{i}m\theta}$ representing the decomposition of the

solution periodic in θ in a Fourier Series. The angular mode number is a parameter of the solution. The first surface integral on the right hand side is on the shear layer S_s and the second surface integral is over all remaining surfaces bounding the domain. Notice that the unit normal for the second integral is the normal out of the domain at the surface in question. The weak formulation continues with the linearized momentum equation [4]

$$\rho = -\frac{\rho_r}{c_r^2}(i\eta_r\phi + \nabla\phi_r \cdot \nabla\phi), \tag{17}$$

which is used to replace ρ in equation (16), the linearized equation of state,

$$p = c_r^2\rho, \tag{18}$$

which is used to produce an alternative form of the momentum equation in terms of acoustic pressure,

$$p = -\rho_r(i\eta_r\phi + \nabla\phi_r \cdot \nabla\phi). \tag{19}$$

Equation (19) is used to define acoustic pressure difference on the shear layer and to post-process the field solution for ϕ to obtain the acoustic pressure field. The acoustic particle velocity and acoustic velocity potential are related according to

$$\mathbf{v} = \nabla\phi. \tag{20}$$

The linearization process also produces the weighted residual formulation for the steady flow,

$$\iiint_V \nabla W \cdot (\rho_r \nabla\phi_r)\,\mathrm{d}V = \iint_S W(\rho_r \nabla\phi_r) \cdot \mathbf{n}\,\mathrm{d}S, \tag{21}$$

and the steady flow momentum equation in terms of the speed of sound,

$$c_r^2 = 1 - \frac{(\gamma - 1)}{2}[\nabla\phi_r \cdot \nabla\phi_r - M_\infty^2], \tag{22}$$

and in terms of the steady flow density,

$$\rho_r = \left[1 - \frac{(\gamma - 1)}{2}(\nabla\phi_r \cdot \nabla\phi_r - M_\infty^2)\right]^{1/(\gamma-1)}. \tag{23}$$

Equations (16) through (23) are in non-dimensional form where ϕ is the acoustic potential, ϕ_r is the local mean flow (reference) potential, ρ is the acoustic density, ρ_r is the local mean flow density, and c_r is the local speed of sound in the mean flow. All quantities are made non-dimensional by using the density in the far field, ρ_∞, the speed of sound in the far field, c_∞, and a reference length which is defined as the duct radius at the source plane, R, where acoustic modal amplitudes are defined. This plane could be the fan plane or the exit guide vane plane, but it is not restricted to these locations. The acoustic potential is non-dimensional with respect to $c_\infty R$, and the acoustic pressure with respect to $\rho_\infty c_\infty^2$. Lengths are made non-dimensional with respect to R. Time is scaled with R/c_∞, leading to the definition of non-dimensional frequency $\eta_r = \omega R/c_\infty$; ω is the dimensional source frequency and $M_\infty = M_a$ is the Mach number in the far field representing the forward flight effect.

Equation (21) is the weighted residual formulation for the calculation of the compressible potential flow within and around the nacelle. Equations (22) and (23) are subsidiary relations that can be used in an iterative solution which at each stage uses a density field derived from the previous iteration step. $\nabla\phi_r$, c_r, ρ_r are required data for the weighted residual formulation of the acoustic problem. In the results reported here only the first iteration of this process is used to define the potential flow field. This is accomplished by solving the incompressible problem and then computing a variation in steady flow density and speed of sound.

The second surface integral in equation (16) provides the boundary conditions on the duct walls and on the source plane. The modelling of duct acoustic treatment in the context of this integral is discussed in a later section. The acoustic source is specified by the complex amplitudes of acoustic duct modes at the source plane. On this plane the FEM modal values of acoustic potential are replaced by the complex amplitudes of the acoustic potential modes by an eigenfunction expansion. The incident acoustic modal amplitudes are input and the reflected modal amplitudes are computed as part of the solution. Details of this procedure are available in references [1–4].

The same surface integral provides the mechanism for introducing the boundary conditions on the artificial baffle and the non-reflecting boundary condition at large distances on the outer boundary of the computational domain. These details are also explained extensively in references [1–4].

Acoustic pressure and particle displacement are continuous across the shear layer. The continuity of particle displacement is implicit in the handling of the surface integral on the shear layer. Continuity of pressure must be explicitly enforced. The implementation of this condition will be discussed presently.

5. COMPUTATIONAL MESH

A particularly sensitive issue which must be resolved is the construction of a mesh which is consistent with the geometry requirements and which can be generated automatically from data describing the nacelle and centre body. It is essential that the mesh be structured to minimize the bandwidth for the linear equation solver. The major constraining feature is that the trailing edge of the fan duct is thin or cusped. In addition, the near field mesh must evolve into a smooth transition to the far field wave envelope mesh.

In order to meet all of these requirements, a mesh which combines quadrilateral and triangular elements has been used. Figure 4 shows the details of the near field mesh. The interior of the duct and the extended jet uses conventional eight-node quadrilateral elements. Most of the exterior region is also composed of quadrilateral elements. However, a fan shaped region of six-node triangular elements is used to allow a transition around the sharp trialing edge. Primarily due to the constraint on the mesh structure for minimizing bandwidth, this transition would not be possible with rectangular elements without introducing severe distortion in the neighbourhood of the trailing edge. The far field mesh utilizes the wave envelope element concept [1–4], and presents no problems. A relatively coarse near and far field mesh is shown in Figure 5 and the wave envelope element region can be seen. Note in Figure 4 that the exhaust duct trailing edge is reflexed, representing the most severe case.

Mesh generation produces two mesh connectivities. For the potential flow code, velocity potential is discontinuous across the shear layer dividing the extended jet from the external flow. Elements are therefore disconnected across the shear layer. For the radiation code, acoustic velocity potential is also discontinuous across the shear layer. Elements above and below the shear layer have additional degrees of freedom on the shear layer boundaries

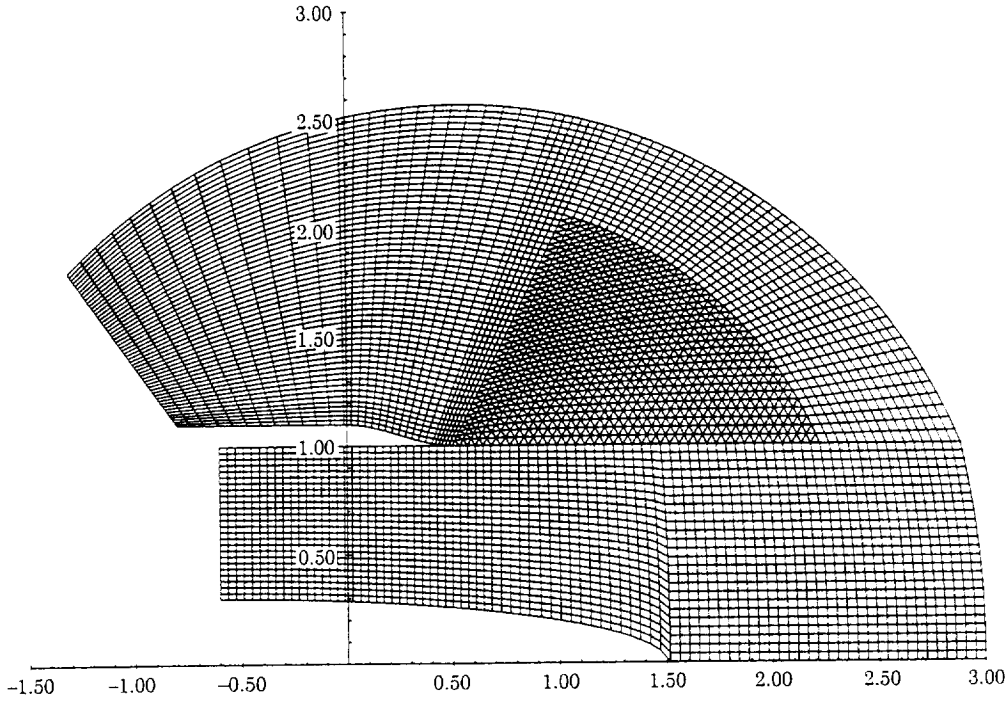

Figure 4. Aft fan duct near field mesh.

representing acoustic particle displacement, which is continuous across the shear layer. The mesh for the radiation code therefore introduces two degrees of freedom at the nodes on the shear layer. There are 11 degrees of freedom for rectangular elements and nine degrees of freedom for triangular elements on the shear layer. Pressure continuity is enforced by

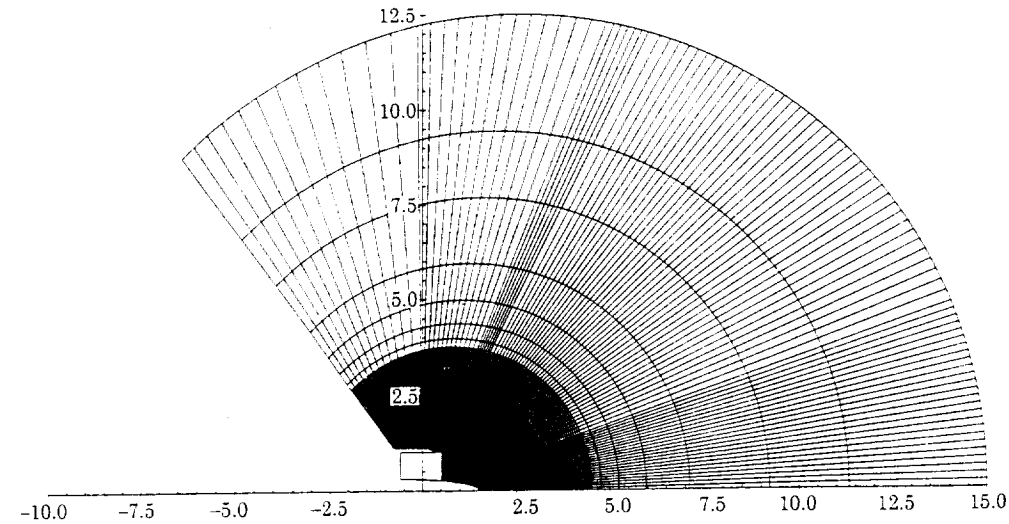

Figure 5. Aft fan duct far field mesh with wave envelope region.

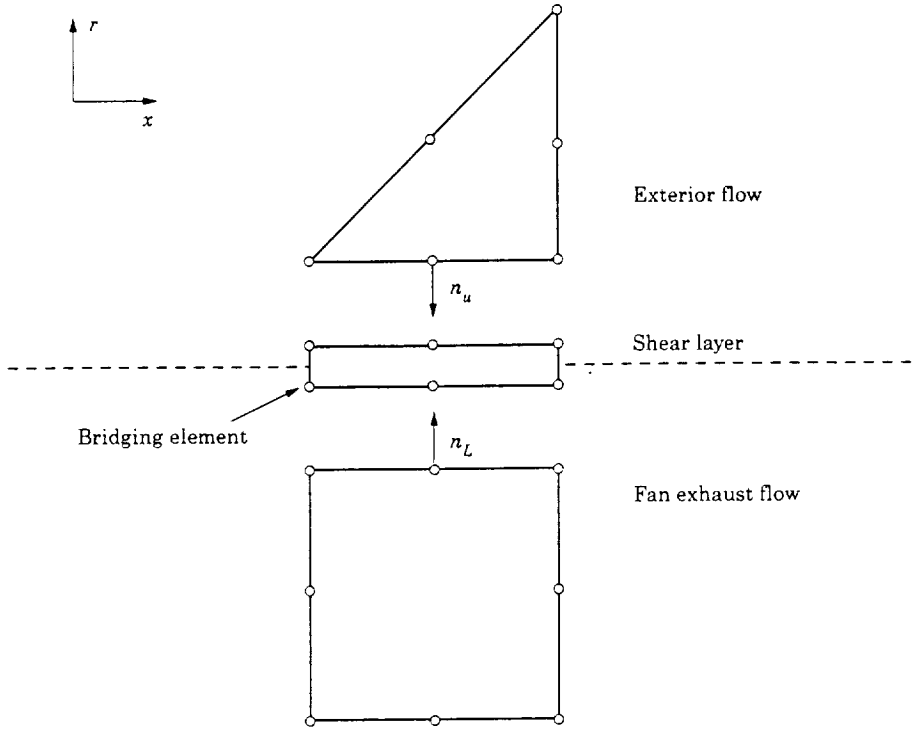

Figure 6. Bridging elements on the shear layer.

using a penalty constraint on the shear layer, and it is not necessary to introduce pressure as an additional variable on the shear layer. However, it has been found convenient to introduce six-node "rectangular" transition elements of zero thickness between the standard elements above and below the shear layer for generating the "penalty element stiffness matrices". In order to maintain consistency in the meshes for the potential flow calculations and radiation calculations, these elements are accounted for in mesh generation for both codes. Details of the elements on the shear layer are shown in Figure 6 where for an example a bridging element is inserted between a triangular element above the shear layer and a rectangular element below the shear layer.

6. STEADY FLOW CALCULATIONS

A potential flow code generates the steady flow field in and around the aft fan duct. Incompressible potential flow has been assumed as a first approximation. Variations in density and speed of sound are based on the isentropic equation of state and incompressible velocity field with specified conditions on Mach number, density, and speed of sound in the far field. It is within the framework of the general formulation to treat the potential mean flow as compressible, and the present approach can be viewed as the "zeroth" iteration of the compressible isentropic case. Fully compressible isentropic mean flow has been used by the first author in acoustic propagation and scattering calculations in pipes in which no far field radiation is modelled. In the type of problem considered here the computational overhead required for the several iterations necessary to produce a compressible mean flow has not been considered justifiable at the present stage of development.

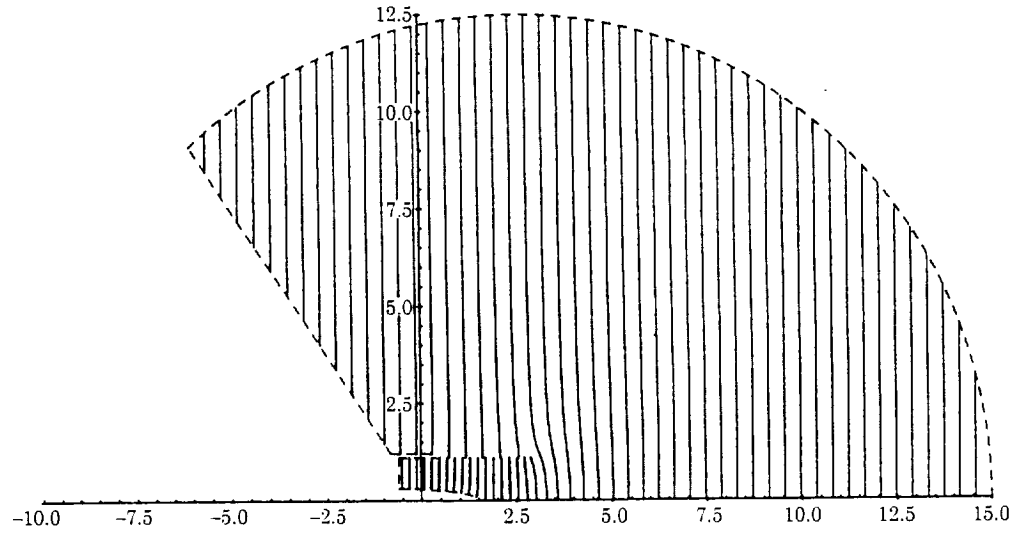

Figure 7. Potential field for the steady flow from the aft fan duct and in the surrounding flow field. This case corresponds to $M_r = 0{\cdot}5$ and forward flight velocity $M_0 = 0{\cdot}2$.

The potential flow field has been structured to include flow in a jet region downstream of the fan duct exit plane. This has been done with the introduction of a "rigid" duct boundary representing the fan exhaust shear layer which extends the prescribed length of the jet. The rigid boundary is introduced by permitting the velocity potential to be discontinuous across the shear layer. At the downstream end of the shear layer the discontinuity in velocity potential is terminated and merging of the interior and external flows is permitted. The merging can produce very high velocities and reverse flow near the termination of the shear layer. This is smoothed out by restricting the velocity near the end of the shear layer to neither go above a reference velocity which is determined midway along the underside of the shear layer (in the jet) nor to go below a similarly determined velocity on the upper side of the shear layer (in the outer flow). In the near field mesh of Figure 4 the shear layer boundary can be seen to extend downstream about two duct radii. The merging distance is adjustable, and is chosen to provide sufficient distance for full effect on the acoustic radiation, and to move the perhaps unrealistic merging region away from the important part of the acoustic field. Computations for the steady flow field are carried out on the same mesh used in the acoustic case. This is done so that the steady flow data is produced in a form compatible with the acoustic mesh. The mesh is invariably much more dense than would be required for the steady flow calculations, however, the problem is symmetric, and the solution routine is considerably faster than for the comparable acoustic problem (about three or four times faster for large meshes).

A typical potential flow field is shown in Figure 7, where the jet and surrounding forward flight effect contours of velocity potential are clearly shown.

7. ACOUSTIC PRESSURE CONTINUITY ON THE SHEAR LAYER

The linearized weak formulation of equation (16) has the subsidiary condition of continuity of acoustic pressure across the shear layer. This condition is not easily satisfied because the formulation is in terms of acoustic velocity potential. However, equation (19) provides a connection between the acoustic velocity potential above and below the shear

layer which can be exploited to implement the continuity condition by using a penalty method [7].

The important features of the penalty method can be described relatively easily. Equation (19) and the condition pressure continuity on the shear layer are used to obtain

$$\Delta p = p_u - p_l = \rho_{r_l}\left(i\eta_r\phi_l + M_l\frac{\partial\phi_l}{\partial x}\right) - \rho_{r_u}\left(i\eta_r\phi_u + M_u\frac{\partial\phi_u}{\partial x}\right) = 0. \tag{24}$$

Equation (24) applies computationally on the shear layer, $r = r_j$, $x_1 \leqslant x \leqslant x_2$, where r_j is the radius of the axially symmetric shear layer and x_1, x_2 are the axial co-ordinates of the left and right ends of the shear layer; x_1 coincides with the trailing edge of the nacelle at the fan exit plane. The subscripts l and u denote values of the steady state and acoustic quantities below and above the shear layer. In the finite element context, the acoustic potentials ϕ_l and ϕ_u can be written notionally in terms of a global interpolation matrix $[N(x)]$. For example,

$$\phi_l(x) = [N(x)]\underline{\phi}_l, \tag{25}$$

where $\underline{\phi}_l$ is the vector of nodal values of $\phi_l(x)$ below the shear layer. The interpolation matrix $[N(x)]$ is a row matrix with elements $N_i(x)$, $i = 1, NN$, where NN is the number of finite element nodes and $N_i(x_j) = 1$, $i = j$, $N_i(x_j) = 0$, $i \neq j$, $j = 1, NN$. The substantial derivative operators in equation (24) are defined such that, for example,

$$D_l(\phi_l) = \rho_{r_l}\left(i\eta_r + M_l\frac{\partial}{\partial x}\right)\phi_l. \tag{26}$$

In vector–matrix format,

$$D_l(\phi_l) = [N(x)][D_l]\underline{\phi}_l, \tag{27}$$

where $[D_l]$ is a diagonal matrix of operators $\rho_{r_l}(i\eta_r + M_l\,\partial/\partial x)$. Equation (24) can be written as

$$[N_p(x)][\phi_l, \phi_u]^T = ([N(x)][D_l] - [N(x)][D_u])[\phi_l, \phi_u]^T = 0. \tag{28}$$

The modified interpolation matrix $[N_p(x)]$ has elements which can be viewed as interpolating $\Delta p(x)$ from nodal values of the acoustic potential on either side of the shear layer. The weighted residual of equation (28) is formed on the shear layer using as weighting functions elements of $[N_p^*(x)]$, which are the complex conjugates of the interpolation functions. This yields

$$\iint_{S_s} [N_p^*(x)]^T[N_p(x)]\,\mathrm{d}S_s[\phi_l, \phi_u]^T = 0. \tag{29}$$

This is a weighted residual (or variational) statement that Δp vanishes on the shear layer. It produces a "stiffness matrix" which is consistent with this statement. If this is appended to the weighted residual formulation of equation (16) with a large multiplier λ, it forces

the weighted residual formulation to have a solution constrained by equation (24). The modified weighted residual statement is written as

$$\iiint_V \{\nabla W \cdot (\rho_r \nabla \phi + \rho \nabla \phi_r) - \mathrm{i}\eta_r W \rho\}\, \mathrm{d}V = \mathrm{i}\eta_r \iint_{S_1} W(\rho_{r_1} - \rho_{r_2})\zeta\, \mathrm{d}S + \iint_S W(\rho_r \nabla \phi + \rho \nabla \phi_r) \cdot \mathbf{n}\, \mathrm{d}S - \lambda \iint_{S_1} \bar{W} \Delta p\, \mathrm{d}S. \tag{30}$$

The weighting functions $\bar{W}(x)$ introduced in equation (30) are the pressure difference interpolation functions identified in equation (28). The penalty integral, equation (29), is introduced along the shear layer and produces penalty stiffness matrices which bridge the shear layer and include nodal values of acoustic potential on both sides of the shear layer. This is most easily implemented in the finite element context by introducing transition or bridging elements on the shear layer as shown in Figure 6. These elements are of zero thickness with three nodes on the top and three on the bottom to connect to the three nodes on the conventional triangular or quadrilateral elements above and below the shear layer. Finite element assembly proceeds as with other elements in the mesh. No new global nodes are introduced and there is no change in the bandwidth of the formulation nor to the sequence of operations in the equation solving procedure.

The boundary integral on S represents natural boundary conditions which must be imposed on the other boundaries of the domain. The far field boundary C_∞ is at a large distance from the nacelle and is a non-reflecting surface on which a radiation condition is applied via the boundary integral. This surface is the outer boundary of wave envelope elements which allow a transition from a fine mesh near the nacelle to a very coarse mesh in the far field. Most of the nacelle and centre body surfaces are rigid, where the normal component of acoustic particle velocity vanishes. In addition, the normal component of the mean flow velocity also vanishes and the flow tangency condition requires that $\nabla \phi_r \cdot \vec{n} = 0$, eliminating the boundary integral. A portion of the fan duct and centre body is acoustically treated. On these surfaces an impedance relation is specified, and this can be introduced through the boundary integral. The acoustic source is also introduced using the boundary integral. Details of the imposition of natural boundary conditions can be found in references [1–4].

In the results presented here there is no difference in steady flow density across the shear layer. The boundary integral on S_1 which arises from considerations of conservation of acoustic particle displacement across the shear layer therefore vanishes.

8. ACOUSTIC TREATMENT ON DUCT WALLS

In the FEM formulation described here provision has been made for acoustic treatment on the duct wall and on the centre body. In the present context the acoustic field is described in terms of an acoustic potential formulation, while the boundary condition relates pressure and particle velocity. The implementation is described in this section.

A locally reacting acoustic lining material specified by its frequency dependent impedance or admittance is placed on an interior surface of the duct. The boundary integral of equation (30) is the mechanism by which the boundary condition imposed by

this acoustic treatment is introduced. On surfaces where acoustic treatment is present the normal component of mean flow velocity vanishes and the lining boundary integral simplifies to

$$I_L = \iint_{S_L} W\rho_r \nabla\phi \cdot \mathbf{n}\, dS, \tag{31}$$

where $\mathbf{v} \cdot \mathbf{n} = \nabla\phi \cdot \mathbf{n}$ is the normal component of acoustic particle velocity, $\mathbf{v}$. The unit normal $\mathbf{n}$ is directed out of the computational domain and therefore into the acoustic treatment. The acoustic treatment is described by a local impedance relationship which connects acoustic pressure to a conceptual wall displacement velocity. In general, the types of acoustic treatment of interest are porous and the wall intself does not displace but the fluid in the pores does. It is the fluid velocity in the porous wall, directed normal to the wall, which is referred to as wall displacement velocity. The impedance relationship is of the form

$$\frac{p}{v_n} = Z = \frac{1}{A}, \tag{32}$$

where p is the non-dimensional acoustic pressure and v_n is the non-dimensional wall displacement velocity, directed into the wall. The impedance Z is a prescribed function of frequency and is non-dimensional with respect to $\rho_\infty c_\infty$, that is, the dimensional impedance would be $\rho_\infty c_\infty Z$. A is defined as the non-dimensional acoustic admittance. The relation between the fluid particle velocity at the wall and the wall velocity is one of continuity of particle displacement. This yields

$$\mathbf{v} \cdot \mathbf{n} = \pm\left(\frac{\partial\zeta}{\partial t} + M_w \frac{\partial\zeta}{\partial x}\right), \tag{33}$$

where $\zeta(x, \theta, t) = \zeta(x)\, e^{i(\eta_r t - m\theta)}$ is the wall displacement normal to the wall mean position, positive directed into the wall, and related to v_n by $v_n = \partial\zeta/\partial t$. M_w is the steady flow velocity at the wall, non-dimensional with respect to c_∞. The choice of positive or negative sign depends on whether the acoustic treatment is on the outer or inner wall of an annular duct. It is assumed that all lined surfaces have negligible curvature in the direction of the duct axis so that the rigorous description of the flow/surface kinematics [6] is simplified. With harmonic time dependence,

$$\mathbf{v} \cdot \mathbf{n} = \frac{1}{i\eta_r}\left(i\eta_r + M_w \frac{\partial}{\partial x}\right) v_n. \tag{34}$$

The relation between acoustic particle velocity and acoustic pressure is

$$\mathbf{v} \cdot \mathbf{n} = \pm\left(i\eta_r + M_w \frac{\partial}{\partial x}\right) Ap. \tag{35}$$

The relation between acoustic pressure and acoustic velocity potential is provided by the acoustic Bernoulli equation of equation (19). Equation (35) can be rewritten

$$\mathbf{v} \cdot \mathbf{n} = \mp\frac{1}{i\eta_r}\left(i\eta_r + M_w \frac{\partial}{\partial x}\right)\left[\rho_r A\left(i\eta_r + M_w \frac{\partial}{\partial x}\right)\phi\right]. \tag{36}$$

The boundary integral becomes

$$\mp \iint_{S_L} \rho_r W \mathbf{v} \cdot \mathbf{n}\, dS = i\eta_r \iint_{S_L} WA\rho_r^2 \phi\, dS + \iint_{S_L} WA\rho_r^2 M_w \frac{\partial \phi}{\partial x}\, dS$$

$$+ \iint_{S_L} W\rho_r M_w \frac{\partial}{\partial x}[A\rho_r \phi]\, dS - \frac{i}{\eta_r} \iint_{S_L} W\rho_r M_r \frac{\partial}{\partial x}\left[A\rho_r M_w \frac{\partial \phi}{\partial x}\right] dS. \quad (37)$$

The upper and lower sign choice depends on whether the outer or inner wall integral is considered. The first two integrals on a boundary where acoustic treatment is present are easy to implement in the finite element formulation because only continuity of acoustic potential is required. The admittance, A, is assumed piecewise continuous and non-zero on a portion of the interior surface of the duct. An integration by parts, which is essentially an application of Stokes' Theorem on the interior surface, is performed to make the last two integrals compatible with the weak formulation. The integral representing the boundary condition on interior surfaces can now be written

$$\mp \iint_{S_L} \rho_r W \mathbf{v} \cdot \mathbf{n}\, dS = i\eta_r \iint_{S_L} WA\rho_r^2 \phi\, dS + \iint_{S_L} WA\rho_r^2 M_w \frac{\partial \phi}{\partial x}\, dS$$

$$- \iint_{S_L} (A\rho_r \phi) \frac{\partial}{\partial x}(W\rho_r M_w)\, dS + \frac{i}{\eta_r} \iint_{S_L} \left(A\rho_r M_w \frac{\partial \phi}{\partial x}\right) \frac{\partial}{\partial x}(W\rho_r M_w)\, dS. \quad (38)$$

Equation (38) is in a form which is appropriate for application of standard finite element techniques to generate "boundary matrices" which are appended to the element stiffness matrices of elements whose outer boundaries represent acoustically treated surfaces.

9. AN ABSORBING BAFFLE

A restriction of the present FEM mesh is the presence of the baffle which is used to limit the computational domain, presumably with little reduction in the quality of the solution. It is assumed that the baffle is swept back at least 90° from the angle of peak radiation, however, this condition is often violated because it requires a mesh generation change to accomplish it. In theory the baffle is non-reflecting at large distances from the nacelle since it is a ray extending from the origin [2]. Near the intersection of the baffle and the nacelle the baffle is a reflecting surface and its presence has the possibility of contaminating the solution with spurious reflections. Experience has shown that the baffle has little effect on the peak lobe in the radiation pattern if the 90° rule is adhered to. However, there has been interest in using the inlet code and aft radiation code to generate the SPL directivity on the full 180° arc around the engine. This would be accomplished by separately obtaining the inlet and aft radiation results and then superposing them. Presumably, the peak lobes fore and aft would be little affected but the region at 90° to the engine axis would be critically dependent on a legitimate superposition of the inlet and aft results. This is not possible to achieve because of the baffle, unless it is completely non-reflecting.

An investigation has been made of the possibility of making the baffle at least partially non-reflecting. This has been done by introducing absorption on the baffle. As in the case of the nacelle acoustic treatment, this is done through the surface integral on S in

equation (30). On the baffle it is assumed that the flow is adequately represented by the uniform Mach number $\mathbf{M}_\infty = M_x\mathbf{i}$. This is true far from the nacelle, and is approximately true near the nacelle. The acoustic density perturbation is given by equation (17) evaluated with $\rho_r = 1$ and $c_r = 1$, assuming that far field steady flow conditions apply on the baffle. The surface integral on the baffle can then be written as

$$\iint_{S_b} W(\rho_r \nabla\phi + \rho \nabla\phi_r) \cdot \mathbf{n}\, dS = \iint_{S_b} W\left[\nabla\phi \cdot \mathbf{n} - (\mathbf{M}_x \cdot \mathbf{n})\left(\frac{\partial\phi}{\partial t} + \mathbf{M}_x \cdot \nabla\phi\right)\right] dS, \quad (39)$$

where $\mathbf{n}$ is the unit normal of the computational domain. The impedance condition on the baffle surface is defined simply as

$$p = \frac{Z_b}{\rho_\infty c_\infty}\mathbf{v} \cdot \mathbf{n}. \quad (40)$$

$Z_b/\rho_\infty c_\infty$ is the non-dimensional impedance and $Z_b/\rho_\infty c_\infty = 1/A$, where A is the non-dimensional admittance. This impedance condition corresponds to no real physical situation but rather is introduced to provide absorption on a notional boundary through which there is a steady mean flow. The acoustic Bernoulli equation (19) and the definition of the acoustic velocity potential

$$\mathbf{v} = \nabla\phi \quad (41)$$

leads to the conclusion that on the baffle,

$$\nabla\phi \cdot \mathbf{n} = -\frac{\rho_\infty c_\infty}{Z_b}\left(\frac{\partial\phi}{\partial t} + \mathbf{M}_\infty \cdot \nabla\phi\right). \quad (42)$$

The boundary integral can therefore be written as

$$\iint_{S_b} W(\rho_r \nabla\phi + \rho \nabla\phi_r) \cdot \mathbf{n}\, dS = -\iint_{S_b} W\left[\left(\frac{\rho_\infty c_\infty}{Z_b} + \mathbf{M}_\infty \cdot \mathbf{n}\right)\left(\frac{\partial\phi}{\partial t} + \mathbf{M}_\infty \cdot \nabla\phi\right)\right] dS. \quad (43)$$

The boundary integral of equation (43) is applied only in the near field portion of the baffle. In the wave envelope region the theoretically non-reflecting character of the far field baffle is left unchanged. The introduction of a locally reacting impedance boundary on the baffle cannot be expected to produce complete absorption any more than on the wall of a duct. As will be shown, only a modest absorption can be achieved.

10. POSTPROCESSING

Postprocessing of the acoustic velocity potential solution using the acoustic Bernoulli equation (19) to obtain acoustic pressure can be carried out in two ways. The approach which is most efficient computes acoustic pressure at the element nodes using the element shape functions. The nodal values are then averaged, to account for the fact that derivatives of potential are not continuous across element boundaries in the FEM formulation. For sufficiently fine meshes this produces acceptable results. Results presented in this paper are obtained by this method.

A second method available for postprocessing acoustic velocity potential to obtain acoustic pressure carries out the calculations at Gauss points in each element. The Gauss

points are known to be points at which optimal accuracy is achieved in the calculation of derivatives and therefore in calculation of acoustic pressure. The number of Gauss points is generally less than the number used in the Gauss integration in the formulation of the element stiffness matrices. The array of solution points on the grid constructed in this way can then be plotted as contours of equal acoustic pressure or equal sound pressure level using one of several available commercial plotting packages.

11. SOLUTION TECHNIQUES

The principal advantage of the FEM formulation described here is that it is computationally relatively efficient and therefore provides a useful tool for design calculations. This efficiency decreases as the non-dimensional frequency of the acoustic source increases, requiring a proportional increase in the mesh density and a disproportionate increase in computation time (by approximately the square of the ratio in mesh density). For this reason it is appropriate to give some observations on the linear equation solving routine which accounts for almost the entire computational time.

Previous fan noise radiation codes [1–4] used a frontal solver due to Irons [8]. This was extremely efficient in the use of active memory, partly because of considerable data transfer using direct access I/O in storing and retrieving element stiffness matrices in the assembly/solution procedure and in retrieving mesh and steady flow data. The resulting direct access files were subsequently read many times in the various FEM operations and in postprocessing. This efficiency in storage was offset by a significant cost in execution time. Nacelle design and source modelling have become the primary uses of the codes and execution time is a primary issue in a work station environment in which storage has become a much less limiting factor. Direct access operations are efficient from a programming standpoint, but inefficient in I/O time. In the version of the radiation code reported here all direct access I/O has been eliminated in favour of active storage or sequential I/O. This has resulted in as much as 50% reduction in computation time, dependent mainly on available fast memory.

Experiments with several popular iterative solution routines show that for the two-dimensional structure of problems considered here the direct solvers are always faster. This is consistent with the experience of other investigators [9]. There are indications that iterative solvers can be faster for similar problems in a three-dimensional geometry. The choice has been made to retain the modified Irons frontal solver.

12. EXAMPLE CALCULATIONS

The example calculations shown here are obtained on a mesh with about 27 000 degrees of freedom which is shown in Figures 4 and 5. This mesh becomes inadequate for non-dimensional frequencies much in excess of $\eta_r = 25$, and with the element distribution shown does better for acoustic radiation toward the sideline (high angular mode number or high radial mode number). Angular mode order corresponds to the value of m in the angular Fourier component $e^{-im\theta}$. Radial modes for a specified angular mode are enumerated beginning with $n = 1$. The geometry of the aft fan duct is generic, including an extended centre body and thin fan duct lip, in this case reflexed. The exterior Mach number is $M_\infty = 0{\cdot}2$ and the jet Mach number at the source plane is $M_j = 0{\cdot}5$.

The first result shows the success of the penalty method in implementing the condition of continuity of acoustic pressure across the shear layer. This is most effectively shown at low frequency because the acoustic field is relatively simple and the discontinuity in acoustic potential and continuity in acoustic pressure is easy to see. The frequency chosen

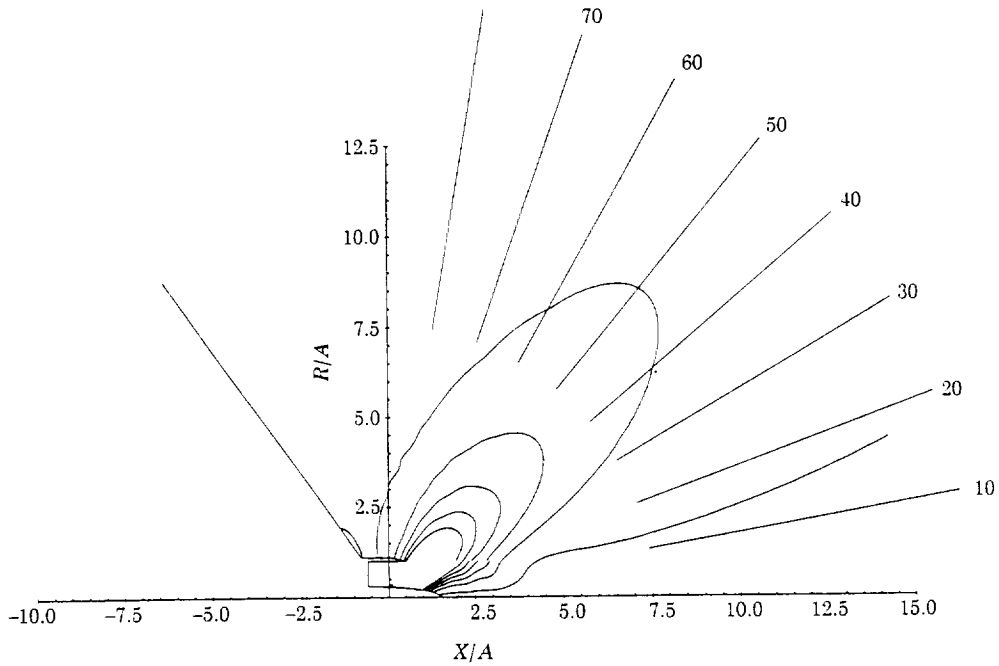

Figure 8. Contours of equal acoustic potential with $M_f = 0{\cdot}5$, $M_0 = 0{\cdot}2$. Reduced frequency $\eta_r = 5{\cdot}0$, input angular mode $m = 2$, radial mode $n = 1$, no acoustic treatment. Acoustic potential is discontinuous across the shear layer.

is $\eta_r = 5$ with an angular mode $m = 2$ and radial mode $n = 1$ input with unit pressure amplitude. The mesh is quite adequate for this low frequency. Figure 8 shows the radiated field in terms of contours of constant acoustic potential magnitude superimposed on the computational domain. In this example only five contours are produced to simplify the plot. The contours range from 15 dB above the maximum level on the outer boundary to 15 dB below. In Figure 8 it is clearly seen that the acoustic potential is discontinuous across the shear layer. Figure 9 shows similar contours of acoustic pressure and these are seen to be continuous across the shear layer. The pressure has been obtained by post-processing the potential field by using equation (19) with FEM interpolation at the nodes. Pressures thus obtained are averaged at common nodes. It is important to note that nodes across the shear layer are not common and the pressure across the shear layer is not averaged. The effectiveness of the penalty method is demonstrated by this example, as is the quality of the solution at this low frequency. Figure 10 shows an additional method of presentation of the radiation directivity. This represents calculations of sound pressure level on a circular arc at a radius of 10 duct radii from the origin, normalized to 100 dB maximum. In this case it emphasizes how broad the principle lobe is near the peak.

The results of Figure 10 can be used to compare the peak radiation angle in the principal lobe in the far field to predictions obtained using ray theory. A code has been written which is based on the analysis of Rice and Saule [10] for estimation of the radiation directivity from an exhaust duct. It is based on an extended analysis since it considers annular ducts while the original work of Rice and Saule considered only circular ducts. Propagation angles in the duct are determined from a formal eigenvalue/eigenfunction analysis and the convection and refraction effects are included as in reference [10]. It is predicted that the group velocity in the duct at the specified frequency and in the specified mode, $\eta_r = 5$, $m = 2$, $n = 1$, is at 34·7°, and the phase velocity is at 51.2°. The peak propagation angle

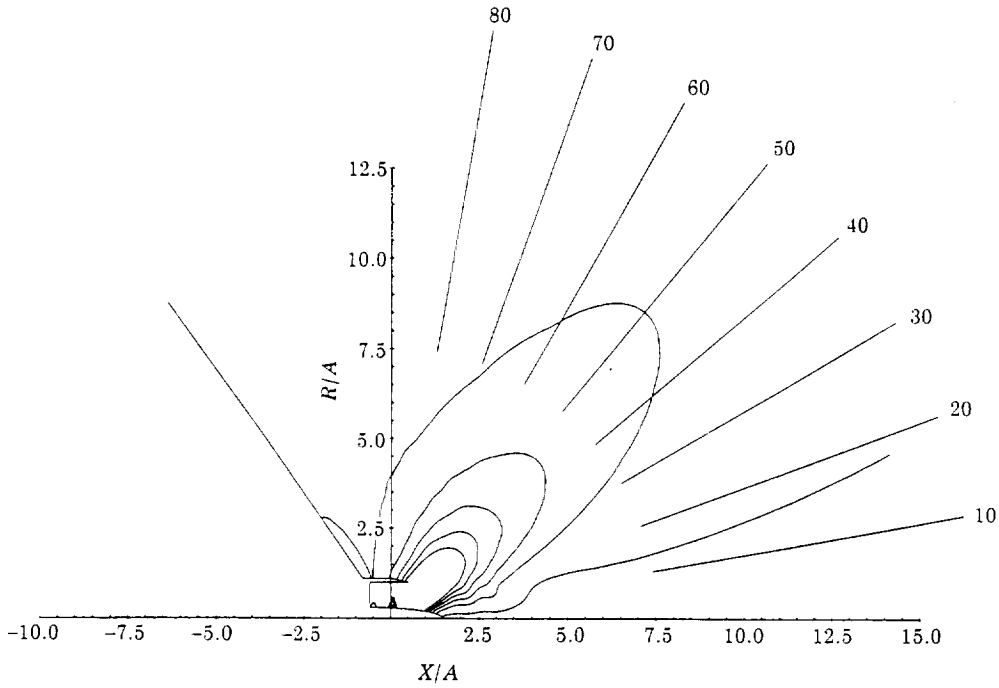

Figure 9. Contours of equal acoustic pressure with $M_j = 0{\cdot}5$, $M_0 = 0{\cdot}2$. Reduced frequency $\eta_r = 5{\cdot}0$, input angular mode $m = 2$, radial mode $n = 1$, no acoustic treatment. Acoustic pressure is continuous across the shear layer.

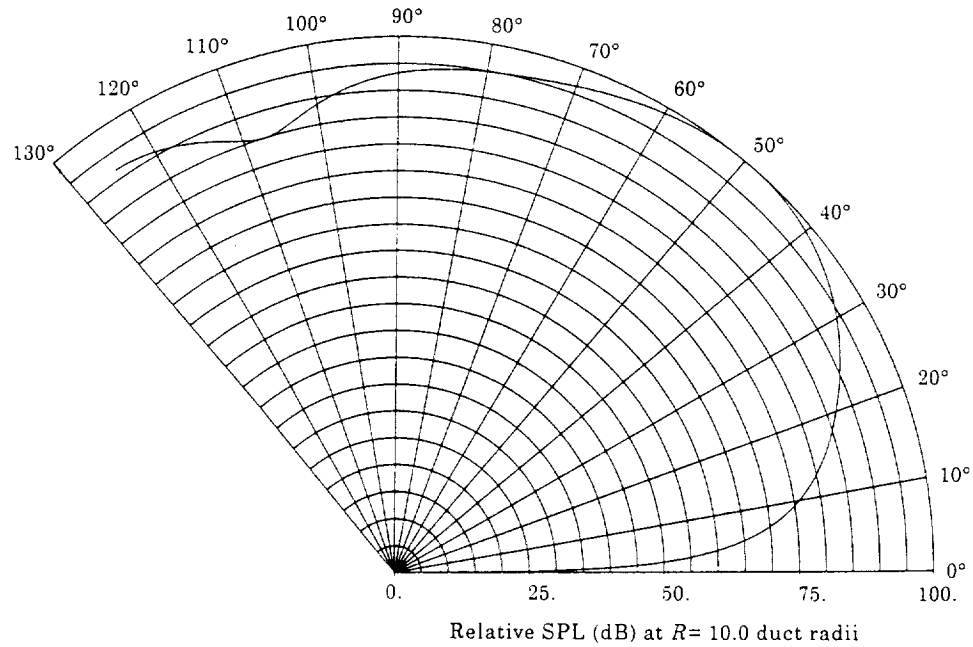

Figure 10. Radiation directivity on a circle of 10 duct radii centred on the computational origin. $M_j = 0{\cdot}50$, $M_0 = 0{\cdot}20$, $\eta_r = 5{\cdot}0$, $m = 2$, $n = 1$.

in the far field is estimated to be 49·5°. The observed angle of peak radiation in Figures 7 and 8 is around 50°, but the peak is so broad that it is difficult to pick the angle precisely. The correlation is excellent, although it must be pointed out that the mesh origin (0·5 duct radii back from the duct exit plane) is used in defining the directivity in this example. The Rice/Saule analysis would be based on an origin at the duct exit plane. Because the peak lobe is so broad there is little point in examining the effect of the origin shift on the stated comparison. This will be done in the next example which produces a sharper peak lobe.

A higher frequency case with a lower angle of peak radiation is the second example. In this case the non-dimensional frequency is $\eta_r = 25$ and the modal input is $m = 10, n = 1$. This is getting close to the limit of resolution for the mesh. Figures 11 and 12 show the two types of presentation for acoustic pressure. Figure 11 showing contours of constant SPL, while generally reasonably clean, emphasizes the assertion that the limit of resolution is close at hand. The breakdown of the mesh adequacy always appears in the near to intermediate field first and is usually related to mesh density in the region between the near field and the wave envelope region. The number of elements required in the generally radial direction is critical, and this can be minimized by bringing the wave envelope region in as close as possible. In the aft radiation case the jet interferes with this, and the wave envelope region must start far enough out that the jet is nearly entirely merged with the exterior flow. Figure 12 shows the polar directivity based on an origin at the exit plane (non-dimensional $x = 0{\cdot}5$) and demonstrates that these far field calculations are generally better than the near field because of the wave envelope interpolation. This mesh has been pushed to $\eta_r = 35$ without complete failure, and has the characteristic that it produces better results for modes which radiate well to the sideline than for those which radiate at relatively small angles to the axis as in these examples. This probably results from the complicated interaction of transmission and reflection of modes at near grazing incidence

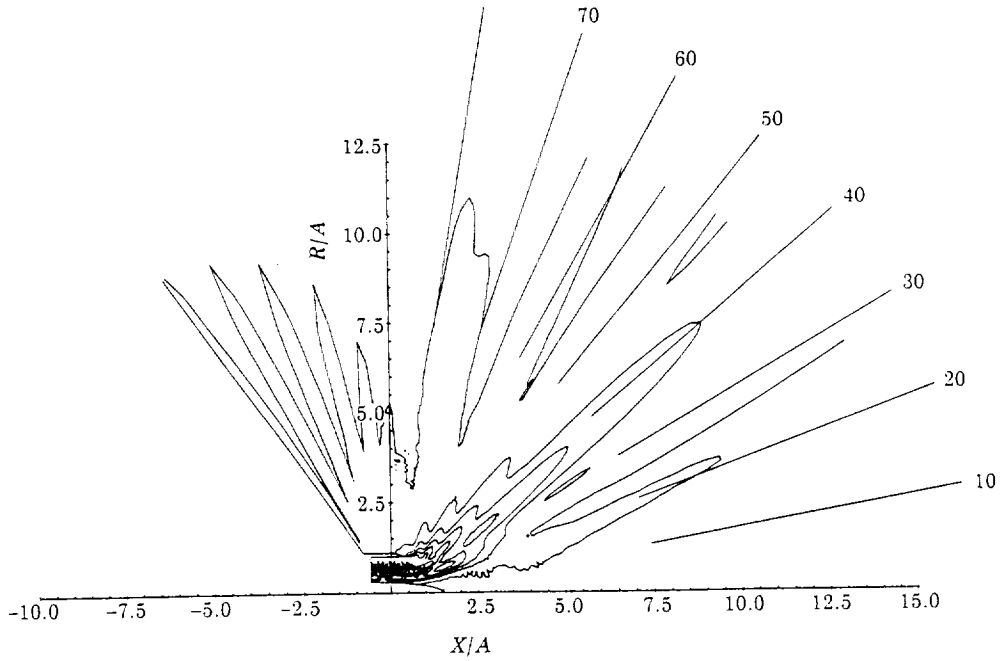

Figure 11. Contours of equal acoustic pressure with $M_j = 0{\cdot}5$, $M_0 = 0{\cdot}2$. Reduced frequency $\eta_r = 25{\cdot}0$, input angular mode $m = 10$, radial mode $n = 1$, no acoustic treatment. Acoustic pressure is continuous across the shear layer.

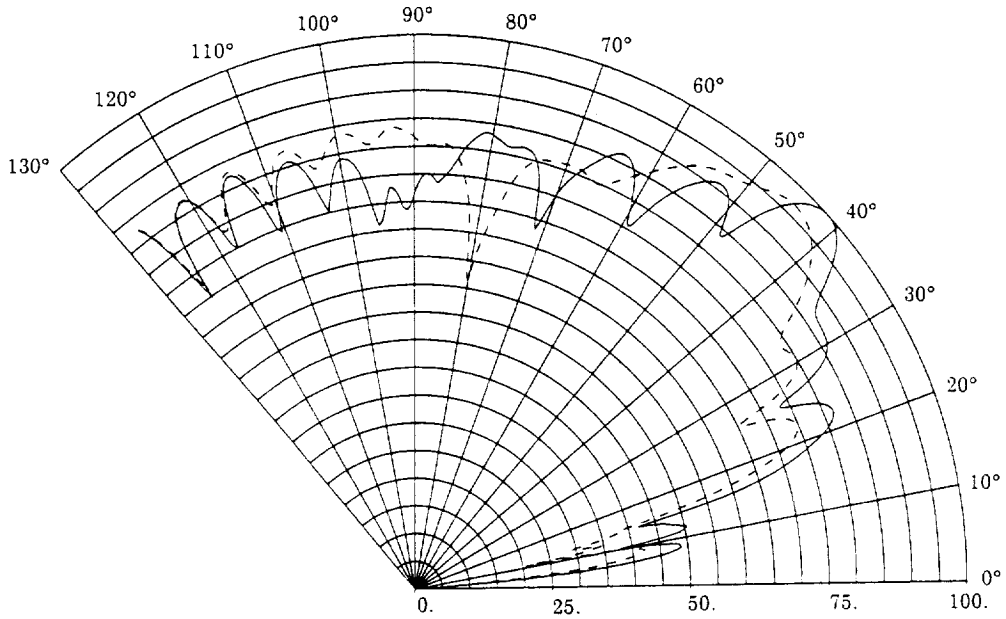

Figure 12. Radiation directivity on a circle of 10 duct radii centred on an origin at the fan duct exit plane. $x = 0{\cdot}5$, $M_f = 0{\cdot}50$, $M_0 = 0{\cdot}20$, $\eta_r = 25{\cdot}0$, $m = 10$, $n = 1$. ——, Case with no acoustic treatment; – –, acoustically treated case with non-dimensional admittance $A = 0{\cdot}811 + i0{\cdot}081$.

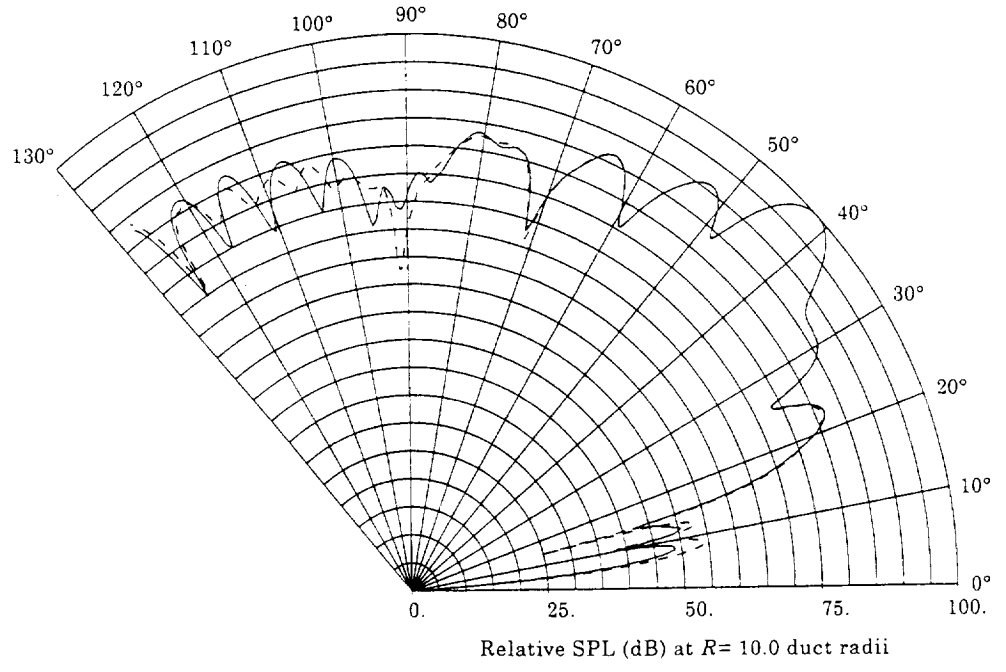

Figure 13. Radiation directivity on a circle of 10 duct radii centred on an origin at the fan duct exit plane. $x = 0{\cdot}5$, $M_f = 0{\cdot}50$, $M_0 = 0{\cdot}20$, $\eta_r = 25{\cdot}0$, $m = 10$, $n = 1$, no acoustic treatment in the duct. ——, Case with the baffle untreated; – – –, case with an absorbing boundary on the baffle in the near field.

at the shear layer. The mesh shown in Figures 4 and 5 has proven to be a good generic structure to work with.

Figure 12 can be used to compare the peak radiation angle in the principal lobe in the far field to predictions obtained using ray theory. It is predicted that the group velocity in the duct at the specified frequency and in the specified mode, $\eta_r = 25$, $m = 10$, $n = 1$, is at 27·4°, and the phase velocity is at 39·4°. The peak propagation angle in the far field is estimated to be 43·9°. The observed angle of peak radiation in Figure 12 is around 42° and is adjusted for the origin shift to the exit plane. The correlation with the Rice/Saule result is good, particularly when it is noted that flow conditions along the shear layer in the FEM calculations are not uniform, and within the jet region the Mach number is reduced below $M_j = 0{\cdot}5$ due to the gradual reduction in radius of the centre body. The effect can be observed if an average Mach number $M_j = 0{\cdot}45$ in the jet is used in the Rice/Saule approximation. The ray prediction would yield 41·9° which is about the same as the FEM prediction which accounts for the non-uniform Mach number in the jet.

An example of the effect of acoustic treatment on the duct walls is also shown in Figure 12. A locally reacting lining with normalized impedance and admittance given by $Z = 1{\cdot}221 - i0{\cdot}122$, $A = 0{\cdot}811 + i0{\cdot}081$ is assumed in the high frequency case. The impedance/admittance is optimum for the $\eta_r = 25$, $M_j = 0{\cdot}5$, $m = 10$, $n = 1$ mode. The outer wall of the fan exhaust duct and the centre body are lined over a length of 0·916 R beginning at 0·074 R forward of the assumed source plane. The attenuated directivity shown in Figure 12 reveals an attenuation of as much as 5 or 6 dB at polar angles below the shifted principal lobe which is now at about 45°. What was once a relatively well-defined principal lobe is now considerably broadened and beyond 45° there are areas in which the SPL is increased, primarily due to filling in of interference notches. The angle shift of the principal lobe is consistent with the fact that the effect of the acoustic treatment would be to increase the angle of the phase velocity and group velocity vectors (lower the cut-off ratio) within the duct.

Finally, Figure 13 is used to show the effect of an attempt to reduce the effects of reflection from the baffle. A resistive "lining" with non-dimensional admittance $A = 0{\cdot}8 + i0{\cdot}0$ has been placed on the baffle in the region of conventional elements (the wave envelope elements in theory should not produce reflections). It is seen that there is an observable change in SPL at large polar angles (near the baffle) and in the region near the exhaust axis where the directly radiated field is at low SPL. Since it is not known what the true reflection free directivity should look like, no conclusion can be drawn other than the baffle does have an effect on the directivity at large angles, and that the effect is modestly changed when the baffle is made dissipative. Perhaps of more importance is the fact that virtually no effect is observed near the principal lobe, suggesting that the baffle has correctly been assumed to be non-intrusive in this region.

While not entirely definitive, the results shown here suggest that the FEM model of aft fan radiation captures the known refraction effects of the shear layer very well. Extensive bench marking of the code against experiments has been carried out by other investigators [11, 12]. Comparisons of calculations and measurements have been very good.

13. CONCLUSION

A finite element model for acoustic propagation and radiation within and exterior to the aft fan duct of a high by-pass turbofan engine has been developed. It is based on the assumption of irrotational acoustic perturbations on an irrotational steady flow. The jet is modelled in the steady flow calculations by a potential flow constrained by a shear layer and allowed to merge with the surrounding flow downstream of the fan duct exit plane.

The formulation is restricted to axisymmetric geometries and harmonic sources described by their angular and radial modal content. The condition of acoustic particle displacement continuity across the shear layer is shown to be satisfied by proper interpretation of a boundary integral which occurs in the FEM formulation. Continuity of acoustic pressure is implemented by introducing a penalty method based on the relationship between acoustic pressure and velocity potential. Example calculations have shown that the continuity of pressure is accurately enforced. Resolution of accurate solutions at high non-dimensional frequencies is limited by mesh density which has implications on storage requirements and execution time. In the present study computations with over 27 000 degrees of freedom have been shown to produce reasonable results up to the reduced frequency $\eta_r = 25$. Doubling the frequency would require an approximate doubling of the density of the mesh.

REFERENCES

1. J. S. PREISSER, R. J. SILCOX, W. EVERSMAN and A. V. PARRETT 1985 *Journal of Aircraft* **22**, 57–62. Flight study of induced turbofan inlet acoustic radiation with theoretical comparisons.
2. W. EVERSMAN, A. V. PARRETT, J. S. PREISSER and R. J. SILCOX 1985 *ASME Journal of Vibration Acoustics, Stress, and Reliability in Design* **107**, 216–223. Contributions to the finite element solution of the fan noise radiation problem.
3. A. V. PARRETT and W. EVERSMAN 1986 *AIAA Journal* **24**, 753–760. Wave envelope and finite element approximations for turbofan noise radiation in flight.
4. I. DANDA ROY and W. EVERSMAN 1995 *ASME Journal of Vibration and Acoustics* **117**, 109–115. Improved finite element modeling of the turbofan engine inlet radiation problem.
5. K. KARAMCHETI 1966 *Principles of Ideal Fluid Aerodynamics*. New York: Wiley. See pp. 190–194, 210–220.
6. M. K. MYERS 1980 *Journal of Sound and Vibration* **71**, 429–434. On the acoustic boundary condition in the presence of flow.
7. T. J. R. HUGHES 1987 *The Finite Element Method, Linear Static and Dynamic Finite Element Analysis*. Englewood Cliffs, NJ: Prentice-Hall. See pp. 185–303.
8. B. M. IRONS 1970 *International Journal for Numerical Methods in Engineering* **2**, 5–32. A frontal solution program for finite element analysis.
9. B. REGAN 1996 *PhD Dissertation, University College Galway, Ireland*. Development of finite element techniques for aeroacoustic applications.
10. E. J. RICE and A. V. SAULE 1980 *NASA TM* 81506. Far field radiation of aft turbofan noise.
11. L. A. HEIDELBERG, D. L. SUTLIFF and M. NALLASAMY 1997 *AIAA Paper AIAA-97-1587, Presented at the 35th Aerospace Sciences Meeting, Reno, NV*. Azimuthal directivity of fan tones containing multiple modes.
12. D. A. TOPOL 1997 *AIAA Paper AIAA-97-1611, Presented at 3rd AIAA/CEAS Aeroacoustics Conference, Atlanta, GA*. Development and evaluation of a coupled fan noise design system.

Journal of Sound and Vibration (1999) **224**(4), 665–687
Article No. jsvi.1999.2235, available online at http://www.idealibrary.com on IDEAL®

MAPPED INFINITE WAVE ENVELOPE ELEMENTS FOR ACOUSTIC RADIATION IN A UNIFORMLY MOVING MEDIUM

WALTER EVERSMAN

Mechanical and Aerospace Engineering and Engineering Mechanics, University of Missouri-Rolla, Rolla, MO 65401, *U.S.A.*

(*Received* 22 *July* 1998, *and in final form* 22 *January* 1999)

Variable order mapped infinite wave envelope elements are developed for finite-element modelling (FEM) of acoustic radiation in a uniformly moving medium. These elements can be used as a non-reflecting boundary condition for computations on an infinite domain in which a radiating body is immersed in a moving medium which is essentially undisturbed outside of the near field. An additional result of this study shows that the mapped wave envelope elements provide a boundary condition equivalent to stiffness, mass, and damping matrices appended to the inner mesh. By choosing the transition between the standard FEM mesh and the mapped infinite wave envelope as a surface of constant phase the mass matrix is caused to vanish identically. This has implications for transient FEM modelling of acoustic radiation. A demonstration of the characteristics of mapped infinite wave envelope elements is given in the context of acoustic radiation from a turbofan inlet for which benchmark results are known.

1. INTRODUCTION

Modelling of acoustic radiation is usually complicated by the requirement that prediction of the acoustic field is required in some finite subdomain of an infinite domain. This requires that computations be limited to the subdomain with a non-reflecting boundary or that the infinite domain be mapped on to a finite computational domain. In finite element modelling this has led to the study of a number of forms of infinite elements [1–3], wave envelope elements [4, 5], and mapped infinite wave envelope elements [6–9]. The several forms of infinite elements in some sense map the infinite domain to a finite domain. Wave envelope elements restrict computations to a large but finite domain bounded by a Sommerfeld radiation condition. The non-reflecting boundary is reached from an inner standard finite-element domain via large elements in which the shape functions are augmented to reflect decay with distance from the source and the temporal and spatial character of outgoing waves. The attributes of infinite elements and wave envelope elements are combined in mapped infinite wave envelope elements.

0022-460X/99/290665 + 23 $30.00/0

Mapped infinite wave envelope elements have been investigated extensively for acoustic radiation in a stationary medium. They have certain apparent advantages as compared to standard wave envelope elements. In the case of harmonic radiation, the most significant advantage is the possibility of adjusting the order of the elements to fit the requirements of the problem. Formulation of the elements reveals the possibility of including within the element shape function an explicit dependence on inverse powers of the distance from the apparent acoustic source, consistent with theoretical results [8]. This fact allows the introduction of mapped infinite wave envelope elements well into what would normally be considered the acoustic near field, reducing mesh refinement and dimensionality. The shape functions in mapped infinite wave envelope elements can accommodate nearfield effects, and this fact can be enhanced by adjusting the order of the interpolation in the elements to fit the problem requirements. A second advantage in the FEM formulation using the mapped infinite wave envelope elements is that the Sommerfeld radiation boundary is infinitely far away and is never explicitly appended as a natural boundary condition. Astley *et al.* [9] also demonstrated the applicability of mapped infinite wave envelope elements to problems in transient acoustic radiation, a feature which has not been exploited in standard wave envelope elements. With an appropriate choice of mesh geometry they show that mapped infinite wave envelope elements provide a boundary condition which is well suited for time-marching solutions. The advantages of the mapped infinite wave envelope elements are not without cost, and the trade-off comes in the form of increased band width of the discretized field equations that is introduced by high order mapped elements. This may offset efficiency gains achieved by reduction of the extent of the computational near field and therefore the standard FEM mesh if bandwidth-sensitive solvers are used.

The study reported here extends the variable order mapped infinite wave envelope concept to uniform steady flows, principally in connection with aeroacoustic problems related to turbofan acoustic radiation. This is a direct extension of the development of Astley *et al.* [8, 9]. They present their formulation in the context of problems in three dimensions in Cartesian co-ordinates. The application here is in a cylindrical co-ordinate system reduced to two dimensions by taking advantage of periodicity of the solution in the angular co-ordinate. The development of the mapped wave envelope elements is completely general and not restricted to this co-ordinate system. Harmonic radiation is considered explicitly; however it is shown here that as in the case of a stationary medium, with a judicious choice of the mesh geometry, the structure of the mapped elements becomes favorable for transient calculations.

2. AN APPLICATION TO TURBOFAN INLET ACOUSTICS

An important problem of acoustic radiation in a moving medium is available in the study of the acoustic field of a turbofan inlet. The noise due to turbo-machinery sources within the inlet is propagated in the inlet and radiated to the (infinite) far field. Acoustic propagation and radiation occurs in a high-speed potential flow which is the net effect of flow into the inlet and the forward flight of the inlet. In the

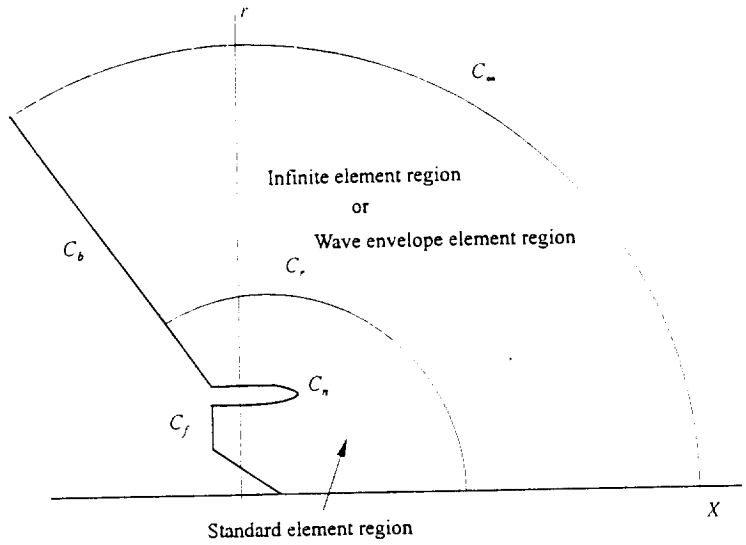

Figure 1. Computational domain showing genetic geometry of the nacelle and boundaries and regions used in the finite element, wave envelope, and mapped infinite wave envelope element formulations.

steady flow far field (perhaps nearer to the inlet than the acoustic far field) acoustic radiation occurs in a uniformly moving medium. It is required to make computations to predict the radiated field in a finite subdomain relatively near the inlet. This has been approached in the past by terminating the computational domain with a Sommerfeld condition on a boundary reached by the use of wave envelope elements [5, 10–12]. Here it is intended to investigate the application of mapped infinite wave envelope elements to obtain closure of the computational domain.

For turbofan inlet acoustic radiation the nacelle geometry and the steady flow field (representing flow into the inlet and forward flight) are assumed to be axially symmetric. The noise source is assumed to be harmonic in time and is decomposed into its angular modal content, allowing a two-dimensional representation of the acoustic field in a plane through the nacelle axis of symmetry. The solution domain is shown in Figure 1. It is the x, r plane in cylindrical co-ordinates. The source plane is designated by C_f. The source is input on this plane by specifying complex amplitudes of incident duct modes [5, 10–12]. The nacelle outer surface is C_n. On this boundary, steady flow and acoustic particle velocities have a vanishing normal component. An artificial baffle C_b formed by a ray from the origin limits the solution domain. The sweep angle is chosen in such a way that minimal effect on the acoustic field is created [13]. The domain of computation is divided into two parts. In an inner region a standard finite-element mesh is used; in the present problem eight-node serendipity elements with the condition that four to five elements per wavelength are required. The near field is terminated on a boundary C_r beyond which farfield elements are used. In previous studies, this region was large but finite and bounded by the surface C_∞, a circle which represents a constant-phase surface

for an acoustic source located at the origin. On this boundary, a radiation condition was specified. Wave envelope elements [5, 10–12] were used in this region. In the present study, the farfield region is extended to infinity and a single layer of mapped infinite wave envelope elements is used to provide a reflection-free boundary on C_r and to compute the acoustic field in the far field as required. The boundary C_∞ is not part of the solution.

3. FINITE ELEMENT FORMULATION

The geometry of the inlet and steady flow field in and around the inlet is axially symmetric. The acoustic field is not axially symmetric but is represented as periodic in a cylindrical co-ordinate system with x being the axis of symmetry, r the cylindrical radius in a circular cross-section at $x = 0$, and θ the angular co-ordinate. Solutions are sought in angular harmonics of a Fourier series enumerated by the angular mode number m. This reduces the solution domain to a two-dimensional x, r plane.

The starting point for the formulation of both the steady mean flow and the acoustic perturbation consists of the inviscid mass and momentum equations and the energy equation in the form of the isentropic equation of state. The acoustic field equations are obtained by considering small perturbations on a steady irrotational mean flow characterized by density ρ_r and speed of sound c_r. This formulation makes it possible to introduce a steady flow velocity potential ϕ_r and an acoustic perturbation velocity potential ϕ. Acoustic perturbations in pressure, density and velocity potential are harmonic in time with frequency η_r and harmonic in the angular co-ordinate θ of the form $p(x, r)e^{i(\eta_r t - m\theta)}$, $\rho(x, r)e^{i(\eta_r t - m\theta)}$, $\phi(x, r)e^{i(\eta_r t - m\theta)}$. In linearized form, the weak formulation is [5, 10–12]

$$\int\int_V \int \{\nabla W \cdot (\rho_r \nabla\phi + \rho \nabla\phi_r) - i\eta_r W \rho\} \, dV = \int_S \int W(\rho_r \nabla\phi + \rho \nabla\phi_r) \cdot \mathbf{n} \, dS \quad (1)$$

The weighting functions are taken as $W(x, r, \theta) = W(x, r)e^{im\theta}$. Angular harmonics proportional to $e^{-im\theta}$ represent the decomposition of the solution periodic in θ in a Fourier series. The angular mode number m is a parameter of the solution. The surface integral is over all surfaces bounding the domain. The unit normal for the surface integral is out of the domain at the surface in question. The weak formulation continues with the linearized momentum equation

$$\rho = -\frac{\rho_r}{c_r^2}(i\eta_r \phi + \nabla\phi_r \cdot \nabla\phi) \quad (2)$$

which is used to replace ρ in equation (1). The linearized equation of state,

$$p = c_r^2 \rho, \quad (3)$$

is used to produce an alternative form of the momentum equation in terms of acoustic pressure,

$$p = -\rho_r(i\eta_r\phi + \nabla\phi_r \cdot \nabla\phi). \tag{4}$$

The acoustic particle velocity and acoustic velocity potential are related according to

$$\mathbf{v} = \nabla\phi. \tag{5}$$

The linearization process also produces the weighted residual formulation for the steady flow,

$$\iiint_V \nabla W \cdot (\rho_r \nabla\phi_r)\,dV = \int_S \int W(\rho_r \nabla\phi_r)\cdot \mathbf{n}\,dS, \tag{6}$$

and the steady flow momentum equation in terms of the speed of sound,

$$c_r^2 = 1 - \frac{(\gamma - 1)}{2}[\nabla\phi_r \cdot \nabla\phi_r - M_\infty^2], \tag{7}$$

and in terms of the steady flow density,

$$\rho_r = \left[1 - \frac{(\gamma - 1)}{2}(\nabla\phi_r \cdot \nabla\phi_r - M_\infty^2)\right]^{1/(\gamma-1)}. \tag{8}$$

Equations (1)–(8) are in non-dimensional form where ϕ is the acoustic potential, ϕ_r is the local mean flow (reference) potential, ρ is the acoustic density, ρ_r is the local mean flow density, p is the acoustic pressure, and c_r is the local speed of sound in the mean flow. All quantities are made non-dimensional by using the density in the far field, ρ_∞, the speed of sound in the far field, c_∞, and a reference length which is defined as the duct radius at the source plane, R, where acoustic modal amplitudes are defined. This plane could be the fan plane or the exit guide vane plane, but it is not restricted to these locations. The acoustic potential is non-dimensional with respect to $c_\infty R$, and the acoustic pressure with respect to $\rho_\infty c_\infty^2$. Lengths are made non-dimensional with respect to R. Time is scaled with R/c_∞, leading to the definition of non-dimensional frequency $\eta_r = \omega R/c_\infty$; ω is the dimensional source frequency. $M_\infty = M_o$ is the Mach number in the far field representing the forward flight effect.

Equation (6) is the weighted residual formulation for the calculation of the compressible potential flow within and around the nacelle. Equations (7) and (8) are subsidiary relations that can be used in an iterative solution which at each stage uses a density field derived from the previous iteration step. $\nabla\phi_r$, c_r, ρ_r are required data for the weighted residual formulation of the acoustic problem. In the results reported here only the first iteration of this process is used to define the potential

flow field. This is accomplished by solving the incompressible problem and then computing a variation in steady flow density and speed of sound.

The surface integral in equation (1) provides the boundary conditions on the duct walls, and at the source. The acoustic source is specified by the complex amplitudes of acoustic duct modes at the source plane. On this plane, the FEM nodal value of acoustic potential are replaced by the complex amplitudes of the acoustic potential modes by an eigenfunction expansion. The incident acoustic modal amplitudes are input and the reflected modal amplitudes are computed as part of the solution. Details of this procedure are available in [5, 10–12].

A previous study [13] shows that the baffle can be positioned to produce practically no effect on typical acoustic radiation patterns. Therefore, there is no contribution from the surface integral on the baffle. In previous studies, the surface integral provided the mechanism for enforcing the Sommerfeld radiation condition on C_∞. In the present application of mapped wave envelope elements the surface integral is never explicitly introduced on a far-field boundary because the assumed form of the solution in the outer region implicitly satisfies the Sommerfield condition.

In terms of acoustic potential the weak formulation is, from equations (1) and (2),

$$\int\int_V \int \frac{\rho_r}{c_r^2}\{c_r^2\,\nabla W\cdot\nabla\phi-(\mathbf{M}_r\cdot\nabla W)(\mathbf{M}_r\cdot\nabla\phi)+\mathrm{i}\eta_r[W(\mathbf{M}_r\cdot\nabla\phi)-(\mathbf{M}_r\cdot\nabla W)\phi]$$

$$-\eta_r^2 W\phi\}\,\mathrm{d}V=\int_S\int\frac{\rho_r}{c_r^2}\{c_r^2 W\,\nabla\phi-\mathbf{M}_r W(\mathbf{M}_r\cdot\nabla\phi)-\mathrm{i}\eta_r\mathbf{M}_r W\phi\}\cdot\mathbf{n}\,\mathrm{d}S, \quad (9)$$

where the local non-dimensional steady flow velocity is $\mathbf{M}_r=\nabla\phi_r$. Equation (9) is the weak formulation in the entire domain, however in the steady flow far field it simplifies considerably with the steady flow given by $\mathbf{M}_r=M_0 i$ and $\rho_r=1$, $c_r=1$. Furthermore, the surface integral on C_∞ has no contribution in the formulation proposed here because there is no longer any surface on which a Sommerfeld radiation condition is to be applied. The weak formulation in the steady flow far field is

$$\int\int_V\int\left\{\nabla W\cdot\nabla\phi-M_0^2\frac{\partial W}{\partial x}\frac{\partial\phi}{\partial x}+\mathrm{i}\eta_r M_0\left(W\frac{\partial\phi}{\partial x}-\frac{\partial W}{\partial x}\phi\right)-\eta_r^2 W\phi\right\}\mathrm{d}V=0. \quad (10)$$

In the cylindrical co-ordinate system used here, some liberty is taken in defining the gradient operations as

$$\nabla W=\frac{\partial W}{\partial x}\mathrm{i}+\frac{\partial W}{\partial r}\mathbf{e}_r+\frac{\mathrm{i}m}{r}W\mathbf{e}_\theta, \quad \nabla\phi=\frac{\partial\phi}{\partial x}\mathrm{i}+\frac{\partial\phi}{\partial r}\mathbf{e}_r-\frac{\mathrm{i}m}{r}\phi\mathbf{e}_\theta, \quad (11, 12)$$

and suppressing factors $e^{\pm im\theta}$ which arise as part of the weighting and trial functions as explained in connection with equation (1). These factors cancel throughout all of the products in equations (9) and (10). Equations (11) and (12) reflect the harmonic angular dependence of ϕ and W. The non-dimensional velocity M_0 in equation (10) is the Mach number of the forward flight.

In the steady flow near field, where the flow is non-uniform, equation (9) is discretized using standard finite-element techniques. Example calculations presented in this study are based on two-dimensional rectangular isoparametric serendipity elements with eight nodes.

In the steady flow far field where the flow is essentially uniform, equation (10) can be discretized using wave envelope elements or by introducing mapped infinite wave envelope elements to obtain closure of the computational domain. It is the formulation in terms of mapped wave envelope elements which is of interest here.

4. THE INFINITE MAPPING

Because of the harmonic dependence on the angle θ the originally three-dimensional weak formulation reduces to two spatial co-ordinates x and r. The x, r plane is shown in Figure 1 where the boundary C_r separates an interior region in which standard FEM descretization is used from an outer region in which mapped wave envelope elements are used. The exterior region must be in the steady flow far field. Figure 2 shows an element in the outer region in the x–r plane of the cylindrical co-ordinate system. The element is bounded by the surface C_r on which

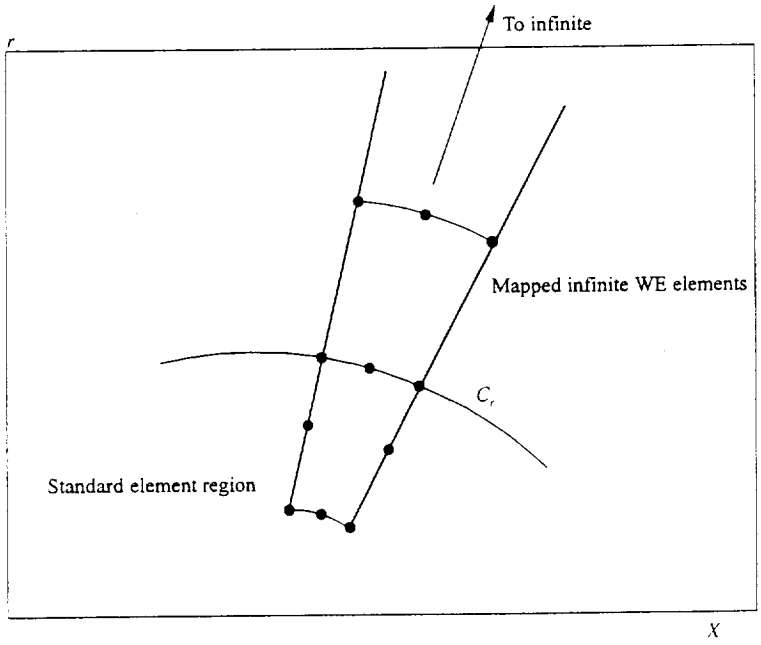

Figure 2. Details of the finite/infinite-element interface.

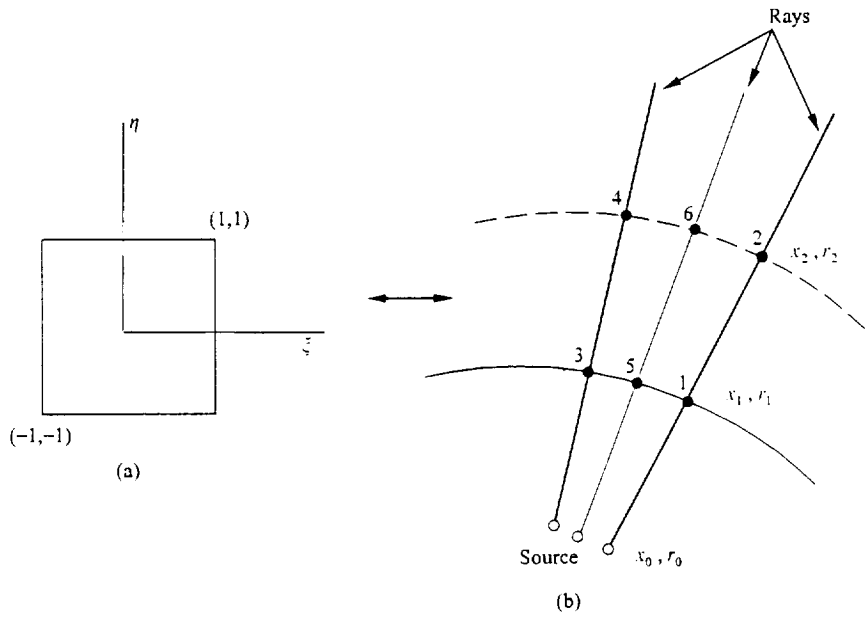

Figure 3. Geometric details of the mapping between the infinite element and the parent element: (a) parent element, (b) mapped wave envelope (WE) element.

it conform with an element of the conventional mesh. The edges of the element are straight lines, extending outward more or less radially, though not necessarily from the axis system origin nor necessarily from a common origin. For the elements used in this investigation which conform with eight-node serendipity elements in the conventional mesh (each with three nodes on C_r), a third radial line between the two edges is required. For simplicity, each of the three straight lines will be referred to as rays. In Figure 1, the outer surface C_∞ is the notional outer boundary of the element at infinity. A ray of an element has an apparent origin at a point x_0, r_0 which in general can be different for each ray. The element maps to a parent element in the ξ, η plane, $-1 \leqslant \xi \leqslant 1$, $-1 \leqslant \eta \leqslant 1$, as shown in Figure 3. The rays of the element map to the ξ axis with $\eta = -1, 0, 1$ in the parent element according to

$$x = \frac{-2\xi}{1-\xi} x_1 + \frac{1+\xi}{1-\xi} x_2, \quad r = \frac{-2\xi}{1-\xi} r_1 + \frac{1+\xi}{1-\xi} r_2, \tag{13, 14}$$

Since

$$\frac{-2\xi}{1-\xi} + \frac{1+\xi}{1-\xi} = 1, \tag{15}$$

the mapping is unchanged by an origin shift. Therefore, it can also be used to yield a mapping relative to the source at x_0, r_0:

$$x - x_0 = \frac{-2\xi}{1-\xi}(x_1 - x_0) + \frac{1+\xi}{1-\xi}(x_2 - x_0), \tag{16}$$

$$r - r_0 = \frac{-2\xi}{1-\xi}(r_1 - r_0) + \frac{1+\xi}{1-\xi}(r_2 - r_0). \tag{17}$$

The node x_1, r_1 is defined by the requirement that the element conform with the conventional element on the boundary C_r. A particularly useful form of the mapping is obtained if the node at x_2, r_2 is located such that $x_2 - x_0 = 2(x_1 - x_0)$ and $r_2 - r_0 = 2(r_1 - r_0)$. This makes the mapping simplify to

$$x - x_0 = \frac{2(x_1 - x_0)}{1-\xi}, \qquad r - r_0 = \frac{2(r_1 - r_0)}{1-\xi}. \tag{18}$$

The mapping has the properties that $\xi = -1$ maps to $x - x_0 = x_1 - x_0$, $r - r_0 = r_1 - r_0$, $\xi = 0$ maps to $x - x_0 = 2(x_1 - x_0)$, $r - r_0 = 2(r_1 - r_0)$, and $\xi = 1$ maps to $x - x_0 = \infty$, $r - r_0 = \infty$. The mapping along a "ray" transforms the infinite domain in the physical co-ordinates to the domain $-1 \leqslant \xi \leqslant 1$ in the parent element. The inverse mapping is

$$\xi = 1 - \frac{2(x_1 - x_0)}{x - x_0}, \qquad \xi = 1 - \frac{2(r_1 - r_0)}{r - r_0}. \tag{19}$$

It is easily deduced that this mapping along a "ray" also applies for the polar radius of the point x, r relative to x_0, r_0, $r_p = \sqrt{(x - x_0)^2 + (r - r_0)^2}$, in the form

$$r_p = \frac{2\sqrt{(x_1 - x_0)^2 + (r_1 - r_0)^2}}{1-\xi} = \frac{2r_{p_1}}{1-\xi} \tag{20}$$

and

$$\xi = 1 - 2r_{p_1}/r_p. \tag{21}$$

This form emphasizes the role of the base node x_0, r_0 as a "source" for the "ray" and the distance r_p as the polar distance from the source.

The infinite-element mapping is completed by a conventional mapping on $-1 \leqslant \eta \leqslant 1$. The element shown in Figure 3 has six nodes numbered as shown. Nodes 1–4 are corner nodes and nodes 5 and 6 are mid-side nodes on C_r and C_2 (the locus of the nodes x_2, r_2). The mapping is of the form

$$x = [M(\xi, \eta)]\mathbf{x}, \quad r = [M(\xi, \eta)]\mathbf{r}, \tag{22}$$

where $[M(\xi, \eta)]$ is a row vector of six shape functions $M_i(\xi, \eta)$ and $\mathbf{x}$, $\mathbf{r}$ are vectors of nodal values of x, r. With the nodal numbering scheme used in Figure 3 the explicit

form of the shape function is

$$M_1(\xi,\eta) = 0{\cdot}5\eta(\eta-1)\frac{-2\xi}{1-\xi}, \qquad M_2(\xi,\eta) = 0{\cdot}5\eta(\eta-1)\frac{1+\xi}{1-\xi},$$

$$M_3(\xi,\eta) = 0{\cdot}5\eta(\eta+1)\frac{-2\xi}{1-\xi}, \qquad M_4(\xi,\eta) = 0{\cdot}5\eta(\eta+1)\frac{1+\xi}{1-\xi},$$

$$M_5(\xi,\eta) = (1-\eta)(1+\eta)\frac{-2\xi}{1-\xi}, \qquad M_6(\xi,\eta) = (1-\eta)(1+\eta)\frac{1+\xi}{1-\xi}. \tag{23}$$

The mapping described here is simply another view of the results presented by Astley *et al.* [8] specialized to the cylindrical co-ordinate system.

In preparation for development of a mapped infinite wave envelope element for a uniformly flowing medium it can also be noted that the results of equations (16)–(21) can be extended to other "distances" along a ray yielding a similar mapping. For example

$$R = \sqrt{(x-x_0)^2 + \beta^2(r-r_0)^2} = \frac{2R_1}{1-\xi}, \tag{24}$$

where $R_1 = \sqrt{(x_1-x_0)^2 + \beta^2(r_1-r_0)^2}$ and $\beta^2 = 1 - M^2$ and M is the Mach number of the uniformly flowing medium. A second useful mapping is

$$\psi = \frac{1}{\beta^2}[-M(x-x_0) + R] = \frac{2\psi_1}{1-\xi}, \tag{25}$$

where $\psi_1 = (1/\beta^2)[-M(x_1-x_0) + R_1]$. These observations are important to the extension of the application of the mapped infinite wave envelope element to acoustic radiation in uniform steady flow.

5. SOURCE SOLUTION IN UNIFORM FLOW

The weak formulation of equation (10) for acoustic radiation in a uniformly moving medium is consistent with the differential equation

$$\left(\frac{\partial}{\partial t} + M\frac{\partial}{\partial x}\right)^2 \phi = \nabla^2\phi. \tag{26}$$

A fundamental harmonic source solution for this equation is

$$\phi = e^{i\eta_r t}\frac{e^{(-i\eta_r/\beta^2)(-Mx + \sqrt{x^2+\beta^2r^2})}}{\sqrt{x^2+\beta^2r^2}}, \tag{27}$$

where $\beta = \sqrt{1 - M^2}$ and $r^2 = y^2 + z^2$. This can be verified by direct substitution or by noting that the transformation of variables

$$x' = \frac{x}{\beta}, \quad r' = r, \quad t' = \frac{M}{\beta}x + \beta t \tag{28}$$

reduces the convected wave equation (26) to the standard wave equation

$$\partial^2\phi/\partial t'^2 = \nabla'^2\phi \tag{29}$$

in the transformed variables which has a fundamental harmonic source solution

$$\phi = e^{i\frac{\eta_r}{\beta}t'} \frac{e^{-i\frac{\eta_r}{\beta}\sqrt{x'^2 + r'^2}}}{\sqrt{x'^2 + r'^2}}. \tag{30}$$

Equation (27) is then obtained replacing the change of variables of equation (28). In terms of the definitions of equations (24) and (25), the fundamental harmonic source solution for source location at x_0, r_0 is

$$\phi = e^{i\eta_r t} \frac{e^{-i\eta_r \psi}}{R}. \tag{31}$$

6. SHAPE FUNCTIONS IN THE INFINITE ELEMENTS

Shape function in the mapped infinite wave envelope elements can be constructed to display the characteristics of the fundamental source solution at large distances from the source in the form

$$\phi = Q(\mathbf{x})e^{-im\theta} R_1 \frac{e^{-i\eta_r(\psi(\mathbf{x}) - \psi_1)}}{R(\mathbf{x})} = P(\mathbf{x})e^{-im\theta} e^{-i\mu(\mathbf{x})}, \tag{32}$$

where the notation $\mathbf{x} = (x, r)$ and $\mu(\mathbf{x}) = \eta_r(\psi(\mathbf{x}) - \psi_1)$ is used and is similar to the notation used by Astley *et al.* [8]. $\mu(\mathbf{x})$ is the phase relative to the surface C_r separating the infinite-element region from the region of standard FEM interpolation and ψ_1 emphasizes that this phase is dependent on the specific "ray" on which equation (32) is evaluated. ψ_1 would be a constant for the entire infinite-element region if C_r is a surface of constant ψ (a "constant-phase surface"), but in general would vary from node to node on C_r. The most direct way to make ψ_1 invariant for the mesh is to construct the mesh so that for all infinite elements x_0, r_0 (the "source point") is common and C_r is a surface of constant ψ ("phase") relative to the common "source". The mesh used by Eversman *et al.* [5, 10–12] has this property (x_0, r_0 are at the mesh origin) and is used in examples in this investigation. At large R, equation (32) should have asymptotic behavior in R consistent with equation (31). The function $P(\mathbf{x})$ should therefore display the

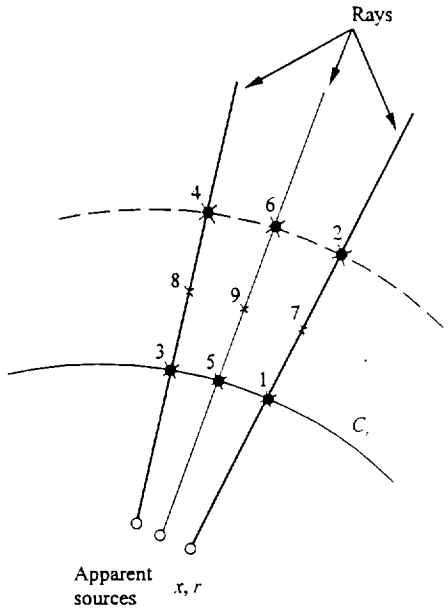

Figure 4. Example of an infinite element with nine × interpolation nodes and six • mapping nodes. This element produces an asymptotic interpolation in the far field of third order in R_1/R.

appropriate asymptotic behavior in R, should be capable of accounting for nearfield effects, and should interpolate in the standard FEM context in the η co-ordinate in the parent element.

In terms of ξ, η co-ordinates of the parent element, $\mu(\mathbf{x})$ and $R(\mathbf{x})/R_1$, have simple forms suggested by equations (24) and (25);

$$\mu(\xi, \eta) = \psi_1 \frac{1+\xi}{1-\xi}, \quad \frac{R_1}{R(\xi, \eta)} = \frac{1}{2}(1-\xi). \tag{34, 35}$$

In equation (34), ψ_1 can be a function of η on the inner boundary of the element $\xi = -1$, interpolated relative to nodal values on C_r. The function $Q(\mathbf{x})$ in equation (32) which accounts for nearfield behavior in the infinite element can be represented by a standard FEM interpolation

$$Q(\xi, \eta) = [S(\xi, \eta)]\underline{Q}, \tag{36}$$

where $\underline{Q}$ is a vector of nodal values of $Q(\mathbf{x})$. There are six nodes involved in the infinite mapping and these can be used as nodes in the interpolation of $Q(\mathbf{x})$. It will generally be appropriate to use more than the mapping nodes by including extra nodes along the rays as shown in Figure 4 which demonstrates the introduction of one extra node midway between the mapping nodes on each ray and suggests a convenient nodal numbering scheme.

The shape functions for the element shown in Figure 4 with the additional node midway between the mapping nodes on a given ray are based on nine-node Lagrangian interpolation with the extra nodes mapped to $\xi = -\frac{1}{3}$. In general, $P(\mathbf{x})$

is interpolated within an element according to

$$P(\xi, \eta) = [N(\xi, \eta)]\underline{Q}, \tag{37}$$

where the shape function $N_i(\xi, \eta)$, the shape function corresponding to node i, is constructed from the mth-order Lagrangian shape function for node i, $L_i^p(\xi, \eta)$, according to

$$P_i(\xi, \eta) = N_i(\xi, \eta) = \tfrac{1}{2}(1 - \xi)L_i^p(\xi, \eta). \tag{38}$$

Some liberty is taken with notation here; $L_i^p(\xi, \eta)$ is defined so that p is the order of interpolation (number of nodes) along the ξ-axis. Along the η-axis the order conforms with the order used in the standard FEM region, which is 3 in the two-dimensional serendipity elements implemented in the model reported here. It is interesting to note that $N_i(\xi, \eta)$ is unity only for nodes with $\xi = -1$ (the Lagrangian interpolation functions have the value unity for all nodes). The vector of nodal values $\underline{Q}$ corresponding to the evaluation of $Q(\mathbf{x})$ only corresponds to nodal value of $P(\mathbf{x})$ for nodes on the surface C_r. Because of this, and because of the phase term $e^{-i\mu(\mathbf{x})}$ in equation (32), which is unity only on the surface C_r, in the infinite elements the solution vector does not correspond to nodal values of acoustic potential at most of the nodes. The potential can be easily reconstructed by postprocessing.

The form of the shape functions defined by equation (38) can be interpreted in global co-ordinate by using equation (24) to show that

$$1 - \xi = 2(R_1/R), \quad \xi = 1 - 2(R_1/R). \tag{39}$$

Equations (38) and (39) suggest that the shape functions in global co-ordinates along a ray are of the form

$$P_i(x, r) = \gamma_1(R_1/R) + \gamma_2(R_1/R)^2 + \gamma_3(R_1/R)^3 + \cdots + \gamma_n(R_1/R)^n, \tag{40}$$

n is determined from the order of Lagrangian interpolation. For a p node interpolation leading to polynomials in ξ of degree $p - 1$ it is determined that $n = p$. A similar result was shown in the case of radiation in a stationary medium [8].

Reference to "variable order" mapped infinite wave envelope elements relates to the choice of the order of the Lagrangian interpolation and therefore to the powers of R_1/R in the asymptotic expansion for the shape function. Conceptually this could be extended to any order, but as pointed out by Astley *et al.* [8] there is a limit imposed by the onset of numerical problems probably related to ill conditioning if the order is too high.

7. WEIGHT FUNCTIONS IN THE INFINITE ELEMENTS

Astley *et al.* [8] show that in order for the boundary integral introduced in the weak formulation to have no contribution on the boundary at infinity it is necessary for the weighting functions to be functions of $\{R_i/R(\mathbf{x})\}^{q+1}$, with $q > 1$.

The weight functions are of the form

$$\phi = Q(\mathbf{x})e^{im\theta}\left(\frac{R_1}{R(\mathbf{x})}\right)^{q+1} e^{i\eta_r(\psi(\mathbf{x})-\psi_1)} = D(\mathbf{x})P(\mathbf{x})e^{im\theta}e^{i\mu(\mathbf{x})} \tag{41}$$

where

$$D(\mathbf{x}) = (R_i/R(\mathbf{x}))^q \tag{42}$$

In the parent element,

$$D(\xi, \eta) = (1/2)^q(1-\xi)^q \tag{43}$$

The weight functions are the complex conjugates of the shape functions multiplied by the additional decay term. In the present investigation $q = 3$. The notation here has been chosen to correspond to that used by Astley *et al.* [8] to emphasize the similarity with their development in the case of a stationary medium. Only the details hidden in the definitions of ψ and R are different.

8. THE WEAK FORMULATION IN THE INFINITE-ELEMENT REGION

The weak formulation of equation (10) for the infinite-element region in which the steady flow is necessarily uniform is obtained by using equations (32) and (43) defining the assumed form of solution and the weight functions in the infinite-element region. The gradient operations on the assumed shape and weighting functions yield

$$\nabla\phi = (\nabla P - i\eta_r \mathrm{P}\nabla\mu)e^{-i\eta_r\mu} \tag{44}$$

and

$$\nabla W = (D\nabla P^* + i\eta_r \mathrm{D}\mathrm{P}\nabla\mu + P\nabla D)e^{i\eta_r\mu}, \tag{45}$$

where the notation

$$\nabla P = \frac{\partial P}{\partial x}\mathbf{i} + \frac{\partial P}{\partial r}\mathbf{e}_r - \frac{im}{r}P\mathbf{e}_\theta, \quad \nabla P^* = \frac{\partial P}{\partial x}\mathbf{i} + \frac{\partial P}{\partial r}\mathbf{e}_r + \frac{im}{r}P\mathbf{e}_\theta \tag{46, 47}$$

is used as in equations (11) and (121) because of the factors $e^{\pm im\theta}$ which are suppressed. By using standard finite-element operations, equation (11) can be formulated at the global level to yield complex element "stiffness" matrices $[\tilde{K}_{ij}]$ defined in terms of real mass, stiffness and damping matrices,

$$[\tilde{K}_{ij}] = -\eta_r^2[M_{ij}] + i\eta_r[\mathrm{C}_{ij}] + [\mathrm{K}_{ij}], \tag{48}$$

where

$$K_{ij} = \int\int_V \int \left\{ D\left[(1-M^2)\frac{\partial P_i}{\partial x}\frac{\partial P_j}{\partial x} + \frac{\partial P_i}{\partial r}\frac{\partial P_j}{\partial r} + \frac{m^2}{r^2} P_i P_j \right] + P_i\left[(1-M^2)\frac{\partial D}{\partial x}\frac{\partial P_j}{\partial x} + \frac{\partial D}{\partial r}\frac{\partial P_j}{\partial r} \right] \right\} \mathrm{d}V, \tag{49}$$

$$M_{ij} = \int\int_V \int DP_iP_j \left\{ 1 - \left[(1-M^2)\left(\frac{\partial \mu}{\partial x}\right)^2 + \left(\frac{\partial \mu}{\partial r}\right)^2 + 2M\frac{\partial \mu}{\partial x} \right] \right\} \mathrm{d}V \tag{50}$$

$$C_{ij} = \int\int_V \int \left\{ DP_i\left[(1-M^2)\frac{\partial \mu}{\partial x}\frac{\partial P_j}{\partial x} + M\frac{\partial P_i}{\partial x} + \frac{\partial \mu}{\partial r}\frac{\partial P_j}{\partial r} \right] - D\left[(1-M^2)\frac{\partial \mu}{\partial x}\frac{\partial P_i}{\partial x} + M\frac{\partial P_j}{\partial x} + \frac{\partial \mu}{\partial r}\frac{\partial P_i}{\partial r} \right] P_j - \left[(1-M^2)\frac{\partial D}{\partial x}\frac{\partial \mu}{\partial x} + M\frac{\partial D}{\partial x} + \frac{\partial D}{\partial r}\frac{\partial \mu}{\partial r} \right] P_iP_j \right\} \mathrm{d}V. \tag{51}$$

The definitions of the stiffness, mass, and damping matrices of equations (49)–(51) are implemented at the element level using the infinite mapping to the parent element. These results reduce to those of Astley *et al.* [8] when the medium is stationary and when account is taken of the operations which are particular to the cylindrical co-ordinate system. It is not difficult to generalize to a three-dimensional Cartesian co-ordinate system.

9. AN IMPORTANT PROPERTY OF THE MASS MATRIX

The mass matrix of equation (50) vanishes if the surface C_r separating the standard finite-element region from the infinite-element region is a surface of constant phase for an apparent acoustic source location x_0, r_0 which is common for all elements. This is shown by referring to the definition of $\mu(\mathbf{x})$,

$$\mu(\mathbf{x}) = \eta_r(\psi(\mathbf{x}) - \psi_1), \tag{52}$$

where

$$\psi(\mathbf{x}) = (1/\beta^2)[-M(x-x_0) + R], \quad R = \sqrt{(x-x_0)^2 + \beta^2(r-r_0)^2}. \tag{53, 54}$$

Since it is stipulated that C_r is a constant phase surface, it follows that ψ_1 is constant. The apparent source location is the same for all elements, leading to the conclusion that x_0, r_0 are constants. It can then be verified that

$$(1-M^2)(\partial\mu/\partial x)^2 + (\partial\mu/\partial r)^2 + 2M(\partial\mu/\partial x) = 1 \tag{55}$$

which from equation (50) leads to the result

$$M_{ij} = 0. \tag{56}$$

This is consistent with the findings of Astley *et al.* [8] in the case of a stationary medium when the surface C_r is a sphere, a constant-phase surface in this case. While of some interest in the time harmonic formulation considered here, the vanishing of the mass matrix is of central importance when a time-dependent formulation is implemented in the stationary medium case. It remains to be established that this is equally important in the case of a uniformly moving medium.

10. TURBOFAN INLET EXAMPLE

Figure 1 shows the generic geometry of a turbofan inlet in an x, r plane of a cylindrical co-ordinate system. The nacelle interior and exterior shape are typical of realistic nacelles. The acoustic source is on the plane C_f and produces a combination of radial modes at a specified angular mode m and non-dimensional frequency η_r. The source strength is specified by the complex mode amplitudes. This type of source would correspond to rotor alone noise or rotor/exit guide vane interaction noise. The frequency is determined by the number of blades on the rotor and the angular mode number by the rotor and exit guide vane blade counts. The nacelle has a forward velocity specified by the Mach number M_0, which is represented for the stationary nacelle by a steady flow directed toward the nacelle. The steady flow into the nacelle is specified by the Mach number M_i, taken to be uniform on the source plane. The steady flow field inside and outside the nacelle, computed on the FEM acoustic mesh, provides input data for the FEM acoustic calculations. This mesh is over refined for the steady flow calculations but this inefficiency is more than offset by the convenience of input data on a mesh compatible with the acoustic mesh.

The details of the FEM acoustic computations with the domain closed by a conventional wave envelope transition region to a Sommerfeld radiation boundary are given in references [5, 10–12]. In this example the propagation and radiation problem is formulated with the standard FEM treatment in the steady flow near field and the domain is closed in the far field by the use of mapped infinite wave envelope elements. The specific case shown is at a reduced frequency $\eta_r = 25$ and angular mode $m = 23$ with only the first radial mode incident. Only one radial mode propagates and it has a cutoff ratio near unity, which indicates that the peak lobe of the radiation pattern will be at a high angle relative to the nacelle axis. In this case it is over 60° to the nacelle axis for the case of $M_i = 0{\cdot}20$ and $M_0 = 0{\cdot}30$. Figure 5 shows the standard mesh in the region which has been abritrarily declared as the steady flow near field. The steady flow far field is where the flow is essentially the $M_0 = 0{\cdot}3$ uniform flow. The outer boundary of this mesh is the surface C_r and it is a circle of constant phase for a source at the axis system origin. The infinite-element region is outside of C_r and not shown. The same inner mesh was used with the outer region consisting of seven layers of standard wave envelope elements extending to 10 duct radii ahead of the inlet for the purpose of producing

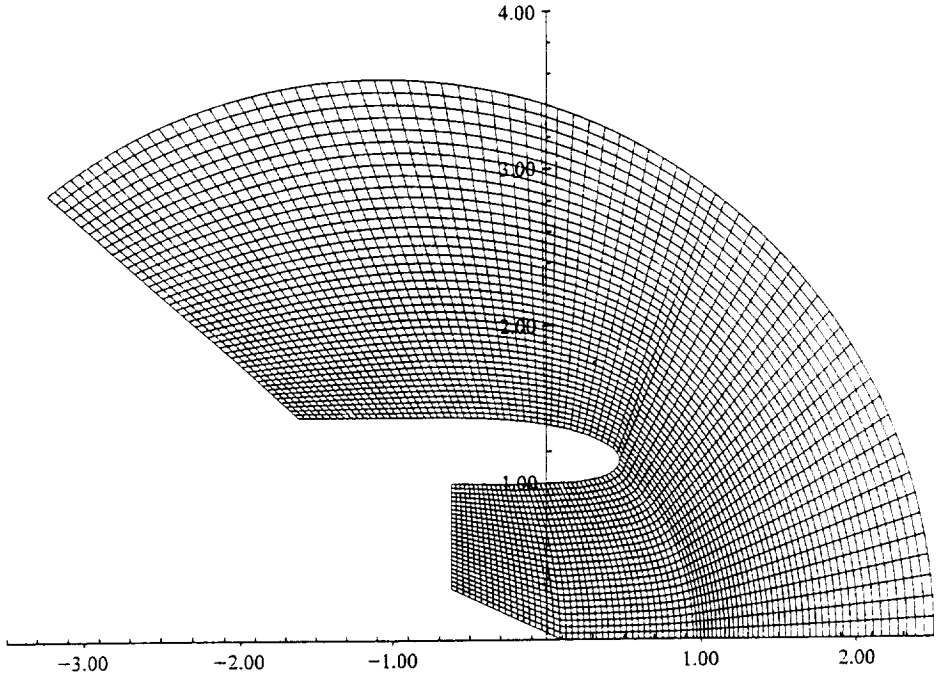

Figure 5. The nearfield mesh of standard finite elements bounded by the surface C_r.

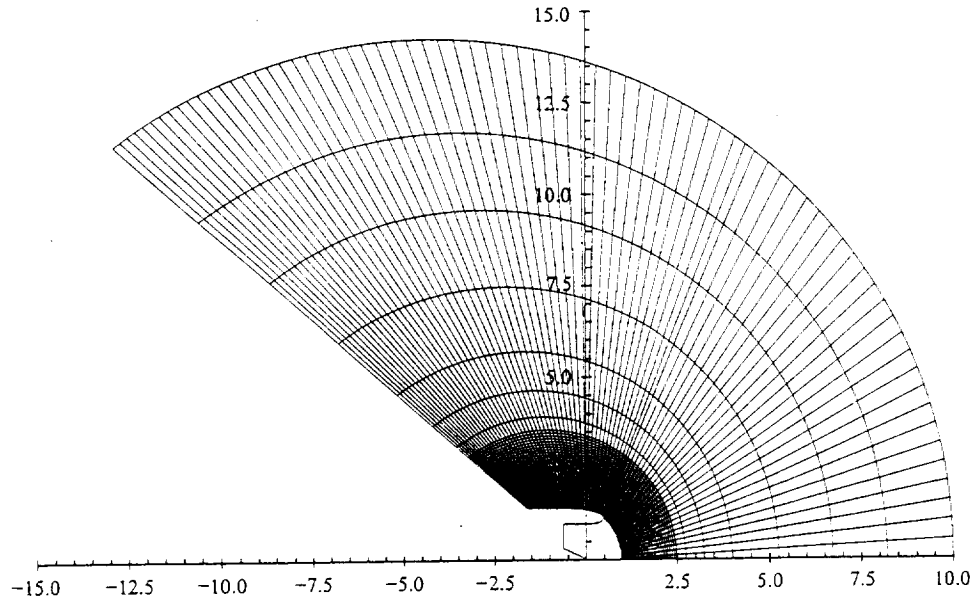

Figure 6. Standard wave envelope mesh used in finite element/wave envelope element formulation.

comparison results. The outer mesh for this case is shown in Figure 6. The standard code has been extensively benchmarked by experiment [12] and by comparison with available approximate analytical results. Numerical experiments have shown that for this frequency radiated fields are particularly difficult to model.

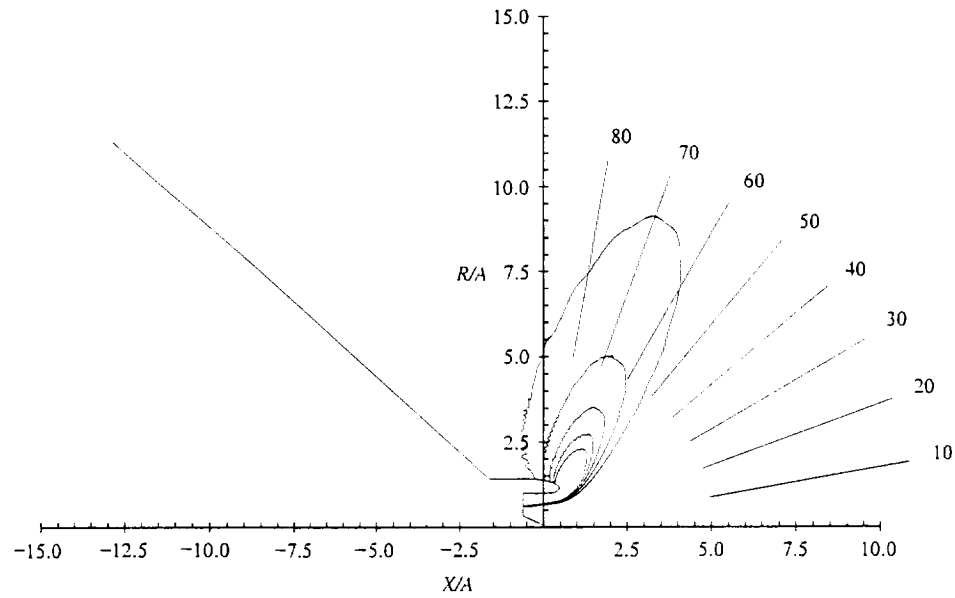

Figure 7. Contours of equal acoustic potential in the entire computational domain for the finite-element/wave envelope element formulation. External mach number $M_0 = 0{\cdot}3$, source plane Mach number $M_i = 0{\cdot}2$, non-dimensional frequency $\eta_r = 25$, angular mode number $m = 23$, first radial mode.

At high angles to the axis the source is certainly not seen as a simple source on C_r as located in this example. It is reasonable to expect that non-reflecting boundary behavior based on an asymptotic approximation representing a simple source would be difficult to achieve.

The results which will be displayed are contours of constant acoustic potential magnitude in an x, r plane superposed on the nacelle geometry. Acoustic potential has been chosen since there is an extra post-processing step to obtain acoustic pressure which introduces its own potential for error, unrelated to the details of the reflection free boundary. Post-processing for pressure in the standard FEM region involve the same operations whether standard wave envelope or mapped infinite wave envelope elements are used in the outer solution. Figure 7 shows the radiation pattern generated by using the standard code (wave envelope elements) and plotting contours of constant acoustic potential in the entire computational domain. Figure 8 shows the same results limited to the region of standard finite elements, which provides a more detailed way of viewing the reflection free performance of the boundary C_r. Figure 9 shows the results when mapped infinite wave envelope elements are used to provide a reflection free boundary. In the case shown the formulation is based on eight-node Lagrangian interpolation in the mapped elements in the ξ direction (eight nodes). This corresponds to introducing R_1/R in the expansion for asymptotic behavior of the farfield solution up to the eighth power [refer to equation (40)]. Element integration is based on 9×3 Gauss points. It was found that five-node Lagrangian interpolation (powers of R_1/R up to five in the asymptotic expansion) was not sufficient.

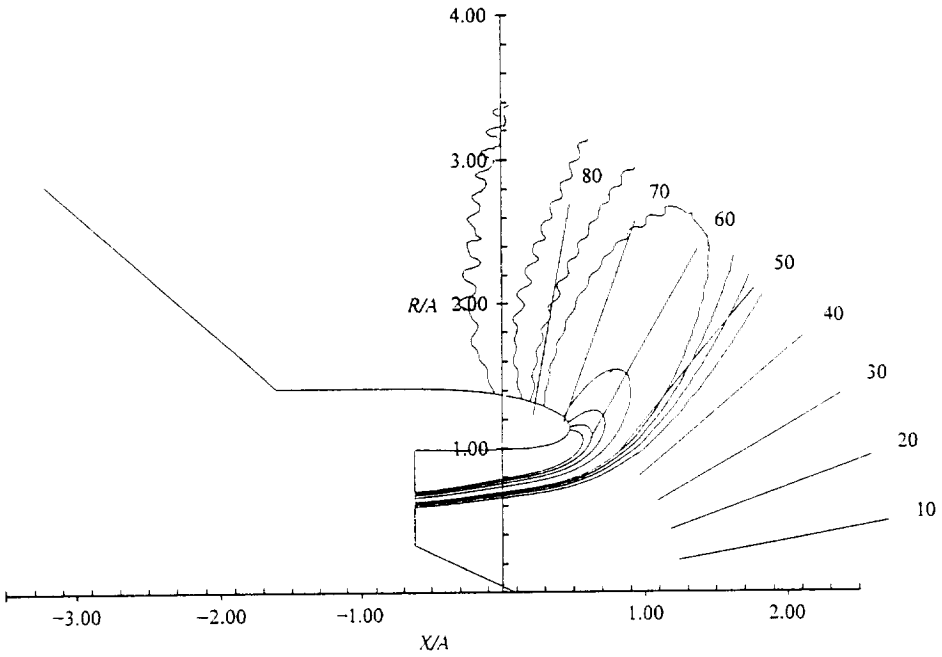

Figure 8. Contours of equal acoustic potential in the standard finite-element region for the finite-element/wave envelope element formulation. External mach number $M_0 = 0{\cdot}3$, source plane Mach number $M_i = 0{\cdot}2$, non-dimensional frequency $\eta_r = 25$, angular mode number $m = 23$, first radial mode.

Figure 7 displaying the entire solution field to the Sommerfeld boundary (10 duct radii of the nacelle axis) suggests significant reflection from the boundary which appears in the waviness of the contours, particularly at higher angles where diffraction around the inlet lip is important and where the nacelle surface interferes with the radiation. The quality of the solution does not improve with the further mesh refinement, indicating that the mesh is suitable for the frequency. Figure 8 zooms in on the region inside C_r and the poor quality of the solution is apparent. In Figure 9 the same level contours are considerably less ragged, indicating that reflection has been essentially eliminated. It is of interest to recall that the computational domain includes the artificial baffle C_b and it appears that it has little effect on the radiated field, consistent with the results reported in reference [13].

The clear conclusion is that poor quality of the solution when standard wave envelope elements are used is due to the inability of the wave envelope elements to provide a completely reflection-free boundary for the complicated source configuration and this location of C_r. In principle expanding C_r should improve the wave envelope element performance, but this has the obvious implication of directly increasing the dimensionality (presuming it is required that the mesh refinement is retained) and the hidden implication of requiring even further mesh refinement due to the growth in element aspect ratio as C_r is expanded.

Variable order mapped infinite wave envelope elements generally will increase the maximum bandwidth of the mesh (the inner mesh may have eight nodes per

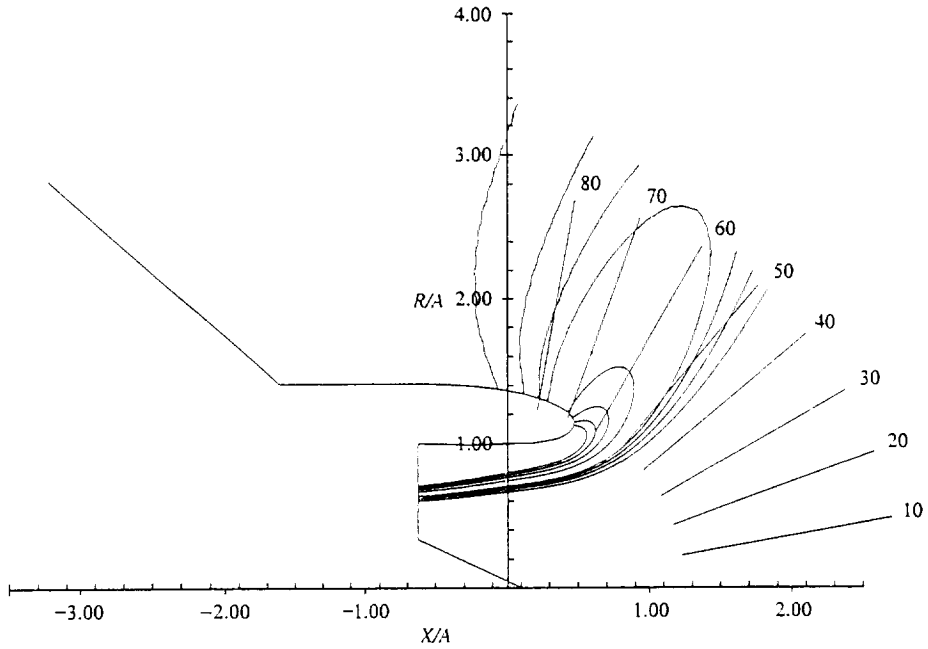

Figure 9. Contours of equal acoustic potential in the standard finite-element region for the finite-element/mapped infinite wave envelope element formulation. External mach number $M_0 = 0{\cdot}3$, source plane Mach number $M_i = 0{\cdot}2$, non-dimensional frequency $\eta_r = 25$, angular mode number $m = 23$, first radial mode. The order of the interpolation in the infinite elements is eighth power in R_i/R.

element and the single infinite element layer has been tested here with as many as 24 nodes per element). In frontal solvers, this tends to slow down the solution even if the total number of nodes is more or less the same in the mapped elements as in the standard wave envelope elements. In the example discussed, a frontal solver is used and the mapped infinite-element computation have an execution time which is in a ratio of about 7/5 compared to the standard wave envelope code. This cost is not unimportant, but must be assessed against the requirements for solution quality. In this case, the infinite-element results are clearly superior.

The question now arises; how much can the computational domain be reduced by using the infinite elements to enhance the reflection-free boundary? To partly address the question, the boundary C_r has been reduced to a radius of two duct radii ahead of the origin. Note in the original mesh of Figure 5 the mesh extends 2·5 duct radii ahead of the origin. In order to maintain approximately the same mesh refinement, the element count between the "highlight circle" (a circle passing through the tip of the inlet lip and intersecting the axis near $r = 1$) has been reduced from 50 to 35. Figure 10 shows acoustic potential level curves in the standard element region for the case using mapped wave envelope elements for closure. The quality of the solution is still substantially superior to that seen in Figure 8 for which closure was achieved using regular wave envelope elements (note that the level curves are not the same in Figures 8 and 10 because they are based on the maximum level on C_r, which differs because C_r differs). The

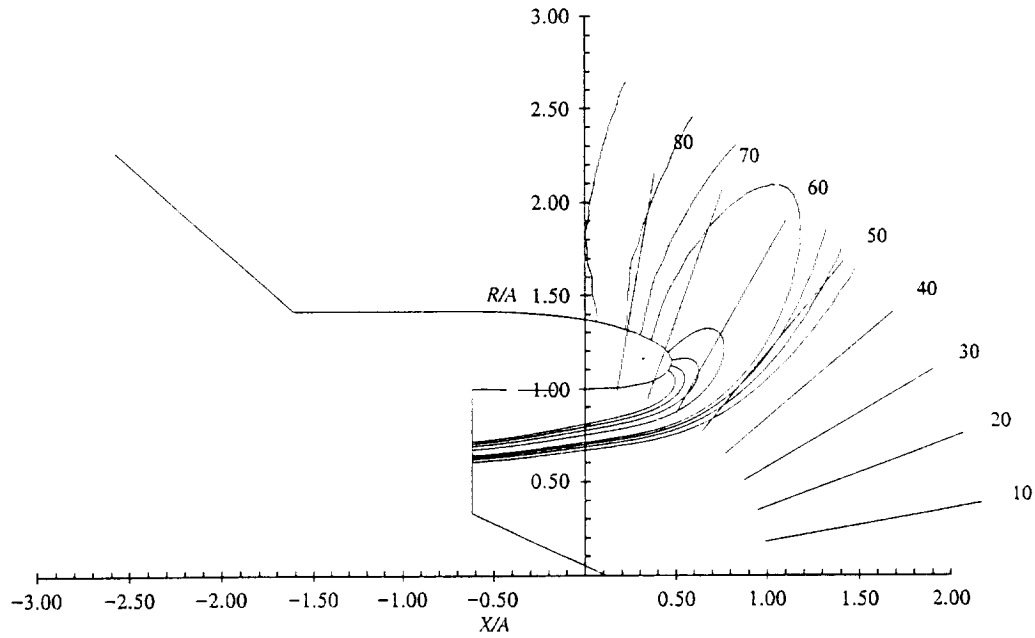

Figure 10. Contours of equal acoustic potential in the standard finite-element region for the finite-element/mapped infinite wave envelope element formulation on a reduced mesh in the standard element region. External mach number $M_0 = 0{\cdot}3$, source plane Mach number $M_i = 0{\cdot}2$, non-dimensional frequency $\eta_r = 25$, angular mode number $m = 23$, first radial mode. The order of the interpolation in the infinite elements is eighth power in R_i/R.

computation time ratio is now nearly 1/1 and the mapped infinite-element results are still superior.

11. CONCLUSION

It has been shown that with suitable modifications mapped infinite wave envelope elements can be used to provide an effective reflection-free boundary for acoustic radiation in a uniform steady flow. The adaptation of the elements to this case is based on the observation that all important "distances" along "rays" map to the parent element in the infinite mapping in exactly the same way. This permits the fundamental solution for radiation from a source in uniform flow to be mapped to the parent element in a form similar to the mapping in the case of a stationary medium. The fundamental solution forms the basis for an asymptotic expansion in R^{-n} in the infinite elements, where R is the "convected radius", $R^2 = x^2 + \beta^2 r^2$. The order of the asymptotic expansion can be chosen to meet the needs of the problem. Element mapping functions are identical to those previously proposed for the stationary medium case and the shape functions are of the same form as those in the stationary medium case with differences only in the details.

Computational examples have been based on acoustic radiation from a turbofan inlet which has been the subject of several previous investigations in which an FEM model was developed with the reflection-free closure of the computational domain

based on standard wave envelope elements. Examples have shown that mapped infinite wave envelope elements provide a superior reflection-free boundary for cases in which the standard wave envelope elements generate reflections which appear in the radiated field. It should be noted that the improved performance may not be without cost. If relatively high order mapped elements (asymptotic behavior to R^{-n} where n is relatively large) are required, the maximum front width of the FEM formulation may be larger than would occur in the standard wave envelope element formulation. For frontal solvers this may decrease computational efficiency. However, this cost has a substantial benefit in the quality of the solution which may not be achievable with the standard wave envelope elemnts without expanding the boundary between standard FEM and the wave envelope element region. In fact, it has been shown that by taking advantage of the reduction in size of the inner region (standard element region) which is achievable with mapped infinite elements it is possible to obtain superior solutions without increasing computation time.

It has been found that the mapped infinite wave envelope element region can be cast in the form of appended mass, damping and stiffness matrices. With a suitable choice of the surface which separates the standard FEM region from the infinite-element region and the restriction that the mapping and shape functions in the infinite elements are based on a common apparent source location, it has been shown that the element mass matrices vanishe. This has previously been shown to be important for transient FEM formulations for radiation in a stationary medium. This suggests that similar investigations should be carried out in the case of uniform external flow.

ACKNOWLEDGMENTS

The work reported here was supported in part by NASA Lewis Research Center under Grant NAG3-2109. Initial stages of the investigation were carried out while the author was an Erskine Fellow in the Department of Mechanical Engineering at the University of Canterbury, Christchurch, New Zealand. Discussions with Professor R. J. Astley were invaluable.

REFERENCES

1. P. BETTESS 1997 *International Journal for Numerical Methods in Engineering* **11**, 53–64. Infinite elements.
2. O. C. ZIENKIEWWICZ, K. BANDO, P. BETTES, C. EMSON and T. C. CHIAM 1985 *International Journal for Numerical Methods in Engineering* **21**, 1229–1251. Mapped infinite elements for exterior wave problems.
3. D. S. BURNETT and R. L. HOLFORD 1998 *Computer Methods in Applied Mechanics and Engieering* **164**, 49–76. An ellipsoidal acoustic infinite element.
4. R. J. ASTLEY and W. EVERSMAN 1983 *Journal of Sound and Vibration* **88**, 47–64. Finite element formulations for acoustical radiation.
5. A. V. PARRETT and W. EVERSMAN 1986 AIAA Journal **24**, 753–759. Wave envelope and finite element approximations for turbofan noise radiation in flight.
6. R. J. ASTLEY and G. J. MACAULAY 1994 *Journal of Sound and Vibration* **170**, 97–118. Mapped wave envelope elements for acoustical radiation and scattering.

7. L. CREMERS and K. R. FYFE 1995 *Journal of the Acoustical Society of America* **97**, 2028–2040. On the use of a variable order infinite wave envelope element for acoustic radiation and scattering.
8. R. J. ASTLEY, G. J. MACAULAY, J.-P. COYETTE and L. CREMERS 1998 *Journal of Acoustical Society of America* **103**, 49–63. Three dimensional wave envelope elements of variable order for acoustic radiation and scattering. Part I. Formulation in the frequency domain.
9. R. J. ASTLEY, J-P. COYETTE and L. CREMERS 1998 *Journal of the Acoustical Society of America* **103**, 64–72. Three dimensional wave envelope elements of variable order for acoustic radiation and scattering. Part II. Formulation in the time domain.
10. W. EVERSMAN, A. V. PARRETT, J. S. PREISSER and R. J. SILCOX 1985 *ASME Journal of Vibration, Acoustics, Stress, and Reliability in Design* **107**, 216–223. Contributions to the finite element solution of the fan noise radiation problem.
11. I. DANDA ROY and W. EVERSMAN 195 *ASME Journal of of Vibration and Acoustics* **117**, 109–115. Improved finite element modeling of the turbofan engine inlet radiation problem.
12. J. S. PREISSER R. J. SILCOX, W. EVERSMAN and A. V. PARRETT 1985 *Journal of Aircraft* **22**, 57–62. Flight study of induced turbofan inlet acoustic radiation with theoretical comparisons.
13. W. EVERSMAN and I. DANDA ROY 1998 *AIAA Paper 98-2250, AIAA/CEAS 4th Aeroacoustics Conference*, 2–4 June, 1998, *Toulouse, France*. The effect of a baffle on acoustic radiation directivity.

A REFLECTION FREE BOUNDARY CONDITION FOR PROPAGATION IN UNIFORM FLOW USING MAPPED INFINITE WAVE ENVELOPE ELEMENTS

Walter Eversman
University of Missouri-Rolla, Rolla, MO, 65401, USA

ABSTRACT

Variable order mapped infinite wave envelope elements are developed for finite element modeling of acoustic radiation in a uniformly moving medium. These elements are used as a non-reflecting boundary condition for computations on an infinite domain in which a radiating body is immersed in a moving medium which is essentially undisturbed outside of the near field. The mapped elements provide a boundary condition equivalent to element stiffness, mass, and damping matrices appended to an inner standard FEM mesh. A demonstration of the performance of mapped elements as influenced by element order is given in the context of acoustic radiation from a turbofan inlet and exhaust.

INTRODUCTION

FEM modeling of acoustic radiation is usually complicated by the requirement that prediction of the acoustic field is sought in some finite sub-domain of an infinite domain. This dictates that computations be limited to the sub-domain with a non-reflecting boundary or that the infinite domain be mapped to a finite computational domain. The investigation reported here seeks an improved non-reflecting boundary condition for aeroacoustics problems in which acoustic radiation in the far field is influenced by steady uniform flow. In order to maintain compatibility with standard FEM solution procedures (for example frontal solvers or other sparse matrix/narrow bandwidth methods), only local types of boundary conditions are considered. In this context boundary conditions which can be categorized as various evolutions of "infinite element" methods [1-5] or "wave envelope element" methods [6,7] have been studied. Mapped infinite wave envelope elements [4,5], which combine the attributes of "infinite" and "wave envelope" elements, have been chosen in this investigation because of their almost seamless compatibility with active FEM codes and meshes. Mapped infinite wave envelope elements limit computations to a finite domain and provide an approximate reflection free boundary. They have been investigated extensively for acoustic radiation in a stationary medium [4,5]. Formulation of the elements reveals the possibility of including within the element shape function an explicit, and

adjustable, dependence on inverse powers of the distance from an apparent acoustic source. This allows the introduction of mapped infinite wave envelope elements well into what would normally be considered the acoustic near field, reducing mesh refinement and dimensionality.

The study reported here extends the variable order mapped infinite wave envelope element concept, as implemented by Astley and co-workers [4,5], to steady uniform flows, principally in connection with aeroacoustic problems related to turbofan acoustic radiation. Most previously reported applications of infinite elements were implemented in two or three dimensions. The application here is in a cylindrical coordinate system reduced to two dimensions by taking advantage of periodicity of the solution in the angular coordinate. References [3-5], and a recent contribution by Astley and Hamilton [8], provide excellent citations to the development of the infinite element concept, leading to the present application.

AN APPLICATION TO TURBOFAN ACOUSTICS

An important problem of acoustic radiation in a moving medium is available in the study of the acoustic field of a turbofan inlet and exhaust. Acoustic propagation and radiation occurs in a high speed potential flow which is the net effect of flow into (out of) the inlet (exhaust) and the forward flight of the nacelle. In the steady flow far field acoustic radiation occurs in a uniformly moving medium. It is required to make computations to predict the radiated field relatively near the inlet [6] (exhaust [7]). This has been approached in the past by terminating the computational domain with a Sommerfeld condition on a boundary reached by the use of wave envelope elements. Here it is intended to investigate the application of mapped infinite wave envelope elements to obtain closure of the computational domain.

The problem is cast here in terms of the turbofan inlet, but an exhaust flow can be modeled with modifications particular to the shear layer boundary between the exhaust jet and the surrounding medium [7]. The geometry of the nacelle and steady flow field in and around it is axially symmetric. The acoustic field is not axially symmetric but is represented as periodic in a cylindrical coordinate system with x being the axis of symmetry, r the cylindrical radius in a circular cross section at $x = 0$, and θ the angular coordinate. Solutions are sought in angular harmonics of a Fourier Series enumerated by the angular mode number m. This reduces the solution domain to a two dimensional x, r plane, shown in Figure 1. The inlet shape in a θ = constant plane is defined by the surface C_n which includes the center body. The surface C_f is the plane on which a source is defined, for example the plane of the fan. The surface C_b is an artificial baffle introduced to limit the computational domain. The boundary C_∞ is the outer boundary of the computational domain.which in principle is infinitely far away, but may be a finite

surface where a radiation condition is introduced.

The acoustic field is assumed to be harmonic in time at non-dimensional frequency η_r. Geometry is non-dimensional based on a reference length generally chosen as the radius of the inlet at the source plane, R. Acoustic and steady flow variables are non-dimensional based on reference values of the speed of sound and density of the medium, ρ_∞ , c_∞, generally defined in the uniform exterior flow. The non-dimensional frequency is $\eta_r = \omega R / c_\infty$, with ω the harmonic source frequency.

In terms of acoustic potential the weak formulation is [3]

$$\iiint_V \frac{\rho_r}{c_r^2}\{c_r^2 \nabla W\cdot\nabla\phi - (\vec{M}_r\cdot\nabla W)(\vec{M}_r\cdot\nabla\phi) + i\eta_r[W(\vec{M}_r\cdot\nabla\phi) - (\vec{M}_r\cdot\nabla W)\phi] - \eta_r^2 W\phi\}\,dV$$

$$= \iint_S \frac{\rho_r}{c_r^2}\{c_r^2 W\nabla\phi - \vec{M}_r W(\vec{M}_r\cdot\nabla\phi) - i\eta_r \vec{M}_r W\phi\}\cdot\vec{n}\,dS \qquad (1)$$

where the local non-dimensional steady flow velocity is $\vec{M}_r = \nabla\phi_r$ and the local non-dimensional density and speed of sound are ρ_r , c_r. The surface integral on the right hand side introduces the noise source on C_f in Figure 1 and a possible impedance boundary condition on C_n inside the inlet. Equation (1) is the weak formulation in the entire domain, however in the steady flow far field it simplifies considerably with the steady flow given by $\vec{M}_r = M_0\, i$ and $\rho_r = 1$, $c_r = 1$. The weak formulation in the steady flow far field where the flow field is uniform at Mach number M_0 is

$$\iiint_V \{\nabla W\cdot\nabla\phi - M_0^2\frac{\partial W}{\partial x}\frac{\partial\phi}{\partial x} + i\eta_r M_0(W\frac{\partial\phi}{\partial x} - \frac{\partial W}{\partial x}\phi) - \eta_r^2 W\phi\}\,dV$$

$$= \iint_S W\{\nabla\phi - (M_0^2\frac{\partial\phi}{\partial x} + i\eta_r M_0\phi)\,\vec{i}\}\cdot\vec{n}\,dS \qquad (2)$$

Equation (2) is obtained from equation (1) by noting that $\vec{M}_r$ is constant and directed along the x axis. The surface integral on the right is only on the outer boundary C_∞ and provides the possibility of introducing the Sommerfeld condition, if required.

In the steady flow near field, where the flow is non-uniform, equation (1) is discretized using standard finite element techniques. Example calculations presented in this study are based

on two-dimensional rectangular isoparametric serendipity elements with eight nodes. In the steady flow far field where the flow is essentially uniform, equation (2) is discretized by introducing mapped infinite wave envelope elements to obtain closure of the computational domain.

THE INFINITE MAPPING

Only a brief summary of the infinite mapping is given here, as it is given in detail elsewhere [4]. Equation (1) is discretized using standard FEM techniques in a near field region bounded by the curve C_r shown in Figure 1. In a far field region, bounded by C_r and C_∞, a notional boundary at infinity, equation (2) is discretized using mapped infinite wave envelope elements. These elements conform with standard elements in the inner standard FEM region on C_r. Figure 2 shows an infinite element in the outer region. The edges of the element are straight lines, extending outward more or less radially, though not necessarily from the axis system origin nor necessarily from a common origin. For the elements used in this investigation a third radial line between the two edges is required. A "ray" of an element has an apparent origin at a point x_0 , r_0 which in general can be different for each ray. The element maps to a parent element in the ξ , η plane, $-1 \le \xi \le 1$, $-1 \le \eta \le 1$ as shown in Figure 2. The rays of the element map to the ξ axis with $\eta = -1$, 0 , 1 in the parent element according to

$$x - x_0 = \frac{2(x_1 - x_0)}{1 - \xi} \quad , \quad r - r_0 = \frac{2(r_1 - r_0)}{1 - \xi} \tag{3}$$

It is easily deduced that this mapping along a "ray" also applies for the polar radius of the point x , r relative to x_0 , r_0, $r_p = \sqrt{(x - x_0)^2 + (r - r_0)^2}$, in the same form

$$r_p = \frac{2\sqrt{(x_1 - x_0)^2 + (r_1 - r_0)^2}}{1 - \xi} = \frac{2 r_{p_1}}{1 - \xi} \tag{4}$$

This form emphasizes the role of the base node x_0 , r_0 as a "source" for the "ray" and the distance r_p as the polar distance from the source. The infinite element mapping is completed by a conventional mapping on $-1 \le \eta \le 1$. It is also noted that the results of equation (4) can be extended to other "distances" along a ray yielding a similar mapping. For example

$$R = \sqrt{(x - x_0)^2 + \beta^2 (r - r_0)^2} = \frac{2 R_1}{1 - \xi} \tag{5}$$

where $R_1 = \sqrt{(x_1 - x_0)^2 + \beta^2 (r_1 - r_0)^2}$ and $\beta^2 = 1 - M^2$ and M is the Mach number

of the uniformly flowing medium. A second useful mapping is

$$\psi = \frac{1}{\beta^2}[-M(x - x_0) + R] = \frac{2\psi_1}{1 - \xi} \tag{6}$$

where $\psi_1 = \beta^{-2}[-M(x_1 - x_0) + R_1]$. These observations are important to the extension of the application of the mapped infinite wave envelope element to acoustic radiation in uniform steady flow.

The weak formulation of equation (2) for acoustic radiation in a uniformly moving medium is consistent with the differential equation

$$(\frac{\partial}{\partial t} + M\frac{\partial}{\partial x})^2 \phi = \nabla^2 \phi \tag{7}$$

Equation (7) has a fundamental harmonic source solution at non-dimensional frequency η_r, for source location at x_0 , r_0 , given by

$$\phi = e^{i\eta_r t} \frac{e^{-i\eta_r \psi}}{R} \tag{8}$$

where ψ and R are defined by equations (5) and (6). Equation (8) can be deduced by transformation of equation (7) by noting that the transformation of variables

$$x' = \frac{x}{\beta} \quad , \quad r' = r \quad , \quad t' = \frac{M}{\beta} x + \beta t \tag{9}$$

reduces the convected wave equation to the standard wave equation

$$\frac{\partial^2 \phi}{\partial t'^2} = \nabla'^2 \phi \tag{10}$$

Equation (10) in the transformed variables has a fundamental harmonic source solution at frequency $\eta'_r = \eta_r / \beta$ which is

$$\phi = e^{i\frac{\eta_r}{\beta} t'} \frac{e^{-i\frac{\eta_r}{\beta}\sqrt{x'^2 + r'^2}}}{\sqrt{x'^2 + r'^2}} \tag{11}$$

Equation (8) is then obtained (within a constant) by replacing the change of variables of equation (9) and accounting for the source location at x_0 , y_0 , z_0 .

SHAPE FUNCTIONS IN THE INFINITE ELEMENTS

Shape functions in the mapped elements can be constructed to display the characteristics of the fundamental source solution at large distances from the source in the form

$$\phi = Q(\vec{x})\, e^{-im\theta}\, R_1 \frac{e^{-i\eta_r(\psi(\vec{x}) - \psi_1)}}{R(\vec{x})} = P(\vec{x})\, e^{-im\theta}\, e^{-i\mu(\vec{x})} \tag{12}$$

where the notation $\vec{x} = (x\ ,\ r)$ and $\mu(\vec{x}) = \eta_r(\psi(\vec{x}) - \psi_1)$ is used. $\mu(\vec{x})$ is the phase relative to the surface C_r separating the infinite element region from the standard FEM and ψ_1 emphasizes that this phase is dependent on the specific "ray" on which equation (12) is evaluated. ψ_1 would be a constant for the entire infinite element region if C_r is a surface of constant ψ (a "constant phase surface"). The most direct way to make ψ_1 invariant for the mesh is to construct the mesh so that for all infinite elements x_0 , r_0 (the "source point") is common and C_r is a surface of constant ψ ("phase") relative to the common "source". The mesh used by Danda Roy and Eversman [6] has this property (x_0 , r_0 are at the mesh origin) and is used in examples in this investigation. At large R equation (12) should have asymptotic behavior in R consistent with equation (8). The function $P(\vec{x})$ should therefore display the appropriate asymptotic behavior in R , should be capable of accounting for near field effects, and should interpolate in the standard FEM context in the η coordinate in the parent element.

In terms of the ξ , η coordinates of the parent element $\mu(\vec{x})$ and $R(\vec{x})/R_1$ have simple forms suggested by equations (5) and (6):

$$\mu(\xi\ ,\ \eta) = \psi_1 \frac{1 + \xi}{1 - \xi} \tag{13}$$

$$\frac{R_1}{R(\xi\ ,\ \eta)} = \frac{1}{2}(1 - \xi) \tag{14}$$

In equation (12) in the most general case ψ_1 can be a function of η on the inner boundary of the element $\xi = -1$, interpolated relative to nodal values on C_r .

The shape function $P_i(\xi\ ,\ \eta)$ corresponding to node i is constructed from the $p\ th$ order Lagrangian shape function $L_i^p(\xi\ ,\ \eta)$, according to

$$P_i(\xi\ ,\ \eta) = N_i(\xi\ ,\ \eta) = \frac{1}{2}(1\ -\ \xi)\,L_i^{p}(\xi\ ,\ \eta) \tag{15}$$

Some liberty is taken with notation here; $L_i^{p}(\xi\ ,\ \eta)$ is defined so that p is the order of interpolation (number of nodes) along the ξ axis. Along the η axis the order conforms with the order used in the standard FEM region, which is 3 in the two dimensional serendipity elements implemented in the model reported here.

The form of the shape functions defined by equation (15) can be interpreted in global coordinates by using equation (15) to suggest that the shape functions in global coordinates along a ray are of the form

$$P_i(x\ ,\ r) = \gamma_1(\frac{R_1}{R}) + \gamma_2(\frac{R_1}{R})^2 + \gamma_3(\frac{R_1}{R})^3 + \ldots\ldots\gamma_n(\frac{R_1}{R})^n \tag{16}$$

n is determined from the order of Lagrangian interpolation. For a p node interpolation leading to polynomials in ξ of degree $p\ -\ 1$ it is determined that $n = p$. A similar result was shown in the case of radiation in a stationary medium [4]. The mapped elements are variable order because n can be chosen for the application.

WEIGHT FUNCTIONS IN THE INFINITE ELEMENTS

In order for the boundary integral introduced in the weak formulation to have no contribution on the boundary at infinity it is necessary for the weighting functions to be functions of $\{R_i / R(\vec{x})\}^{q+1}$, with $q > 1$ [4]. The weight functions are of the form

$$W = Q(\vec{x})\,e^{im\theta}\left(\frac{R_1}{R(\vec{x})}\right)^{q+1} e^{i\eta_r(\psi(\vec{x})\ -\ \psi_1)} = D(\vec{x})\,P(\vec{x})\,e^{im\theta}\ e^{i\mu(\vec{x})} \tag{17}$$

where

$$D(\vec{x}) = \left(\frac{R_i}{R(\vec{x})}\right)^{q} \tag{18}$$

In the parent element

$$D(\xi\ ,\ \eta) = \left(\frac{1}{2}\right)^{q}(1\ -\ \xi)^{q} \tag{19}$$

The weight functions are the complex conjugates of the shape functions multiplied by the additional decay term.

THE WEAK FORMULATION IN THE INFINITE ELEMENT REGION

The weak formulation of equation (2) for the infinite element region in which the steady flow is necessarily uniform is obtained by using equations (12) and (17) defining the assumed form of solution and the weight functions in the infinite element region. The gradient operations on the assumed shape and weighting functions yield

$$\nabla\phi = (\nabla P - i\eta_r P \nabla\mu)\, e^{-i\eta_r \mu} \tag{20}$$

and

$$\nabla W = (D\nabla P^* + i\eta_r D P \nabla\mu + P\nabla D)\, e^{i\eta_r \mu} \tag{21}$$

The superscript (*) denotes the complex conjugate of the operation $\nabla P = P_x \vec{i} + P_r \vec{e}_r - i\frac{m}{r} P \vec{e}_\theta$, which is defined explicitly for the cylindrical coordinate system and takes into account the angular harmonics depending on m. By using standard finite element operations equation (2) can be formulated to yield complex element "stiffness" matrices $\left[\tilde{K}_{ij}\right]$ defined in terms of real mass, stiffness and damping matrices

$$\left[\tilde{K}_{ij}\right] = -\eta_r^2 \left[M_{ij}\right] + i\eta_r \left[C_{ij}\right] + \left[K_{ij}\right] \tag{22}$$

where

$$K_{ij} = \iiint_V \{D[(1 - M^2)\frac{\partial P_i}{\partial x}\frac{\partial P_j}{\partial x} + \frac{\partial P_i}{\partial r}\frac{\partial P_j}{\partial r} + \frac{m^2}{r^2} P_i P_j] + P_i[(1 - M^2)\frac{\partial D}{\partial x}\frac{\partial P_j}{\partial x} + \frac{\partial D}{\partial r}\frac{\partial P_j}{\partial r}]\}\, dV \tag{23}$$

$$M_{ij} = \int\int\int_V D P_i P_j \{ 1 - [(1 - M^2)(\frac{\partial \mu}{\partial x})^2 + (\frac{\partial \mu}{\partial r})^2 + 2M\frac{\partial \mu}{\partial x}] \} dV \tag{24}$$

$$\begin{aligned} C_{ij} = \int\int\int_V \{ & D P_i [(1 - M^2)\frac{\partial \mu}{\partial x}\frac{\partial P_j}{\partial x} + M\frac{\partial P_j}{\partial x} + \frac{\partial \mu}{\partial r}\frac{\partial P_j}{\partial r}] \\ & - D[(1 - M^2)\frac{\partial \mu}{\partial x}\frac{\partial P_i}{\partial x} + M\frac{\partial P_i}{\partial x} + \frac{\partial \mu}{\partial r}\frac{\partial P_i}{\partial r}] P_j \\ & - [(1 - M^2)\frac{\partial D}{\partial x}\frac{\partial \mu}{\partial x} + M\frac{\partial D}{\partial x} + \frac{\partial D}{\partial r}\frac{\partial \mu}{\partial r}] P_i P_j \} dV \end{aligned} \tag{25}$$

The definitions of the stiffness, mass, and damping matrices of equations (23)-(25) are implemented at the element level using the infinite mapping to the parent element. These results reduce to those of reference [4] when the medium is stationary and when account is taken of the operations which are particular to the cylindrical coordinate system.

The mass matrix of equation (24) vanishes if the surface C_r separating the standard finite element region from the infinite element region is a surface of constant phase for an apparent acoustic source location x_0 , r_0 which is common for all elements. This is shown by referring to the definition of $\mu(\vec{x})$,

$$\mu(\vec{x}) = \eta_r(\psi(\vec{x}) - \psi_1) \tag{26}$$

where

$$\psi(\vec{x}) = \frac{1}{\beta^2}[-M(x - x_0) + R] \tag{27}$$

and

$$R = \sqrt{(x - x_0)^2 + \beta^2(r - r_0)^2} \tag{28}$$

Since it is stipulated that C_r is a constant phase surface, it follows that ψ_1 is constant. The

apparent source location is the same for all elements, leading to the conclusion that x_0 , r_0 are constants. It can then be verified that

$$(1 - M^2)(\frac{\partial \mu}{\partial x})^2 + (\frac{\partial \mu}{\partial r})^2 + 2M\frac{\partial \mu}{\partial x} = 1 \qquad (29)$$

which from equation (24) leads to the result $M_{ij} = 0$. This is consistent with the findings of Astley, Macaulay, Coyette, and Cremers [1] in the case of a stationary medium when the surface C_r is a sphere, a constant phase surface in this case. While of some interest in the time harmonic formulation considered here, the vanishing of the mass matrix is of central importance when a time dependent formulation is implemented in the stationary medium case [2]. It remains to be established that this is equally important in the case of a uniformly moving medium. It should be noted that the result $M_{ij} = 0$ assumes that FEM interpolations and integrations are exact. There is in fact approximation error which is small as verified in calculations reported here. However in transient calculations this should be considered [5].

TURBOFAN NACELLE EXAMPLES

Computational examples will be given to demonstrate the performance of mapped infinite wave envelope elements as compared to standard wave envelope elements and in particular the performance of the new elements as a function of the expansion order will be examined. The codes which uses standard wave envelope elements [6,7] have a substantial history of benchmarking against experiment and simple test cases and can comfortably be used as a basis for evaluating the mapped elements

Figure 1 shows the generic geometry of a turbofan inlet in an x , r plane of a cylindrical coordinate system. The acoustic source is on the plane C_f and produces a combination of radial modes at a specified angular mode m and non-dimensional frequency η_r . The source strength is specified by complex modal amplitudes [6]. The nacelle has a forward velocity specified by the Mach number M_0 , which is represented for the stationary nacelle by a steady flow directed toward the nacelle. The steady flow into the nacelle is specified by the Mach number M_i , taken to be uniform on the source plane. The steady flow field inside and outside the nacelle computed on the FEM acoustic mesh provides data for the FEM acoustic calculations. Figure 1 indicates that the computational domain is limited by an artificial baffle C_b . Acoustic radiation is highly directional and it has been shown that the baffle can be oriented to have only minimal influence on the radiated field. This baffle is introduced to limit the dimensionality of the FEM discretization.

The details of the FEM acoustic computations with the domain closed by a conventional wave envelope transition region to a Sommerfeld radiation boundary are given in [6]. In a first example given here the propagation and radiation problem is formulated with a standard FEM discretization in the steady non-uniform flow near field and the domain is completed in the far field by the use of standard wave envelope elements. The specific case shown is at a reduced frequency $\eta_r = 25$ and angular mode $m = 23$ with only the first radial mode incident. Only one radial mode propagates and it has a cutoff ratio near unity, which suggests that the peak lobe of the radiation pattern will be at a high angle relative to the nacelle axis. Steady flow is defined by $M_0 = 0.3$ and $M_i = 0.2$. This case could correspond to rotor noise for a mildly supersonic tip speed rotor with 23 blades. The conventional FEM mesh for this example is shown in Figure 3 (as used in the infinite element implementation). Infinite elements provide the reflection free boundary condition on the outer boundary. The domain limiting baffle is swept back more than 130 degrees from the duct axis. The mesh refinement is at close to the limit for the non-dimensional frequency considered. The proximity of the boundary C_r to the nacelle is limited by the extent of the non-uniform flow field generated by flow around the nacelle.

The results which are displayed are contours of constant acoustic potential magnitude in an x , r plane superposed on the nacelle geometry. Figure 4 , for wave envelope closure of the computational domain, shows the radiation pattern in terms of contours of constant acoustic potential magnitude in the acoustic near field, that is, in the standard FEM region. Acoustic contours show a single lobe of radiation with the highest level on the transition surface C_r corresponding to the closed contour. Considerable evidence of reflection from the wave envelope element region is revealed by the wavy quality of the iso-potential contours. In this case the transition surface C_r (a constant phase surface) intersects the x axis at 2.5 duct radii.. This distance is apparently insufficient to achieve a good non-reflecting boundary using the wave envelope elements, which in this case consists of seven layers of elements extending to 10 duct radii on the x axis where the Sommerfeld condition is imposed. Mesh refinement has virtually no effect on the quality of the solution. The case depicted with radiation to the sideline is difficult because of the geometrical complexity of the source.

Figure 5, 6, and 7 show similar results when mapped infinite wave envelope elements of order 8 , 9, and 10 (the asymptotic expansion in powers of R_1 / R up to 8, 9, 10) are used to provide a reflection free boundary. In this case the transition boundary C_r intersects the x axis at 2.0 duct radii, closer to the nacelle than for the results of Figure 4. The mesh refinement is approximately the same as used in Figure 4, and the element count is lower. There is progressively less evidence of reflection (waviness of the contours) as the element order is increased in successive figures. There is only a modest improvement between the order 9

expansion of Figure 6 and the order 10 expansion of Figure 7. The baffle limiting the computational domain, as noted in Figure 1, accounts for most of the residual evidence of reflection. Note that the iso-acoustic pressure contours of Figure 4 do not distribute in exactly the same way as those in Figures 5, 6, and 7 (they normalize on a different boundary). The result is that there are contours closer to the baffle in the latter cases, and these seem to show a small effect of the baffle. Timing in all of the cases shown is very nearly equivalent.

The infinite element mapping and shape functions have also been used to generate the solution in the far field, and this is shown in Figure 8 where acoustic pressure contours are displayed. Acoustic pressure is obtained by post-processing acoustic potential [6.7] and is less accurate for a given mesh resolution because post-processing requires the spatial derivative of potential. In general, it is found that the solution for either potential or pressure is better in the infinite element region than in the conventional FEM region. This is because the infinite elements have shape functions which include the spatially harmonic character of the solution. The effect of reflection from the baffle is clearly shown, however the principal lobe of radiation is essentially unaffected by the baffle.

As a final example to demonstrate the robustness of the reflection free boundary condition acoustic radiation from a turbofan exhaust is considered. Figure 9 shows the geometry with a potential flow jet issuing from the nacelle to represent exhaust flow. The mesh used in this implementation is shown in Figure 10. Note that there is a region of triangular elements that is used to work around the sharp trailing edge of the duct without unacceptable element distortion. This has been found to be the most convenient mesh strategy consistent with the goal of keeping a simple, but optimal node numbering scheme for the frontal solver which is used.

The FEM formulation in the interior region is somewhat more complicated than in the inlet case, requiring continuity of acoustic pressure and particle displacement across the shear layer separating the jet from the exterior flow [7]. The length of the jet region forces the inner region in which standard FEM methods are used to be of much larger extent than in the inlet case. The case considered here is at non-dimensional frequency $\eta_r = 25$, with angular mode $m = 23$, $n = 1$ incident. The jet Mach number is $M_j = 0.5$ and the exterior flow Mach number is $M_o = 0.2$. The standard FEM region ends at 3.75 duct radii from the origin (on the axis of symmetry). The jet shear layer ends at 1.0 duct radii from the axis origin, which corresponds with the tip of the center body. However, potential flow mixing persists for some considerable distance beyond this point. Figure 11 shows contours of constant acoustic potential in the near field generated with standard wave envelope elements providing the reflection free boundary condition. Figure 12 shows similar contours generated with the domain closed using tenth order mapped infinite wave envelope elements. The improvement with the mapped infinite elements is

substantial

Some interesting properties of the solution are revealed in Figures 11 and 12. In the interior of the duct evidence is seen of standing waves along the duct wall. This is due to reflection at the duct termination. Discontinuity of acoustic potential (required by the physics of the problem), though not great, is seen across the shear layer between the jet and the surrounding flow. This is difficult to see due to the size of the figures, but it can be observed most clearly near the duct lip. The contours shown cover a range of 40 dB. There is a substantial improvement in the quality of the contours generated with the mapped elements. This is in spite of the fact that the mesh density used is marginal for the non-dimensional frequency considered and the fact that with the extended jet the boundary of the conventional FEM region is very close to the "extended" body. Figure 13 shows the post-processed acoustic pressure solution in both the near and far field. The effect of the baffle is noted to not substantially alter the principal lobe of radiation.

CONCLUSION

With suitable modifications mapped infinite wave envelope elements can be used to provide an effective reflection free boundary for acoustic radiation in a uniform steady flow. The fundamental solution for a source in uniform flow forms the basis for an asymptotic expansion in R^{-q} in the infinite elements, where R is the "convected radius", $R^2 = x^2 + \beta^2 r^2$. The order of the asymptotic expansion can be chosen to meet the needs of the problem. Element mapping functions are identical to those previously proposed for the stationary medium case and the shape functions are of the same form as those in the stationary medium case with differences only in the details. Examples show that mapped infinite wave envelope elements provide a superior reflection free boundary for cases in which standard wave envelope elements generate reflections which appear in the radiated field. It has been demonstrated in the nacelle inlet case that this improved reflection free performance can be achieved on a reduced mesh.

REFERENCES

1. P. Bettess 1977 International Journal for Numerical Methods in Engineering 11, 53-64. Infinite elements.

2. O. C. Zienkiewicz, K. Bando, P. Bettess, C. Emson, T. C. Chiam 1985 International Journal for Numerical Methods in Engineering 21, 1229-1251. Mapped infinite elements for exterior wave problems.

3. D. S. Burnett and R. L. Holford 1998 Computer Methods in Applied Mechanics and Engineering 164, 49-76. An ellipsoidal acoustic finite element.

4. R. J. Astley, G. J. Macaulay, J-P. Coyette, and L. Cremers 1998 Journal of the Acoustical Society of America 103(1), 49-63. Three dimensional wave envelope elements of variable order for acoustic radiation and scattering. Part I. Formulation in the frequency domain.
5. R. J. Astley, J-P. Coyette, and L. Cremers 1998 Journal of the Acoustical Society of America 103(1), 64-72. Three dimensional wave envelope elements of variable order for acoustic radiation and scattering. Part II. Formulation in the time domain.
6. I. Danda Roy and W. Eversman 1995 ASME Journal of Vibration and Acoustics 117(1), January, 1995, 109-115. Improved finite element modeling of the turbofan engine inlet radiation problem.
7. W. Eversman and D. Okunbor 1998 Journal of Sound and Vibration 213(2),235-257. Aft fan duct acoustic radiation.
8. R. J. Astley and J. A. Hamilton 2000 Journal of Computational Acoustics (in press). Numerical studies of conjugated infinite elements for acoustic radiation.

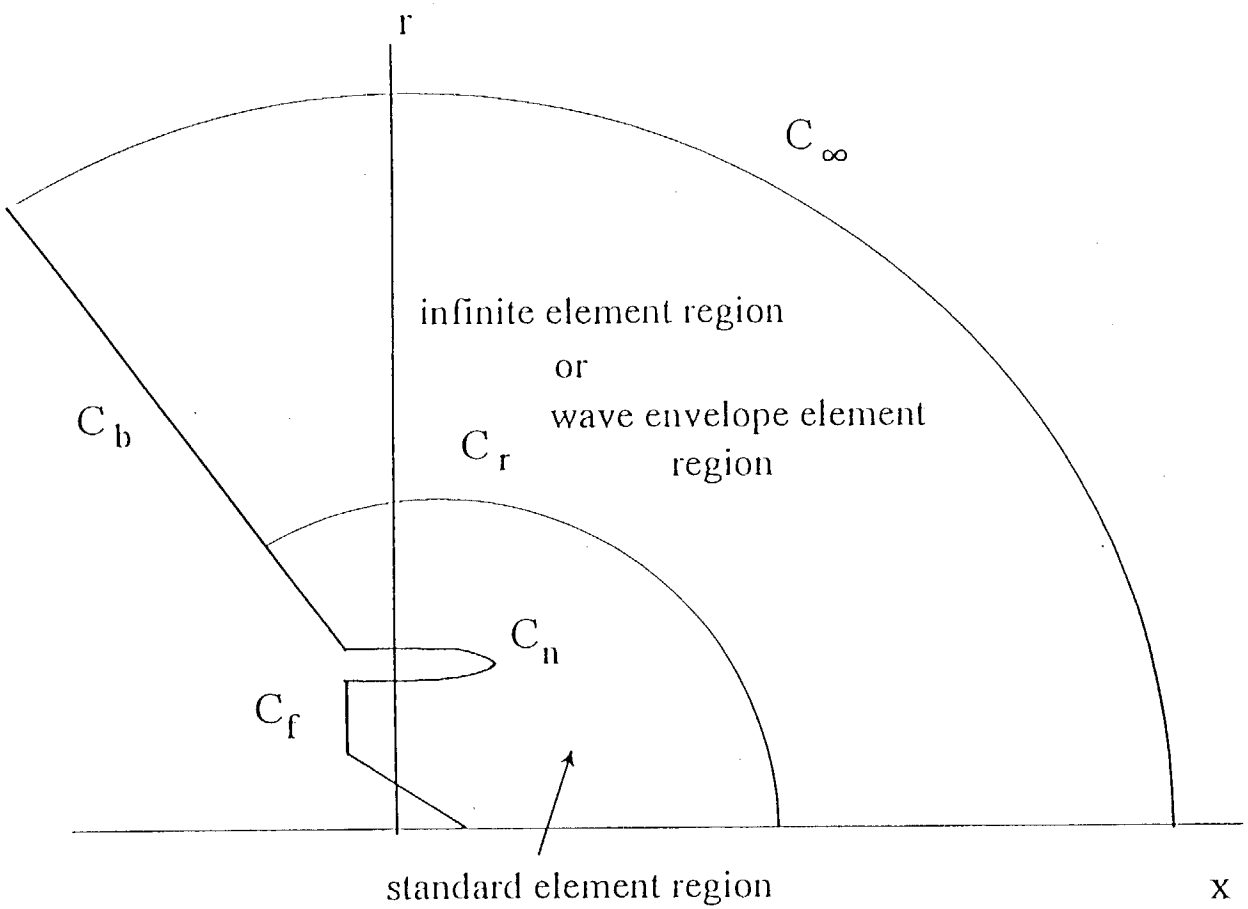

Figure 1. Computational domain in the x , r plane of a cylindrical coordinate system. C_b is an artificial baffle to limit the computational domain with minimal influence on the solution.

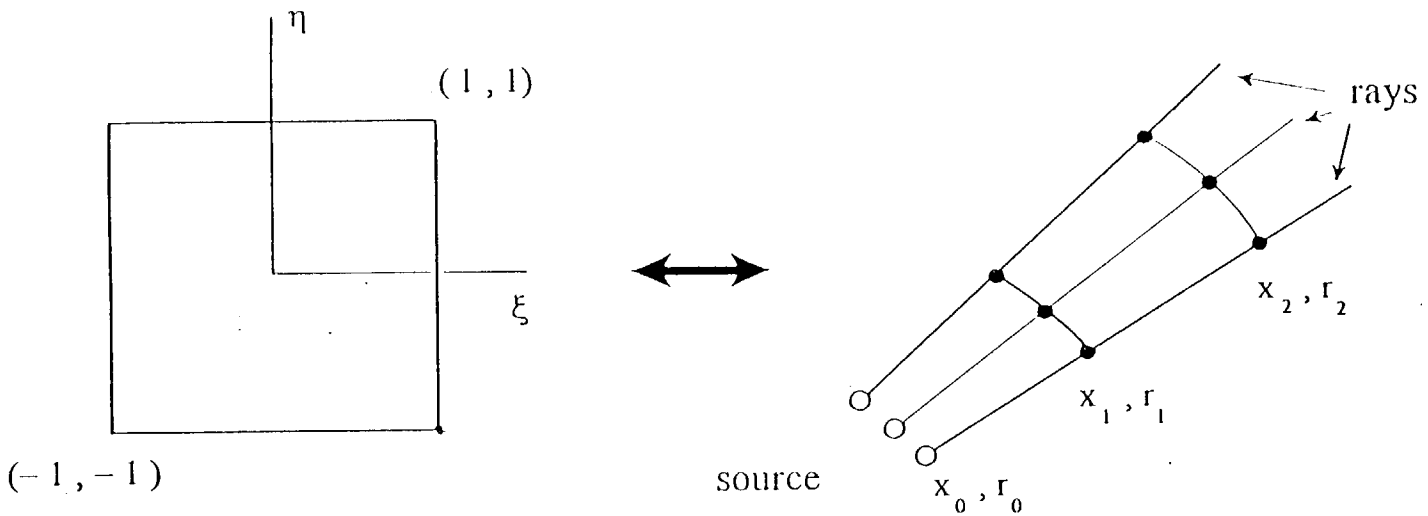

Figure 2. The infinite element mapping emphasizing "sources" and "rays".

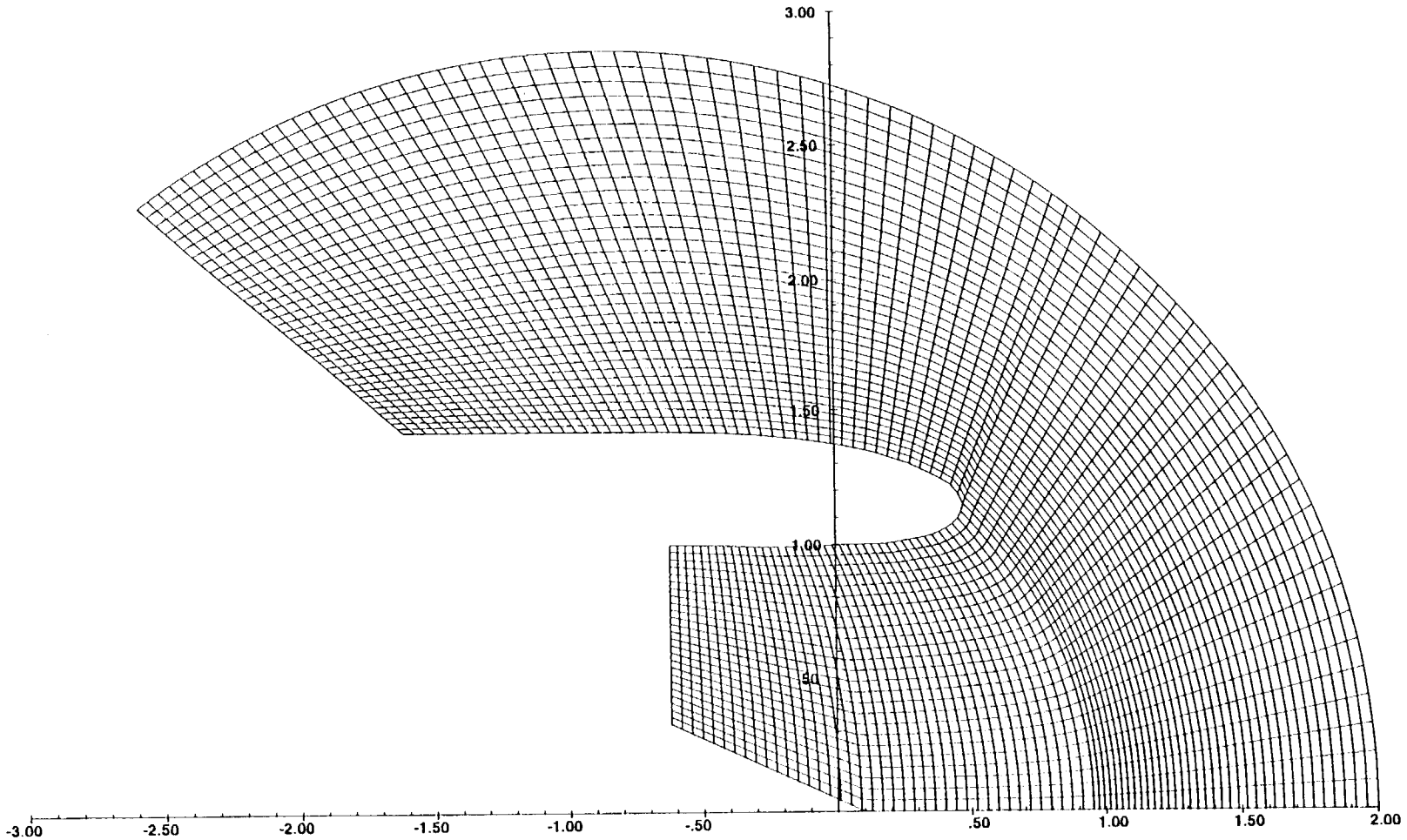

Figure 3. Standard FEM mesh used for inlet radiation showing domain limiting baffle. Radiation condition on the outer boundary implemented with mapped infinite wave envelope elements.

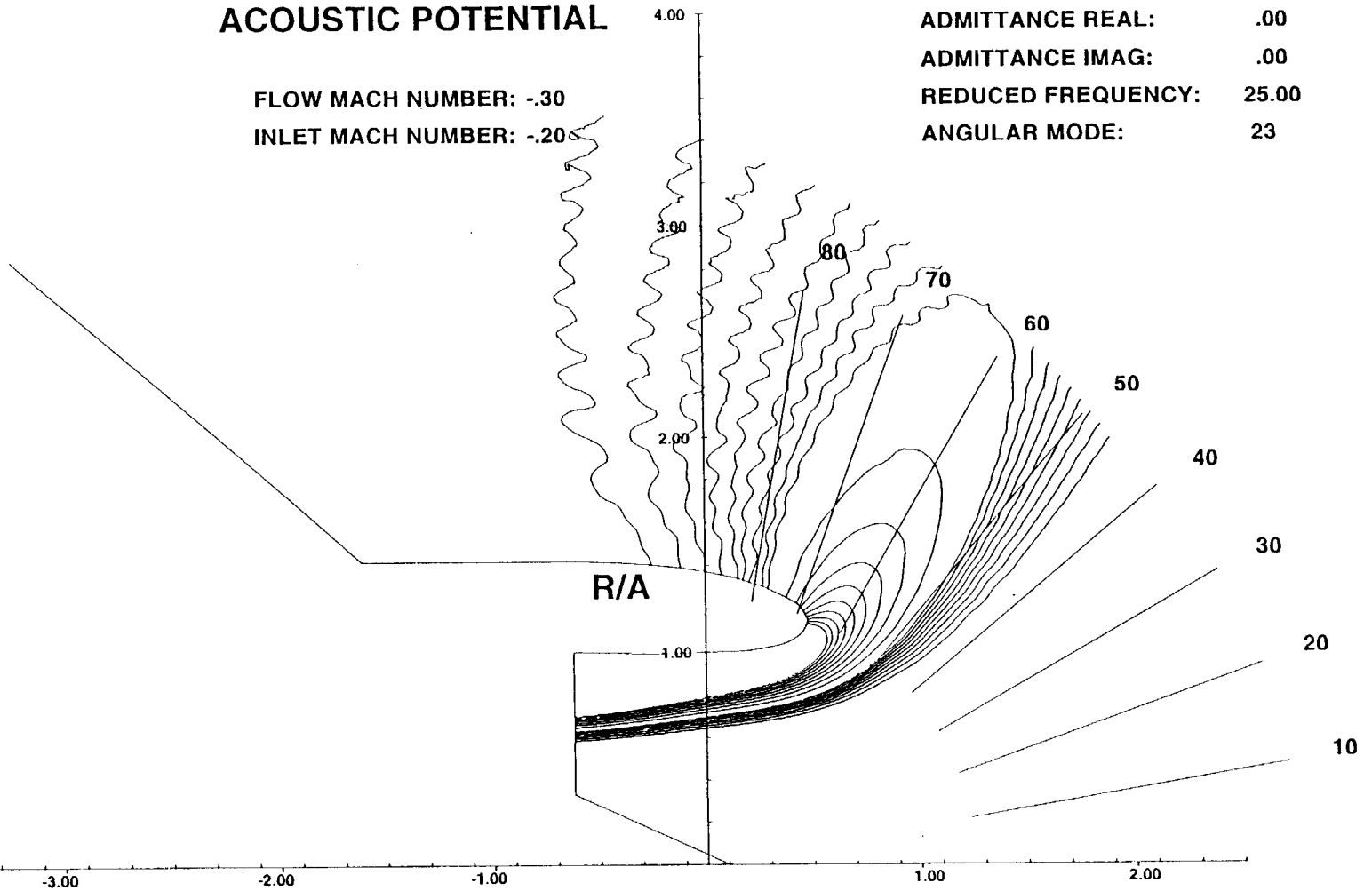

Figure 4. Near field iso-acoustic potential contours calculated using standard wave,envelope element reflection free boundary at 2.5 duct radii (on the x-axis). Frequency $\eta_r = 25$, inlet Mach number $M_i = 0.2$, flight Mach number $M_o = 0.3$, angular mode $m = 23$, radial mode $n = 1$.

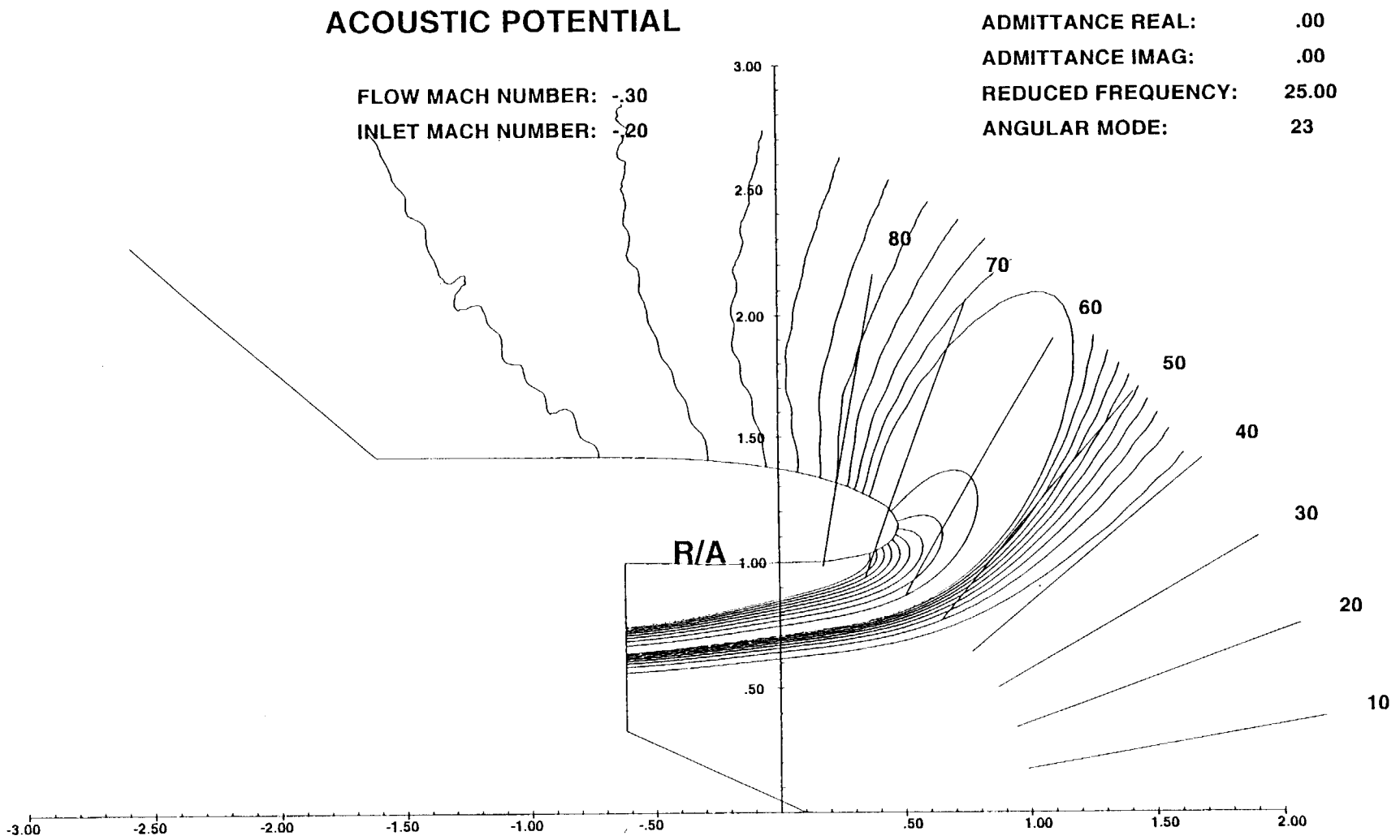

Figure 5. Near field iso-acoustic potential contours calculated using eighth order mapped wave envelope element reflection free boundary at 2.0 duct radii (on the x-axis). Frequency $\eta_r = 25$, inlet Mach number $M_i = 0.2$, flight Mach number $M_o = 0.3$, angular mode $m = 23$, radial mode $n = 1$.

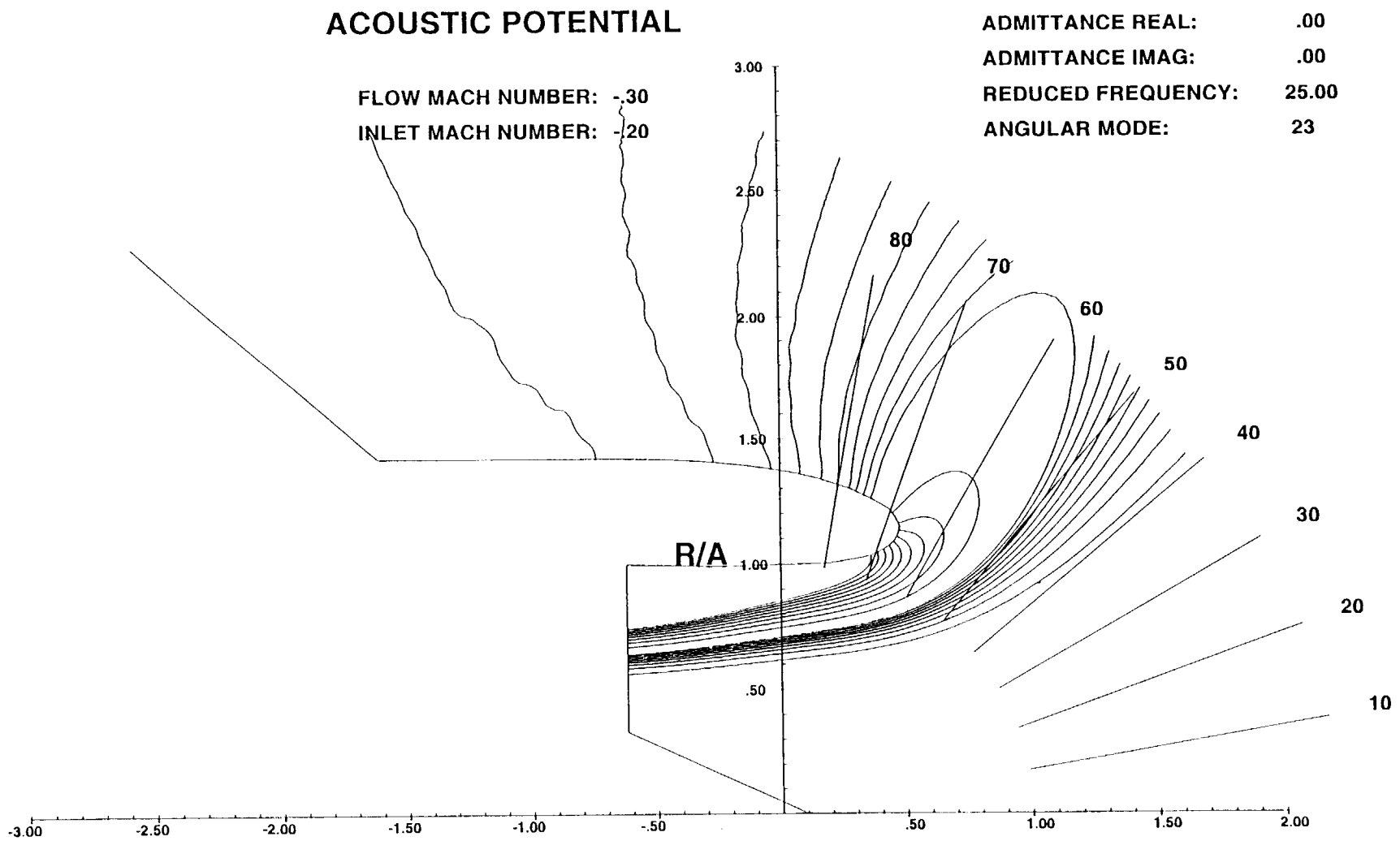

Figure 6. Near field iso-acoustic potential contours calculated using ninth order mapped wave envelope element reflection free boundary at 2.0 duct radii (on the x-axis). Frequency η_r = 25, inlet Mach number M_i = 0.2 , flight Mach number M_o = 0.3 , angular mode m = 23, radial mode n = 1.

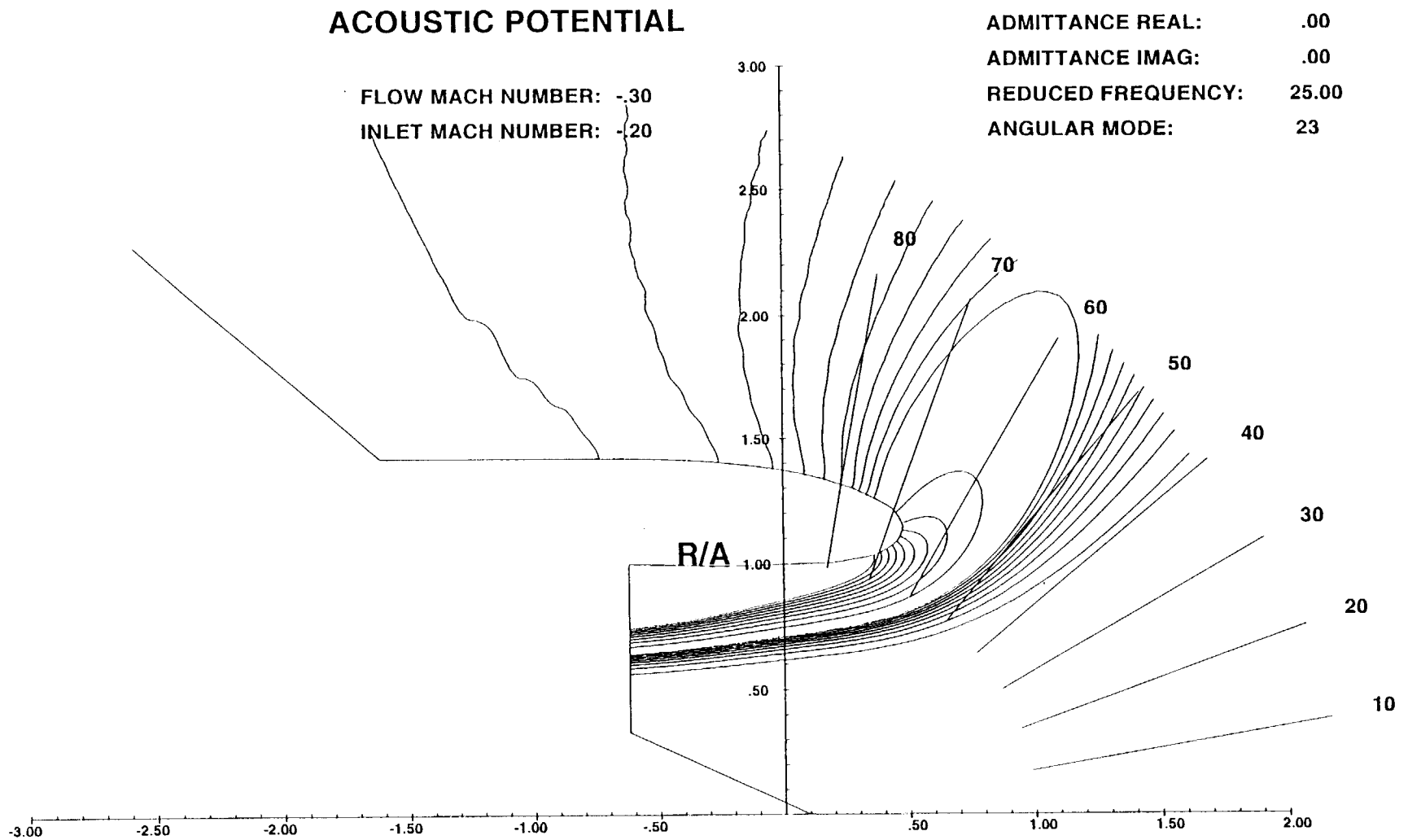

Figure 7. Near field iso-acoustic potential contours calculated using tenth order mapped wave envelope element reflection free boundary at 2.0 duct radii (on the x-axis). Frequency η_r = 25, inlet Mach number M_i = 0.2 , flight Mach number M_o = 0.3 , angular mode m = 23, radial mode n = 1.

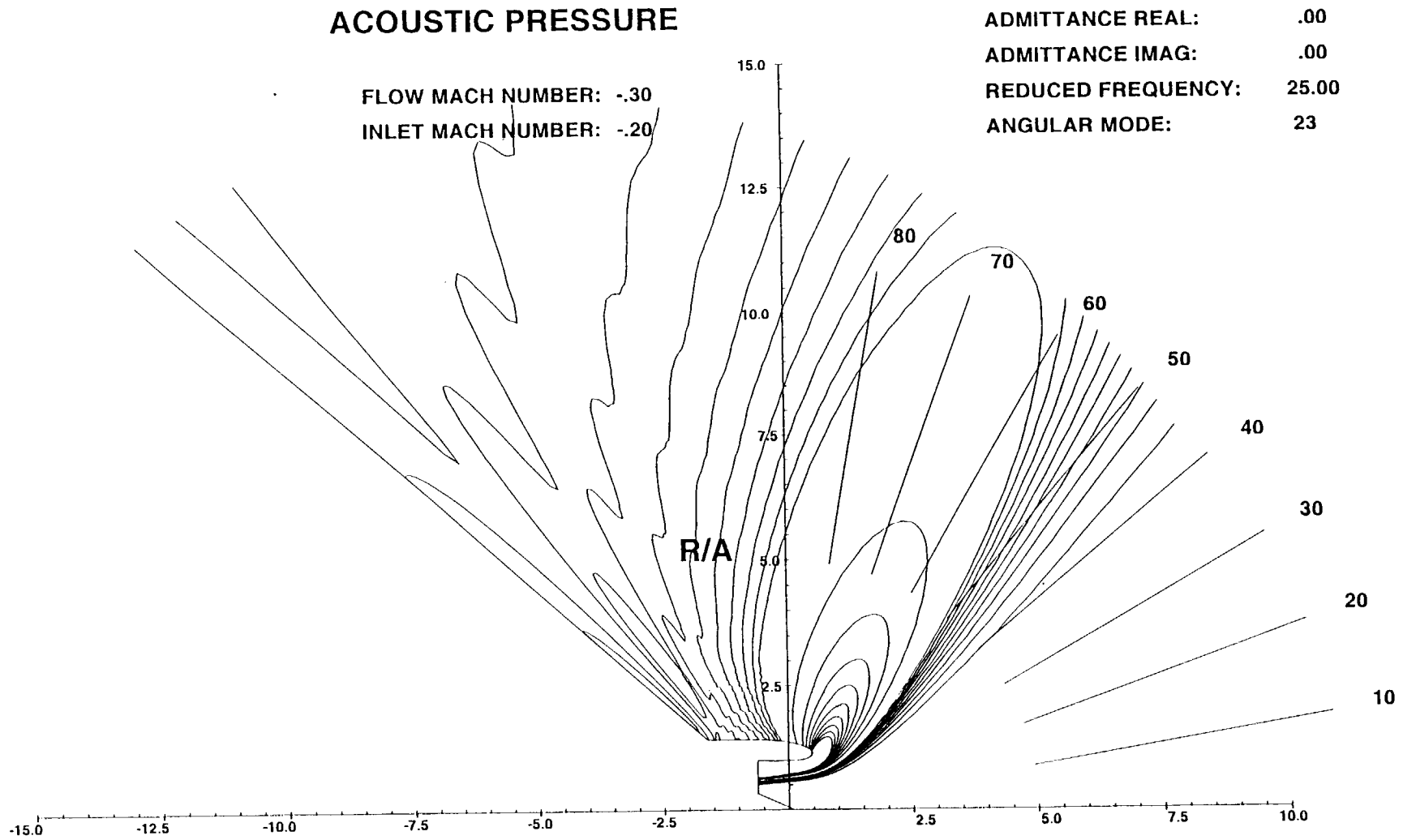

Figure 8. Near and far field iso-acoustic potential contours calculated using tenth order mapped wave envelope element reflection free boundary at 2.0 duct radii (on the x-axis). Frequency η_r = 25, inlet Mach number M_i = 0.2 , flight Mach number M_o = 0.3 , angular mode m = 23, radial mode n = 1.

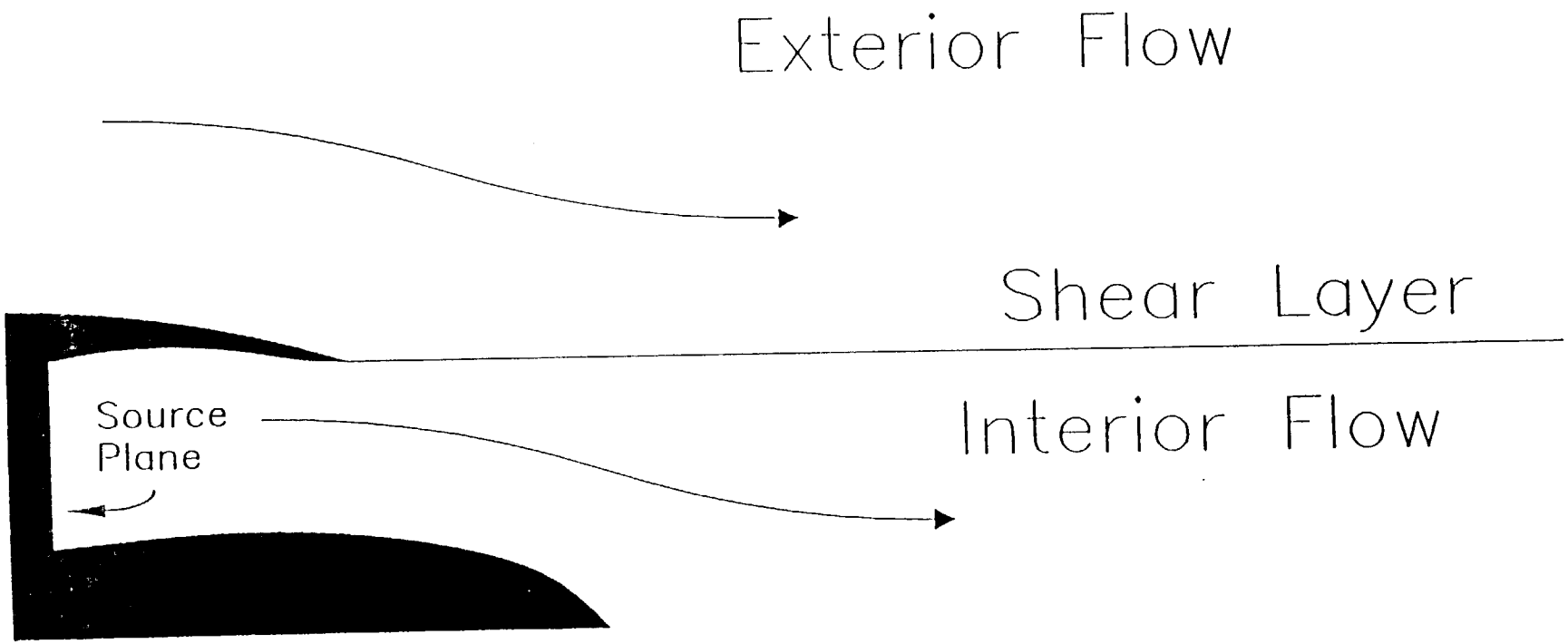

Figure 9. Geometry of a generic exhaust duct showing the shear layer separating the exhaust flow and external flow.

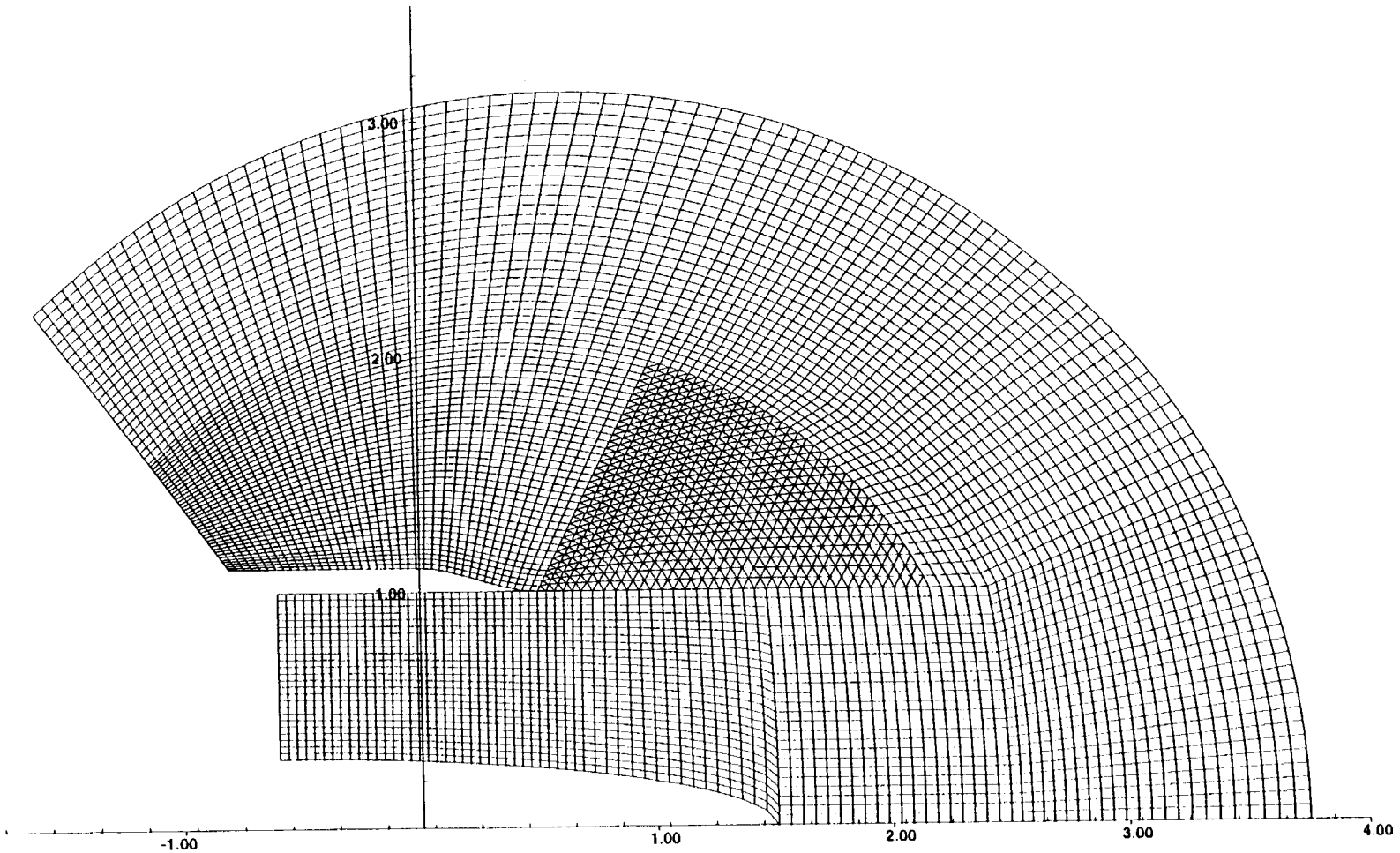

Figure 10. Standard FEM mesh used for aft fan duct radiation showing domain limiting baffle and region of triangular elements. Mapped infinite wave envelope element closure on the outer boundary

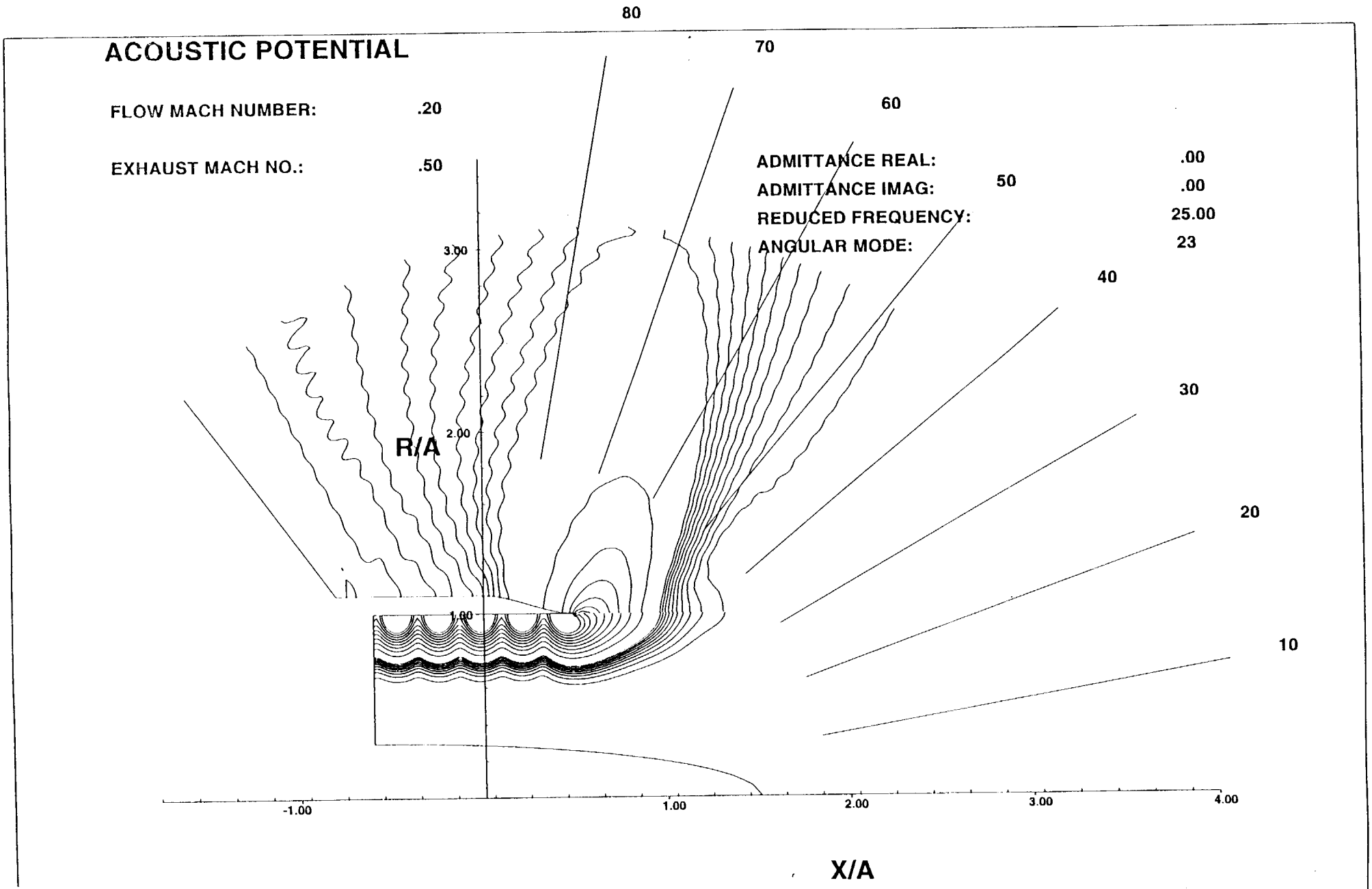

Figure 11. Exhaust duct near field iso-acoustic potential contours calculated using standard wave envelope element reflection free boundary at 2.5 duct radii (on the x-axis). Frequency η_r = 25, exhaust Mach number M_i = 0.5, flight Mach number M_o = 0.2, angular mode m = 23, radial mode n = 1.

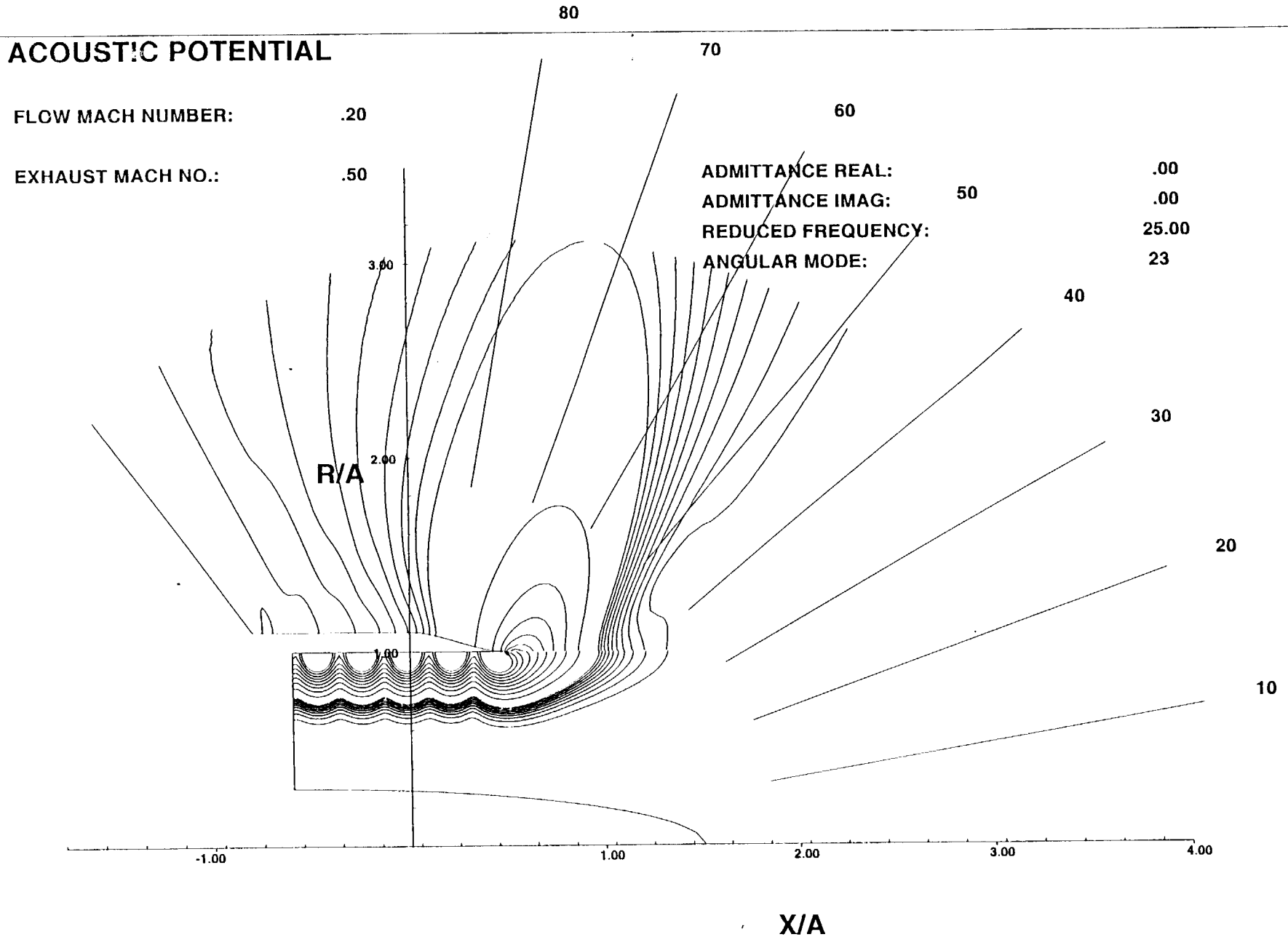

Figure 12. Exhaust duct near field iso-acoustic potential contours calculated using tenth order mapped wave envelope element reflection free boundary at 2.5 duct radii (on the x- axis). Frequency η_r = 25, exhaust Mach number M_i = 0.5 , flight Mach number M_o = 0.2 , angular mode m = 23, radial mode n = 1.

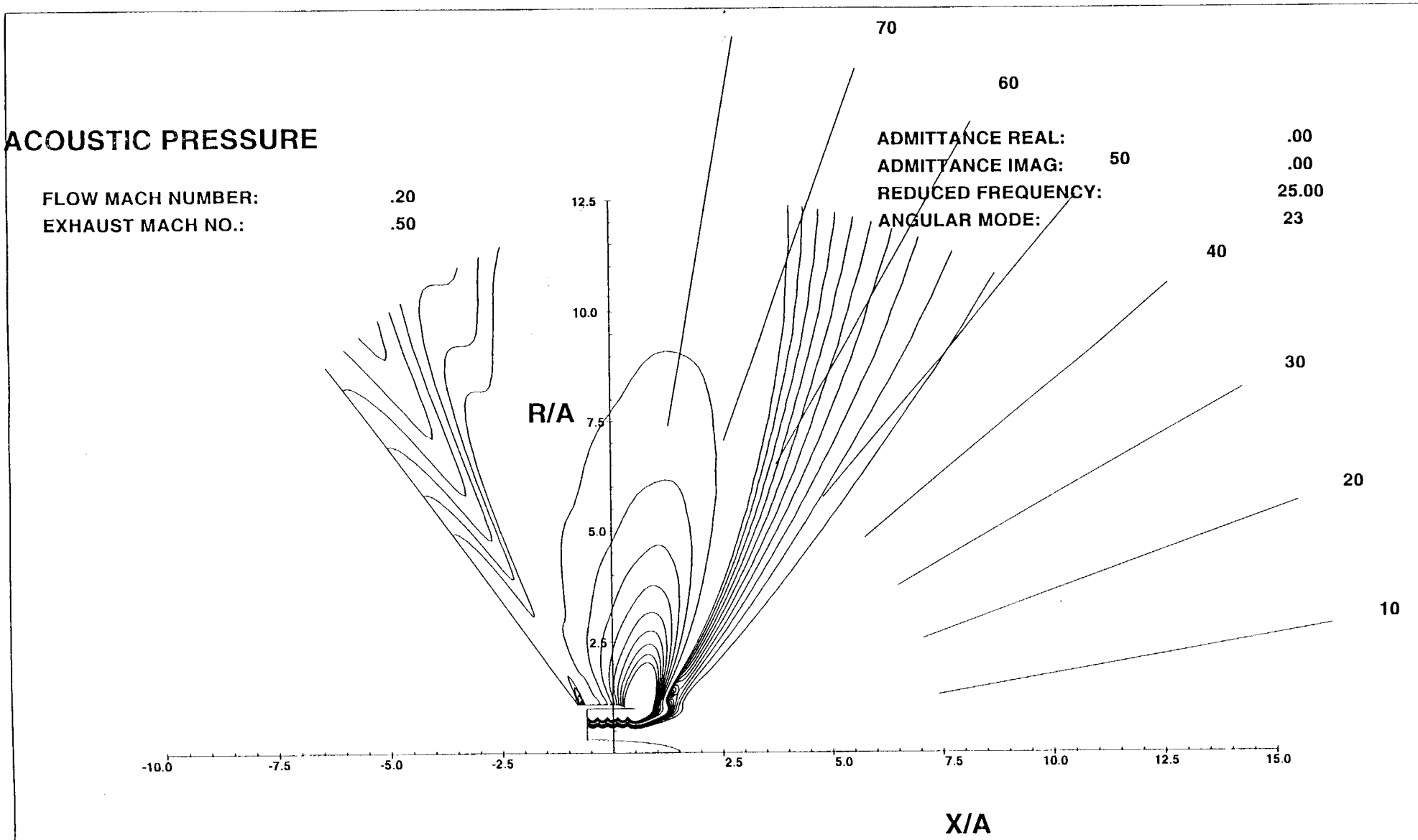

Figure 13. Exhaust duct near and far field iso-acoustic potential contours calculated using tenth order mapped wave envelope element reflection free boundary at 2.5 duct radii (on the x- axis). Frequency η_r = 25, exhaust Mach number M_i = 0.5 , flight Mach number M_o = 0.2 , angular mode m = 23, radial mode n = 1.

A NUMERICAL COMPARISON BETWEEN MULTIPLE-SCALES AND FEM SOLUTION FOR SOUND PROPAGATION IN LINED FLOW DUCTS

Sjoerd W. Rienstra[1] & Walter Eversman[2]

[1] Dept. Mathematics and Computing Science, Eindhoven University of Technology, The Netherlands

[2] Dept. Mechanical and Aerospace Engineering and Engr. Mechanics, University of Missouri - Rolla

Abstract

An explicit, analytical, multiple-scales solution for modal sound transmission through slowly varying ducts with mean flow and acoustic lining, is tested against a numerically "exact" finite element solution. The test geometry taken is representative of a high-bypass turbo fan aircraft engine, with typical Mach numbers of 0.5–0.7, circumferential mode numbers m of 10–40, dimensionless wave numbers of 10–50, and both hard and acoustically treated inlet walls of impedance $Z = 2 - \mathrm{i}$. Of special interest is the presence of the spinner, which incorporates a geometrical complexity which could previously only be handled by fully numerical solutions. The results in predicted power attenuation loss show in general a very good agreement. The results in iso-pressure contour plots show good comparison in the cases where scattering into many higher radial modes can occur easily (high frequency, low angular mode), and again a very good agreement in the other cases.

Introduction

The calculational complexities of the multiple-scales solution for modal sound transmission through slowly varying ducts with mean flow and acoustic lining (presented in [1]), are no more than for the classical modal solution for a straight duct. The multiple-scales solution is an approximation utilizing the axial slope of the duct walls as small parameter. This slope is for aerodynamical reasons indeed invariably small in any aero-engine duct.

Therefore, this multiple-scales solution provides an interesting alternative in aero-engine applications, as it both allows for the advantages of the analytical approach (speed of calculation and relative simplicity of programming), and variable geometries including spinner and mean flow variation.

The final approximation error in realistic geometries, however, is difficult to determine, except for an order of magnitude estimate saying that it scales on this slope. It is therefore of interest to directly compare the analytical approximation with a state of the art fully numerical solution of the same physical model. This is the subject of the present paper.

As a first step towards exploring the possibilities, a series of tests are carried out, comparing the analytical results with results of the finite element solution, given in [2], of a compressible inviscid isentropic irrotational mean flow, superimposed by linear acoustic perturbations.

Physical model

We consider a circular symmetrical duct with a compressible inviscid perfect isentropic irrotational gas flow, consisting of a mean flow and acoustic perturbations. To the mean flow the duct is hard-walled, but for the acoustic field the duct is lined with an impedance wall. In view of the adopted aero-engine geometry, the inner wall (corresponding to the spinner) will be hardwalled, without lining.

We make dimensionless: spatial dimensions on a typical duct radius R_∞, densities on a reference value ρ_∞, velocities on a reference sound speed c_∞, time on R_∞/c_∞, pressure on $\rho_\infty c_\infty^2$, and velocity potential on $R_\infty c_\infty$. Note that the corresponding reference pressure p_∞ satisfies $\rho_\infty c_\infty^2 = \gamma p_\infty$, where $\gamma = 1.4$ is the (constant) ratio of specific heats at constant pressure and volume.

The fluid in the duct is described by

$$\tilde{\rho}_t + \nabla\cdot(\tilde{\rho}\tilde{\mathbf{v}}) = 0, \qquad (1a)$$

$$\tilde{\rho}(\tilde{\mathbf{v}}_t + \tilde{\mathbf{v}}\cdot\nabla\tilde{\mathbf{v}}) + \nabla\tilde{p} = 0, \qquad (1b)$$

$$\gamma\tilde{p} = \tilde{\rho}^\gamma,\ \tilde{c}^2 = \frac{\mathrm{d}\tilde{p}}{\mathrm{d}\tilde{\rho}} = \tilde{\rho}^{\gamma-1} \qquad (1c,d)$$

(with boundary and initial conditions), where $\tilde{\mathbf{v}}$ is particle velocity, $\tilde{\rho}$ is density, $\tilde{p}$ is pressure, $\tilde{c}$ is sound speed (all dimensionless).

Since we assumed the flow to be irrotational, we may introduce a velocity potential $\tilde{\phi}$, such that $\tilde{\mathbf{v}} = \nabla\tilde{\phi}$, and the above momentum equation may be integrated to a variant of Bernoulli's equation

$$\frac{\partial\tilde{\phi}}{\partial t} + \frac{1}{2}|\tilde{\mathbf{v}}|^2 + \frac{\tilde{c}^2}{\gamma-1} = \text{const.} \qquad (2)$$

This flow is split up into a stationary mean flow part, and an acoustic perturbation. This acoustic part varies harmonically in time with circular frequency ω, and with small amplitude to allow linearization.

In the usual complex notation we write then

$$\tilde{\mathbf{v}} = \mathbf{V} + \mathbf{v}\mathrm{e}^{\mathrm{i}\omega t},\ \tilde{\phi} = \Phi + \phi\mathrm{e}^{\mathrm{i}\omega t},$$
$$\tilde{\rho} = D + \rho\mathrm{e}^{\mathrm{i}\omega t},\ \tilde{p} = P + p\mathrm{e}^{\mathrm{i}\omega t},$$
$$\tilde{c} = C + c\mathrm{e}^{\mathrm{i}\omega t}.$$

Substitution and linearization yields:

- mean flow field

$$\nabla\cdot(D\mathbf{V}) = 0, \qquad (3a)$$

$$\frac{1}{2}|\mathbf{V}|^2 + \frac{C^2}{\gamma-1} = E \qquad (3b)$$

$$C^2 = \gamma P/D = D^{\gamma-1}; \qquad (3c)$$

- acoustic field

$$\mathrm{i}\omega\rho + \nabla\cdot(D\nabla\phi + \rho\mathbf{V}) = 0, \qquad (4a)$$

$$\mathrm{i}\omega\phi + \mathbf{V}\cdot\nabla\phi + \frac{p}{D} = 0, \qquad (4b)$$

$$p = C^2\rho, \qquad (4c)$$

where E is a constant, and the acoustic perturbation of $\tilde{c}$ is further ignored. The integration constant in equation (4b) may be absorbed by ϕ. For the mean flow the duct wall is solid, so the normal velocity vanishes at the wall. The subsonic mean flow is determined by conditions of uniformity upstream, the constant E, and an axial mass flux πF.

For the acoustic part the outer duct wall is a locally reacting impedance wall with complex impedance Z. The pertaining boundary condition is for a point near the wall but still (just) inside the mean flow. For arbitrary mean flow along a (smoothly) curved wall, with normal $\mathbf{n}$ directed into the wall, this was given by Myers [3], eq. 15, as

$$\mathrm{i}\omega(\mathbf{v}\cdot\mathbf{n}) = \left[\mathrm{i}\omega + \mathbf{V}\cdot\nabla - \mathbf{n}\cdot(\mathbf{n}\cdot\nabla\mathbf{V})\right]\left(\frac{p}{Z}\right). \qquad (5)$$

Geometry

The reference values taken for non-dimensionalization are at the source plane $x = 0$, including the outer radius for length scale.

The outer radius R_2 and inner radius R_1 are described by the following formulas

$$R_2(x) = 1 - 0.18453x'^2 + 0.10158\frac{\mathrm{e}^{-11(1-x')} - \mathrm{e}^{-11}}{1-\mathrm{e}^{-11}}, \qquad (6)$$

$$R_1(x) = \max[0, 0.64212 - (0.04777 + 0.98234x'^2)^{1/2}], \qquad (7)$$

where $x' = x/L$ and $L = 1.86393$ is the length of the duct; see figure (1)

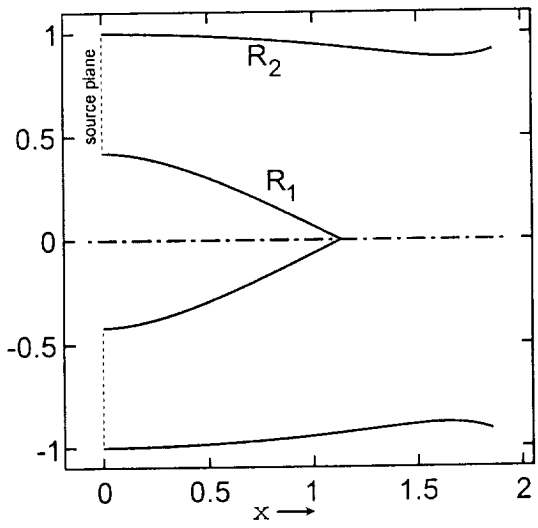

Figure 1: Geometry

The mean flow is selected such that at the source plane $x = 0$ the Mach number is equal to -0.5, and the dimensionless density equal to 1. The corresponding axial Mach number and dimensionless density variation (based on the quasi-one dimensional mean flow solution; see below) is depicted in figure (2).

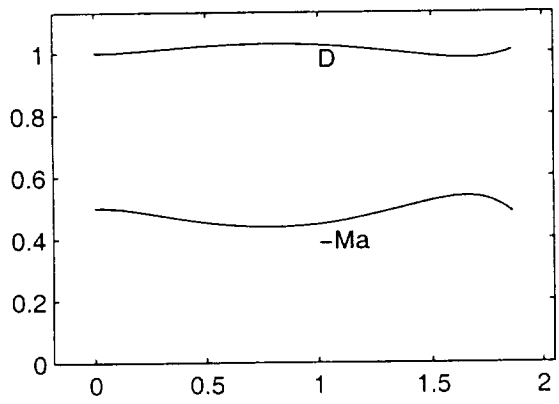

Figure 2: Mach number and density

Multiple scales solution

For the success of the analytical solution it is essential that the mean flow and the acoustic field are approximated on the same footing. An arbitrary, ad-hoc, mean flow field would not allow the present explicit solution. So the mean flow used for the multiple scales solution is not exactly the same as the one used for the finite element solution. They are, however, in terms of approximation of the same level. Therefore, we give here the mean flow and the acoustic field together.

The approximation is based on the assumption that geometry and mean flow vary slowly, *i.e.* on a length scale much larger than a typical duct diameter or wave length. This is, of course, for aerodynamical reasons the case inside an aero-engine inlet duct. We introduce the ratio between a typical diameter and this length scale as the small parameter ε, and rewrite the duct surface (in radial coordinates (x, r, θ))

$$r = R_1(X), \quad r = R_2(X), \quad X = \varepsilon x. \tag{8}$$

By rewriting $R_{1,2}$ as a function of slow variable X, rather than x, we have made our formal assumption of slow variation explicit in a convenient and simple way. Although in the final result ε will play no explicit rôle, a representative value of ε will be necessary for an order of magnitude estimate of the approximation error.

By assuming that the mean flow is nearly uniform with axial variations in X only, we find that small axial mass variations can only be balanced by a small radial flow, so

$$\mathbf{V} \simeq U_0(X)\mathbf{e}_x + \varepsilon V_1(X, r)\mathbf{e}_r$$

and similarly are $P \simeq P_0(X)$, $D \simeq D_0(X)$, and $C \simeq C_0(X)$ to leading order only dependent on X. It follows that

$$U_0(X) = \frac{F}{D_0(X)(R_2^2(X) - R_1^2(X))}$$

with V_1, D_0, P_0 and C_0 are given by the well known one dimensional gas flow equations (see *e.g.* [1]).

The acoustic field is assumed to be described by mode-like solutions of the form

$$\phi(x, r, \theta; \varepsilon) = A(X, r; \varepsilon)\, \mathrm{e}^{-\mathrm{i}m\theta - \mathrm{i}\varepsilon^{-1}\int^X \mu(\xi)\,\mathrm{d}\xi} \tag{9}$$

After expanding $A = A_0 + \varepsilon A_1 + O(\varepsilon^2)$ and $\mu = \mu_0 + O(\varepsilon^2)$ (any possible μ_1 can be absorbed by A_1), and substitution in equations and boundary conditions, we find for A_0 a Bessel-type equation in r, so we obtain the slowly varying mode

$$A_0 = N(X)J_m(\alpha(X)r) + M(X)Y_m(\alpha(X)r) \tag{10}$$

where J_m and Y_m are the m-th order Bessel function of the first and second kind. Radial eigenvalue α and M/N are determined by the boundary condition, while

$$\alpha^2 + \mu^2 = \Omega^2/C_0^2, \quad \Omega = \omega - \mu U_0.$$

The crux of the solution is the determination of amplitude $N(X)$, as a function of X. This is determined by the next order equation for A_1. It is, however, not necessary to solve this complicated equation. A solvability condition [1] is enough to generate a differential equation in X for N, which can be solved exactly. The general solution for the hollow cylinder ($R_1 \equiv 0$, $M \equiv 0$) is given by

$$\left(\frac{Q_0}{N}\right)^2 = \left(\frac{D_0\omega\sigma R_2^2}{2C_0}\left(1 - \frac{m^2 - \zeta_2^2}{\alpha^2 R_2^2}\right) + \frac{D_0 U_0}{\Omega}\zeta_2\right) J_m(\alpha R_2)^2 \tag{11}$$

where Q_0 is an integration constant, and $\zeta_2 = \Omega^2 D_0 R_2/\mathrm{i}\omega Z_2$, $\sigma^2 = 1 - (C_0^2 - U_0^2)\alpha^2/\omega^2$. The solution for the annular cylinder is more complicated, although explicit, and can be found in [1]

Finite element solution

A numerical model for sound propagation is based on a finite element discretization of

the steady flow field equations (3a-3c) and the acoustic field equations (4a-4c). The weak formulation of equation (3a) for the steady compressible flow in the duct is in terms of the steady flow velocity potential Φ and steady flow density D,

$$\iiint_V \nabla W \cdot (D\nabla\Phi)\,\mathrm{d}V = \iint_S W(D\nabla\Phi)\cdot\mathbf{n}\,\mathrm{d}S. \tag{12}$$

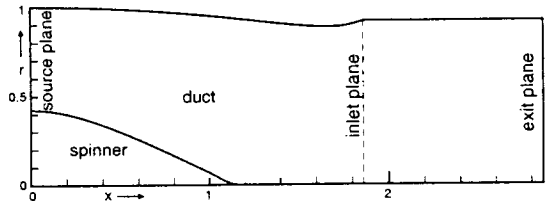

Figure 3: Computational domain FEM

Weighting functions W are from the class of continuous functions on the volume V of the duct bounded by the duct surface S, which includes the duct walls and source and exit planes. A solution for Φ is sought in the class of continuous functions. The unit normal is directed out of the duct. The duct geometry and the steady flow field are axially symmetric favoring the introduction of a cylindrical coordinate system with x axis coincident with the axis of symmetry, r axis in the source plane at $x = 0$, and the angular coordinate θ locating the r axis in the $x = 0$ plane (see figure 3 for the computational domain). The steady flow field is represented in an (x, r)-plane, and is two-dimensional. A standard finite element formulation of equation (12) is based on eight node isoparametric serendipity elements.

Equations (3b) and (3c) are subsidiary relations that are used in an iterative solution in which at each stage the finite element discretization of equation (12) is solved with a density and speed of sound field derived from the previous iteration step. The boundary integral on the right hand side, which is a natural boundary condition, specifies the mass flow rate on the source plane. A forced boundary condition setting the level of the potential is required on the exit plane (figure 3). It is assumed that the source plane and exit plane are located remotely enough from regions of nonuniformity in the duct so that at the source and exit planes the flow velocity is uniform, permitting the natural and forced boundary conditions to be easily implemented. In practical calculations in the type of duct considered this turns out not to be restrictive.

The mean flow in the duct given by figure 3, with a uniform Mach number at the source plane $M = -0.5$, is directed from right to left (an inlet flow). The duct shape defined by equations (6) and (7) begins at the source plane $x = 0$ and is extended beyond the nominal termination used in the analytical development in a uniform duct to allow the flow field to become uniform at the exit plane. No extension is used at the source end and the extension at the exit end is probably longer than necessary. $\nabla\Phi$, C, D are required data for the FEM solution for acoustic propagation.

A finite element model for acoustic propagation is based on a weak formulation of equations (4a-4c). Acoustic perturbations in pressure, density and velocity potential are harmonic in time with frequency ω and harmonic in the angular coordinate θ of the form $p(x, r)$, $\rho(x, r)$, and $\phi(x, r)$ times the complex exponent $\mathrm{e}^{\mathrm{i}\omega t - \mathrm{i}m\theta}$. The weak formulation [2] is

$$\iiint_V \{\nabla W\cdot(D\nabla\phi + \rho\nabla\Phi) - \mathrm{i}\omega W\rho\}\,\mathrm{d}V = \iint_S W(D\nabla\phi + \rho\nabla\Phi)\cdot\mathbf{n}\,\mathrm{d}S \tag{13}$$

The weighting functions are taken as $W(x, r)\,\mathrm{e}^{\mathrm{i}m\theta}$. Angular harmonics proportional to $\mathrm{e}^{-\mathrm{i}m\theta}$ represent the decomposition of the solution periodic in θ in a Fourier Series. The angular mode number m is a parameter of the solution. The surface integral is over all surfaces bounding the domain. The unit normal for the surface integral is out of the domain at the surface in question. The weak formulation continues with the linearized momentum equation (4b) and linearized equation of state (4c), to rewrite equation (13) in the form

$$\iiint_V \frac{D}{C^2}\Big\{C^2\nabla W\cdot\nabla\phi - (\mathbf{V}\cdot\nabla W)(\mathbf{V}\cdot\nabla\phi) + \mathrm{i}\omega\Big[W(\mathbf{V}\cdot\nabla\phi) - (\mathbf{V}\cdot\nabla W)\phi\Big] - \omega^2 W\phi\Big\}\,\mathrm{d}V = \iint_S \frac{D}{C^2}\Big\{C^2 W\nabla\phi - \mathbf{V}W(\mathbf{V}\cdot\nabla\phi) - \mathrm{i}\omega\mathbf{V}W\phi\Big\}\cdot\mathbf{n}\,\mathrm{d}S \tag{14}$$

Note that the local steady flow dimensionless velocity $\mathbf{V}$ is equivalent to the reference Mach

number M_r which in fact is local steady flow velocity divided by the speed of sound at the source plane.

The surface integral on the right hand side of equation (14) is the natural boundary condition. On the duct walls this provides the boundary condition for either rigid walls (the integral vanishes) or for a normally reacting lining with an impedance specified by equation (5). In the present FEM implementation equation (5) is simplified by the elimination of the term involving $\mathbf{n}\cdot(\mathbf{n}\cdot\nabla\mathbf{V})$ on the right hand side. In the duct geometry studied here this term, which depends on the nonuniformity of the steady flow field, is of little importance in affecting attenuation (even though it is asymptotically small but not negligible, and crucial in completing the analytical formulation).

Details of the FEM procedure for discretization of equation (14), and other references, can be found in [2]. A discussion of the implementation of the impedance boundary condition is available in reference [5].

On the source plane and exit plane the natural boundary condition is used to introduce the noise source and non-reflecting boundary conditions. On these planes the acoustic potential is recast via an eigenmode expansion such that the acoustic potential is given in terms of the complex amplitudes of the right and left propagating acoustic duct modes appropriate for the geometry and flow conditions which prevail there [6]. On the source plane, $x = 0$ in the present study, right propagating modal amplitudes at the source plane are specified via a forced boundary condition. Left running (reflected) modal amplitudes at the source plane and right running modal amplitudes at the exit plane are unknown and part of the solution. Left running modal amplitudes at the exit plane are forced to vanish, imposing a non-reflecting boundary condition. Details of the modal boundary condition are available in reference [4].

Finite element discretization for acoustic propagation is carried out on the same grid with the same element type as used in the steady flow model. Required data generated in the steady flow representation is transferred directly to the acoustic analysis. Mesh density is governed by the demands of the acoustic problem and is substantially more refined than would be required in the steady flow analysis.

The FEM solution proceeds with the computation of the acoustic potential field. Post-processing by the use of equation (4b) generates the acoustic pressure field. The solution also includes reflected modal amplitudes and transmitted modal amplitudes. Acoustic power reflection and transmission characteristics are computed directly from the input modal amplitudes and computed reflected and transmitted modal amplitudes. Reciprocity characteristics of the scattering matrices and acoustic power balances are also monitored as a check of computational accuracy in the case of no acoustic treatment on the duct walls [7].

Post processed acoustic pressures are represented on iso-pressure amplitude contour plots superimposed on the duct geometry. Comparison of FEM and multiple scales results is based on visual comparison of these contours, but perhaps more importantly on the basis of computed power transmission coefficients.

Differences between Multiple Scales and FEM Formulations

There are minor differences between the multiple scales solution and the finite element model. The field equations (3a)-(3c) and (4a)-(4c) are exactly the same in both cases, including the convention for non-dimensionalization. The implementation of the impedance boundary condition in the FEM formulation neglects the $\mathbf{n}\cdot(\mathbf{n}\cdot\nabla\mathbf{V})$-term in equation (5). This is done principally to simplify the FEM implementation of this difficult boundary term (it requires a gradient of the steady flow velocity which is already the gradient of the steady flow potential). For a cylindrical duct this term is to leading order in ε equal to $\frac{\partial}{\partial r}V \simeq \varepsilon U R_X/R$. So it is small, but asymptotically not smaller than any other effect due to duct variation. Nevertheless, we found as yet no indication that the effect on attenuation predictions is significant.

The FEM formulation includes the propagation of many modes and therefore scattering is an integral part of the solution. This is manifested by reflection of the incident mode and other modes which are not incident as well as the transmission of modes which are not incident. The multiple scales method utilizes the fact that in the smooth parts of the duct any scattering into other modes is normally negligible. The propagating sound is still mode-like, albeit not in the strict sense of self similar straight duct modes, but mode-like solutions with slowly varying amplitude and phase.

At abrupt changes in geometry scattering into other radial modes may be included (not done here) by methods like mode-matching.

The FEM solution requires the source to be represented in terms of input modal amplitudes for eigenmodes for a duct with hard walls. The source is always located in a section of the duct which has rigid walls. The net effect is that there is always a transition from a rigid wall to an impedance wall at both ends of the duct in the FEM model. This has implications for scattering which are not readily quantifiable.

In the multiple-scales analysis the general solution is built up from a summation over slowly varying modes. The natural way to test its validity is therefore to study a single, soft-wall, mode. In order to generate an equivalent input in the FEM model it is necessary to represent the soft wall eigenmode as an eigenmode expansion of hard wall eigen modes. Since this sound field distribution, presented to the lined duct, essentially "fits" directly into one soft-wall mode, only little reflection at the source plane is to be expected. A single mode multiple-scales analysis is therefore simulated by a multiple mode FEM solution.

Finally, it is noted that the FEM model requires conditions at the source and exit planes which give rise to reflected modal amplitudes and to the reflection free termination (or specified or computed reflection characteristics). These conditions do not play an immediate role in the analytical solution, with left and right running waves already given explicitly. Although inherent in any practical application, we have not tried to model these conditions in the analytical part of the present tests in order not to obscure the comparison and to restrict the sound field to that of a single, right-running, mode.

It is not possible to make FEM and multiple-scales models exactly equivalent, nor should it be, since the multiple-scales solution is an approximation based on well documented assumptions. It is a goal of the numerical comparisons to be given here to investigate how successfully the multiple-scales solution represents the more exact FEM model.

Results

The cases considered are grouped as the following 4 series of iso-pressure contour plots: the first radial mode of

fig. 4 $m = 10,\ \omega = 10,$
fig. 5 $m = 10,\ \omega = 16,$
fig. 6 $m = 10,\ \omega = 50,$
fig. 7 $m = 40,\ \omega = 50,$

is input under the following conditions:

fig. a hard wall, no flow,
fig. b hard wall, flow,
fig. c soft wall, no flow,
fig. d soft wall, flow.

The left column of the figures is the numerical FEM solution, the right column the analytical MS (multiple scales) solution. "Soft wall" denotes a wall impedance $Z = 2 - \mathrm{i}$. "Flow" denotes a mean flow with Mach number -0.5 at the source plane. "First radial mode" denotes in general the mode with smallest real part of radial eigenvalue α. For the soft walls the predicted attenuation (10 log of ratio of acoustic power through source and inlet plane) is given in the caption of the figures. For the hard walls the attenuation is either zero (mode is cut on) or infinite (mode is cut-off and reflection is negligible).

The selected cases do not show turning point behaviour (hard-wall cut-on, cut-off transition).

The possible differences between FEM and MS are due to the following errors or modelling discrepancies.

1. The approximation error of $O(\varepsilon^2)$. For this we need an estimate of ε. Suitable is a typical value of $\frac{\mathrm{d}}{\mathrm{d}x}R_2 = \varepsilon\frac{\mathrm{d}}{\mathrm{d}X}R_2 = O(\varepsilon)$. From formula (6) it appears that R_2' varies between -0.12 and 0.12 along [0,1.75], but increases to 0.4 in the lip region [1.75,L]. If we take $\varepsilon = 0.1$, the estimated approximation error is a few percent.
2. Small but inherent reflection in FEM at inlet plane and lip region.
3. Not exactly the same source in soft wall cases, since FEM uses a source defined by an expansion in a finite number (15) of hard wall modes, a small distance ($\frac{1}{100}L$) away from the lined section.
4. Slightly different impedance definition in flow cases.
5. Slightly different mean flow. In MS the mean flow field is approximated to the same level as the acoustic field.

For highly attenuated or only cut-off modes ($m = 10, \omega = 10$) of fig. 4a-d, the agreement is almost perfect. None of the above errors seem

to play a role.

For the series ($m = 10$, $\omega = 16$) of fig. 5, with 1 (no flow) or 2 (flow) modes cut-on, the agreement is good in the iso-contour plots, and almost perfect in attenuation. Some wiggles are visible in fig. 5b what is probably error type 1, due to interference with the other cut-on radial modes.

The high frequency series ($m = 10, \omega = 50$) of fig. 6 has very low acoustic pressure values near the duct axis, and many radial modes cut on (at source plane, no flow: 9, flow: 11). We see strong interference with these higher modes. The most important region near the outer wall, however, is in very good agreement, and for no flow the attenuation agrees exactly. With flow the 1st and 2nd radial soft wall modes happen to be rather close to each other, and a residual second mode (due to error 3) leads to a slightly (0.5 dB) different attenuation.

The high m, high frequency ($m = 40, \omega = 50$) series of fig. 7 has 2 (no flow) and 3 (flow) radial modes cut on, giving rise to some wiggles in figs. 7a,b. Effects due to error 3 are probably visible in fig. 7d, although the predicted attenuation agrees very well. The (academic!) difference in attenuation of fig. 7c (195 and 210 dB) is no numerical round-off error, but due to the fact that the plotted mode is least attenuated at the inlet but not at the source plane. Residual modes due to error 3 are likely to dominate in the FEM solution near the source plane, leading to a different attenuation.

Conclusions

Any selection of test cases is necessarily limited. It would have been easy to create a more or a less favourable comparison, by making a suitable selection of geometry and parameters. This is not done here. We have defined the test runs entirely on the basis of their relevance to turbo fan engine inlet duct applications, and we have not skipped unfavourable cases afterwards. The only restriction we made was that no cut-on/off transition in the hard walled duct be present. This phenomenon is not yet included in the analytical solution, while at the same time, of course, it is absent in any lined duct.

So considering the fact that the cases are likely to be a representative cross section of reality, we think the conclusion is justified that the MS and FEM solutions compare favourably, both in iso-pressure contours and in predicted attenuation. Principle differences are related to scattering at inlet plane, and to input mode synthesis. The best results are obtained with lining (reducing importance of reflection) and when the modal structure permits few or no cut-on scattered modes. The attenuation differs in general no more than a few tenths of a dB.

The correlation shows that MS is definitely useful in applications for assessing liner performance in realistic geometries. Both extending the theory, and further comparison with FEM, for example with an MS implementation that includes a complete modal spectrum and open end reflection, is therefore to be recommended.

Acknowledgement

The contribution of Professor Eversman was partially supported by NASA Lewis Research Center under Grant NAG 3-2109.

References

[1] S.W. Rienstra, 1999 Sound transmission in slowly varying circular and annular ducts with flow, *Journal of Fluid Mechanics* **380**, 279–296. Also: *AIAA* No-98-2311, 4th AIAA/CEAS Aeroac. Conf. Toulouse 1998.

[2] I. Danda Roy and W. Eversman, 1995 Improved finite element modeling of the turbofan engine inlet radiation problem. *ASME Journal of Vibration and Acoustics* **117**(1), 109–115.

[3] M.K. Myers, 1980 On the acoustic boundary condition in the presence of flow. *Journal of Sound and Vibration* **71**(3), 429–434.

[4] W. Eversman and K.J. Baumeister, 1986 Modeling wind tunnel wall effects on the radiation characteristics of acoustic sources. *Journal of Aircraft* **23**(6), 455–463.

[5] W. Eversman and D. Okunbor, 1998 Aft fan duct acoustic radiation. *Journal of Sound and Vibration* **213**(2), 235–257.

[6] W. Eversman, 1991 *NASA Reference Publication 1258.* Aeroacoustics of Flight Vehicles: Theory and Practice. *Volume 2:* Noise Control. Theoretical models for duct acoustic propagation and radiation.

[7] W. Eversman, 1999 A reverse flow theorem and acoustic reciprocity in compressible potential flows. *Paper 3aPA3* 137th Reg. Meeting of the Ac. Soc. of Am. and 2nd Conv. of Europ. Acoust. Assoc.: Forum Acusticum 99, 15-19 March,1999, Berlin.

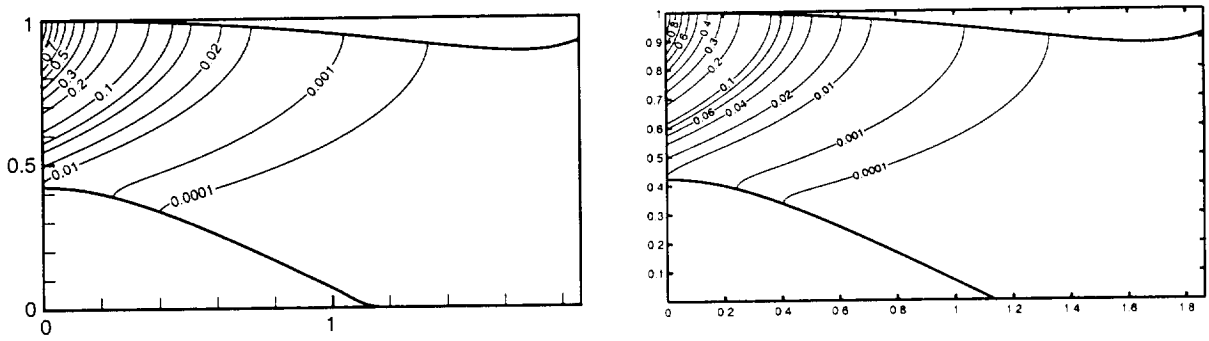

Figure 4a: $m = 10$, $\omega = 10$, hard wall, no flow

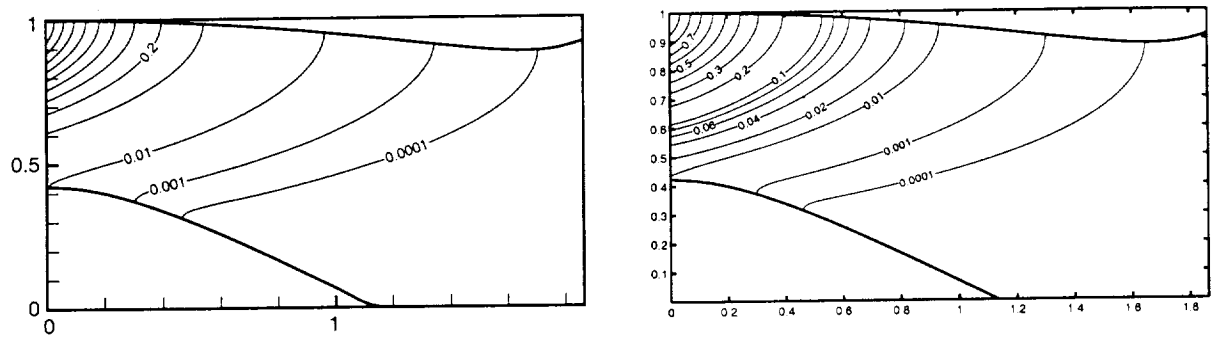

Figure 4b: $m = 10$, $\omega = 10$, hard wall, flow

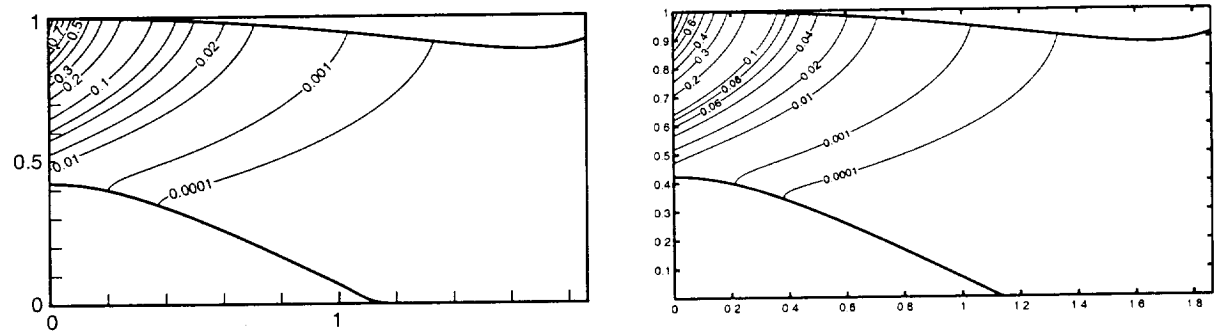

Figure 4c: $m = 10$, $\omega = 10$, soft wall, no flow;
att. 120 dB (MS)

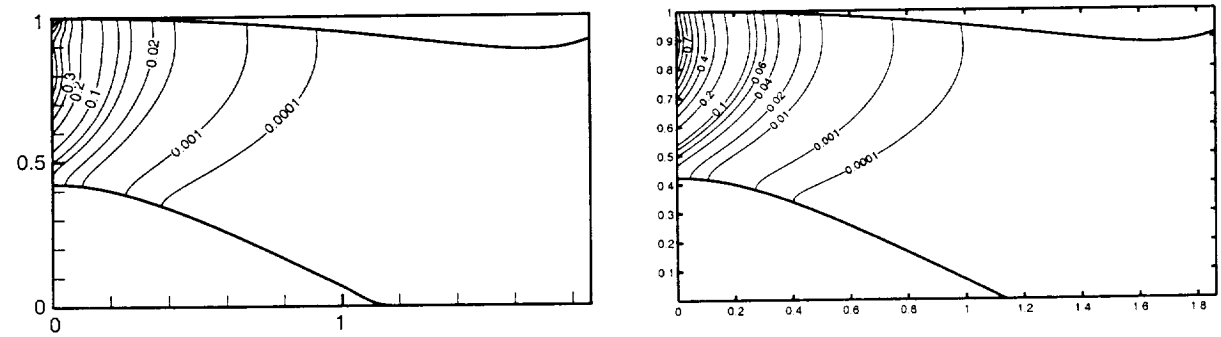

Figure 4d: $m = 10$, $\omega = 10$, soft wall, flow;
att. 164 dB (MS)

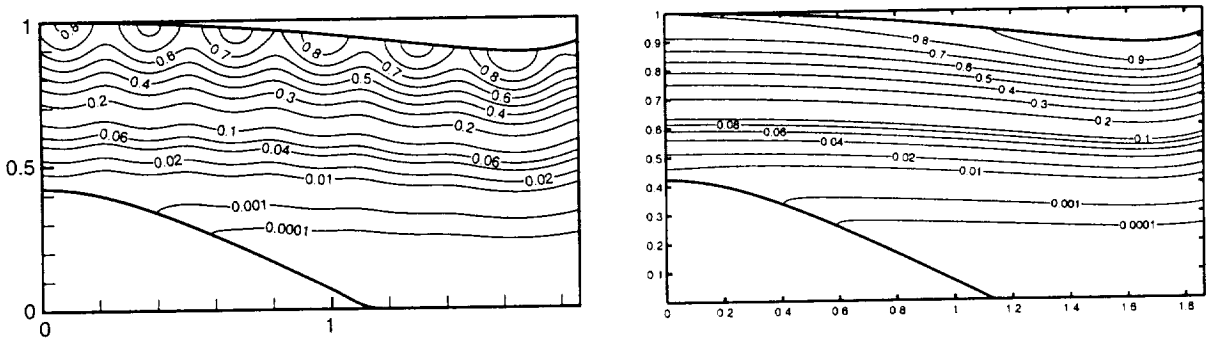

Figure 5a: $m = 10, \omega = 16$, hard wall, no flow

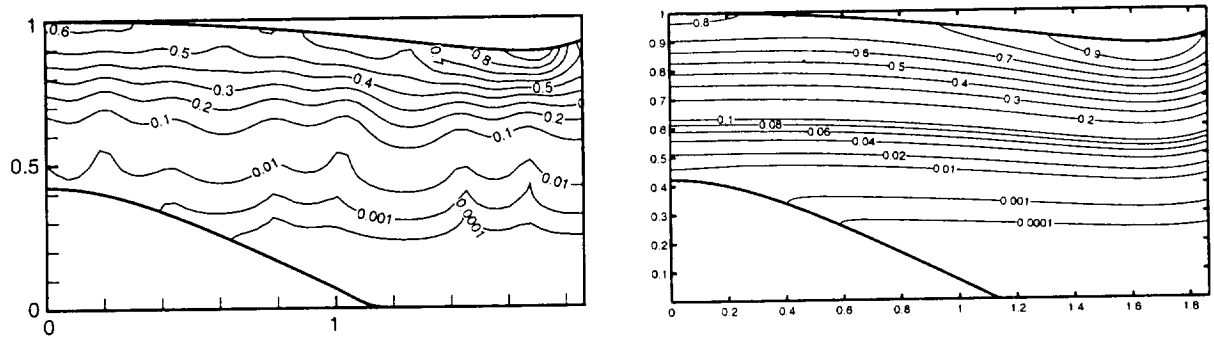

Figure 5b: $m = 10, \omega = 16$, hard wall, flow

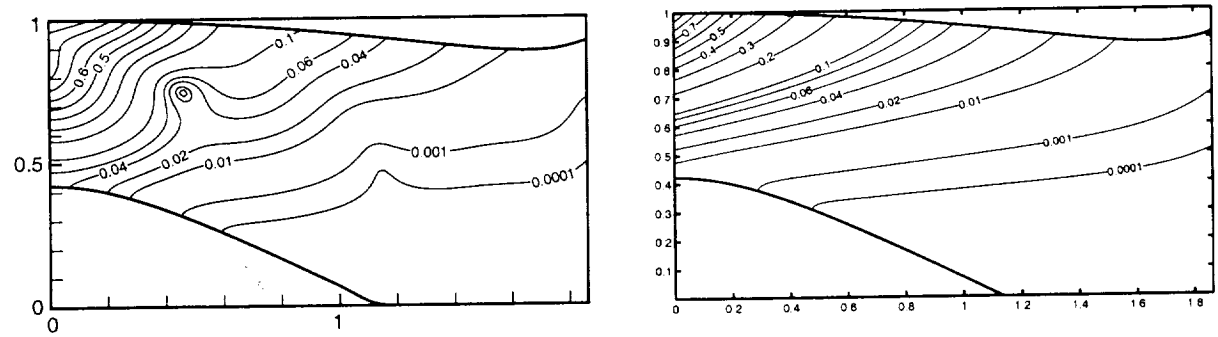

Figure 5c: $m = 10, \omega = 16$, soft wall, no flow;
att. 51.57 dB (FEM), 51.64 dB (MS)

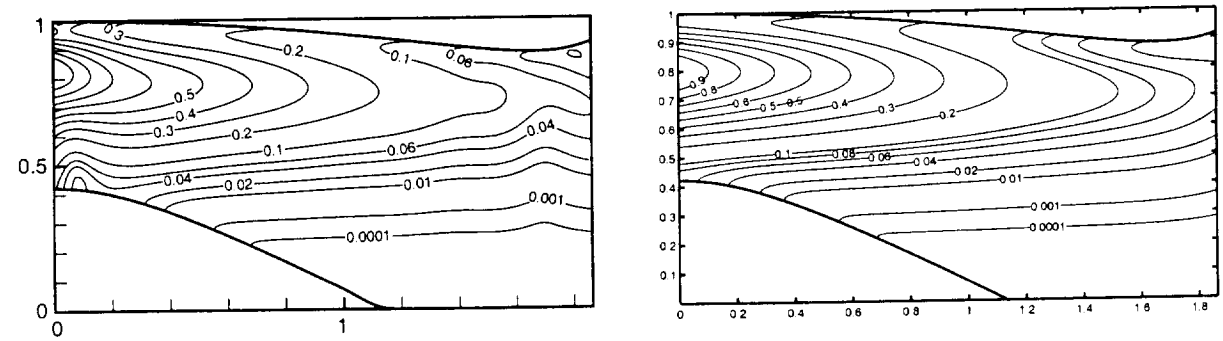

Figure 5d: $m = 10, \omega = 16$, soft wall, flow;
att. 27.2 dB (FEM), 27.1 dB (MS)

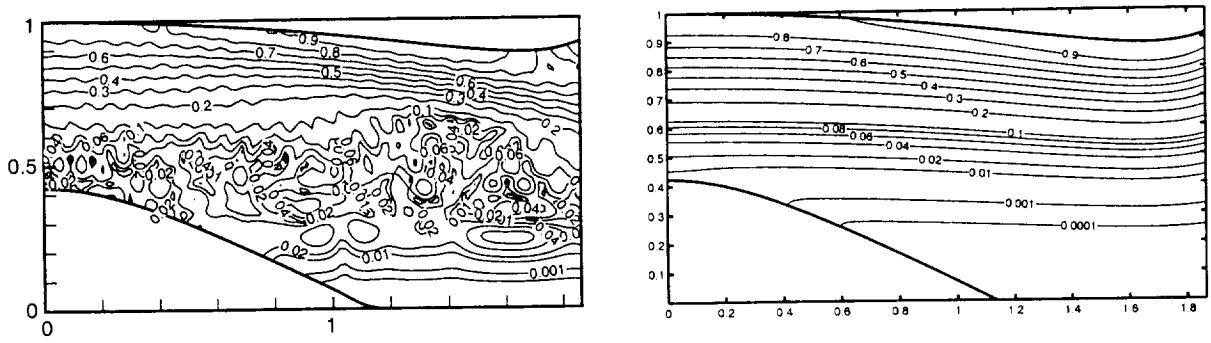

Figure 6a: $m = 10, \omega = 50$, hard wall, no flow

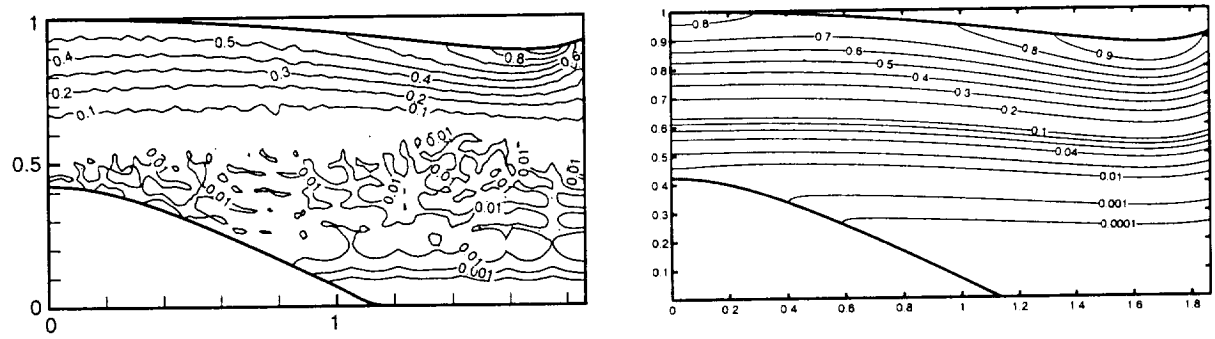

Figure 6b: $m = 10, \omega = 50$, hard wall, flow

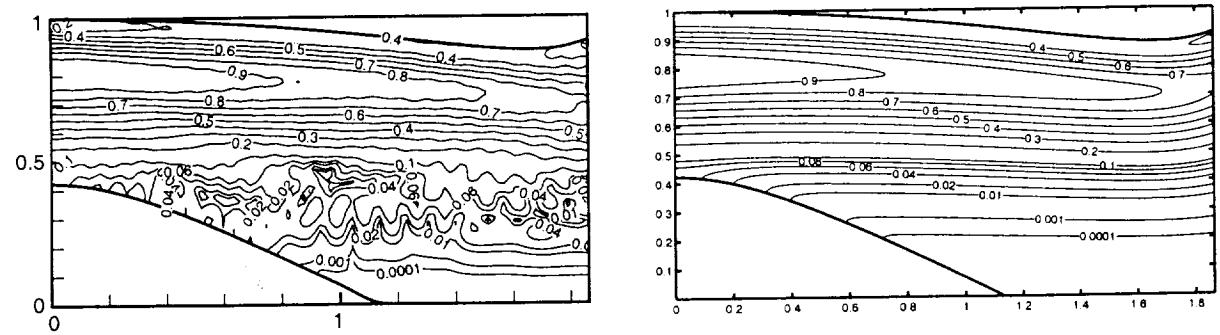

Figure 6c: $m = 10, \omega = 50$, soft wall, no flow;
att. 3.49 dB (FEM), 3.49 dB (MS)

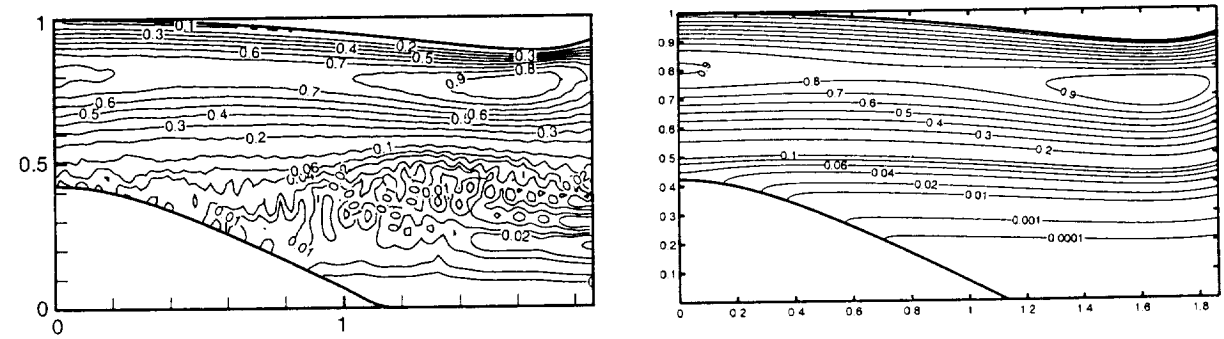

Figure 6d: $m = 10, \omega = 50$, soft wall, flow;
att. 1.49 dB (FEM), 0.92 dB (MS)

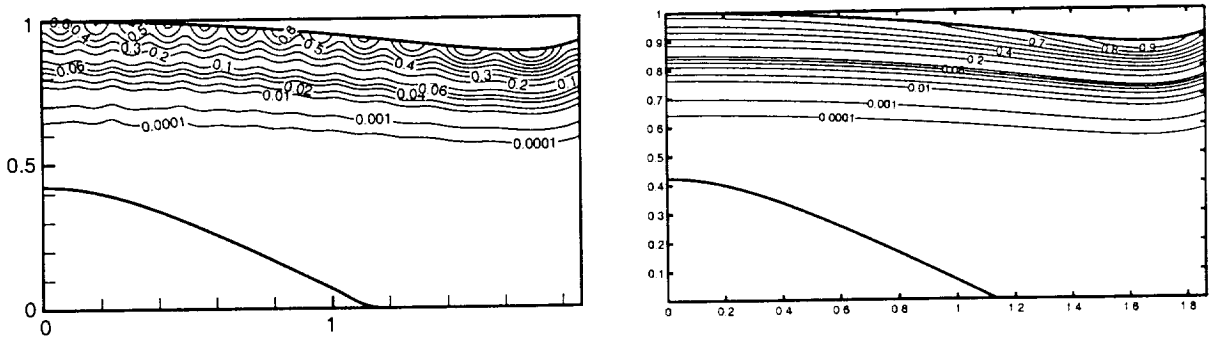

Figure 7a: $m = 40$, $\omega = 50$, hard wall, no flow

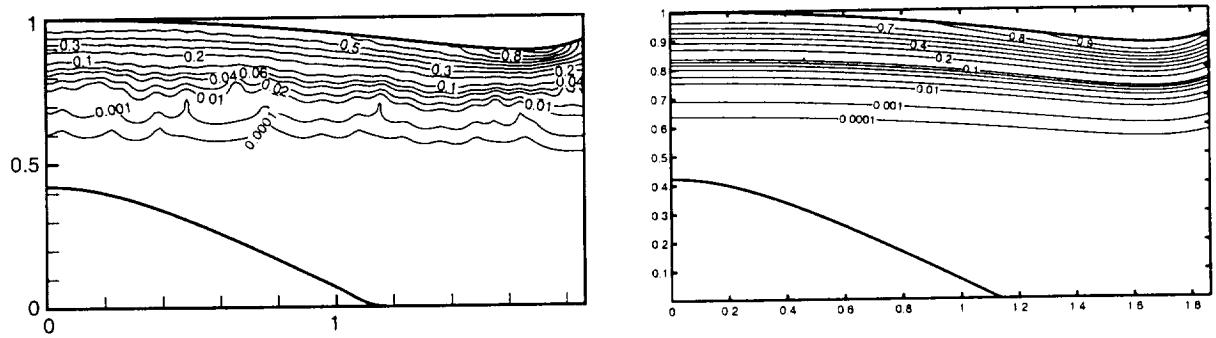

Figure 7b: $m = 40$, $\omega = 50$, hard wall, flow

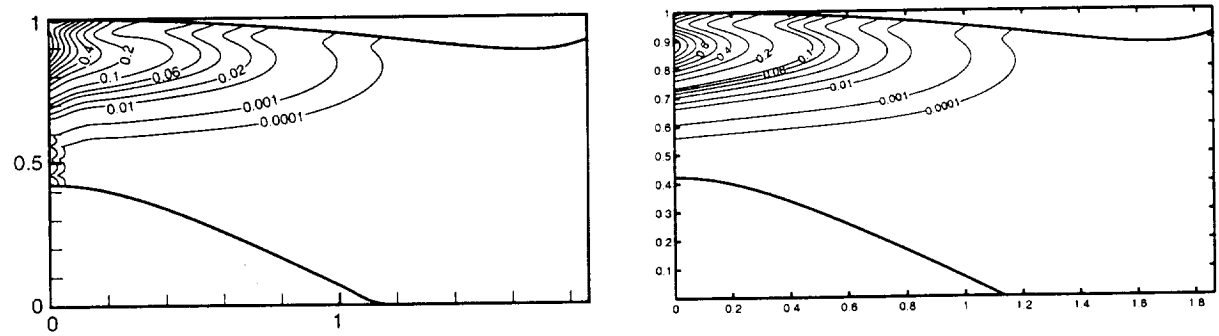

Figure 7c: $m = 40$, $\omega = 50$, soft wall, no flow;
att. 195.6 dB (FEM), 210.4 dB (MS)

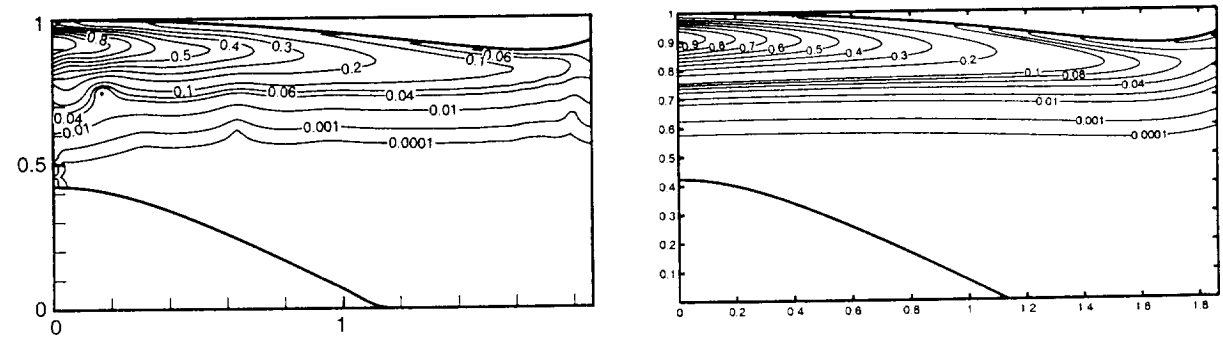

Figure 7d: $m = 40$, $\omega = 50$, soft wall, flow;
att. 28.4 dB (FEM), 28.6 dB (MS)

AIAA-2000-1953

ACOUSTIC PROPAGATION AT HIGH FREQUENCIES IN DUCTS

Eivind Listerud* and Walter Eversman†
Mechanical and Aerospace Engineering and
Engineering Mechanics
University of Missouri-Rolla
Rolla, MO 65401

ABSTRACT

In order to achieve satisfactory results with finite element formulations for pressure in a propagating acoustic field with relatively high non-dimensional frequencies, the problem of ever-diminishing mesh size must be resolved. The convected potential formulation describing an acoustic field introduces problems not addressed in the simple Helmholtz equation. Post-processing to calculate pressure is necessary and this leads to additional dimensionality problems beyond those encountered in modeling acoustic potential due to an inaccuracy appearing in the calculation of the potential derivatives. This oscillating erroneous behavior is rooted in the element shape functions and modifications have been made, using elements of higher order, to contain this discrepancy enough to where post-processing does not add significantly to the dimensionality problem. In so doing, satisfactory pressure models for non-dimensional frequencies up to 100 in a variable area circular duct with a wide range of subsonic Mach numbers and angular modes can be calculated in a reasonable sized domain.

INTRODUCTION

Application of the finite element method (FEM) in modeling acoustic propagation leads to problems of large dimensionalities when high frequencies are considered. A mesh of about 10 nodes per wavelength is considered adequate resolution in order to achieve acceptable results in modeling propagating waves. Simply reducing the mesh size is certainly an option. However, it becomes quickly impractical and computationally expensive. Several approaches have been studied in order to deal with the dimensionality problem.

One common approach is to lower the number of nodes required per wavelength. In acoustic radiation to the far field the development of infinite elements, which incorporates spatially harmonic radiation into the shape functions, has greatly reduced the far field dimensionality problem[1-3]. The earliest approach was based on exponential decays with radial distance[1]. Later, and with more success, mapped infinite elements were developed based on the asymptotic behavior of the far field and the correct spherical or cylindrical decay was incorporated[2]. Burnett[3] extended this method to use prolate spheroidal coordinates, allowing it to be more flexible in modeling objects with large aspect ratios, i.e. reducing the extent of the conventional mesh in the near field, thus reducing the overall mesh. A variation of the infinite element method is that of the wave envelope element method which restricts the computations to a large but finite domain[4-7]. Astley[4] incorporated the use of complex conjugates weighting as opposed to Galerkin weighting, reducing the integrals to simpler forms, thus enabling Gauss-Legendre integration. The penalty was a non-symmetric coefficient matrix, although with less frequency dependence. This method was also capable of reducing the reach of the conventional element domain while extending into flow problems[5-7]. Mapped infinite wave envelope elements have attributes of both infinite and wave envelope elements. This technique has recently been extended to include three-dimensional elements of variable order[8], sperhoidal elements of variable order to improve modeling around a slender or flat object[9], and a non-reflective boundary with uniform steady flow[10]. The mapped infinite wave envelope elements can be used in what is normally considered the acoustic near field because of their adjustable interpolation order, thus reducing mesh refinement and dimensionality to a greater extent than with previous approaches. Chadwick and Bettes[11] modeled the phase p and the wave envelope A rather than the potential ϕ (the potential of a traveling wave is expressed as

* Graduate Student, Member AIAA.
† Curators' Professor, Associate Fellow AIAA.

$\phi=Ae^{ip}$) for finite wave envelope elements and were able to use a coarser mesh in the near field. This was later extended to infinite elements[12]. The penalty however is that an iteration procedure is necessary. All of the previously mentioned approaches are well suited in an exterior region. Inside a duct, however, the complexity of the acoustic field makes for limited success. In fact, Astley and Eversman[13] suggested the use of traditional wave envelope elements inside a duct before they were used in the far field, but it was effective in only special circumstances.

The most traditional FEM approach in dealing with short waves is to let the mesh size decrease while the piecewise polynomials of degree p are constant. This is known as the h-version, while the p-version leaves a fixed mesh and allows p to increase. These have been combined and extended into the adaptive hp-version. For a detailed background and method of implementation see references [14] and [15]. In the field of acoustics this method has recently been used in modeling the Helmholtz equation for non-dimensional frequencies up to 30π [16]. Although a significant decrease in total degrees of freedom is achievable because of its adaptive behavior, it is computationally expensive due to the iteration procedure, despite exponential convergence. The nodal density is still needed at about 10 nodes per wavelength for reasonable errors.

The incorporation of wavelike behavior into the elements has not been limited to infinite and wave-envelope elements. Babuška and Melenk introduced the partition of unity method (PUM) based on introducing prior knowledge about the governing differential equation into non-polynomial functions used for the solution approximation, rather than traditional (mapped) polynomials[17]. These special functions approximate well the exact solution and the wave direction at each node is implicitly determined. It is advantageous to use a set of plane wave solutions of the homogenized Helmholtz equation as the local function basis. Computational cost is still a problem compared to non-iterative approaches. In reference [17] it is also suggested that PUM is suited well for a mesh-less formulation. More recently, an element-free one-dimensional Galerkin method was applied to the Helmholtz equation[18].

The combination of PUM and a standard FEM has been called the generalized finite element method and seems to offer a significant reduction in dimensionality versus standard FEM without requiring re-meshing[19]. In a recent presentation Bettes and Laghrouche extended this idea to the Helmholtz short wave problem[20]. An approach based on a somewhat similar idea as that behind the PUM was that of residual-free bubble functions[21]. It added these functions to the piecewise linear polynomials and used subspaces where these functions satisfied the differential equation strongly and solved analytically for them. This was applied to the Helmholtz equation for relatively low non-dimensional frequencies (<10). Franca and Macedo extended this to a more flexible two level method[22]. They used a submesh defined in each element interior and solved the differential equation numerically for the bubble functions, allowing for irregular meshes.

It is important to note that the methods used in reference [14] to [22] have all been applied when solving the Helmholtz equation. The introduction of a moving medium in the acoustic field has lead to a different approach. The FEM model used in this paper is potential based and post-processes to find the acoustic pressure. This convected potential formulation introduces problems not encountered in working with the Helmoltz equation. Among them is the consideration of an effective wavelength, due to flow velocity and while the potential solution abide by the expected nodes per wavelength ratio of 10 to 12, the calculation of pressure which involves the derivative of the potential solution apparently does not. The nodal density required by the post-processing adds greatly to the dimensionality of the problem. An investigation into the cause of the shortcoming and possible simple modifications for this model was conducted. The variation in the order of the polynomials was performed for both a quasi-one dimensional and an axially symmetric system. The results were considered in a ducted acoustic field with non-dimensional frequencies up to 100 and a wide range of propagating modes. It involved large area variations and most of the subsonic flow range. The behavior of this high frequency complex acoustic field was studied and the post-processing problem was greatly diminished while a possible method for an extension to improve the dimensionality of the overall system was considered.

FORMULATON OF PROBLEM

The problem in question is the propagating acoustic field in a moving medium inside a circular non-uniform duct. A typical geometry of such a duct is seen in figure1. The

noise source is at the left end and the medium may flow in either direction with left to right considered positive direction. The acoustic field description is based on a convective potential formulation obtained by considering unsteady acoustic perturbations on a steady compressible potential flow. Eversman et. al. previously developed a FEM model for the turbofan engine inlet radiation problem[5,6]. This FEM model is basically the same without the exterior region but with the capability of handling compressible flow. An extensive description of the formulations and the computational scheme can be found in reference [6] and the references therein. However, a summary of the major features of the approach will follow.

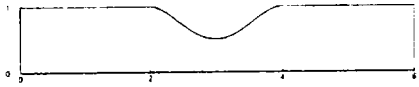

Figure 1. Non-dimensional computational domain

It is assumed that the moving medium is non-viscous and that all processes are isentropic. The field equations for both the potential flow and the acoustic perturbations in non-dimensional forms are derived from the non-dimensional continuity, momentum, and energy equations, the latter in the form of the isentropic equation of state:

$$\frac{\partial \rho}{\partial t} + \nabla \cdot (\rho \vec{V}) = 0 \qquad (1)$$

$$\frac{\partial \vec{V}}{\partial t} + (\vec{V} \cdot \nabla)\vec{V} = -\frac{1}{\rho}\nabla p \qquad (2)$$

$$p = \frac{1}{\gamma}\rho^{\gamma} \qquad (3)$$

p, ρ, and $\vec{V}$ are non-dimensional pressure, density, and velocity, respectively. γ is the ratio of specific heats. The non-dimensional speed of sound is

$$c^2 = \frac{\gamma p}{\rho} = \rho^{\gamma - 1} \qquad (4)$$

ρ_r is the reference density and c_r is the reference speed of sound and are taken as their respective values at the source plane. The reference length R is defined as the duct radius at this plane. Pressure has been made non-dimensional by $\rho_r c_r^2$, density by ρ_r, velocities and speed of sound by c_r, velocity potential by $c_r R$, and time by R/c_r. The introduction of velocity potential and the linearization of the conservation equations to the first order in acoustic perturbation yields

$$\nabla \cdot (\rho \cdot \nabla \phi_0) = 0 \qquad (5)$$

for steady mean flow, and

$$\frac{\partial \rho}{\partial t} + \nabla \cdot (\rho_0 \nabla \phi + \rho \nabla \phi_0) = 0 \qquad (6)$$

for the acoustic perturbations, where ϕ_0 and ρ_0 are the mean flow potential and density, respectively, and ϕ and ρ are acoustic potential and density. The mean flow and acoustic densities are determined by

$$\rho_0 = \left[1 - \frac{(\gamma - 1)}{2}\nabla \phi_0 \cdot \nabla \phi_0)\right]^{\frac{1}{\gamma - 1}} \qquad (7)$$

$$\rho = -\frac{\rho_0}{c_0^2}\left[\frac{\partial \phi}{\partial t} + (\nabla \phi_0 \cdot \nabla \phi)\right] \qquad (8)$$

where $c_0^2 = \rho_0^{\gamma - 1}$ is the local speed of sound. The acoustic pressure is related to the acoustic potential by

$$p = -\rho_0\left[\frac{\partial \phi}{\partial t} + (\nabla \phi_0 \cdot \nabla \phi)\right] \qquad (9)$$

A standard finite element Galerkin approximation is used to solve the problem. The computational domain is modeled using either quasi-one-dimensional or axially symmetric formulations with mesh elements of different order. The solution is achieved through three steps:

- *The time invariant mean compressible flow problem.* Equation (5) is solved in the domain in an iterative procedure for the flow potential.
- *Uniform duct eigenvalue problem.* A uniform duct eigenvalue problem is solved on the fan face in order to express the fan and exit face boundary conditions in terms of duct eigenfunctions.
- *Acoustic propagation problem.* Equation (6) is solved for the acoustic potential, using equation (8). The solution is desired in the case of a harmonic source on the source plane with time and angular dependence given by $e^{i(\eta_r t - m\theta)}$ where η_r is the non-dimensional input frequency ($\eta_r = \omega R / c_r$, ω is the input frequency) and m is the angular mode number.

The acoustic pressure distribution in the duct is calculated through post processing of the acoustic potential solution, using equation (9).

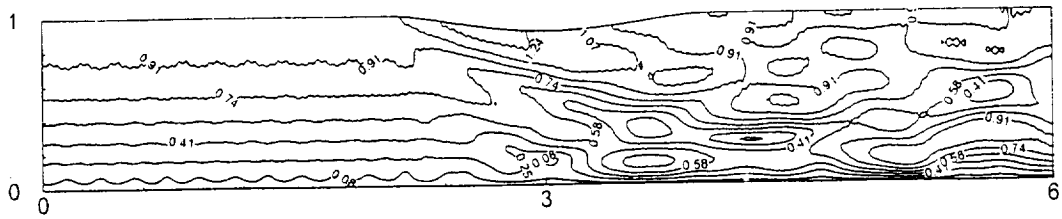

Figure 2a. Pressure contours using quadratic elements for $\eta_r = 25$, $M_i = .1$, m = 1, and $N/\lambda = 11.1$

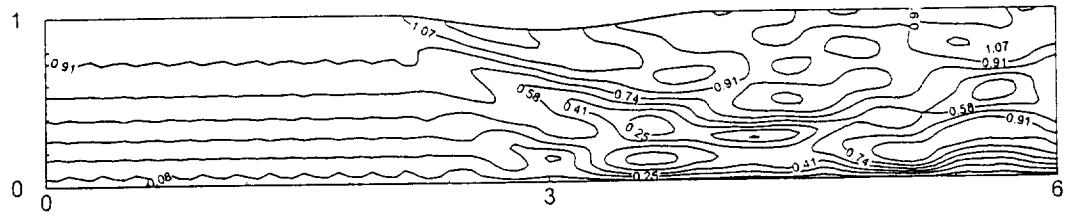

Figure 2b. Pressure contours using cubic elements for $\eta_r = 25$, $M_i = .1$, m = 1, and $N/\lambda = 11.3$

As far as dimensionality is concerned the difficulties of this model lie within this process. For high values of input frequency the nodal density of the mesh necessary to achieve acceptable pressure results has to significantly exceed 10 nodes per wavelength. An attempt to reduce the overall dimensionality problem can not be made until this ratio applies to satisfactory pressure calculations.

RESULTS AND DISCUSSION

In this section some numerical results are given to demonstrate the improvements made in reducing dimensionality of the domain. The solution of the acoustic radiation problem yields the acoustic velocity potential at the nodes of the mesh. The solution that yields the acoustic pressure is obtained from equation (9) as

$$p = -\rho_0 \left[i\eta_r \phi + (\nabla \phi_0 \cdot \nabla \phi) \right] \qquad (10)$$

Pressure at a node is calculated from the elements sharing that node and the value of pressure is obtained as the average of the nodal pressure found in each element. An improvement in results can be obtained by evaluating acoustic pressure at Gauss points inside the elements rather than at nodes and plot these, as is done in reference [6]. However, this will not totally eliminate the inaccuracies in the results. As seen in equation (10) pressure calculations require derivatives of acoustic potential because of the moving medium. This is the source of the difficulties of this model.

Figure 2a shows pressure distribution for a relatively simple acoustic field with non-dimensional frequency of 25. This mesh has a nodal density of about 11 nodes per wavelength, N/λ, and 9021 degrees of freedom (DOF) and is more than adequate for finding satisfactory potential, ϕ. In fact only a nodal density of 9 nodes per wavelength is needed in certain regions due to the flow effect. The flow in this case varies from Mach .1 to .13 and the effective wavelength λ_e is given according to $\lambda_e = (1+M)\lambda$. As seen, even at these very low Mach numbers the improper behavior of pressure is present. This behavior is actually so strong that the total number of DOF needs to be doubled before significant improvement can be seen. The root of this problem lies in the calculations of the potential derivatives, or the acoustic velocities, and the use of quadratic serendipity elements. In this case the acoustic propagation and the flow are predominately axial. This makes $\partial\phi/\partial x$ the more significant part of $\nabla\phi$ in equation (10) when calculating pressure. The derivative at each node is calculated from the average based on every derivative calculated at that node, thus assuring continuity. But since quadratic serendipity elements are used $\partial\phi/\partial x$ is linear in

x and quadratic in r while $\partial\phi/\partial r$ is quadratic in x and linear in r. When studying the acoustic velocity components separately the error appears to lie predominately in the axial direction of $\partial\phi/\partial x$. The error of $\partial\phi/\partial r$ in the radial direction, which is linear in r, does not affect the pressure for one main reason. $\partial\phi/\partial r$ is of small magnitude and is multiplied with the relatively small flow velocity component in the r-direction. In addition, for this case $\partial\phi/\partial x$ in the axial direction behaves much more smoothing than $\partial\phi/\partial r$ in radial direction. $\partial\phi/\partial r$ in the radial direction experiences more reflection from the outside wall and because of the harmonic appearance of the error, it is possible that there is some cancellation of the error because of this reflection since it does not appear as strong in the radial $\partial\phi/\partial r$ as in the axial $\partial\phi/\partial x$, both of which are linear in r and x, respectively. The error is of such a nature that it often appears more distinct in the simpler regions, not those heavily exposed to reflection and scattering. The order of the velocity components in different directions is at the core of the unacceptable behavior. A change to Lagrangian elements will have no effect on the order of the acoustic velocity terms, only on the number of terms involved. The increase in the appearance of error in certain regions, especially along the outside wall, occurs because the magnitude of $\partial\phi/\partial x$ increases here. The error will decrease with increased nodal density.

The same acoustic field was modeled in figure 2b using cubic serendipity elements and almost the identical nodes per wavelength value. Again the mesh is adequate for finding acceptable acoustic potential. In this case there are only 7066 DOF due to the use of cubic serendipity elements rather than quadratic ones. There are no visible traces in the pressure contours of the error encountered previously. However, studying the acoustic velocity components there are small tendencies for this erroneous oscillating behavior, despite having terms of at least quadratic order. It is clear that the error can not be completely eliminated using cubic elements. This will, however, greatly contain it in numerous cases. The effect of the error on the pressure increases as the flow speed increases. This can be seen in figure 3a where Mach number ranges from .5 to .73. With the effective wavelength λ_e being more than one and a half of λ the value of 11.1 for N/λ is far more than needed for satisfactory potential results. Yet pressure is far from acceptable in the quadratic case. It is important to note again that the error occurs in the calculation of the acoustic velocity and that an erroneous $\nabla\phi$ is amplified by $\nabla\phi_0$, not in the acoustic potential calculation (which is satisfactory for N/λ_e greater than 10). The reason the error appears greater as M increases is the product term involving $\nabla\phi_0$ in equation (9). The magnitude of the error in the acoustic velocity is not affected by flow velocity. There are similar tendencies for cubic elements, however not noticeable as seen in figure 3b. Exactly how much impact the presence of a moving medium in an acoustic field has on the modeling becomes clear when the flow is directed into the acoustic propagation. The effect of flow in the opposite direction makes it necessary to increase the nodal density to a N/λ of 17 in order to account for the effective wavelength adjustment. The flow speed ranges from –.3 to -.4 and this means N/λ_e is about 10.5. Reference [6] addressed this in considering turbofan inlet problems and it is clear from figure 4a how much more sensitive the problem becomes. The degrees of freedom necessary in the quadratic case for satisfactory potential results have increased to 22541, yet the pressure contours are far from acceptable. The cubic model has to require 16354 DOF in order to have 17 nodes per wavelength and to handle the potential, but this is also enough to handle pressure.

In cases with higher angular mode numbers it is generally easier to model acoustic pressure, as seen comparing figures 3a and 5a, in which the only difference is higher angular mode number in the latter case. The mode number increase appears to cause a decrease in the magnitude of $\partial\phi/\partial x$ over large regions of the domain, except along the outside wall. It basically shifts the acoustic velocity and pressure gradients away from the x-axis. It also causes an increase in $\partial\phi/\partial r$ in the radial direction relative to $\partial\phi/\partial x$. This will not increase the appearance of the error overall since $\partial\phi/\partial r$ in the radial direction is multiplied by the radial flow velocity component which is still small.

The case involving larger contraction of the cross-sectional area causes the most complex acoustic field. This will greatly increase both the radial flow component and the radial acoustical velocity component ($\partial\phi/\partial r$ in the radial direction increases more than that in the axial

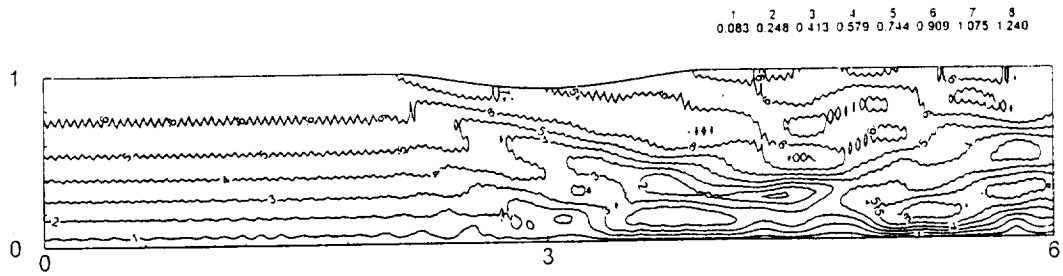

Figure 3a. Pressure contours using quadratic elements for $\eta_r = 25$, $M_i = .5$, m = 1, and $N/\lambda = 11.1$

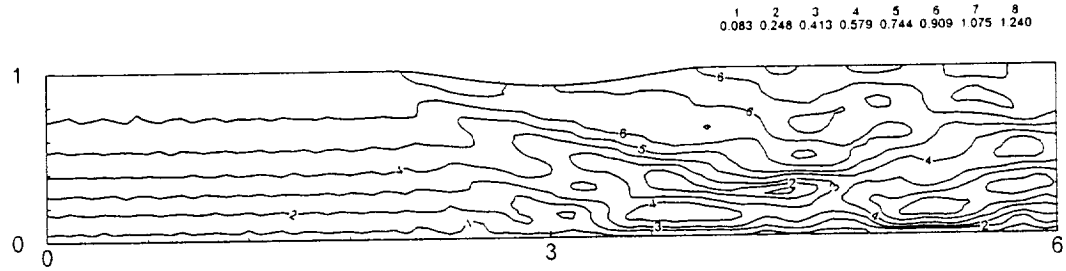

Figure 3b. Pressure contours using cubic elements for $\eta_r = 25$, $M_i = .5$, m = 1, and $N/\lambda = 11.3$

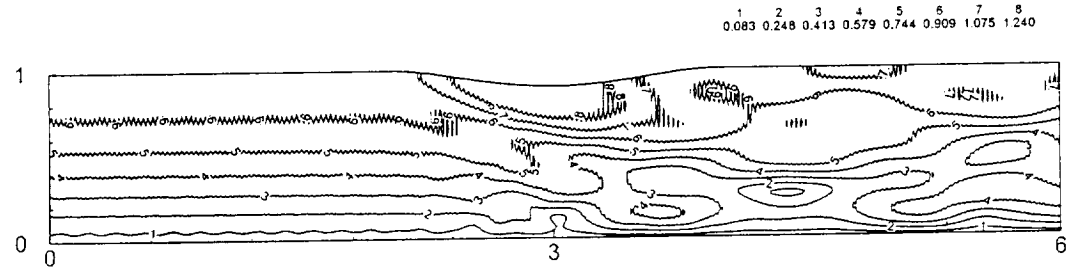

Figure 4a. Pressure contours using quadratic elements for $\eta_r = 25$, $M_i = -.3$, m = 1, and $N/\lambda = 17$

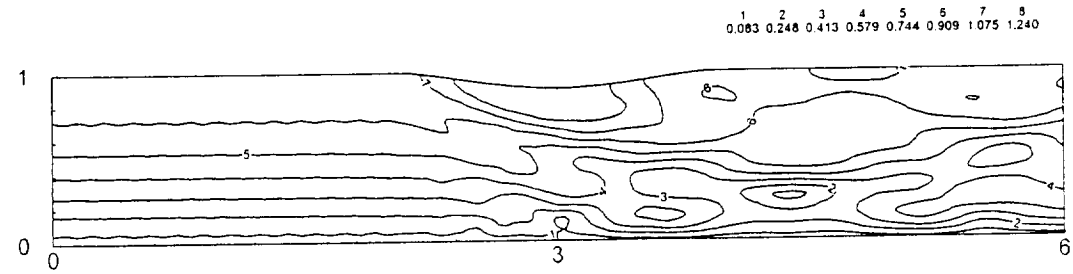

Figure 4b. Pressure contours using cubic elements for $\eta_r = 25$, $M_i = -.3$, m = 1, and $N/\lambda = 17$

direction), as well as reflection and scattering. The flow speed ranges from .1 to .24, indicating an N/λ of 9 would be adequate for potential calculations. This time the magnitudes of $\partial\phi/\partial r$ are significant, yet because the behavior across the duct of $\partial\phi/\partial r$ is influenced by reflection and scatter the error might be subjected to some cancellations. $\partial\phi/\partial x$ in the axial direction is still a problem, but now the reflection and scatter also make an impact in this direction for most of the domain. More significant, it is no longer

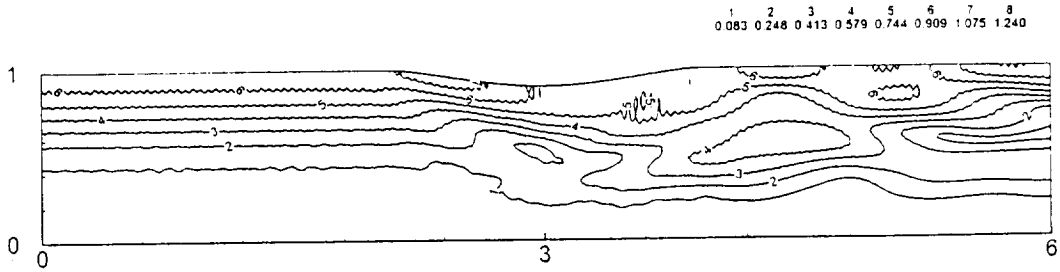

Figure 5a. Pressure contours using quadratic elements for $\eta_r = 25$, $M_i = .5$, m = 5, and $N/\lambda = 11.1$

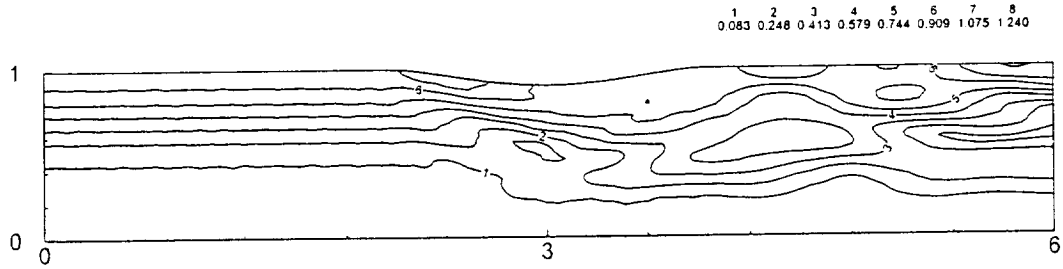

Figure 5b. Pressure contours using cubic elements for $\eta_r = 25$, $M_i = .5$, m = 5, and $N/\lambda = 11.3$

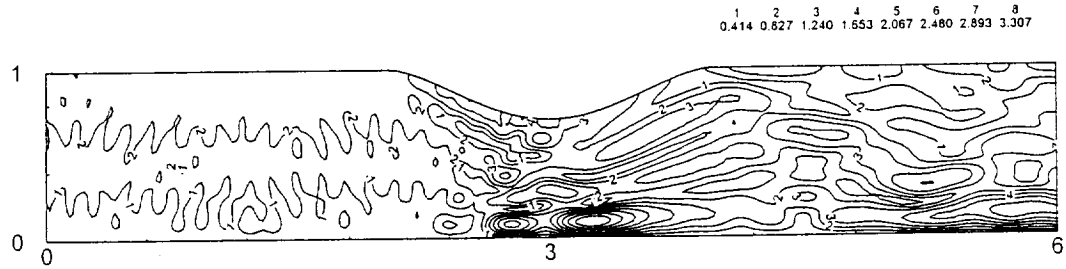

Figure 6a. Pressure contours using quadratic elements for $\eta_r = 25$, $M_i = .1$, m = 1, and $N/\lambda = 11.1$

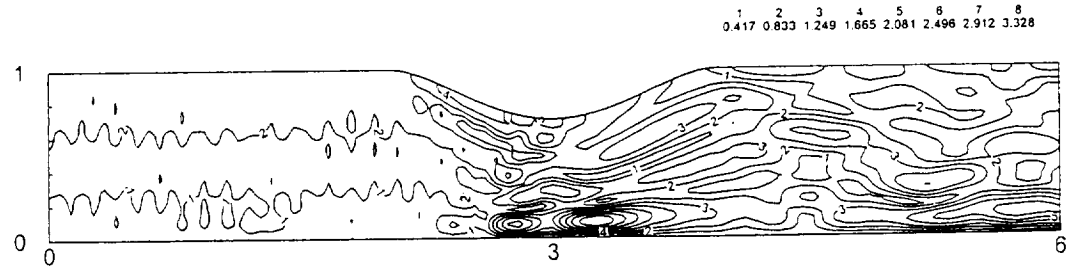

Figure 6b. Pressure contours using cubic elements for $\eta_r = 25$, $M_i = .1$, m = 1, and $N/\lambda = 11.3$

totally dominating equation (10) and thus the error it carries becomes diluted. The quadratic model is capable of modeling this case and there are not any significant differences when comparing the quadratic and cubic models (figures 6a and b). The area contraction will cause large increases in pressure magnitudes. Note that this is not why the error seems unnoticeable. In a smooth field larger acoustic velocity values will lead to the larger errors. If the same contour values as in previous figures were used, the error would still not be noticeable in this case.

The overall tendencies seen in figures 2a to 6b stay the same as the frequency is increased. Figure 7 gives an overview of the necessary nodal density for acceptable pressure results for both the quasi-one dimensional and cylindrical cases. These results model the acoustical field in a duct with a .9 area contraction ratio, inlet Mach number of .1, and an angular mode of 1 (, as in figures 2a and b). The tolerance level for what can be viewed acceptable has been more stringent in these cases for the sake of consistency. The computational time for two-dimensional quadratic and cubic elements beyond non-dimensional frequencies of 50 and 100, respectively, becomes excessive.

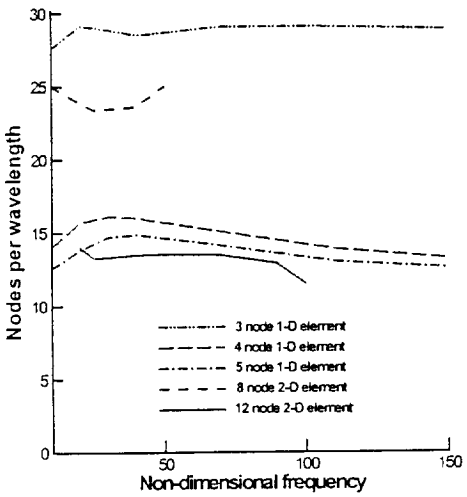

Figure 7. Nodal density vs. non-dimensional frequency

The most important result is that with elements of cubic order the error can be contained enough to the point that the accuracy of the potential solution becomes the deciding factor in determining nodal density, not the post-processed calculation of pressure. Note that the benefit of going to even higher order elements, as is done in the one-dimensional case, is questionable. Very little seems to be gained. While overall the cubic serendipity elements perform better than quadratic serendipity elements in modeling pressure there are also some possible problems in its performance. Although nodal density might be the same in both cubic and quadratic models, the cubic elements cover a larger domain and therefore there is a larger gradient within this element, causing derivatives of greater magnitude to be calculated. A decrease in element size can correct the problem, however this will erase the gains made in reducing dimensionality.

The use of cubic elements, although not totally eliminating the errors occurring in the post-processing, has contained those inadequacies enough to where certain high frequency models that previously were impractical to study due to dimensionality problems, now can be calculated in reasonable time. The first set of problems involves the acoustic field in a duct at a non-dimensional frequency of 50 and the impact of the area contraction ratio changing from .9 to .5. The flow velocity ranges from Mach number of .1 to .13 in a, from .1 to .24 in b, and from .1 to .5 in c, with an angular mode of 1. This model is seen in figures 8a to c and requires 27631 DOF.

To model an acoustic field with a non-dimensional frequency of 100, angular modes ranging from 1 to 20, and the flow velocity varying from Mach .3 to .4 in figures 9a and b and Mach .25 to .9 in figures 10a and b, a domain of 91906 DOF is needed. Figures 9a and b compares angular modes. The same for figures 10a and b, but with larger area contractions, thus higher flow velocities. Figures 9a and 10a shows the effect of changing the cross-sectional area. With the same degrees of freedom and a flow speed ranging from Mach .3 to .4, but in the opposite direction, the model is limited to satisfactory results for non-dimensional frequencies up to 70. The computer time for this model using an HP Visualize C200 with a specfloat FP95 of 21.4 was about 30 to 40 minutes for the incompressible flow code and about 100 minutes for the acoustic propagation code. Each case in figures 8a to c took only about 15 minutes for both flow and propagation calculations combined.

CONCLUSION

It is questionable if cubic elements will be suitable for models having a non-dimensional frequency much beyond 100. It is apparent they can give acceptable results for nodal densities not much greater than those required for potential calculations. However, the tendencies of the oscillating errors are still present and this probably needs to be resolved before an attempt can be made at going below the 10 nodes per wavelength required for satisfactory results in the potential formulation. Since this error seems to be a function of both nodal density and the order of the shape functions it calls for further study into the use of various shape functions and other types of elements.

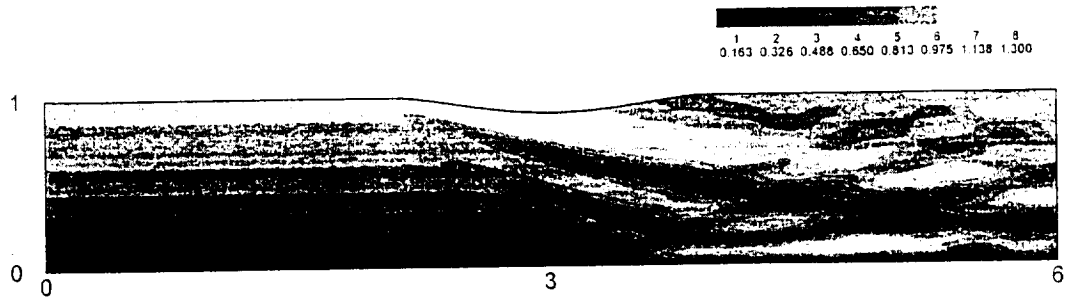

Figure 8a. Pressure contours for $\eta_r = 50$, $M_i = .1$, m = 1, and $N/\lambda = 11.3$

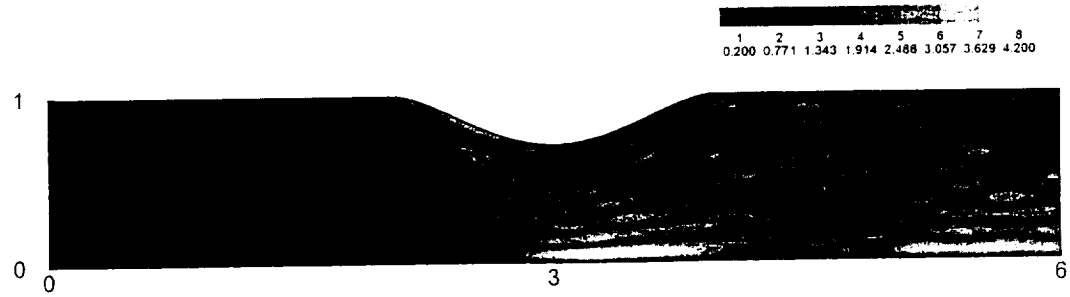

Figure 8b. Pressure contours for $\eta_r = 50$, $M_i = .1$, m = 1, and $N/\lambda = 11.3$

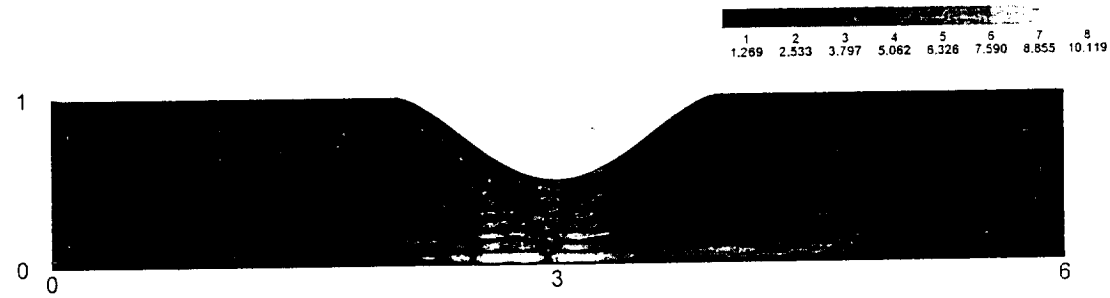

Figure 8c. Pressure contours for $\eta_r = 50$, $M_i = .1$, m = 1, and $N/\lambda = 11.3$

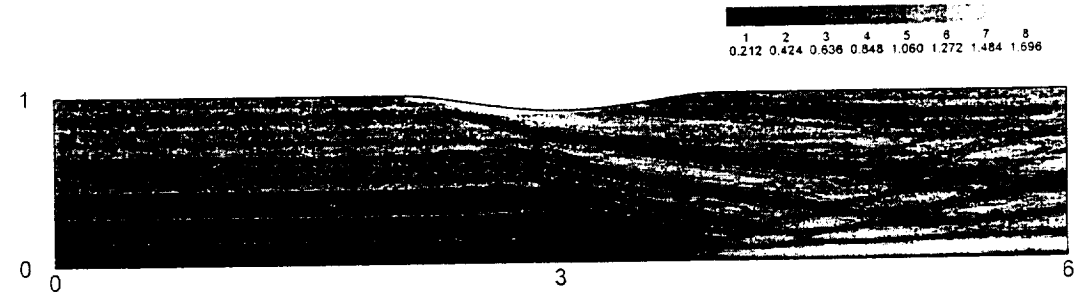

Figure 9a. Pressure contours for $\eta_r = 100$, $M_i = .3$, m = 1, and $N/\lambda = 10.4$

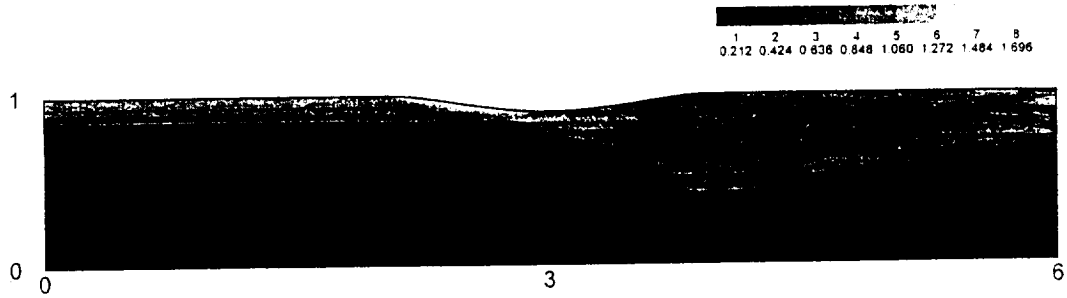

Figure 9b. Pressure contours for $\eta_r = 100$, $M_i = .3$, m = 20, and $N/\lambda = 10.4$

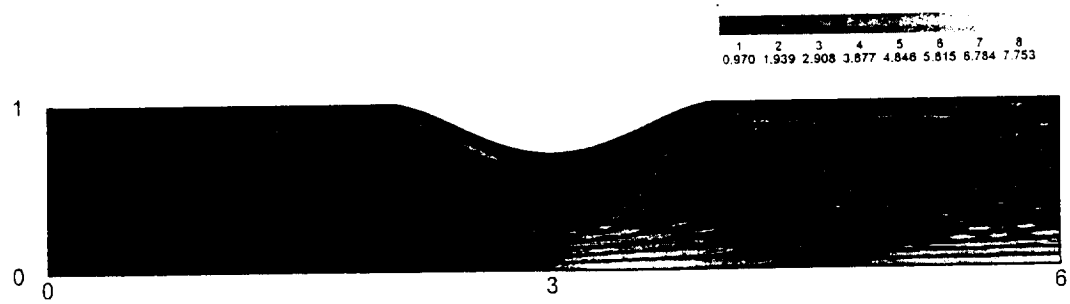

Figure 10a. Pressure contours for $\eta_r = 100$, $M_i = .25$, m = 1, and $N/\lambda = 10.4$

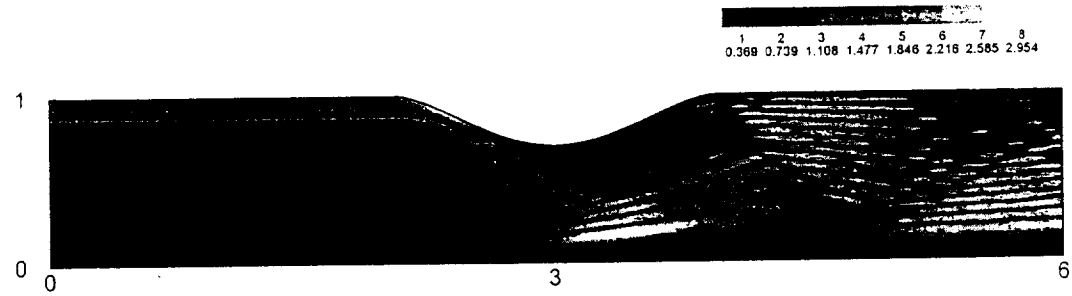

Figure 10b. Pressure contours for $\eta_r = 100$, $M_i = .25$, m = 10, and $N/\lambda = 10.4$

AKNOWLEDGEMENT

The work reported here was supported under a grant to University of Missouri-Rolla by NASA Glenn Research Center.

REFERENCES

1. P. Bettess, 'Infinite elements', International Journal for Numerical Methods in Engineering, **11**, 53-64 (1977).
2. O. C. Zienkiewicz, K. Bando, P. Bettess, C. Emson, and T. C. Chen, 'Mapped infinite elements for exterior wave problems', International Journal for Numerical Methods in Engineering, **21**, 1229-1252 (1985).
3. D. S. Burnett, 'A three-dimensional acoustic infinite element based on a prolate sperhoidal multipole expansion', Journal of the Acoustical Society of America, **96** (5), 2798-2816 (1994).
4. R. J. Astley and W. Eversman, 'Finite element formulation for acoustical radiation', Journal of Sound and Vibration, **88**, 47-64 (1983).
5. A. V. Parrett and W. Eversman, 'Wave envelope and finite element approximations for turbofan noise radiation in flight', AIAA Journal, **24**, 753-759 (1986).
6. I. Danda Roy and W. Eversman, 'Improved finite element modeling of the turbofan engine inlet radiation problem', ASME Journal of Vibration and Acoustics, **117**, 109-115 (1995).
7. R. J. Astley, 'Transient wave envelope elements for wave problems', Journal of Sound and Vibration, **192**, 245-261 (1996).
8. R. J. Astley, G. J. Macaulay, J-P. Coyette, and L. Cremers, 'Three-dimensional wave-envelope elements of variable order for

acoustoc radiation and scattering. Part I. Formulation in the frequency domain', Journal of the Acoustical Society of America, **103** (1), 49-63 (1998).
9. R. J. Astley, 'Mapped spheroidal wave-envelope elements for unbounded wave problems', International Journal for Numerical Methods in Engineering, **41**, 1235-1254 (1998).
10. W. Eversman, 'Mapped infinite wave envelope elements for acoustic radiation in a uniformly moving medium', Journal of Sound and Vibration, **224**, 665-687 (1999).
11. E. Chadwick and P. Bettess, 'Modelling of progressive short waves using wave envelopes', International Journal for Numerical Methods in Engineering, **40**, 3229-3245 (1997).
12. E. Chadwick, P. Bettess, and O. Laghrouche, 'Diffraction of short waves modeled using new mapped wave envelope finite and infinite elements', International Journal for Numerical Methods in Engineering, **45**, 335-354 (1999).
13. R. J. Astley and W. Eversman, 'A note on the utility of a wave envelope approach in finite element duct transmission studies', Journal of Sound and Vibration, **76**, 595-601 (1981).
14. I. Babuška and M. Suri, 'The p and h-p versions of the finite element method, basic principles and properties', SIAM Review, **36**, 578-632 (1994).
15. L. Demkowicz, K. Gerdes, C. Schwab, A. Bajer, and T. Walsh, 'HP90: A general and flexible Fortran 90 hp-FE code', Computing and Visualization in Science, **1**, 145-163 (1998).
16. F. Ihlenburg and I. Babuška, 'Finite element solution of the Helmholtz equation with high wave number part II: The h-p version of the FEM', SIAM Journal of Numerical Analysis, **34** (1), 315-358 (1997).
17. I. Babuška and J. M. Melenk, 'The partition of unity method', International Journal for Numerical Methods in Engineering, **40**, 727-758 (1997).
18. S. Suleau and Ph. Bouillard, 'One-dimensional dispersion analysis for the element-free Galerkin method for the Helmholtz equation', International Journal for Numerical Methods in Engineering, **47**, 1169-1188 (2000).
19. T. Strouboulis, K. Copps, and I. Babuška, 'The generalized finite element method: an example of its implementation and illustration of its performance', International Journal for Numerical Methods in Engineering, **47**, 1401-1417 (2000).
20. O. Laghrouche and P. Bettess, 'Special finite elements for the Helmholtz short wave problem', paper presented at ICTCA'99, 4th International Conference on Theoretical and Computational Acoustics, May 1999, Trieste, Italy.
21. L. P. Franca, C. Farhat, A. P. Macedo, and M. Lesoinne, 'Residual-free bubbles for the Helmholtz equation', International Journal for Numerical Methods in Engineering, **40**, 4003-4009 (1997).
22. L. P. Franca and A. P. Macedo, 'A two-level finite element method and its application to the Helmholtz equation', International Journal for Numerical Methods in Engineering, **43**, 23-32 (1998).

THE BOUNDARY CONDITION AT AN IMPEDANCE WALL IN A NONUNIFORM DUCT WITH POTENTIAL MEAN FLOW

Walter Eversman
Mechanical and Aerospace Engineering
and Engineering Mechanics
University of Missouri-Rolla,
Rolla, MO, 65401, USA

ABSTRACT

The boundary condition at an impedance wall in a duct with a steady mean flow requiring the specification of the normal component of acoustic particle velocity is examined. It is found that when implemented in the weak formulation of the finite element method it can be considerably simplified. The boundary condition would appear to require data which includes the tangential derivative of the tangential mean flow velocity, the normal derivative of the normal component of mean flow velocity, and the derivatives of the mean flow density and the boundary admittance along the boundary. It is shown that with suitable rearrangement the normal and tangential velocity derivatives can be eliminated, as can the derivatives of the mean flow density and admittance. The boundary condition becomes only slightly more complicated than the corresponding boundary condition when mean flow is absent, and is no more difficult to implement, requiring only local values of tangential mean flow velocity, density, and admittance which are already required as data for the weak formulation of the field equation.

INTRODUCTION

Figure 1 shows the geometry of a typical non-uniform duct section. The duct is of non-uniform cross section with walls S_w which in general include an acoustically absorbing section

imbedded in an otherwise acoustically rigid wall. Absorption characteristics of the boundary are given in terms of the admittance A for a locally reacting liner. The duct in Figure 1 is depicted as axially symmetric, however the results obtained here do not depend on such an idealization. The duct geometry includes the definition of a unit normal $\vec{n}$ directed out of the fluid region, and therefore into the duct wall. The notional displacement of the duct wall, normal to the wall, is given by ζ which is a function of location on the wall. In harmonic motion with time dependence $e^{i\eta_r t}$ the admittance relates this displacement to the acoustic pressure according to

$$i\eta_r \zeta = Ap \tag{1}$$

When this admittance relation is applied to acoustic propagation in ducts with steady mean flow it produces what appears to be a very difficult boundary condition at the admittance wall. Myers [1] derived the correct boundary condition which relates the normal component of acoustic particle velocity to the particle displacement in non-viscous flow for harmonic acoustic perturbations at frequency η_r as

$$\vec{v}\cdot\vec{n} = i\eta_r\zeta + \vec{V}_r\cdot\nabla\zeta - \zeta\,\vec{n}\cdot(\vec{n}\cdot\nabla)\,\vec{V}_r \tag{2}$$

Here $\vec{v}\cdot\vec{n}$ is the normal component of acoustic particle velocity at the wall and $\vec{V}_r$ is the tangential mean flow velocity at the wall. Propagation in non-uniform ducts is normally modeled under the assumption that the mean flow and acoustic perturbation are defined by a steady flow potential such that $\vec{V}_r = \nabla\phi_r$, and by an acoustic potential such that $\vec{v} = \nabla\phi$ and an acoustic momentum equation

$$p = -\rho_r[i\eta_r\phi + \vec{V}_r\cdot\nabla\phi] \tag{3}$$

A combination of equations (1), (2), and (3) produces a single boundary condition in terms of acoustic potential which is difficult to implement in numerical schemes. It is found that data required to model the boundary condition includes the derivative of the impedance and mean flow density along the boundary. In addition, and much more of a problem, is the requirement for the tangential derivative of the tangential component of mean flow and the normal derivative of the normal component of mean flow. These present particular difficulties because the mean flow data in finite element propagation models is generally obtained from a potential formulation for the steady flow and the required derivatives of velocity require second derivatives of the potential.

The boundary condition described by equations (1), (2), and (3) has been implemented in a finite element scheme by Eversman and Okunbor [2]. They used an approximation, argued to be adequate for ducts with changes in cross section which are relatively small, which ignores the term requiring the normal derivative of the normal component of mean flow velocity, and additionally ignores the effect of duct wall curvature on the calculation of the rates of change of quantities along the wall. The approximation for the tangential derivative of the tangential component of mean flow velocity is retained. The computation of this derivative is not considered to be very accurate. None of these approximations are thought to be significant for attenuation calculations in the geometries considered.

Rienstra [3] has approached the modeling of acoustic propagation in ducts with slowly varying cross section by a perturbation scheme, and the analysis procedure requires the full modeling of the boundary condition. However, because his procedure is analytic the implementation of the boundary condition presents no difficulty and the issues which arise in a numerical model are not present.

The motivation for the present investigation is the requirement to verify a reciprocity relationship which exists for acoustic propagation in non-uniform ducts with mean flow and absorbing linings. In order to show reciprocity no approximation in the boundary condition is permissible. Numerical experiments conducted with the approximate model of the boundary condition described in [2] suggest that reciprocity is nearly satisfied, but one is not fully

convinced that the small discrepancies are in the approximate model or in the reciprocity principle. The following work derives a model of the boundary condition for the FEM formulation which is exact within the FEM formalism, is easy to implement, and will replace the approximation in [2]. Work to be subsequently reported will show that the new boundary condition results in a numerical substantiation of the reciprocity principle [4,5].

FINITE ELEMENT FORMULATION FOR DUCT PROPAGATION

Application of finite element modeling to acoustic propagation in nonuniform ducts with steady mean potential flow has been previously reported [2]. A formulation in terms of acoustic potential is used to reduce the field equations to a single scalar variable. In this investigation the geometry of the duct and steady flow field is axially symmetric. The acoustic field is not axially symmetric but is represented as azimuthally periodic in a cylindrical coordinate system with x being the axis of symmetry, r the cylindrical radius in a circular cross section at $x = 0$, and θ the angular coordinate. Solutions are sought in angular harmonics of a Fourier Series in θ enumerated by the angular mode number m . This reduces the solution domain to a two dimensional x , r plane, shown in Figure 1. The duct shape in a θ = constant plane shows the surface S which defines the duct shape and could include an inner surface for an annular duct. Part of S includes S_w , which is a locally reacting acoustic treatment.

The acoustic field is assumed to be harmonic in time at non-dimensional frequency η_r. Geometry is non-dimensional based on a reference length generally chosen as the radius of the inlet at the source plane, R. Acoustic and steady flow variables are non-dimensional based on reference values of the speed of sound and density of the medium, ρ_∞ , c_∞, generally defined at the plane of the acoustic source. The non-dimensional frequency is $\eta_r = \omega R / c_\infty$, with ω the harmonic source frequency.

Reference [2] discusses in detail the finite element modeling of acoustic propagation in and near ducts carrying mean flow. The field equations for continuity and momentum and the isentropic equation of state are used in a weighted residual statement to obtain an integral

formulation which is then written in discrete form using standard FEM procedures. In terms of acoustic potential the weak formulation is

$$\iiint_V \frac{\rho_r}{c_r^2}\{c_r^2 \nabla W\cdot\nabla\phi - (\vec{V}_r\cdot\nabla W)(\vec{V}_r\cdot\nabla\phi) + i\eta_r[W(\vec{V}_r\cdot\nabla\phi) - (\vec{V}_r\cdot\nabla W)\phi] - \eta_r^2 W\phi\}\,dV$$

$$= \iint_S \frac{\rho_r}{c_r^2}\{c_r^2 W\nabla\phi - \vec{V}_r W(\vec{V}_r\cdot\nabla\phi) - i\eta_r \vec{V}_r W\phi\}\cdot\vec{n}\,dS \qquad (4)$$

where the local non-dimensional steady flow velocity is $\vec{V}_r = \nabla\phi_r$, with ϕ_r the non-dimensional steady flow velocity potential. The local non-dimensional density and speed of sound are ρ_r , c_r. The surface integral on the right hand side introduces the noise source and termination conditions on S_0 or S_L and a possible impedance boundary condition on S inside the duct. In the present investigation it is the impedance boundary condition which is of interest on S_w , a portion of S. In equation (4), the weighted residuals statement, W represents an arbitrary weighting function selected from the class of continuous functions. In this weak formulation the approximation to the solution ϕ is also chosen from the class of continuous functions

At a duct wall the mean flow is tangential to the wall and $\vec{V}_r\cdot\vec{n} = 0$ causing the boundary integral (the contribution to the right hand side of equation (1) related to the impedance condition) to become

$$I_b = \iint_{S_w} \rho_r W\nabla\phi\cdot\vec{n}\,dS \qquad (5)$$

With the Myers boundary condition [1] and with $\nabla\phi_r\cdot\vec{n} = 0$ on the duct wall surface S_w, the integral of equation (5) on S_w becomes

$$I_b = \int_{S_w}\int \{ \rho_r W [i\eta_r \zeta + \vec{V}_r \cdot \nabla \zeta - \zeta \vec{n} \cdot (\vec{n} \cdot \nabla) \vec{V}_r] \} \, dS \tag{6}$$

The following vector identities (suggested in a similar context by Moehring [6]) are introduced (with account taken of the special circumstances of the present problem):

$$\rho_r W \vec{V}_r \cdot \nabla \zeta = \rho_r \vec{V}_r \cdot \nabla W \zeta - \rho_r \zeta \vec{V}_r \cdot \nabla W$$

$$\nabla \cdot \rho_r \vec{V}_r = 0$$

$$\rho_r \vec{V}_r \cdot \nabla W \zeta = \nabla \cdot \rho_r W \zeta \vec{V}_r \tag{7}$$

$$\vec{n} \cdot \vec{V}_r = 0$$

$$\rho_r W \zeta \vec{n} \cdot (\vec{n} \cdot \nabla) \vec{V}_r = \vec{n} \cdot (\vec{n} \cdot \nabla) \rho_r W \zeta \vec{V}_r$$

$$\vec{n} \cdot \nabla \times (\vec{n} \times \rho_r W \zeta \vec{V}_r) = \nabla \cdot \rho_r W \zeta \vec{V}_r - \vec{n} \cdot (\vec{n} \cdot \nabla) \rho_r W \zeta \vec{V}_r$$

With the use of the identities of equations (7), equation (6) can then be reformulated as

$$I_b = \int_{S_w}\int \{ \rho_r \zeta [i\eta_r W - \vec{V}_r \cdot \nabla W] \} \, dS + \int_{S_w}\int \{ \vec{n} \cdot \nabla \times (\vec{n} \times W \rho_r \zeta \vec{V}_r) \} \, dS \tag{6}$$

Following the development of Moehring [6], the last integral can be written as a line integral on

the boundary Γ of the surface S_w by using Stokes' Theorem. The boundary curve Γ should enclose the portion of S_w on which there is a non-zero admittance, but should be located where the admittance vanishes, as shown in Figure 2. Γ consists of closed curves Γ_1 and Γ_2 circumscribed on the duct wall at either end of the duct, chosen to be outside the region in which the lining of finite length has non-zero admittance, that is, in the regions in which the duct wall is rigid. There is of course a portion of Γ which runs along the duct wall between Γ_1 and Γ_2 to complete the closed curve of Stokes' Theorem, but this curve is traversed twice, once in each direction, and has no net contribution. To make use of Stokes' Theorem it is required that the acoustic field and the wall displacement be continuous on S_w. Hence, if the acoustic treatment is of limited length imbedded in an otherwise rigid wall duct, the transition from rigid wall to admittance wall, as well as the variation of admittance along the treated wall, must be continuous. If this condition is met, Stokes' Theorem can be cast in the form

$$\int_{S_w}\int \{\vec{n}\cdot\nabla\times(\vec{n}\times\rho_r W\zeta\vec{V}_r)\}\,dS = \int_{\Gamma_1}(\vec{n}\times\rho_r W\zeta\vec{V}_r)\cdot d\vec{\Gamma} + \int_{\Gamma_2}(\vec{n}\times\rho_r W\zeta\vec{V}_r)\cdot d\vec{\Gamma} \qquad (7)$$

The integral on the surface S_w vanishes if the line integrals vanish. On a hard wall the line integrals vanish because the boundary displacement vanishes. This means that if the condition for the use of Stokes' Theorem is met, then the integral of equation (6) is

$$I_b = \int_{S_w}\int \{\rho_r\zeta[i\eta_r W - \vec{V}_r\cdot\nabla W]\}\,dS \qquad (8)$$

At a wall of admittance A equations (1) and (2) are used to replace the wall displacement ζ and the pressure with velocity potential ϕ. The result is the new weighted residual boundary integral on the duct surface S_w

$$I_b = -\int_{S_w}\int A\rho_r^2 \{ i\eta_r W\phi + W\vec{V}_r\cdot\nabla\phi - \phi\vec{V}_r\cdot\nabla W - \frac{1}{i\eta_r}(\vec{V}_r\cdot\nabla W)(\vec{V}_r\cdot\nabla\phi)\}\, dS \quad (9)$$

The weighted residual form of the boundary condition of equation (9) is a considerable simplification of the boundary condition which would result by a direct use of equations (1), (2) and (3). In the latter case it would be found that the derivatives of the admittance A and the steady flow density ρ_r are required. In addition the tangential derivative of the component of mean flow velocity tangential to the wall and the normal derivative of the normal component of mean flow velocity at the wall are required. Current implementations of the FEM formulation from which the steady potential flow field is obtained are not well suited for the accurate determination of these second derivatives of velocity potential. The modified version of the boundary condition neither requires data which is not directly determined from the potential flow model nor requires any operations which are not required in the discretization of the field equations (left hand side of equation (4)).

The restriction that the admittance is continuous on the duct wall is related to modeling difficulties addressed by other authors. Moehring [6] has noted that in the acoustic potential formulation for discontinuous admittance variation there is no clear condition to be imposed on the acoustic field or wall displacement at the discontinuity. Rebel and Ronneberger [7] have shown that the condition of admittance discontinuity and the assumption of potential flow at the wall (no boundary layer) causes a problem with the underlying physics of the flow related to the absence of shear stresses. In this analysis these issues have been eliminated by requiring that the admittance vary continuously. In practical terms, this is accomplished by making "discontinuities" rapid, but continuous, variations (easily done by an appropriate definition of the local admittance). One suspects that numerically this may be a non-issue, because in the weak FEM formulation the role of discontinuities is reduced.

AN ALTERNATE APPROACH

An alternate approach to the simplified boundary condition is available which produces a boundary condition useful for numerical models which are not based on the weighted residuals formulation. The Myers boundary condition of equation (4) can be written

$$\rho_r \vec{v} \cdot \vec{n} = i\eta_r \rho_r \zeta + \rho_r \vec{V}_r \cdot \nabla\zeta - \rho_r \zeta \vec{n} \cdot (\vec{n} \cdot \nabla) \vec{V}_r \tag{10}$$

The steady flow continuity equation

$$\nabla \cdot \rho_r \vec{V}_r = 0 \tag{11}$$

is used to establish that

$$\rho_r \vec{V}_r \cdot \nabla \zeta = \nabla \cdot \rho_r \zeta \vec{V}_r \tag{12}$$

It can also be shown that since on the duct wall $\vec{n} \cdot \vec{V}_r = 0$,

$$\rho_r \zeta \vec{n} \cdot (\vec{n} \cdot \nabla) \vec{V}_r = \vec{n} \cdot (\vec{n} \cdot \nabla) \rho_r \zeta \vec{V}_r \tag{13}$$

With these results it can be shown that

$$\vec{n} \cdot (\vec{n} \cdot \nabla) \rho_r \zeta \vec{V}_r = \frac{\partial}{\partial n} (\rho_r \zeta V_{r_n}) \tag{14}$$

and

$$\nabla \cdot \rho_r \zeta \vec{V}_r = \frac{\partial}{\partial \tau} (\rho_r \zeta V_{r_\tau}) + \frac{\partial}{\partial n} (\rho_r \zeta V_{r_n}) \tag{15}$$

Directions tangential and normal to the duct wall at the wall surface are denoted by τ , n . V_{r_τ} , V_{r_n} are the tangential and normal components of the steady flow velocity. At the duct wall V_{r_n} vanishes. Therefore, the boundary condition on the duct wall is

$$\rho_r \vec{v} \cdot \vec{n} = i\eta_r \rho_r \zeta + \frac{\partial}{\partial \tau}(\rho_r \zeta V_{r_\tau}) \tag{16}$$

This form of the boundary condition, not in weighted residual form, could be used, for example, in a finite difference formulation. With ζ replaced by equation (1) and p replaced by equation (3), it is found that derivatives along the wall of mean flow density, wall admittance, and mean flow velocity are required, however the normal derivative of the normal flow velocity component is not required. Equation (16) can be used in the weighted residual formulation to reproduce equation (9), with the same restrictions.

CONCLUSION

The Myers acoustic boundary condition at an admittance wall in a non-uniform duct carrying potential mean flow [1] has been restructured using identities of vector calculus to obtain a form well suited for finite element predictions of propagation. If applied without simplification the boundary condition would require data on the spatial derivative along the wall of mean flow density, the tangential spatial derivative of the tangential mean flow velocity at the wall, the normal spatial derivative of the normal mean flow velocity at the wall, and the spatial derivative along the wall of the admittance. After simplification only local values of density, tangential flow velocity and admittance are required. The normal component of mean flow velocity is eliminated completely. Implementation of the boundary condition is easily accomplished in finite element models.

An alternate approach has been used to simplify the Myers boundary condition in a form useful for numerical modeling not based on the weighted residuals approach of finite element

analysis. The normal derivative of the normal mean flow velocity component at the wall is eliminated, however derivatives along the wall of mean flow density and velocity and wall admittance are retained.

The net effect of the boundary condition on prediction of attenuation in ducts in FEM models has been found to be minor when compared to a former approximation introduced for computational efficiency (the new exact formulation is found to be even more computationally simple). For calculations made to validate acoustic reciprocity, the exact form of the boundary condition introduced here is essential, and it is found that predicted reciprocity relationships are accurately verified [4,5].

ACKNOWLEDGMENT

The work reported here is supported by a grant to the University of Missouri-Rolla by NASA Glenn Research Center.

REFERENCES

1. M. K. Myers 1980 Journal of Sound and Vibration 71(3),429-434. On the acoustic boundary condition in the presence of flow.

2. W. Eversman and D. Okunbor 1998 Journal of Sound and Vibration 213(2),235-257. Aft fan duct acoustic radiation.

3. S. W. Rienstra 1999 Journal of Fluid Mechanics 380, 279-296. Sound transmission in slowly varying circular and annular ducts.

4. W. Eversman 2000 Journal of Sound and Vibration (in preparation). A reverse flow theorem and acoustic reciprocity in compressible potential flows.

5. W. Eversman 2000 Journal of Sound and Vibration (in preparation). Numerical experiments on acoustic reciprocity in compressible potential flows

6. W. Moehring 2000 Journal of Fluid Mechanics (in review). Energy conservation, time reversal invariance and reciprocity in ducts with flow.

7. J. Rebel and D. Ronneberger 1992 Journal of Sound and Vibration 158, 469-496. The effect of shear stress on the prpagation and scattering of sound in flow ducts.

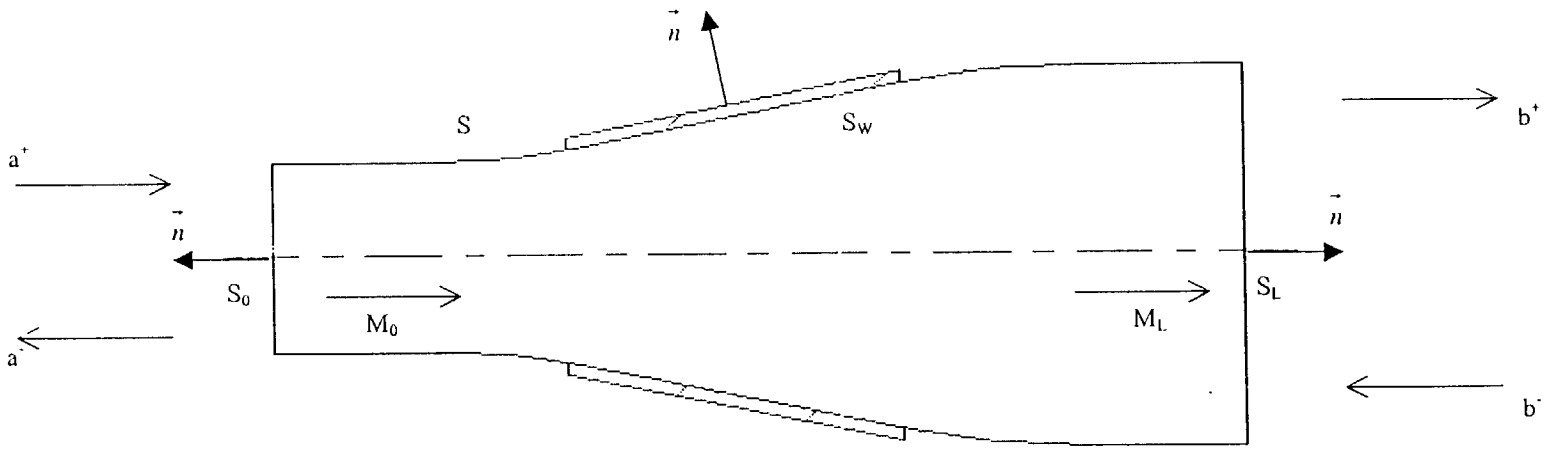

Figure 1. An x, r section of a non-uniform duct showing essential modeling features, including acoustic treatment and steady mean flow.

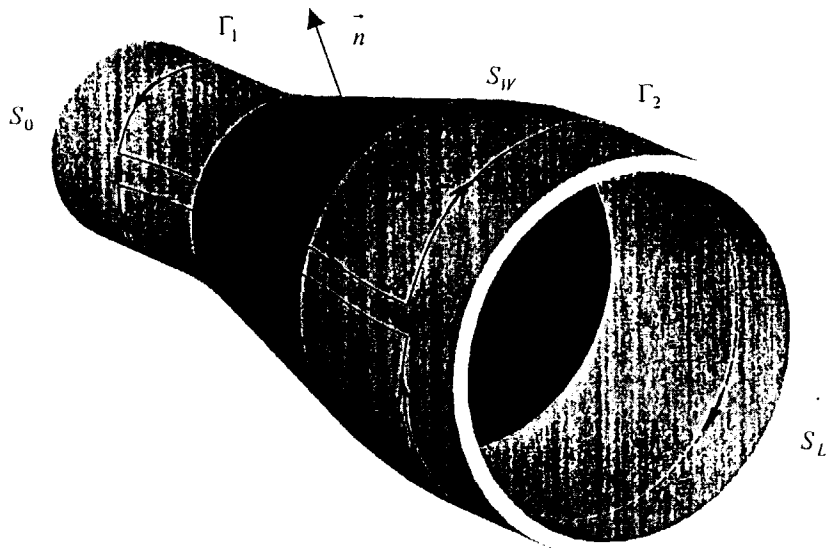

Figure 2. A non-uniform acoustically treated duct segment, showing the integration contour used in the application of Stokes Theorem.

A REVERSE FLOW THEOREM AND ACOUSTIC RECIPROCITY IN COMPRESSIBLE POTENTIAL FLOWS

Walter Eversman
Mechanical and Aerospace Engineering
and Engineering Mechanics
University of Missouri-Rolla
Rolla, MO 65401

ABSTRACT

A reverse flow theorem for acoustic propagation in compressible potential flow has been obtained directly from the field equations without recourse to energy conservation arguments. A reciprocity theorem for the scattering matrix for propagation of acoustic modes in a duct with either acoustically rigid walls or acoustically absorbing walls follows. It is found that for a source at a specific end of the duct, suitably scaled reflection matrices in direct and reverse flow have a reciprocal relationship. Scaled transmission matrices obtained for direct flow and reversed flow with simultaneous switching of source location from one end to the other also have a reciprocal relationship. Numerical verification of the reciprocal relationships is given in a companion paper.

INTRODUCTION

The general principle of acoustic reciprocity in a medium at rest is well known and is derived in [1] by direct manipulation of the field equations in the case of harmonic time dependence. By essentially using this starting point, Eversman [2] has demonstrated and numerically verified reciprocal properties of the scattering matrix for acoustic modes incident, reflected, and transmitted in a non-uniform duct in the absence of mean flow. Moehring [3] , by using an approach based on energy conservation, has arrived at the same result when differences in definitions of the normalization of acoustic modes are considered. Moehring's approach depends on a suitable definition of acoustic energy density and acoustic energy flux, which are

well known in the case of propagation in a stationary medium. Since the result of Moehring [3] depends on the normal derivative of the acoustic energy flux vanishing on the walls of the duct, it would appear to exclude dissipative walls. However, the classical result [1] concludes that reciprocal relations still hold provided the duct walls have a locally reacting impedance model (whether dissipative or not) where for harmonic disturbances acoustic particle velocity is proportional to acoustic pressure. Reciprocity based on energy conservation is more restrictive than necessary.

An appropriate definition of acoustic energy and energy flux also exists for propagation in a compressible potential flow [4]. On this basis, Moehring [3] extended his observations on properties of the scattering matrix to include non-uniform ducts with rigid walls and potential mean flow with the result that the reciprocal properties also depend on flow reversal. Godin [5] has studied extensively issues of acoustic energy, acoustic reciprocity, and flow reversal theorems in a highly generalized sense directly from the field equations. He has not specifically addressed the simpler case of propagation in non-uniform ducts with compressible irrotational flow, citing Moehring [3] as having demonstrated reverse flow reciprocity in this case [6]. Godin's citations to the literature can be consulted for an extensive survey of the field.

Here the goal is to approach the acoustic reciprocity problem in a compressible potential flow in non-uniform ducts directly from the field equations in much the same way as the classical formulation in the case of a stationary medium [1]. Furthermore, it is intended to show that reciprocity holds for a finite length dissipative lining imbedded in an otherwise rigid wall. A foundation for such a formulation in the case of uniform flows was given by Flax [7,8] in connection with unsteady lifting surface theory. The application to potential flows in non-uniform ducts given here yields a reciprocity relationship (perhaps more appropriately referred to as a flow reversal theorem [5]) which is in terms of acoustic potential and acoustic density perturbations on an irrotational compressible mean flow. It also can be given entirely in terms of acoustic potential perturbations. The reverse flow reciprocity formulation which is obtained does not begin with an energy conservation law and leads to a form similar to Moehring [3]. This investigation is not restricted to a duct with rigid walls. The reverse flow reciprocity theorem is then used to establish reciprocal properties of the scattering matrix for propagation of acoustic

modes in a non- uniform duct with acoustically absorbing walls.

In the present paper the theoretical frame work is established for the reciprocity (flow reversal) relationship, and it is specialized for examining the reciprocal relations which exist between duct modes propagating in compressible mean flow. In a companion paper [9], the results derived here are substantiated by numerical experiments based on a finite element simulation using a new implementation of the boundary condition introduced by the presence of acoustic treatment, the subject of a second companion paper [10].

ACOUSTIC PROPAGATION IN A COMPRESSIBLE POTENTIAL FLOW

An extensive discussion of both linear and non-linear formulations for acoustic propagation in potential flows has been given by Campos [11]. His work includes a number of citations to previous work and is the basis for contributions directed mainly toward analytic or semi-analytic solutions for propagation in ducts (see for example [12,13]). The investigation reported here has been part of the development of numerical modeling methods for acoustic propagation in non-uniform ducts and therefore the final form of the governing equations is specialized for that purpose.

The acoustic field equations are obtained by the consideration of unsteady perturbations on a steady compressible potential flow. Accuracy in calculation of both the steady and unsteady flow fields is necessary for computational verification of the theoretical results obtained. The starting point for the formulation of both the steady mean flow and the acoustic perturbation consists of the mass and momentum equations and the energy equation in the form of the isentropic equation of state:

$$\frac{\partial \hat{\rho}}{\partial t} + \nabla\cdot(\hat{\rho}\,\vec{V}) = 0 \tag{1}$$

$$\frac{\partial \vec{V}}{\partial t} + (\vec{V}\cdot\nabla)\vec{V} = -\frac{1}{\hat{\rho}}\nabla\hat{p} \tag{2}$$

$$\frac{\hat{p}}{p_0} = \left(\frac{\hat{\rho}}{\rho_0} \right)^{\gamma} \tag{3}$$

$\hat{p}$, $\hat{\rho}$, $\vec{V}$ are fluid properties pressure, density, and velocity, at this point in dimensional form. p_0 , ρ_0 are reference values of pressure and density. It is assumed that the mean flow and acoustic perturbations are irrotational and that a potential $\hat{\phi}$ exists such that $\vec{V} = \nabla\hat{\phi}$. Acoustic perturbations are assumed on the steady mean flow such that $\hat{\phi} = \phi_r + \phi$, $\hat{\rho} = \rho_r + \rho$ and $\hat{p} = p_r + p$. The linearized continuity equation is

$$\frac{\partial \rho}{\partial t} + \nabla\cdot(\rho_r \nabla\phi + \rho\nabla\phi_r) = 0 \tag{4}$$

The linearized momentum equation, for irrotational acoustic perturbations, is

$$\rho = -\frac{\rho_r}{c_r^2}\left(\frac{\partial\phi}{\partial t} + \nabla\phi_r\cdot\nabla\phi \right) \tag{5}$$

This is used to replace ρ in equation (4) and the linearized equation of state,

$$p = c_r^2 \rho \tag{6}$$

is used to produce an alternative form of the momentum equation in terms of acoustic pressure,

$$p = -\rho_r\left(\frac{\partial\phi}{\partial t} + \nabla\phi_r\cdot\nabla\phi \right) \tag{7}$$

Equation (7) is used to post-process the field solution for ϕ to obtain the acoustic pressure field. The acoustic particle velocity and acoustic velocity potential are related according to

$$\vec{v} = \nabla\phi \tag{8}$$

The perturbation process also produces the conservation equation for the steady flow

$$\nabla\cdot(\rho_r\nabla\phi_r) = 0 \tag{9}$$

and the steady flow momentum equation in terms of the speed of sound

$$c_r^2 = 1 - \frac{(\gamma - 1)}{2}[\nabla\phi_r\cdot\nabla\phi_r - M_\infty^2] \tag{10}$$

and in terms of the steady flow density

$$\rho_r = [1 - \frac{(\gamma - 1)}{2}(\nabla\phi_r\cdot\nabla\phi_r - M_\infty^2)]^{\frac{1}{\gamma - 1}} \tag{11}$$

Equations (4) through (11) are now in non-dimensional form where ϕ is the acoustic potential, ϕ_r is the local mean flow (reference) potential, ρ is the acoustic density, ρ_r is the local mean flow density, and c_r is the local speed of sound in the mean flow. All quantities are made non-dimensional by using the density ρ_∞ and the speed of sound c_∞ at some point, in this case the radius at the plane $x = 0$. Stagnation conditions could also serve as the reference. A reference length R is defined as some characteristic dimension at the plane $x = 0$. In the case of a circular duct the reference length is the duct radius at $x = 0$. The acoustic potential is non-dimensional with respect to $c_\infty R$, and the acoustic pressure with respect to $\rho_\infty c_\infty^2$. Lengths are made non-dimensional with respect to R. Time is scaled with R/c_∞. In the case of harmonic time dependence this leads to the definition of non-dimensional frequency $\eta_r = \omega R/c_\infty$. ω is the dimensional source frequency. M_∞ is the Mach number at the reference point.

Equation (9) is the field equation for the calculation of the compressible potential mean flow. Equations (10) and (11) are subsidiary relations that can be used in an iterative solution which at each stage uses a density field derived from the previous iteration step. $\nabla\phi_r$, c_r, ρ_r are required data for the formulation of the acoustic problem.

REVERSE FLOW RECIPROCITY PRINCIPLE

The application of a reciprocity relationship for acoustic propagation in potential flows in non-uniform ducts has lagged behind the exploitation of the comparable results for propagation in a quiescent medium, not because of the difficulty in posing the principle, but probably because of the difficulty in producing solutions which could be used to test it. Numerical solutions for duct propagation using the Finite Element Method (FEM) are now achievable [14] and provide the capability of determining the complete acoustic field in a duct (and in the far field of a duct of finite length) as well as the scattering matrix for a non-uniform duct inserted in an otherwise uniform duct of infinite length. This provides opportunity for testing the reciprocity principle and suggests the development of such a principle for benchmarking of FEM calculations.

The intent here is to approach the reciprocity principle independent of considerations of energy conservation. A counterpart exists in the literature of unsteady lifting surface theory in the Reverse Flow Theorem of Flax [7,8] . A reciprocity principle for acoustic propagation in non-uniform potential flows in ducts can be obtained by an extension of the formulation of Flax.

Consider the volume Ω shown in Figure 1, which is the interior of a nonuniform duct of arbitrary cross section. In examples the duct will be assumed axisymmetric (circular or annular), but the principle derived is independent of the duct cross section. The duct walls can be rigid or locally reacting. The unit normal $\vec{n}$ is directed out of the volume at each surface. The source plane S_s is where the acoustic source is specified and the exit plane S_e terminates the duct and may have a reflection matrix specified. For computations the exit plane will be assumed non-reflecting. A typical computational problem would seek to specify the acoustic field within the duct and the scattering matrix at the source plane for incident acoustic modes. Equations (4) and (5) specify the acoustic field within Ω subject to appropriate boundary conditions on S, the surface of Ω.

Let $\phi_1 e^{i\eta_r t}$ be a harmonic solution for the acoustic velocity potential for the case of a mean flow specified everwhere in the duct by its reference Mach number $\vec{M}_r = \nabla\phi_r$ and with specified boundary conditions. Let $\phi_2 e^{i\eta_r t}$ be a second harmonic solution for exactly the same duct with different source conditions, but with the flow reversed, $-\vec{M}_r = -\nabla\phi_r$. It is important to note that in reversed flow the reference density ρ_r and reference speed of sound c_r are

unaltered. Because of equation (4), in the case of a harmonic source at non-dimensional frequency η_r, it follows that

$$\iiint_{\Omega} \{\phi_2[i\eta_r\rho_1 + \nabla\cdot(\rho_r\nabla\phi_1 + \nabla\phi_r\rho_1)] - \phi_1[i\eta_r\rho_2 + \nabla\cdot(\rho_r\nabla\phi_2 - \nabla\phi_r\rho_2)]\}\, d\Omega = 0 \qquad (12)$$

With application of the divergence theorem equation (12) is reconfigured to

$$\iint_{S} \{\phi_2[(\rho_r\nabla\phi_1 + \nabla\phi_r\rho_1)] - \phi_1[(\rho_r\nabla\phi_2 - \nabla\phi_r\rho_2)]\}\cdot\vec{n}\, dS$$

$$- \iiint_{\Omega} \{\nabla\phi_2\cdot\nabla\phi_r\rho_1 + \nabla\phi_1\cdot\nabla\phi_r\rho_2 - i\eta_r(\phi_2\rho_1 - \phi_1\rho_2)\}\, d\Omega = 0 \qquad (13)$$

The acoustic density in the two solutions is defined according to

$$\rho_1 = -\frac{\rho_r}{c_r^2}(i\eta_r\phi_1 + \nabla\phi_r\cdot\nabla\phi_1) \quad , \quad \rho_2 = -\frac{\rho_r}{c_r^2}(i\eta_r\phi_2 - \nabla\phi_r\cdot\nabla\phi_2) \qquad (14)$$

Equations (14) are used to eliminate the remaining volume integral in equation (12), leaving the reciprocity principle in terms of acoustic density and potential in a form convenient for subsequent development

$$\iint_{S} \{\phi_2[(\rho_r\nabla\phi_1 + \nabla\phi_r\rho_1)] - \phi_1[(\rho_r\nabla\phi_2 - \nabla\phi_r\rho_2)]\}\cdot\vec{n}\, dS = 0 \qquad (15a)$$

An alternate form, in terms of the acoustic pressure, obtained by using equation (7), is

$$\iint_{S} \{(\frac{p_2}{\rho_r} - \nabla\phi_r\cdot\nabla\phi_2)[(\rho_r\nabla\phi_1 + \nabla\phi_r\rho_1)] - (\frac{p_1}{\rho_r} + \nabla\phi_r\cdot\nabla\phi_1)[(\rho_r\nabla\phi_2 - \nabla\phi_r\rho_2)]\}\cdot\vec{n}\, dS = 0 \qquad (15b)$$

In establishing reciprocal relationships for the scattering matrix it is important in this development that Equation (15a) or (15b) have contributions only on the source and exit planes, S_s and S_e. This requires that the integrand vanish on the duct walls. For a duct with rigid walls

this occurs because $\nabla\phi_r \cdot \vec{n} = 0$, $\nabla\phi_1 \cdot \vec{n} = 0$, and $\nabla\phi_2 \cdot \vec{n} = 0$ on the walls. In the case when mean flow is absent , $\nabla\phi_r$ vanishes and ρ_r is constant, leading to

$$\int_S \int \{p_2 \vec{v}_1 - p_1 \vec{v}_2\} \cdot \vec{n}\, dS = 0 \tag{16}$$

For a locally reacting wall admittance in the absence of mean flow, acoustic pressure is proportional to particle velocity. This makes the integrand vanish on the walls of the duct, and equation (16) has contributions only on the source and exit planes. Reciprocal properties of the scattering matrix are therefore valid in the absence of flow for normally reacting impedance walls. This is in spite of the fact that acoustic power is not conserved.

When mean flow is present and the walls are normally reacting further examination is required to establish that equation 15(a) has no contribution on the duct walls. Myers [15] has shown that the boundary condition at a normally reacting acoustic lining which relates the boundary displacement ζ to the component of the acoustic particle velocity normal to the undisplaced surface is

$$\nabla\phi \cdot \vec{n} = i\eta_r \zeta + \vec{M}_r \cdot \nabla\zeta - \zeta\, \vec{n} \cdot (\vec{n} \cdot \nabla)\vec{M}_r \tag{17}$$

With $\nabla\phi_r \cdot \vec{n} = 0$ on the duct wall surfaces S_w , lined or unlined, and $\vec{M}_r = \nabla\phi_r$ the integral of equation (15a) on S_w becomes

$$\begin{aligned} I_w = \int_{S_w} \int \{ & \rho_r \phi_2 [\, i\eta_r \zeta_1 + \vec{M}_r \cdot \nabla\zeta_1 - \zeta_1 \vec{n} \cdot (\vec{n} \cdot \nabla)\vec{M}_r] \\ & - \rho_r \phi_1 [\, i\eta_r \zeta_2 - \vec{M}_r \cdot \nabla\zeta_2 + \zeta_2 \vec{n} \cdot (\vec{n} \cdot \nabla)\vec{M}_r] \}\, dS \end{aligned} \tag{18}$$

The following vector identities are introduced (with account taken of the special circumstances of the present problem):

$$\rho_r \phi \vec{M}_r \cdot \nabla\zeta = \rho_r \vec{M}_r \cdot \nabla\phi\zeta - \rho_r \zeta\, \vec{M}_r \cdot \nabla\phi$$

$$\nabla \cdot \rho_r \vec{M}_r = 0$$

$$\rho_r \vec{M}_r \cdot \nabla \phi \zeta = \nabla \cdot \rho_r \phi \zeta \vec{M}_r$$

$$\vec{n} \cdot \vec{M}_r = 0$$

$$\rho_r \phi \zeta \vec{n} \cdot (\vec{n} \cdot \nabla) \vec{M}_r = \vec{n} \cdot (\vec{n} \cdot \nabla) \rho_r \phi \zeta \vec{M}_r$$

$$\vec{n} \cdot \nabla \times (\vec{n} \times \rho \phi \zeta \vec{M}_r) = \nabla \cdot \rho_r \phi \zeta \vec{M}_r - \vec{n} \cdot (\vec{n} \cdot \nabla) \rho_r \phi \zeta \vec{M}_r$$

Equation (18) can then be reformulated as

$$I_w = \int\int_{S_w} \{ \rho_r \zeta_1 [i\eta_r \phi_2 - \vec{M}_r \cdot \nabla \phi_2] - \rho_r \zeta_2 [i\eta_r \phi_1 + \vec{M}_r \cdot \nabla \phi_2] \} \, dS$$

$$+ \int\int_{S_w} \{ \vec{n} \cdot \nabla \times (\vec{n} \times \rho_r \phi_2 \zeta_1 \vec{M}_r) + \vec{n} \cdot \nabla \times (\vec{n} \times \rho_r \phi_1 \zeta_2 \vec{M}_r) \} \, dS \tag{19}$$

The case considered here is an admittance wall imbedded in an otherwise rigid wall. Therefore, as shown in figure (2), acoustic treatment extends less than the full length of the duct. This is physically realistic, and is also consistent with the type of reciprocity relation between duct modal amplitudes which is sought. Following the development of Moehring [16], the last integral can be written as a line integral on the boundary Γ of the surface S_w by using Stokes' Theorem. Since the surface S_w consists of the wall of the duct (in general of varying cross section), Γ Is chosen to consist of closed curves Γ_1 and Γ_2 circumscribed on the duct wall outside of the region of the lining, and therfore where the duct wall is rigid. There is also a portion of Γ which runs along the duct wall between Γ_1 and Γ_2 to complete the closed curve of Stokes' Theorem, but this curve is traversed twice, once in each direction, and has no net contribution. To make use of Stokes' Theorem it is required that the acoustic field and the wall displacement be continuous on S_w. Hence, since the acoustic treatment is of limited

length imbedded in an otherwise rigid wall duct, the transition from rigid wall to admittance wall, as well as the variation of admittance along the treated wall, must be continuous. If this condition is met, Stokes' Theorem can be cast in the form

$$\int\int_{S_w} \{\vec{n}\cdot\nabla\times(\vec{n}\times\rho_r\phi\zeta\,\vec{M}_r)\}\,dS = \int_{\Gamma_1}(\vec{n}\times\rho_r\phi\zeta\,\vec{M}_r)\cdot d\vec{\Gamma} + \int_{\Gamma_2}(\vec{n}\times\rho_r\phi\zeta\,\vec{M}_r)\cdot d\vec{\Gamma} \tag{20}$$

The integral on the surface S_w vanishes if the line integrals vanish. On a hard wall the line integrals vanish because the boundary displacement vanishes. This means that if the condition for the use of Stokes' Theorem is met, then the integral of equation (19) is

$$I_w = \int\int_{S_w} \{\rho_r\zeta_1[i\eta_r\phi_2 - \vec{M}_r\cdot\nabla\phi_2] - \rho_r\zeta_2[i\eta_r\phi_1 + \vec{M}_r\cdot\nabla\phi_1]\}\,dS \tag{20}$$

With equation (7) this becomes

$$I_w = \int\int_{S_w} \{\zeta_2 p_1 - \zeta_1 p_2\}\,dS \tag{21}$$

At a wall of admittance A there is a relation between pressure and wall velocity which is frequency dependent and of the form

$$i\eta_r\zeta = Ap \tag{22}$$

The integral I_w vanishes and equation (14) has contributions only on the portion of the surface area S which corresponds to duct cross sections beyond the impedance wall, on the surfaces S_s And S_e. With appropriate restrictions on the impedance wall, the reciprocity principle is therefore unchanged for hard and soft wall ducts.

The restriction on the impedance wall is interesting. If admittance is indeed discontinuous along the wall, then ζ has to be discontinuous. Moehring [16] has noted that for discontinuous admittance variation there is no clear condition to be imposed on the acoustic field or wall

displacement at the discontinuity. Rebel and Ronneberger [17] has shown that the condition of admittance discontinuity and the assumption of potential flow at the wall (no boundary layer) causes a problem with the underlying physics of the flow. What is known is that a numerical procedure such as the FEM restricts the solution for acoustic potential to continuous functions, and the lining displacement never appears in the final field equations and boundary condition. Thus one suspects that the restriction to continuously varying admittance is not a critical issue in numerical comparisons, but it may be in comparisons with experiment.

Equation (14) can also be written entirely in terms of acoustic potential

$$\int\int_S \phi_2 \{\rho_r(\nabla\phi_1 - \frac{1}{c_r^2}\vec{M}_r\vec{M}_r\cdot\nabla\phi_1) - i\eta_r\frac{\rho_r}{c_r^2}\vec{M}_r\phi_1\}\cdot\vec{n}\,dS$$

$$-\int\int_S \phi_1 \{\rho_r(\nabla\phi_2 - \frac{1}{c_r^2}\vec{M}_r\vec{M}_r\cdot\nabla\phi_2) + i\eta_r\frac{\rho_r}{c_r^2}\vec{M}_r\phi_2\}\cdot\vec{n}\,dS = 0 \qquad (23)$$

where the area S is now understood to include only the source and exit planes S_s and S_e.

APPLICATION TO A NON-UNIFORM DUCT

The discussion here is presented for a duct with a straight x axis, but is more complicated only in the notation if the axis is not straight. Figure 2 shows a representative non-uniform duct with cross section $S(x)$ defined on $0 \le x \le L$, $S(0) = S_0$, $S(L) = S_L$ There is a steady mean potential flow in the duct $\vec{M}(x,\vec{r})$, defined as

$$\vec{M}(x,\vec{r}) = \frac{c_\infty}{c(x,\vec{r})}\vec{M}_r(x,\vec{r}) = \frac{1}{c_r(x,\vec{r})}\nabla\phi_r \qquad (24)$$

$\vec{M}_r$ is a non-dimensional velocity based on the reference speed of sound c_∞. $M(x,\vec{r})$ is the local Mach number defined in the usual way and $c(x,\vec{r})$ is the local (dimensional) speed of sound. $(x,\vec{r})$ denotes a point in a cross section at x in a coordinate system appropriate for the

duct geometry. The corresponding reversed flow is $-\vec{M}$. The non-dimensional frequency η can also be defined locally (local speed of sound but with reference length R) according to

$$\eta_r = \frac{\omega R}{c_\infty} = \frac{\omega R}{c}\frac{c}{c_\infty} = c_r \eta \tag{25}$$

η is a local non-dimensional frequency based on the local speed of sound. In terms of local Mach number and non-dimensional frequency, equation (23) becomes

$$\iint_{S_0+S_L} \rho_r \phi_2 \{ [\nabla\phi_1 - \vec{M}(\vec{M}\cdot\nabla\phi_1)] - i\eta\vec{M}\phi_1 \}\cdot\vec{n}\, dS$$

$$- \iint_{S_0+S_L} \rho_r \phi_1 \{ [\nabla\phi_2 - \vec{M}(\vec{M}\cdot\nabla\phi_2)] + i\eta\vec{M}\phi_2 \}\cdot\vec{n}\, dS = 0 \tag{26}$$

It is assumed that at the inflow end of the duct at $x = 0$ the steady mean flow is uniform on the cross section with $\vec{M}(x,\vec{r}) = M_0 i$, and at the outflow end $x = L$ the steady mean flow is uniform with $\vec{M}(x,\vec{r}) = M_L i$. Reference density ρ_{r_0} and ρ_{r_L} and local non-dimensional frequency η_0 and η_L are defined similarly. The assumption of uniform conditions implies that the inflow and outflow planes are well removed from the non-uniform region of the duct. In computational examples it is found that for ducts with circular or annular cross sections uniform inlet and outlet ducts of length two duct radii ahead of and beyond the non-uniformity are sufficient. At $x = 0$ the outward unit normal $\vec{n} = -i$ and at $x = L$ the normal is $\vec{n} = i$. With these observations the reciprocity principle of equation (26) becomes

$$\rho_{r_0} \iint_{S_0} \phi_2 \{(1 - M_0^2)\frac{\partial \phi_1}{\partial x} - i\eta_0 M_0 \phi_1\} dS$$

$$- \rho_{r_0} \iint_{S_0} \phi_1 \{(1 - M_0^2)\frac{\partial \phi_2}{\partial x} + i\eta_0 M_0 \phi_2\} dS$$

$$= \rho_{r_L} \iint_{S_L} \phi_2 \{(1 - M_L^2)\frac{\partial \phi_1}{\partial x} - i\eta_L M_L \phi_1\} dS \qquad (27)$$

$$- \rho_{r_L} \iint_{S_L} \phi_1 \{(1 - M_L^2)\frac{\partial \phi_2}{\partial x} + i\eta_L M_L \phi_2\} dS$$

CIRCULAR DUCT EXAMPLE

In the regions of uniform flow at the ends of the duct at $x = 0$ and $x = L$ acoustic potential can be approximated by an N term eigenfunction expansion in terms of duct modes (Figure 2). In the case of a circular duct the expansion can be expressed at $x = 0$ in vector-matrix form for angular dependence $e^{-im\theta}$ as

$$\phi_m(x,r,\theta) = \left[\Phi_m(r)\right]\left[e_m^+(x)\right]\left\{a_m^+\right\}e^{-im\theta} + \left[\Phi_m(r)\right]\left[e_m^-(x)\right]\left\{a_m^-\right\}e^{-im\theta} \qquad (28)$$

The derivative is

$$\frac{\partial \phi_m}{\partial x}(x,r,\theta) = \left[\Phi_m(r)\right]\left[e_m^+(x)\right]\left[-ik_x^+\right]\left\{a_m^+\right\}e^{-im\theta} + \left[\Phi_m(r)\right]\left[e_m^-(x)\right]\left[-ik_x^-\right]\left\{a_m^-\right\}e^{-im\theta} \qquad (29)$$

$\left[\Phi(r)\right]$ is a $1 \times N$ row matrix of duct radial modes, the same for both right and left propagating modes. $\left[e_m^+(x)\right]$ and $\left[e_m^-(x)\right]$ are $N \times N$ diagonal matrices with typical elements $e^{-ik_{x\,mn}^{\pm} x}$. $\left[-ik_x^+\right]$ and $\left[-ik_x^-\right]$ are $N \times N$ diagonal matrices with typical elements $-ik_{x\,mn}^{\pm}$. $\left\{a_m^-\right\}$

and $\{a_m^-\}$ are $N \times 1$ vectors of modal amplitude coefficients for right (positive x) and left (negative x) modes. A similar expansion with modal amplitudes $\{b_m^+\}$ and $\{b_m^-\}$ applies at $x = L$. The axial wave numbers are given in the nominal flow for modes which are cut on by

$$\left(\frac{k_{x\,mn}^{\pm}}{\eta}\right)_1 = \frac{1}{1-M^2}\left[-M \pm \sqrt{1-(1-M^2)\left(\frac{\kappa_{mn}\sigma}{\sigma\eta}\right)^2}\right] \tag{30a}$$

and for modes which are cut off by

$$\left(\frac{k_{x\,mn}^{\pm}}{\eta}\right)_1 = \frac{1}{1-M^2}\left[-M \mp i\sqrt{(1-M^2)\left(\frac{\kappa_{mn}\sigma}{\sigma\eta}\right)^2-1}\right] \tag{30b}$$

In reversed flow for cut on modes

$$\left(\frac{k_{x\,mn}^{\pm}}{\eta}\right)_2 = \frac{1}{1-M^2}\left[M \pm \sqrt{1-(1-M^2)\left(\frac{\kappa_{mn}\sigma}{\sigma\eta}\right)^2}\right] \tag{31a}$$

and for cut off modes

$$\left(\frac{k_{x\,mn}^{\pm}}{\eta}\right)_1 = \frac{1}{1-M^2}\left[M \mp i\sqrt{(1-M^2)\left(\frac{\kappa_{mn}\sigma}{\sigma\eta}\right)^2-1}\right] \tag{31b}$$

The non-dimensional frequency η is based on the local speed of sound and the reference radius. $\kappa_{mn}\sigma$ are eigenvalues determined from the uniform duct eigenproblem [18] in a uniform duct with local radius possibly different than the reference radius. In the case of the circular duct

they are determined from $J_m'(\kappa_{mn}\sigma) = 0$, with J_m being the Bessel function. m is the angular mode number and n, $1 \le n \le N$, is the radial mode number. σ is the ratio of the local duct radius to the reference radius, $\sigma = R_l / R$. $\sigma\eta$ is therefore non-dimensional frequency based on local speed of sound and local duct radius. At $x = 0$ where the reference radius and c_∞ are defined, $\sigma = 1$ and $\eta = \eta_r$. At $x = 0$ the diagonal matrices $\left|e_m^+(0)\right|$ and $\left|e_m^-(0)\right|$ become identity matrices. At $x = L$ $\left|e_m^+(L)\right|$ and $\left|e_m^-(L)\right|$ can be absorbed into the amplitude coefficients. The convention on the sign choice in equation (30) corresponding to $k_{x\,mn}^+$ is that the positive sign is chosen if the radical is real and the minus sign is chosen if the radical is imaginary. The opposite choices are made for $k_{x\,mn}^-$. $k_{x\,mn}^+$ then corresponds to waves propagating in the positive x direction (except for the possibility that with Mach number negative some propagating waves may appear not to propagate in the positive x direction due to convection) and to cut-off modes decaying in the positive x direction. The opposite interpretation applies for $k_{x\,mn}^-$.

With these observations, deleting the implied dependence on the mode number m, and taking the reversed flow solution to have angular dependence $e^{im\theta}$, it is possible to express the solution ϕ_1 and its counterpart reversed flow solution ϕ_2 as

$$\phi_1 = [\Phi]\{a_1^+\}e^{-im\theta} + [\Phi]\{a_1^-\}e^{-im\theta} \tag{32}$$

$$\frac{\partial\phi_1}{\partial x} = [\Phi]\left[-ik_{x_1}^+\right]\{a_1^+\}e^{-im\theta} + [\Phi]\left[-ik_{x_1}^-\right]\{a_1^-\}e^{-im\theta} \tag{33}$$

The corresponding reversed flow solution is

$$\phi_2 = [\Phi]\{a_2^+\}e^{im\theta} + [\Phi]\{a_2^-\}e^{im\theta} \tag{34}$$

$$\frac{\partial\phi_2}{\partial x} = [\Phi]\left[-ik_{x_2}^+\right]\{a_2^+\}e^{im\theta} + [\Phi]\left[-ik_{x_2}^-\right]\{a_2^-\}e^{im\theta} \tag{35}$$

It is important to note that the eigenvalues and eigenfunctions are independent of angular dependence $e^{-im\theta}$ or $e^{im\theta}$. The choice of angular dependence in the two solutions eliminates the angular dependence in the integrals of equation (27). The physical implication is that of a spinning mode which has the same vector sense with respect to the flow direction. In calculations, scattering coefficients do not depend on the sign of m.

In carrying out the integrals of equation (21), the notation

$$\iint_{S_0} [\Phi]^T [\Phi] \, dS = [J_0] \tag{36}$$

$$\iint_{S_L} [\Phi]^T [\Phi] \, dS = [J_L] \tag{37}$$

is introduced. $[J_0]$ and $[J_L]$ are $N \times N$ diagonal matrices resulting from the orthogonality of the duct eigenfunctions at $x = 0$ and $x = L$. For a circular duct the eigenfunctions $\Phi_{mn}(r)$ are Bessel functions of the first kind of order m. In numerical implementations it is convenient to generate the Bessel functions, solve the related eigenproblem, and generate $[J_0]$ and $[J_L]$ using an FEM formulation.

With the eigenfunction expansions of equations (32)-(35) the integrals of equation (27) can be written

$$\begin{aligned}
&\rho_{r_0} \iint_{S_0} \phi_2 \{(1 - M_0^2) \frac{\partial \phi_1}{\partial x} - i\eta_0 M_0 \phi_1\} \, dS \\
&\quad = \rho_{r_0} [(1 - M_0^2)(\{a_2^+\}^T + \{a_2^-\}^T)[J_0]([-ik_{x\,01}^+]\{a_1^+\} + [-ik_{x\,01}^-]\{a_1^-\}) \\
&\qquad - i\eta_0 M_0 (\{a_2^+\}^T + \{a_2^-\}^T)[J_0](\{a_1^+\} + \{a_1^-\})]
\end{aligned} \tag{38}$$

$$\begin{aligned}
&\rho_{r_0} \iint_{S_0} \phi_1 \{(1 - M_0^2) \frac{\partial \phi_2}{\partial x} + i\eta_0 M_0 \phi_2\} \, dS \\
&\quad = \rho_{r_0} [(1 - M_0^2)(\{a_1^+\}^T + \{a_1^-\}^T)[J_0]([-ik_{x\,02}^+]\{a_2^+\} + [-ik_{x\,02}^-]\{a_2^-\}) \\
&\qquad + i\eta_0 M_0 (\{a_1^+\}^T + \{a_1^-\}^T)[J_0](\{a_2^+\} + \{a_2^-\})]
\end{aligned} \tag{39}$$

$$\rho_{r_L} \int\int_{S_L} \phi_2 \{(1 - M_L^2)\frac{\partial \phi_1}{\partial x} - i\eta_L M_L \phi_1\} dS$$

$$= \rho_{r_L}[(1 - M_L^2)(\{b_2^+\}^T + \{b_2^-\}^T)[J_L]([-ik_{x\ L1}^+]\{b_1^+\} + [-ik_{x\ L1}^-]\{b_1^-\})$$

$$- i\eta_L M_L(\{b_2^+\}^T + \{b_2^-\}^T)[J_L](\{b_1^+\} + \{b_1^-\})] \tag{40}$$

$$\rho_{r_L} \int\int_{S_L} \phi_1 \{(1 - M_L^2)\frac{\partial \phi_2}{\partial x} + i\eta_L M_L \phi_2\} dS$$

$$= \rho_{r_L}[(1 - M_L^2)(\{b_1^+\}^T + \{b_1^-\}^T)[J_L]([-ik_{x\ L2}^+]\{b_2^+\} + [-ik_{x\ L2}^-]\{b_2^-\})$$

$$+ i\eta_L M_L(\{b_1^+\}^T + \{b_1^-\}^T)[J_L](\{b_2^+\} + \{b_2^-\})] \tag{41}$$

The notation $k_{x\ 01}^{\pm}$ designates the axial wave number evaluated at $x = 0$ for the nominal flow direction. $k_{x\ 02}^{\pm}$ corresponds to reversed flow. $k_{x\ L1}^{\pm}$ designates the axial wave number evaluated at $x = L$ for the nominal flow direction. $k_{x\ L2}^{\pm}$ corresponds to reversed flow. In equations (38)-(41) amplitude coefficients $\{a^{\pm}\}$ are associated with an eigenfunction expansion at $x = 0$ and $\{b^{\pm}\}$ correspond to $x = L$. With the use of equations (30a) and (30b), introduce the following definitions for the nominal flow direction for propagating modes (k_x real)

$$\alpha_1^+ = \rho_r[-i(1 - M^2)k_{x_1}^+ - i\eta M] = -i\rho_r\eta\sqrt{1 - (1 - M^2)\left(\frac{\kappa\sigma}{\sigma\eta}\right)^2} \tag{42}$$

$$\alpha_1^- = \rho_r[-i(1 - M^2)k_{x_1}^- - i\eta M] = i\rho_r\eta\sqrt{1 - (1 - M^2)\left(\frac{\kappa\sigma}{\sigma\eta}\right)^2} \tag{43}$$

and for cut-off modes (k_x complex)

$$\alpha^+_1 = \rho_r[-i(1 - M^2)k^+_{x_1} - i\eta M] = -\rho_r\eta\sqrt{(1 - M^2)\left(\frac{\kappa\sigma}{\sigma\eta}\right)^2 - 1} \tag{44}$$

$$\alpha^-_1 = \rho_r[-i(1 - M^2)k^-_{x_1} - i\eta M] = \rho_r\eta\sqrt{(1 - M^2)\left(\frac{\kappa\sigma}{\sigma\eta}\right)^2 - 1} \tag{45}$$

Analogous definitions can be introduced in reversed flow using equations (31a) and (31b). For example, for a propagating mode

$$\alpha^+_2 = \rho_r[-i(1 - M^2)k^+_{x_2} + i\eta M] = -i\rho_r\eta\sqrt{1 - (1 - M^2)\left(\frac{\kappa\sigma}{\sigma\eta}\right)^2} \tag{46}$$

It becomes apparent that the definitions do not change in reversed flow so the conclusion is made that $\alpha^+_2 = \alpha^+_1 = \alpha^+$ and $\alpha^-_2 = \alpha^-_1 = \alpha^-$ for both propagating and cut-off modes. Furthermore, it is apparent that $\alpha^- = -\alpha^+$ and these are to be evaluated at $x = 0$ and $x = L$ as required.

Equations (36)-(41) can be rewritten in the form

$$\begin{aligned}
&\rho_{r_0}\int\int_{S_0}\phi_2\{(1 - M_0^2)\frac{\partial\phi_1}{\partial x} - i\eta_0 M_0\phi_1\}\,dS \\
&= \{a_2^+\}^T[J_0][\alpha^+_0]\{a_1^+\} + \{a_2^+\}^T[J_0][\alpha^-_0]\{a_1^-\} \\
&\quad + \{a_2^-\}^T[J_0][\alpha^+_0]\{a_1^+\} + \{a_2^-\}^T[J_0][\alpha^-_0]\{a_1^-\}
\end{aligned} \tag{47}$$

$$\rho_{r_0} \int_{S_0} \int \phi_1 \{(1 - M_0^2) \frac{\partial \phi_2}{\partial x} - i\eta_0 M_0 \phi_2\} dS$$

$$= \{a_1^+\}^T [J_0][\alpha^+_0]\{a_2^+\} + \{a_1^+\}^T [J_0][\alpha^-_0]\{a_2^-\}$$

$$+ \{a_1^-\}^T [J_0][\alpha^+_0]\{a_2^+\} + \{a_1^-\}^T [J_0][\alpha^-_0]\{a_2^-\} \tag{48}$$

$$\rho_{r_L} \int_{S_L} \int \phi_2 \{(1 - M_L^2) \frac{\partial \phi_1}{\partial x} - i\eta_L M_L \phi_1\} dS$$

$$= \{b_2^+\}^T [J_L][\alpha^+_L]\{b_1^+\} + \{b_2^+\}^T [J_L][\alpha^-_L]\{b_1^-\}$$

$$+ \{b_2^-\}^T [J_L][\alpha^+_L]\{b_1^+\} + \{b_2^-\}^T [J_L][\alpha^-_L]\{b_1^-\} \tag{49}$$

$$\rho_{r_L} \int_{S_L} \int \phi_1 \{(1 - M_L^2) \frac{\partial \phi_2}{\partial x} - i\eta_L M_L \phi_2\} dS$$

$$= \{b_1^+\}^T [J_L][\alpha^+_L]\{b_2^+\} + \{b_1^+\}^T [J_L][\alpha^-_L]\{b_2^-\}$$

$$+ \{b_1^-\}^T [J_L][\alpha^+_L]\{b_2^+\} + \{b_1^-\}^T [J_L][\alpha^-_L]\{b_2^-\} \tag{50}$$

The diagonal matrices $[\alpha^{\pm}_0]$ and $[\alpha^{\pm}_L]$ are have elements defined by equations (42)-(46). Elements α_0 are evaluated at $x = 0$ and α_L are evaluated at $x = L$ and the distinction

between nominal flow and reversed flow disappears. At $x = L$ the modal amplitudes are b_n^+ and b_n^-. Modal amplitudes a_n^+ and a_n^- and b_n^+ and b_n^- are related by the acoustic potential scattering matrix according to

$$\begin{Bmatrix} a^- \\ b^+ \end{Bmatrix} = [S] \begin{Bmatrix} a^+ \\ b^- \end{Bmatrix} \tag{51}$$

where the scattering matrix is defined as

$$[S] = \begin{bmatrix} [R] & [\tilde{T}] \\ [T] & [\tilde{R}] \end{bmatrix} \tag{52}$$

Contained in $[S]$ are the usual reflection matrix $[R]$ and transmission matrix $[T]$ for acoustic modes incident at $x = 0$ and reflection and transmission matrices $[\tilde{R}]$ and $[\tilde{T}]$ for modes incident at $x = L$. There will be a scattering matrix $[S_1]$ for nominal mean flow and a second one $[S_2]$ for reversed flow. The relationship between $[S_1]$ and $[S_2]$ can be obtained using the reciprocity theorem.

When the integral evaluations of equations (47)-(50) are used in equation (27) there is considerable simplification due to the fact that $\alpha_0^- = -\alpha_0^+ = -\alpha_0$ and $\alpha_L^- = -\alpha_L^+ = -\alpha_L$. The diagonal matrices $[\alpha_0]$ and $[\alpha_L]$ are constructed by evaluating equation (42)- (45) at $x = 0$ or $x = L$ for each acoustic mode included in the acoustic potential expansions of equations (32) or (35). $[J_0][\alpha_0]$ and $[J_L][\alpha_L]$ are diagonal and therefore equal to their transpose. The result of the simplifications is

$$\{a_1^-\}^T [J_0][\alpha_0]\{a_2^+\} + \{b_1^+\}^T [J_L][\alpha_L]\{b_2^-\} =$$

$$\{a_2^-\}^T [J_0][\alpha_0]\{a_1^+\} + \{b_2^+\}^T [J_L][\alpha_L]\{b_1^-\} \tag{53}$$

Equation (53) can be written in partitioned form

$$\begin{Bmatrix} a_1^- \\ b_1^+ \end{Bmatrix}^T \begin{bmatrix} [J_0][\alpha_0] & \\ & [J_L][\alpha_L] \end{bmatrix} \begin{Bmatrix} a_2^+ \\ b_2^- \end{Bmatrix} = \begin{Bmatrix} a_2^- \\ b_2^+ \end{Bmatrix}^T \begin{bmatrix} [J_0][\alpha_0] & \\ & [J_L][\alpha_L] \end{bmatrix} \begin{Bmatrix} a_1^+ \\ b_1^- \end{Bmatrix} \tag{54}$$

Equation (54) is rewritten by introducing the definition of the scattering matrix from equation (51) and by using the definition

$$\begin{bmatrix} [J_0][\alpha_0] & \\ & [J_L][\alpha_L] \end{bmatrix} = [J][\alpha] \tag{55}$$

The result is

$$\begin{Bmatrix} a_1^+ \\ b_1^- \end{Bmatrix}^T [S_1]^T [J][\alpha] \begin{Bmatrix} a_2^+ \\ b_2^- \end{Bmatrix} = \begin{Bmatrix} a_2^+ \\ b_2^- \end{Bmatrix}^T [S_2]^T [J][\alpha] \begin{Bmatrix} a_1^+ \\ b_1^- \end{Bmatrix} \tag{56}$$

Equation (56) reveals that

$$[S_1]^T [J][\alpha] = [J][\alpha][S_2] \tag{57}$$

or

$$[J][\alpha][S_1] = ([J][\alpha][S_2])^T \tag{58}$$

Equations (57) and (58) show that a weighted version of the nominal flow acoustic potential

scattering matrix and similarly weighted version of the reversed flow acoustic potential scattering matrix are transposes of one another. In terms of the acoustic potential reflection and transmission coefficient matrices the result is

$$[R_1]^T [J_0] [\alpha_0] = [J_0] [\alpha_0] [R_2] \tag{59}$$

$$[\tilde{R}_1]^T [J_L] [\alpha_L] = [J_L] [\alpha_L] [\tilde{R}_2] \tag{60}$$

$$[T_1]^T [J_L] [\alpha_L] = [J_0] [\alpha_0] [\tilde{T}_2] \tag{61}$$

$$[\tilde{T}_1]^T [J_0] [\alpha_0] = [J_L] [\alpha_L] [T_2] \tag{62}$$

The reciprocal relationships of equations (59)-(62) involve acoustic potential reflection and transmission coefficient matrices, with diagonal elements representing reflection and transmission coefficients in the incident modes (here referred to as direct reflection or transmission) and off diagonal reflection and transmission coefficients from the incident mode to another mode. Equations (59) and (60) show that direct acoustic potential reflection coefficients are invariant in reversed flow. The transmission coefficient matrix pairs $[T_1]$, $[T_2]$ and $[\tilde{T}_1]$, $[\tilde{T}_2]$ are not reciprocally related but the pairs $[T_1]$, $[\tilde{T}_2]$ and $[\tilde{T}_1]$, $[T_2]$ are related by equations (61) and (62). These results for acoustic potential reflection and transmission coefficient matrices are more interesting than those obtained for acoustic pressure reflection and transmission coefficient matrices in the absence of flow [2] because they identify a relationship between reflection coefficient matrices in nominal and reversed flow which includes the observation that the direct reflection coefficient (in the incident mode) is invariant to flow direction.

RECIPROCITY IN TERMS OF ACOUSTIC PRESSURE

The entire development to this point has been carried out in terms of acoustic potential because the field equations (4) and (5) favor this formulation. Equation (7) provides a direct relationship between acoustic pressure and acoustic potential which can be used to restructure the reciprocity results in terms of acoustic pressure modal amplitudes. In terms of local non-dimensional frequency and local Mach number in a uniform section of duct with uniform flow, equation (7) can be rewritten as

$$p = -\rho_r c_r \left(i\eta\phi + M\frac{\partial\phi}{\partial x} \right) \tag{63}$$

With equation (63) a connection between acoustic potential modal amplitudes and acoustic pressure modal amplitudes can be established. Consider an acoustic mode propagating in the uniform section with the axial wave number given by equations (30 a,b) or (31 a,b). By referring, for example, to equation (33), the pressure amplitude can be found in terms of the potential amplitude in nominal flow as

$$p^{\pm}_{1} = -i\eta\rho_r c_r \left(1 - M\frac{k_x^{\pm}}{\eta}\right) \phi_1^{\pm} = \frac{1}{\beta^{\pm}}\,\phi_1^{\pm} \tag{64}$$

and in reversed flow by

$$p^{\pm}_{2} = -i\eta\rho_r c_r \left(1 + M\frac{k_x^{\pm}}{\eta}\right) \phi^{\pm}_{2} = \frac{1}{\beta^{\mp}}\,\phi_2^{\pm} \tag{65}$$

These relations between acoustic pressure modal coefficients and acoustic potential modal coefficients are evaluated at $x = 0$ and $x = L$ to produce transformations between acoustic potential modal amplitudes $\{a^{\pm}\}$, $\{b^{\pm}\}$ and acoustic pressure modal amplitudes $\{c^{\pm}\}$, $\{d^{\pm}\}$:

$$\begin{Bmatrix} a_1^- \\ b_1^+ \end{Bmatrix} = \begin{bmatrix} \beta_0^- & \\ & \beta_L^+ \end{bmatrix} \begin{Bmatrix} c_1^- \\ d_1^+ \end{Bmatrix} = [B^{\mp}] \begin{Bmatrix} c_1^- \\ d_1^+ \end{Bmatrix} \tag{66}$$

$$\begin{Bmatrix} a_1^+ \\ b_1^- \end{Bmatrix} = \begin{bmatrix} \beta_0^+ & \\ & \beta_L^- \end{bmatrix} \begin{Bmatrix} c_1^+ \\ d_1^- \end{Bmatrix} = [B^{\pm}] \begin{Bmatrix} c_1^+ \\ d_1^- \end{Bmatrix} \tag{67}$$

$$\begin{Bmatrix} a_2^- \\ b_2^+ \end{Bmatrix} = \begin{bmatrix} \beta_0^+ & \\ & \beta_L^- \end{bmatrix} \begin{Bmatrix} c_2^- \\ d_2^+ \end{Bmatrix} = [B^{\pm}] \begin{Bmatrix} c_2^- \\ d_2^+ \end{Bmatrix} \tag{68}$$

$$\begin{Bmatrix} a_2^+ \\ b_2^- \end{Bmatrix} = \begin{bmatrix} \beta_0^- & \\ & \beta_L^+ \end{bmatrix} \begin{Bmatrix} c_2^- \\ d_2^- \end{Bmatrix} = [B^{\mp}] \begin{Bmatrix} c_2^+ \\ d_2^- \end{Bmatrix} \tag{69}$$

The $2N \times 2N$ diagonal matrices $[B^{\pm}]$ and $[B^{\mp}]$ have coefficients defined by equations (64) and (65) for each mode, evaluated at the appropriate end of the duct, arranged along the diagonal. Equations (66)-(69) and equation (51) provide a relationship between the scattering matrices for acoustic potential and the scattering matrices for acoustic pressure:

$$[\bar{S}_1] = [B^{\mp}]^{-1} [S_1] [B^{\pm}] \tag{70}$$

$$[\bar{S}_2] = [B^{\pm}]^{-1}[S_2][B^{\mp}] \tag{71}$$

$[S_1]$, $[S_2]$ are the scattering matrices in nominal and reversed flow for acoustic potential modal amplitudes and $[\bar{S}_1]$, $[\bar{S}_2]$ are the scattering matrices for acoustic pressure modal amplitudes. Equations (66)-(71) and equation (56) are used to arrive at the reciprocity relationship for acoustic pressure modal amplitudes in terms of the nominal flow and reverse flow acoustic pressure scattering matrices:

$$[B^{\pm}]^{-1}[\bar{S}_1]^T[J][\alpha][B^{\mp}] = [B^{\pm}][J][\alpha][\bar{S}_2][B^{\mp}]^{-1} \tag{72}$$

The four reciprocal relationships are:

$$[\beta_0^+]^{-1}[\bar{R}_1]^T[J_0][\alpha_0][\beta_0^-] = [\beta_0^+][J_0][\alpha_0][\bar{R}_2][\beta_0^-]^{-1} \tag{73}$$

$$[\beta_L^-]^{-1}[\bar{\tilde{R}}_1]^T[J_L][\alpha_L][\beta_L^+] = [\beta_L^-][J_L][\alpha_L][\bar{\tilde{R}}_2][\beta_L^+]^{-1} \tag{74}$$

$$[\beta_0^+]^{-1}[\bar{T}_1]^T[J_L][\alpha_L][\beta_L^+] = [\beta_0^+][J_0][\alpha_0][\bar{\tilde{T}}_2][\beta_L^+]^{-1} \tag{75}$$

$$[\beta_L^-]^{-1}[\bar{\tilde{T}}_1]^T[J_0][\alpha_0][\beta_0^-] = [\beta_L^-][J_L][\alpha_L][\bar{T}_2][\beta_0^-]^{-1} \tag{76}$$

The reciprocal relationships of equations (73)-(76) involve acoustic pressure reflection and transmission coefficient matrices, with diagonal elements representing reflection and transmission coefficients in the incident modes (here referred to as direct reflection or transmission) and off diagonal reflection and transmission coefficients from the incident mode to another mode. From equations (73) and (74) it is seen that in terms of acoustic pressure modal amplitudes direct reflection and transmission coefficients in nominal flow and reversed flow are not invariant but are simply related. Transmission coefficient matrix pairs $[\bar{T}_1]$, $[\bar{T}_2]$ and $[\bar{\tilde{T}}_1]$, $[\bar{\tilde{T}}_2]$ are not directly related but pairs $[\bar{T}_1]$, $[\bar{\tilde{T}}_2]$ and $[\bar{\tilde{T}}_1]$, $[\bar{T}_2]$ are related by

equations (75) and (76). The result in the case of a plane wave incident is particularly simple and will be given in the following section.

Because of the way in which equations (73)-(76) were developed, the weighted, or scaled, matrices on the right and left hand sides are equivalent to their counterparts in equations (59)-(62). This convenient definition of scaled pressure reflection and transmission matrices makes them numerically equal to their scaled acoustic potential counterparts.

ACOUSTIC POWER CONSIDERATIONS

Reciprocal relations between scattering coefficients in uniform duct sections bounding a non-unifom section obtained above are of theoretical interest and are also a useful tool for benchmarking numerical models of duct propagation. Also of interest in this respect are acoustic power transmission and reflection characteristics of the nonuniform section. For a rigid wall duct acoustic power conservation provides a valuable benchmark and for an acoustically treated duct acoustic power transmission calculations are required to assess performance. In this section acoustic power formulations appropriate for the propagation model are obtained.

There are two commonly used types of acoustic intensity formulations in moving media [19]. The Type I definition due to Morfey [4] is valid as part of a conservation law in non-uniform ducts for compressible potential flow, while the Type II formulation due to Ryshov and Shefter [20] is valid as part of a conservation law only for uniform flow, and therefore only for uniform ducts. In the following development the Type I definition of acoustic intensity is used in the uniform flow sections on either end of the nonuniformity to obtain acoustic power expressions.

The Type I acoustic intensity is defined in non-dimensional form as the time average acoustic energy flux

$$\frac{\vec{I}}{\rho_\infty c_\infty^3} = \left\langle \frac{\vec{N}}{\rho_\infty c_\infty^3} \right\rangle = \left\langle p\vec{v} + \rho_r c_r (\vec{M}\cdot\vec{v})\vec{v} + \frac{1}{\rho_r c_r}\vec{M}p^2 + \vec{M}(\vec{M}\cdot\vec{v})p \right\rangle \qquad (77)$$

where $\bar{M}$ is the local Mach number of the flow and ρ_r, c_r are local values of the non-dimensional mean flow density and speed of sound in the mean flow. For propagation in uniform flow in the direction of the x axis equation (77) simplifies to the scalar form

$$\frac{I}{\rho_\infty c_\infty^3} = \left\langle (1+M^2)pu + \rho_r c_r M u^2 + \frac{1}{\rho_r c_r} M p^2 \right\rangle \tag{78}$$

Acoustic power is obtained by integration over a cross section. For the circular cross section

$$\frac{P}{A_{ref}\rho_\infty c_\infty^3} = \iint_S \left\langle (1+M^2)pu + \rho_r c_r M u^2 + \frac{1}{\rho_r c_r} M p^2 \right\rangle dS \tag{79}$$

A modal expansion as given by equations (32) and (33) is used to obtain an acoustic power in terms of acoustic potential modal amplitudes. Because of orthogonality of the duct eigenfunctions and because the duct eigenfunctions are the same for propagation with and against the flow, the evaluation of acoustic power is considerably simplified. The result can be cast in the form of a "power matrix"

$$\frac{P}{A_{ref}\rho_\infty c_\infty^3} = \begin{Bmatrix} a^{*+} \\ a^{*-} \end{Bmatrix}^T \begin{bmatrix} P_{nn}^{++} & P_{nn}^{-+} \\ P_{nn}^{+-} & P_{nn}^{--} \end{bmatrix} \begin{Bmatrix} a^{+} \\ a^{-} \end{Bmatrix} = \begin{Bmatrix} a^{*+} \\ a^{*-} \end{Bmatrix}^T [P] \begin{Bmatrix} a^{+} \\ a^{-} \end{Bmatrix} \tag{80}$$

where, for example, a^* denotes the complex conjugate of a. The power matrix $[P]$ is structured in diagonal blocks due to orthogonality of the acoustic eigenfunctions. The diagonal blocks consist of power coefficients for positive and negative acoustic modes. The off-diagonal blocks represent power due to interaction of positive and negative modes with the same eigenfunction. If the amplitude coefficients are for acoustic potential, the power coefficients are

$$P_{nn}^{++} = \frac{1}{4}\eta^2\rho_r c_r J_{nn}\{(1+M^2)[\frac{k_x^{++}}{\eta}(1-M\frac{k_x^{+}}{\eta}) + \frac{k_x^{+}}{\eta}(1-M\frac{k_x^{++}}{\eta})]$$

$$+ 2M(\frac{k_x^{++}}{\eta})(\frac{k_x^{+}}{\eta}) + 2M(1-M\frac{k_x^{++}}{\eta})(1-M\frac{k_x^{+}}{\eta})\}$$

$$= \frac{1}{4}\eta^2\rho_r c_r J_{nn}\{2M + (1-M^2)(\frac{k_x^{++}}{\eta} + \frac{k_x^{+}}{\eta})\} \tag{81a}$$

$$P_{nn}^{--} = \frac{1}{4}\eta^2\rho_r c_r J_{nn}\{(1+M^2)[\frac{k_x^{--}}{\eta}(1-M\frac{k_x^{-}}{\eta}) + \frac{k_x^{-}}{\eta}(1-M\frac{k_x^{--}}{\eta})]$$

$$+ 2M(\frac{k_x^{--}}{\eta})(\frac{k_x^{-}}{\eta}) + 2M(1-M\frac{k_x^{--}}{\eta})(1-M\frac{k_x^{-}}{\eta})\}$$

$$= \frac{1}{4}\eta^2\rho_r c_r J_{nn}\{2M + (1-M^2)(\frac{k_x^{--}}{\eta} + \frac{k_x^{-}}{\eta})\} \tag{81b}$$

$$P_{nn}^{+-} = \frac{1}{4}\eta^2\rho_r c_r J_{nn}\{(1+M^2)[\frac{k_x^{+*}}{\eta}(1-M\frac{k_x^{-}}{\eta}) + \frac{k_x^{-}}{\eta}(1-M\frac{k_x^{+*}}{\eta})]$$

$$+ 2M(\frac{k_x^{+*}}{\eta})(\frac{k_x^{-}}{\eta}) + 2M(1-M\frac{k_x^{+*}}{\eta})(1-M\frac{k_x^{-}}{\eta})\}$$

$$= \frac{1}{4}\eta^2\rho_r c_r J_{nn}\{2M + (1-M^2)(\frac{k_x^{+*}}{\eta} + \frac{k_x^{-}}{\eta})\} \tag{81c}$$

$$P_{nn}^{++} = -P_{nn}^{--} = \frac{1}{2}\eta^2 \rho_r c_r J_{nn} \sqrt{1 - (1 - M^2)(\frac{\kappa\sigma}{\kappa\eta})^2}$$

$$P_{nn}^{+-} = -P_{nn}^{-+} = 0 \tag{83}$$

There is no interaction power for cut on modes.

For cut off modes

$$k_x^{+} = k_x^{-*} \quad , \quad k_x^{-} = k_x^{+*}$$

$$\frac{k_x^{+*}}{\eta} + \frac{k_x^{-}}{\eta} = 2\frac{k_x^{-}}{\eta} \quad , \quad \frac{k_x^{-*}}{\eta} + \frac{k_x^{+}}{\eta} = 2\frac{k_x^{+}}{\eta}$$

$$\frac{k_x^{+*}}{\eta} + \frac{k_x^{+}}{\eta} = -\frac{2M}{(1 - M^2)} \quad , \quad \frac{k_x^{-*}}{\eta} + \frac{k_x^{-}}{\eta} = -\frac{2M}{(1 - M^2)} \tag{84}$$

and the acoustic power transmission coefficients are

$$P_{nn}^{++} = P_{nn}^{++} = 0$$

$$P_{nn}^{+-} = -P_{nn}^{-+} = \frac{i}{2}\eta^2 \rho_r c_r J_{nn} \sqrt{(1 - M^2)(\frac{\kappa\sigma}{\kappa\eta})^2 - 1} \tag{85}$$

For cut off there is only power related to the interaction of positive and negative modes. It is noted that the acoustic power coefficients based on acoustic potential amplitude are invariant to the direction of the flow.

In the case the amplitude coefficients are for acoustic pressure, the power coefficients can be obtained by making use of equation (64) which relates pressure amplitudes to acoustic potential amplitudes. The results are

$$P_{nn}^{++} = \frac{J_{nn}}{4\rho_r c_r}\left\{(1+M^2)\left(\frac{\frac{k_x^{++}}{\eta}}{1-M\frac{k_x^{++}}{\eta}}+\frac{\frac{k_x^{+}}{\eta}}{1-M\frac{k_x^{+}}{\eta}}\right)+2M\left(\frac{\frac{k_x^{++}}{\eta}}{1-M\frac{k_x^{++}}{\eta}}\right)\left(\frac{\frac{k_x^{+}}{\eta}}{1-M\frac{k_x^{+}}{\eta}}\right)+2M\right\} \tag{86a}$$

$$P_{nn}^{--} = \frac{J_{nn}}{4\rho_r c_r}\left\{(1+M^2)\left(\frac{\frac{k_x^{--}}{\eta}}{1-M\frac{k_x^{--}}{\eta}}+\frac{\frac{k_x^{-}}{\eta}}{1-M\frac{k_x^{-}}{\eta}}\right)+2M\left(\frac{\frac{k_x^{--}}{\eta}}{1-M\frac{k_x^{--}}{\eta}}\right)\left(\frac{\frac{k_x^{-}}{\eta}}{1-M\frac{k_x^{-}}{\eta}}\right)+2M\right\} \tag{86b}$$

$$P_{nn}^{+-} = \frac{J_{nn}}{4\rho_r c_r}\left\{(1+M^2)\left(\frac{\frac{k_x^{+*}}{\eta}}{1-M\frac{k_x^{+*}}{\eta}}+\frac{\frac{k_x^{-}}{\eta}}{1-M\frac{k_x^{-}}{\eta}}\right)+2M\left(\frac{\frac{k_x^{+*}}{\eta}}{1-M\frac{k_x^{+*}}{\eta}}\right)\left(\frac{\frac{k_x^{-}}{\eta}}{1-M\frac{k_x^{-}}{\eta}}\right)+2M\right\} \tag{86c}$$

$$P_{nn}^{-+} = \frac{J_{nn}}{4\rho_r c_r}\left\{(1+M^2)\left(\frac{\frac{k_x^{-*}}{\eta}}{1-M\frac{k_x^{-*}}{\eta}}+\frac{\frac{k_x^{+}}{\eta}}{1-M\frac{k_x^{+}}{\eta}}\right)+2M\left(\frac{\frac{k_x^{-*}}{\eta}}{1-M\frac{k_x^{-*}}{\eta}}\right)\left(\frac{\frac{k_x^{+}}{\eta}}{1-M\frac{k_x^{+}}{\eta}}\right)+2M\right\}$$

(86d)

The conclusions drawn from this formulation in terms of acoustic pressure amplitude coefficients are similar to those obtained from the acoustic potential form. The acoustic power coefficients for the case of cut on modes are

$$P_{nn}^{++} = \frac{1}{2\rho_r c_r} J_{nn} \frac{1}{(1-M\frac{k_x^{+}}{\eta})^2}\sqrt{1-(1-M^2)(\frac{\kappa\sigma}{\kappa\eta})^2}$$

$$P_{nn}^{--} = -\frac{1}{2\rho_r c_r} J_{nn} \frac{1}{(1-M\frac{k_x^{-}}{\eta})^2}\sqrt{1-(1-M^2)(\frac{\kappa\sigma}{\kappa\eta})^2}$$

$$P_{nn}^{+-} = -P_{nn}^{-+} = 0$$

(87)

For modes which are cut off, the acoustic power coefficients are

$$P_{nn}^{++} = P_{nn}^{++} = 0$$

$$P_{nn}^{+-} = \frac{i}{2\rho_r c_r} J_{nn} \frac{1}{(1-M\frac{k_x^{-}}{\eta})^2}\sqrt{(1-M^2)(\frac{\kappa\sigma}{\kappa\eta})^2-1}$$

$$P_{nn}^{+-} = -\frac{i}{2\rho_r c_r} J_{nn} \frac{1}{(1 - M\frac{k_x^+}{\eta})^2} \sqrt{(1 - M^2)(\frac{\kappa\sigma}{\kappa\eta})^2 - 1} \tag{88}$$

The power coefficients in terms of acoustic pressure amplitudes depend on the direction of the mean flow, but conclusions drawn about the vanishing or non-vanishing of the power coefficients for cut on and cut off modes are the same as in the case of acoustic potential amplitudes.

The common result of both formulations is that elements of the diagonal blocks of the power matrix vanish for cut off modes and elements of the off-diagonal blocks vanish for cut on modes. For cut on modes there is no power contribution due to interaction of positive and negative propagating modes. For cut off modes there is no power contribution due to individual positive and negative modes but there is power due to the interaction of positive and negative modes.

Acoustic power at $x = 0$ is written in terms of the power matrix and the amplitude coefficients (either potential or pressure formulation)

$$\begin{aligned}\Pi_0 = &\{a^{*+}\}^T [P_{nn}^{++}{}_0] \{a^+\} + \{a^{*+}\}^T [P_{nn}^{+-}{}_0] \{a^-\} \\ &+ \{a^{*-}\}^T [P_{nn}^{-+}{}_0] \{a^+\} + \{a^{*-}\}^T [P_{nn}^{--}{}_0] \{a^-\}\end{aligned} \tag{89}$$

With the source considered to be at $x = 0$, the reflection matrix can be used to replace reflected modal amplitudes to yield

$$\Pi_0 = \{a^{*+}\}^T [P^{++}_{nn\,0}] \{a^{+}\} + \{a^{*+}\}^T [P^{+-}_{nn\,0}] [R_2] \{a^{+}\}$$

$$+ \{a^{*+}\}^T [R_2^*]^T [P^{-+}_{nn\,0}] \{a^{+}\} + \{a^{*+}\}^T [R_2^*]^T [P^{--}_{nn\,0}] [R_2] \{a^{+}\} \tag{90}$$

This result requires interpretation. If only cut on modes are included among the incident modes a^+ then there is no interaction power and the net power is accounted for by the sum of incident power and reflected power, represented by the first and last terms. If among the incident modes there are ones which are cut off, then there is an additional component of net power due to interaction of incident and reflected cutoff modes, represented by the middle two terms. In this case the net power is not conveniently partitioned between incident and reflected contributions.

Acoustic power at the exit end of the duct, $x = L$, is similarly written in terms of modal amplitudes

$$\Pi_L = \{b^{*+}\}^T [P^{++}_{nn\,L}] \{b^{+}\} \tag{91}$$

The termination is assumed to be reflection free, so only right modes are present. The modal amplitudes are related to the source modal amplitudes via the transmission matrix. This yields.

$$\Pi_L = \{a^{*+}\}^T [T_1^*]^T [P^{++}_{nn\,L}] [T_1] \{a^{+}\} \tag{92}$$

The form of equations (89)-(92) is the same in direct or reverse flow, however for multi-modal propagation no simple relation between acoustic power in nominal and reversed flow appears to exist, nor is there a simple relation when the source location is reversed. As will be shown in a companion paper, there are simple relationships for power under flow reversal and source reversal for a one dimensional model of propagation valid at low frequencies.

For a rigid wall duct energy conservation requires that $\Pi_L = \Pi_0$. For an acoustically treated duct a metric for performance of the lining is the transmission loss defined by

$$TL = 20 \log_{10} \frac{\Pi_L}{\Pi_0} \tag{93}$$

The presence of possible mode interaction power somewhat complicates the traditional definition of transmission loss, and there could also be an argument for replacing Π_0 with only the first term in equation (90), this being the incident power.

CONCLUSION

A reverse flow theorem for acoustic propagation in compressible potential flow has been obtained directly from the field equations without recourse to energy conservation arguments. A reciprocity theorem for the scattering matrix for propagation of acoustic modes in a duct with either hard walls, or a section of locally reacting absorbing wall imbedded in an otherwise hard wall, follows. It is found that for a source at a specific end of the duct, suitably scaled reflection matrices in direct and reverse flow have a reciprocal relationship. Scaled transmission matrices obtained for direct flow and reversed flow with simultaneous switching of source location from one end to the other also have a reciprocal relationship.

The approach presented here is an alternative to the approach of Moehring [3,16], with the distinction that no energy conservation condition is used. It has been exploited to provide explicit reciprocal relations which are of theoretical interest, but which also have the more pragmatic significance of providing a convenient means for benchmarking large scale propagation codes such as those used in this investigation.

Numerical verification of the reciprocal relationships is the subject of a companion paper.

REFERENCES

1. A. D. Pierce 1981 Acoustics:an Introduction to its Physical Princilples and Applications, Mc-Graw-Hill, 195-198.

2. W. Eversman 1979 Journal of Sound and Vibration 47(4), 515-521. A reciprocity relationship for transmission in non-uniform hard walled ducts without flow.

3. W. Moehring 1978 Journal of the Acoustical Society of America 64(4), 1186-1189. Acoustic energy flux in nonhomogeneous ducts.

4. C. L. Morfey 1971 Journal of Sound and Vibration 14, 159-170. Acoustic energy in non-uniform flows.

5. O. A. Godin 1997 Wave Motion 25(2), 143-167. Reciprocity and energy theorems for waves in a compressible inhomogeneous moving fluid.

6. O. A. Godin 1997 Acoustical Physics 43(6), 688-693. Reciprocity and energy conservation for waves in the system:inhomogeneous fluid flow-anisotropic solid body.

7. A. H. Flax 1952 Journal of the Aeronautical Sciences 19(6), 361-374. General reverse flow and variational theorems for lifting surfaces in nonstationary compresible flow

8. A. H. Flax 1953 Journal of the Aeronautical Sciences 20(2), 120-126. Reverse flow and variational theorems for lifting surfaces in nonstationary compressible flow.

9. W. Eversman 2000 Journal of Sound and Vibration. Numerical experiments on acoustic reciprocity in compressible potential flows. (In review).

10. W. Eversman 2000 Journal of Sound and Vibration. Simplification of the boundary condition at an impedance wall in a nonuniform duct with compressible potential mean flow. (In review)

11. L. M. B. C. Campos 1986 Journal of Sound and Vibration 110(1), 41-47. On linear and non-linear wave equations for the acoustics of high speed potential flows.

12. L. M. B. C. Campos 1987 Journal of Sound and Vibration 117(1), 131-151. On longitudinal

acoustic propagation in convergent and divergent nozzle flows.

13. L. M. B. C. Campos 1996 Journal of Sound and Vibration 196(5), 611-633. On the acoustics of low mach number bulged, throated and baffled nozzles.

14. I. Danda Roy and W. Eversman 1995 ASME Journal of Vibration and Acoustics 117(1), January, 1995, 109-115. Improved finite element modeling of the turbofan engine inlet radiation problem.

15. M. K. Myers 1980 Journal of Sound and Vibration 71(3),429-434. On the acoustic boundary condition in the presence of flow.

16. W. Moehring 2000 Journal of Fluid Mechanics (in review), Energy conservation, time reversal invariance and reciprocity in ducts with flow.

17. J. Rebel and D. Ronneberger 1992 Journal of Sound and Vibration 158, 469-496. The effect of shear stress on the propagation and scattering of sound in flow ducts.

18. W. Eversman 1991 NASA Reference Publication 1258. Aeroacoustics of Flight Vehicles: Theory and Practice, Volume 2: Noise Control, 101-163. Theoretical Models for Duct Acoustic Propagation and Radiation.

19. W. Eversman 1979 Journal of Sound and Vibration 62(4), 517-532. Acoustic energy in ducts: further observations.

20. O. S. Ryshov and G. M. Shefter 1962 Journal of Applied Mathematics and Mechanics 26, 1293-1309. On the energy of acoustic waves propagating in moving media.

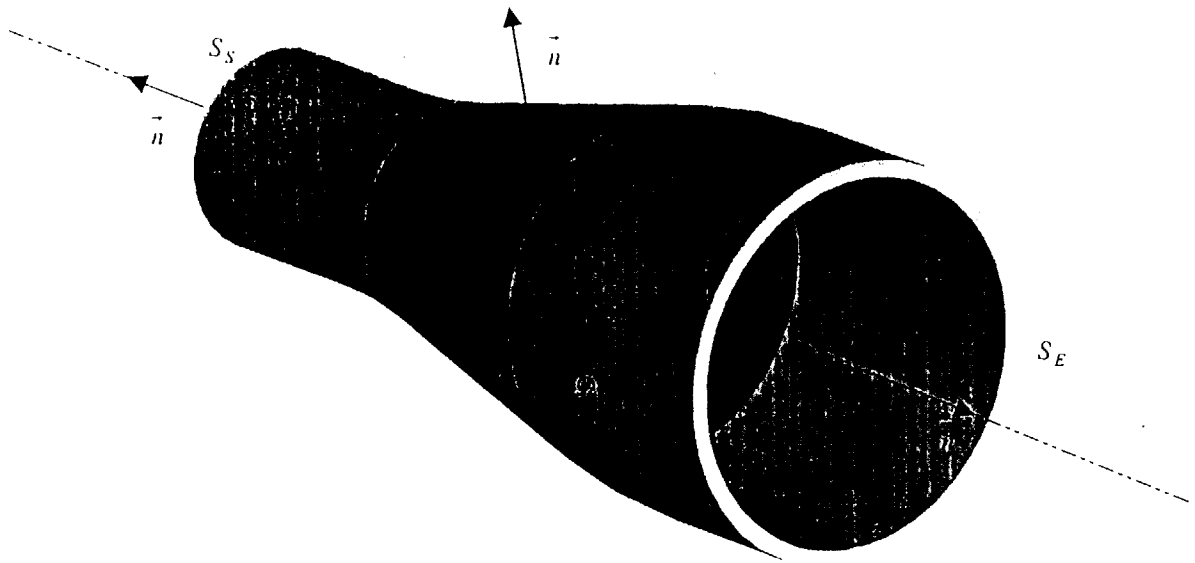

Figure 1. A general duct configuration showing volume and surface important in the development.

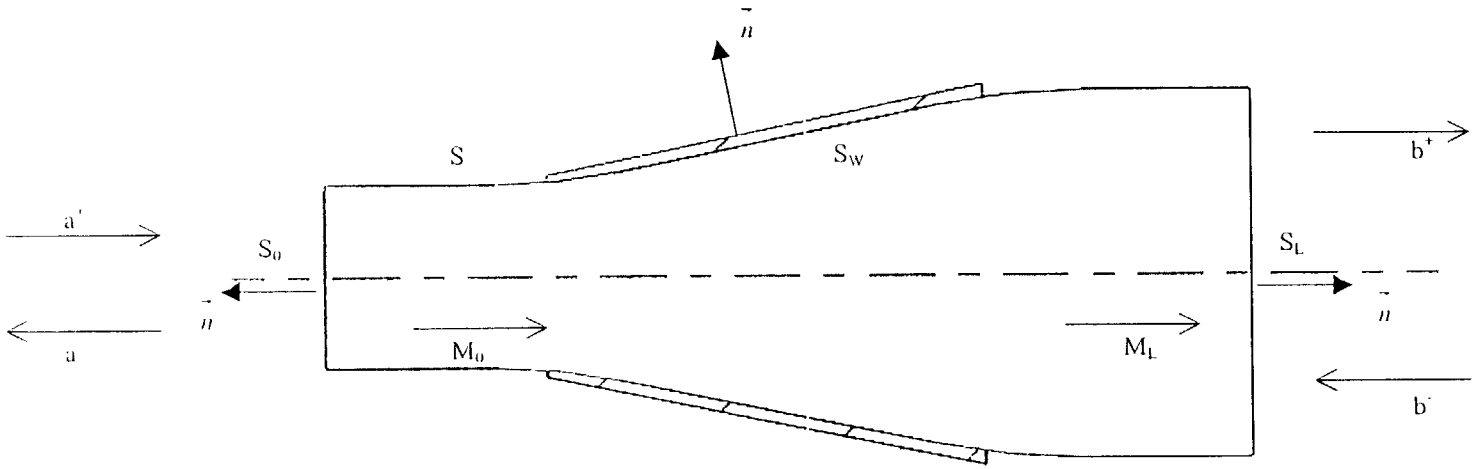

Figure 2. A duct configuration showing uniform extensions and appropriate surface normals.

RECIPROCITY AND ACOUSTIC POWER IN ONE DIMENSIONAL COMPRESSIBLE POTENTIAL FLOWS

Walter Eversman
Mechanical and Aerospace Engineering
and Engineering Mechanics
University of Missouri-Rolla
Rolla, MO 65401

ABSTRACT

A reverse flow theorem for one dimensional acoustic propagation in compressible potential flow has been obtained directly from the field equations without recourse to energy conservation arguments. Reciprocity relationships for the scattering coefficients for propagation are derived. It is found that for a source at a specific end of the duct, suitably scaled reflection coefficients in direct and reverse flow have a reciprocal relationship. Scaled transmission coefficients obtained for direct flow and reversed flow with simultaneous switching of source location from one end to the other also have a reciprocal relationship. Reciprocal relations and power conservation arguments are used to show that scaled power reflection and transmission coefficients are invariant to flow reversal and switching of source location from one end of the duct to the other. Numerical verification of the reciprocal relationships is given in a companion paper in which multiple mode propagation and one dimensional propagation are considered

INTRODUCTION

In a companion paper [1] an acoustic reciprocity theorem in a compressible potential flow in non-uniform ducts has been obtained directly from the field equations. It was shown that reciprocity holds for ducts with rigid walls and for ducts with a finite length dissipative lining imbedded in an otherwise rigid wall. In the present investigation the methodology of [1] is applied to the simpler case of one dimensional propagation, valid for low frequencies, that is large wave length to geometric cross section dimension ratio. The principal simplification is that

acoustic treatment is no longer a possibility within the acoustic formulation. The energy formulation of Moehring [2,3] then becomes a straight forward option because dissipative linings and cut-off modes do not need to be considered. However, here the approach of [1] based directly on the field equations is used .

Aside from finding a reciprocity relationship, a goal here is to expand upon an invariance property for acoustic power transmission in converging-diverging ducts found by Davis [4]. This turns out to be a result of reciprocity and energy conservation.

In another companion paper [5], the reciprocity relations found in [1] and in the present paper are substantiated by numerical experiments based on a finite element simulation.

RECIPROCITY IN ONE-DIMENSIONAL FLOW

In some cases it is possible to use a one-dimensional approximation for steady flow and acoustic perturbations. A reverse flow reciprocity relationship can be obtained in this case using the method of [1]. Figure 1 shows the duct under consideration, which is in fact three dimensional, but it is assumed that the large wave length limit exists so that acoustic propagation is one dimensional at each cross section. Furthermore, the duct shape is restricted so that the mean flow at a cross section can also be treated as one dimensional. The cross sectional shape of the duct is not a consideration in this one dimensional approximation. The one-dimensional acoustic continuity equation is

$$A\frac{\partial \rho}{\partial t} + \nabla\cdot(\rho_r A\frac{\partial \phi}{\partial x} + \rho A\frac{\partial \phi_r}{\partial x}) = 0 \tag{1}$$

where A is the local cross sectional area of the duct. The one-dimensional acoustic momentum equation is

$$\rho = -\frac{\rho_r}{c_r^2}(i\eta_r\phi + M_r\frac{\partial \phi}{\partial x}) \tag{2}$$

or

$$p = -\rho_r (i\eta_r \phi + M_r \frac{\partial \phi}{\partial x}) \tag{3}$$

The steady flow is obtained from

$$\frac{\partial}{\partial x}(\rho_r A \frac{\partial \phi}{\partial x}) = 0 \tag{4}$$

and the relations between mean flow velocity and mean flow potential and acoustic particle velocity and acoustic potential are

$$M_r = \frac{\partial \phi_r}{\partial x} \tag{5}$$

$$u = \frac{\partial \phi}{\partial x} \tag{6}$$

The acoustic relationship between pressure and density is

$$p = c_r^2 \rho \tag{7}$$

Mean flow speed of sound is determined by

$$c_r^2 = 1 - \frac{(\gamma - 1)}{2}[\nabla \phi_r \cdot \nabla \phi_r - M_\infty^2] \tag{8}$$

and the mean flow density is

$$\rho_r = [1 - \frac{(\gamma - 1)}{2}(\nabla\phi_r \cdot \nabla\phi_r - M_\infty^2)]^{\frac{1}{\gamma - 1}} \tag{9}$$

Equations (1) and (9) are non-dimensional using the density ρ_∞ and the speed of sound c_∞ at some point, in this case the plane $x = 0$. Stagnation conditions could also serve as the reference. A reference length R is a (hypothetical) radius corresponding to a (circular) source "plane" at $x = 0$, the reference cross sectional area. Acoustic potential is non-dimensional with respect to $c_\infty R$, and the acoustic pressure with respect to $\rho_\infty c_\infty^2$. Lengths are made non-dimensional with respect to R. Time is scaled with R/c_∞. In the case of harmonic time dependence this leads to the definition of non-dimensional frequency $\eta_r = \omega R/c_\infty$. ω is the dimensional source frequency. M_∞ is the Mach number at the reference point. With this convention, the reference non-dimensional frequency η_r and the local non-dimensional frequency η are defined as in [1] where the restriction of one dimensional propagation is not invoked. Non-dimensionalization described here differs from the usual one dimensional development in which some characteristic duct length is generally used as a reference length. The convention used here makes everything consistent with [1], in particular the non-dimensional frequency η_r.

Consider the duct shown in Figure 2, which is locally of arbitrary cross section, and is terminated on each end by a section of uniform duct, of length sufficient to assure uniform mean flow and propagation in terms of acoustic modes. The source plane $x = 0$ is where the acoustic source is specified and the exit plane $x = L$ terminates the duct. For computations the exit plane will be assumed non-reflecting. In general, a typical computational problem would seek to specify the acoustic field within the duct and the scattering matrix at the source plane for incident acoustic modes. Figure 2, originally presented in support of the discussion in [1], can be used here to highlight the one dimensional approximation. It is assumed that the mean flow is everywhere described in terms of the axial coordinate x so that in the nonuniform section $M(x,r) = M(x)$. Acoustic propagation is assumed to also depend only on the axial coordinate, so that it is locally planar. The duct walls do not provide a boundary condition in the one-dimensional approximation so that the unit normal $\vec{n}$ there plays no role. The unit normal on the

terminating planes is axially directed. Equations (1) through (9) specify the acoustic field in the duct of Figure 2 subject to the restrictions noted.

Let $\phi_1 e^{i\eta_r t}$ be a harmonic solution for the acoustic velocity potential for the case of a mean flow specified everywhere in the duct by its reference Mach number $\vec{M}_r = \nabla\phi_r$ and with specified boundary conditions. Let $\phi_2 e^{i\eta_r t}$ be a second harmonic solution for exactly the same duct with different source conditions, but with the flow reversed, $-\vec{M}_r = -\nabla\phi_r$. It is important to note that in reversed flow the reference density ρ_r and reference speed of sound c_r are unaltered. Because of equation (1), in the case of a harmonic source at non-dimensional frequency η_r, it follows that

$$\int \{\phi_2[i\eta_r A\rho_1 + \nabla\cdot(\rho_r A\nabla\phi_1 + \vec{M}_r A\rho_1)] - \phi_1[i\eta_r A\rho_2 + \nabla\cdot(\rho_r A\nabla\phi_2 - \vec{M}_r A\rho_2)]\}dx = 0 \tag{10}$$

Here, for ease of notation, and for a degree of similarity with [1], the gradient operator is used to denote

$$\nabla = \frac{\partial}{\partial x}\vec{e}_x \tag{11}$$

and

$$\vec{M}_r = M_r\vec{e}_x \tag{12}$$

with $\vec{e}_x$ the unit vector in the x direction. With application integration by parts, which is equivalent to the divergence theorem in [1], and by using equation (2) to partially replace ρ_1 and ρ_2, and to subsequently eliminate the remaining integral on x, equation (12) is reduced to

$$[\phi_2(\rho_r A\frac{\partial\phi_1}{\partial x} + M_r A\rho_1) - \phi_1(\rho_r A\frac{\partial\phi_2}{\partial x} - M_r A\rho_2)]_0^L = 0 \tag{13}$$

When this is written entirely in terms of acoustic potential the result is

$$[\,A\rho_r\{\phi_2[(1-M^2)\frac{\partial\phi_1}{\partial x} - i\eta M\phi_1] - \phi_1[(1-M^2)\frac{\partial\phi_2}{\partial x} + i\eta M\phi_2]\}\,]_0^L = 0 \qquad (14)$$

In [1], eigenfunction expansions are used to define the acoustic potential field in the uniform flow regions at $x = 0$ and $x = L$. This is still appropriate, with the simplification that only the plane waves propagate, and no analysis is required to determine the modes and wave numbers.

There is one "mode" propagating in each direction in the uniform duct sections, so that there is only a superposition of a right and left wave, given for example here for the nominal flow solution at $x = 0$ in the form [1]

$$\phi_1 = a_1^+ + a_1^- \qquad (15)$$

$$\frac{\partial\phi_1}{\partial x} = (-ik_{x_1}^+)\,a_1^+ + (-ik_{x_1}^-)\,a_1^- \qquad (16)$$

The axial wave numbers are

$$\left(\frac{k_{x_{mn}}^{\pm}}{\eta}\right)_1 = \frac{1}{1-M^2}(-M \pm 1) \qquad (17)$$

$$\left(\frac{k_{x_{mn}}^{\pm}}{\eta}\right)_2 = \frac{1}{1-M^2}(M \pm 1) \qquad (18)$$

The superscript choice $\pm$ corresponds to right and left waves. η and M represent local values of non-dimensional frequency and Mach number determined by the local speed of sound, with η still based on the reference length. The operator arising in equation (14)

$$L\{\phi\} = (1 - M^2)\frac{\partial \phi}{\partial x} - i\eta M\phi = \alpha\,\phi \tag{19}$$

introduces the parameters α^+ and α^- corresponding to right and left waves, for example at $x = 0$,

$$\alpha^+_1 = \rho_r[-i(1 - M^2)k^+_{x_1} - i\eta M] = -i\rho_r\eta \tag{20}$$

$$\alpha^-_1 = \rho_r[-i(1 - M^2)k^-_x - i\eta M] = i\rho_r\eta \tag{21}$$

Similar expressions exist for $\alpha^{\pm}_2$, in reversed flow. It is noted that $\alpha^+_2 = \alpha^+_1 = \alpha$ and $\alpha^-_2 = \alpha^-_1 = -\alpha$. α is evaluated at the ends $x = 0$ and $x = L$ as required.

With these definitions, equation (14) can be rearranged in a matrix form [1] ,

$$\begin{Bmatrix} a^-_1 \\ b^+_1 \end{Bmatrix}^T \begin{bmatrix} A_0\,\alpha_0 & \\ & A_L\,\alpha_L \end{bmatrix} \begin{Bmatrix} a^+_2 \\ b^-_2 \end{Bmatrix} = \begin{Bmatrix} a^-_2 \\ b^+_2 \end{Bmatrix}^T \begin{bmatrix} A_0\,\alpha_0 & \\ & A_L\,\alpha_L \end{bmatrix} \begin{Bmatrix} a^+_1 \\ b^-_1 \end{Bmatrix} \tag{22}$$

Modal amplitudes a^+_n and a^-_n and b^+_n and b^-_n , acoustic potential wave amplitudes at $x = 0$ and $x = L$, are related by the acoustic potential scattering matrix according to

$$\begin{Bmatrix} a^- \\ b^+ \end{Bmatrix} = [S] \begin{Bmatrix} a^+ \\ b^- \end{Bmatrix} \tag{23}$$

where the scattering matrix is defined as

$$[S] = \begin{bmatrix} R & \tilde{T} \\ T & \tilde{R} \end{bmatrix} \tag{24}$$

R and T are the reflection and transmission coefficients for a source at $x = 0$ with a reflection free termination at $x = L$. $\tilde{R}$ and $\tilde{T}$ are reflection and transmission coefficients for a source at $x = L$ and reflection free at $x = 0$. There will be a scattering matrix $[S_1]$ for nominal mean flow and a second one $[S_2]$ for reversed flow. Equations (23) and (24) can be used in equation (22) to obtain

$$\begin{Bmatrix} a_1^+ \\ \\ b_1^- \end{Bmatrix}^T [S_1]^T [A][\alpha] \begin{Bmatrix} a_2^+ \\ \\ b_2^- \end{Bmatrix} = \begin{Bmatrix} a_2^+ \\ \\ b_2^- \end{Bmatrix}^T [S_2]^T [A][\alpha] \begin{Bmatrix} a_1^+ \\ \\ b_1^- \end{Bmatrix} \tag{25}$$

where the definition

$$\begin{bmatrix} A_0\alpha_0 & & \\ & & \\ & & A_L\alpha_L \end{bmatrix} = [A][\alpha] \tag{26}$$

is introduced. The scattering matrices for nominal and reversed flow are $[S_1]$ and $[S_2]$. The implications of equation (26) are summarized by the reciprocity relations

$$([S_1]^T [A][\alpha]) = [A][\alpha][S_2] \tag{27}$$

and

$$[A][\alpha][S_1] = ([A][\alpha][S_2])^T \tag{28}$$

Equation (27) and (28) are used to establish the following relationships for the acoustic potential reflection and transmission coefficients:

$$R_1 = R_2 \tag{29}$$

$$\tilde{R}_1 = \tilde{R}_2 \tag{30}$$

$$\tilde{T}_2 A_0 \alpha_0 = T_1 A_L \alpha_L \tag{31}$$

$$\tilde{T}_1 A_0 \alpha_0 = T_2 A_L \alpha_L \tag{32}$$

By using the definitions of α_0 and α_L Defined by equations (20) and (21) evaluated at $x = 0$ and $x = L$, equations (31) and (32) are written

$$T_1 = \frac{A_0}{A_L} \frac{\rho_{r_L}}{\rho_{r_0}} \frac{c_{r_L}}{c_{r_0}} \left(\frac{\rho_{r_0}}{\rho_{r_L}} \right)^2 \tilde{T}_2 \tag{33}$$

$$T_2 = \frac{A_0}{A_L} \frac{\rho_{r_L}}{\rho_{r_0}} \frac{c_{r_L}}{c_{r_0}} \left(\frac{\rho_{r_0}}{\rho_{r_L}} \right)^2 \tilde{T}_1 \tag{34}$$

Equations (29) and (30) produce the interesting result that the acoustic potential reflection coefficients, at the left end and at the right end are invariant to flow direction. No reciprocal relationships link the left to right transmission coefficients T_1 and T_2 or the right to left transmission coefficients $\tilde{T}_1$ and $\tilde{T}_2$ in nominal flow and reversed flow. Equation (33) links the left to right transmission coefficient T_1 in nominal flow to the right to left transmission coefficient $\tilde{T}_2$ in reversed flow. Equation (34) links the left to right transmission coefficient in reversed flow T_2 to the right to left transmission coefficient $\tilde{T}_1$ in nominal flow.

The reciprocal results of equations (29)-(32) are for acoustic potential modal amplitudes. In the case of acoustic pressure modal amplitudes a transition to acoustic potential modal amplitudes is made through equation (3). The transformations from acoustic potential to acoustic pressure for right and left waves in nomnal and reversed flow are

$$\phi^+_1 = \beta^+ p_1^+ \quad , \qquad \phi^-_1 = \beta^- p_1^- \tag{35}$$

$$\phi^+_2 = \beta^- p_2^+ \quad , \qquad \phi^-_2 = \beta^+ p_2^- \tag{36}$$

where

$$\beta^{+} = \frac{1 + M}{-i\eta\rho_r c_r} \quad , \quad \beta^{-} = \frac{1 - M}{-i\eta\rho_r c_r} \tag{37}$$

Mach number and non-dimensional frequency are based on the local speed of sound. Non-dimensional frequency is still based on the reference length. Non-dimensional density and non-dimensional speed of sound are evaluated locally.

Equations (35) and (36) are used to introduce pressure modal amplitudes in equation (22). The scattering matrix is now in terms of pressure scattering coefficients

$$[\bar{S}] = \begin{bmatrix} \bar{R} & \bar{\tilde{T}} \\ \bar{T} & \bar{\tilde{R}} \end{bmatrix} \tag{38}$$

After following the same steps leading to equations (29)-(32), reciprocity relations for acoustic pressure scattering coefficients are found to be

$$\bar{R}_1 A_0 \alpha_0 \frac{\beta^{-}_0}{\beta^{+}_0} = \bar{R}_2 A_0 \alpha_0 \frac{\beta^{-}_0}{\beta^{-}_0} \qquad or \qquad \bar{R}_1 = \frac{(1 + M_0)^2}{(1 - M_0)^2} \bar{R}_2 \tag{39}$$

$$\bar{\tilde{R}}_1 A_L \alpha_L \frac{\beta^{+}_L}{\beta^{-}_L} = \bar{\tilde{R}}_2 A_L \alpha_L \frac{\beta^{-}_L}{\beta^{+}_L} \qquad or \qquad \bar{\tilde{R}}_1 = \frac{(1 - M_L)^2}{(1 + M_L)^2} \bar{\tilde{R}}_2 \tag{40}$$

$$\bar{T}_1 A_L \alpha_L \frac{\beta^{+}_L}{\beta^{+}_0} = \bar{\tilde{T}}_2 A_0 \alpha_0 \frac{\beta^{+}_0}{\beta^{+}_L} \qquad or \qquad \bar{T}_1 = \frac{A_0}{A_L} \frac{\rho_{r_o}}{\rho_{r_n}} \frac{c_{r_o}}{c_{r_n}} \frac{(1 + M_0)^2}{(1 + M_L)^2} \bar{\tilde{T}}_2 \tag{41}$$

$$\overline{\tilde{T}}_1 A_0 \alpha_0 \frac{\beta^-_0}{\beta^-_L} = \overline{T}_2 A_L \alpha_L \frac{\beta^-_L}{\beta^+_L} \qquad or \qquad \overline{T}_2 = \frac{A_0}{A_L} \frac{\rho_{r_0}}{\rho_{r_\eta}} \frac{c_{r_0}}{c_{r_\eta}} \frac{(1 - M_0)^2}{(1 - M_L)^2} \overline{\tilde{T}}_1 \tag{42}$$

Equations (39)-(42) are written both implicitly in terms of coefficients defined above and explicitly in terms of local area and flow conditions. The mach number is for the nominal flow.

Pressure reflection coefficients are not invariant in reversed flow but are reciprocally related as given by equations (39) and (40). No reciprocal relationships link the left to right transmission coefficients $\overline{T}_1$ and $\overline{T}_2$ or the right to left transmission coefficients $\overline{\tilde{T}}_1$ and $\overline{\tilde{T}}_2$ in nominal flow and reversed flow. Equation (41) links the left to right transmission coefficient $\overline{T}_1$ in nominal flow to the right to left transmission coefficient $\overline{\tilde{T}}_2$ in reversed flow. Equation (42) links the left to right transmission coefficient in reversed flow $\overline{T}_2$ to the right to left transmission coefficient $\overline{\tilde{T}}_1$ in nominal flow.

ACOUSTIC POWER CONSIDERATIONS

In the case of one dimensional propagation, additional results can be obtained by the consideration of acoustic power. The definition of acoustic intensity due to Morfey [6] is valid as part of a conservation law in non-uniform ducts for compressible potential flow. This definition of acoustic intensity is used in the uniform flow sections on either end of the nonuniformity to obtain acoustic power expressions.

For propagation in uniform flow the Morfey intensity formulation simplifies to the scalar form

$$\frac{I}{\rho_\infty c_\infty^3} = \left\langle (1 + M^2) pu + \rho_r c_r M u^2 + \frac{1}{\rho_r c_r} M p^2 \right\rangle \tag{44}$$

Acoustic power is obtained by integration over a cross section, to yield

$$\frac{P}{A_{ref}\rho_\infty c_\infty^3} = \iint_S \left\langle (1+M^2)pu + \rho_r c_r Mu^2 + \frac{1}{\rho_r c_r} Mp^2 \right\rangle dS \tag{45}$$

A modal expansion as given by equations (26) and (27) is used to obtain an acoustic power in terms of acoustic potential modal amplitudes. The result is

$$\frac{P}{A_{ref}\rho_\infty c_\infty^3} = a^{+*} P_{11}^{++} a^{+} + a^{-*} P_{11}^{--} a^{-} \tag{46}$$

where, for example, a^{+*} denotes the complex conjugate of a. Power can be represented in terms of acoustic potential amplitudes as in equation (46) in uniform duct sections at $x = 0$ and $x = L$. The power coefficients P_{11}^{++} and P_{11}^{--} are one dimensional analogs of power matrices introduced in [1]. No acoustic power is attributed to the interaction of acoustic modes because there are no cut-off modes in this one dimensional model. The power coefficients can be easily obtained by using the results for the plane wave mode from the general expressions of [1],

$$P_{11}^{++} = \frac{1}{2}\rho_{r_\eta} c_{r_\eta} \eta_0^2 A_0 \quad , \quad P_{11}^{--} = -\frac{1}{2}\rho_{r_\eta} c_{r_\eta} \eta_0^2 A_0 \tag{47}$$

Energy conservation arguments lead to the conclusion that $\Pi_{inc} + \Pi_{ref} = \Pi_{trans}$. This is the traditional result, simplified from the result of [1] because of the absence of interaction power associated with cut-off modes. Incident power at $x = 0$ is given by

$$\Pi_{inc} = a^{+*} R_1^* P_{11}{}_0^{++} R_1 a^{+}$$

Reflected power in nominal and reversed flow at $x = 0$ is given by

$$\Pi_{ref} = a^{+*} R_1^* P_{11}{}_0^{--} R_1 a^{+} \quad , \quad \Pi_{ref} = a^{+*} R_2^* P_{11}{}_0^{--} R_2 a^{+} \tag{48}$$

Transmitted power in nominal and reversed flow $x = L$ is given by

$$\Pi_{trans} = a^{+^*} T_1^* P_{11}^{++}{}_L T_1 a^+ \quad , \quad \Pi_{trans} = a^{+^*} T_2^* P_{11}^{++}{}_L T_2 a^+ \tag{48}$$

Subscripts on the power coefficients denote the uniform section in which they are evaluated. From equation (29) $R_1 = R_2$, that is, the acoustic potential reflection coefficient is invariant to flow direction, as is P_{11}. Therefore, the power reflection coefficient defined by either

$$R_{\pi_\theta} = \frac{R_1^* P_{11_\eta} R_1}{P_{11_\eta}} = |R_1|^2 \quad or \quad R_{\pi_\theta} = \frac{R_2^* P_{11_\eta} R_2}{P_{11_\eta}} = |R_2|^2 \tag{49}$$

The power reflection coefficient is invariant to flow direction, $R_{\pi_\theta} = R_{\pi_\theta}$. It is concluded that the power transmission coefficient are also invariant to flow direction, $T_{\pi_\theta} = T_{\pi_\theta}$. A similar development based on equation (30) would show that $\tilde{R}_{\pi_\theta} = \tilde{R}_{\pi_\theta}$ and therefore that $\tilde{T}_{\pi_\theta} = \tilde{T}_{\pi_\theta}$.

It is now possible to connect the power transmission coefficients when the source is moved from one end of the duct to the other. For a source at $x = 0$ the power transmission coefficient (the ratio of transmitted to incident power) is in nominal flow

$$T_{\pi_\theta} = \frac{P_{11_\upsilon}}{P_{11_\eta}} |T_1|^2 = \frac{\rho_{r_\upsilon}}{\rho_{r_\eta}} \frac{c_{r_\eta}}{c_{r_\upsilon}} \frac{A_L}{A_0} |T_1|^2 \tag{50}$$

For a source at $x = L$ in reverse flow the power transmission coefficient is defined for right to left power according to

$$\tilde{T}_{\pi_\theta} = \frac{\tilde{T}_2^* P_{11_\eta} \tilde{T}_2}{P_{11_\upsilon}} = \frac{P_{11_\eta}}{P_{11_\upsilon}} |\tilde{T}_2|^2 = \frac{\rho_{r_\eta}}{\rho_{r_\upsilon}} \frac{c_{r_\upsilon}}{c_{r_\eta}} \frac{A_0}{A_0} |\tilde{T}_2|^2 \tag{51}$$

Equations (50) and (51) are deduced by using the definitions of incident and transmitted power appropriately evaluated at $x = 0$ or $x = L$. The reciprocal relationship of equation (31) is used to replace $\tilde{T}_2$ in equation (51) yielding the result

$$\tilde{T}_{\pi_\theta} = \frac{\rho_{r_o}}{\rho_{r_n}} \frac{c_{r_n}}{c_{r_o}} \frac{A_L}{A_0} |T_1|^2 \tag{52}$$

It has thus been shown that $\tilde{T}_{\pi_\theta} = T_{\pi_\theta}$. It is therefore concluded that $T_{\pi_\theta} = T_{\pi_\theta} = \tilde{T}_{\pi_\theta} = \tilde{T}_{\pi_\theta}$ and thence from power conservation arguments that $R_{\pi_\theta} = R_{\pi_\theta} = \tilde{R}_{\pi_\theta} = \tilde{R}_{\pi_\theta}$. This completes the interesting result that for the one dimensional model power reflection and transmission coefficients are invariant to flow reversal and switching of the source location.

The result that $T_{\pi_\theta} = \tilde{T}_{\pi_\theta}$ states that the transmission coefficient for the nominal flow direction is the same from either end of the duct. This result contains the invariance theorem of Davis [4], but also admits a generalization. Davis found that for a converging-diverging non-uniformity in an otherwise uniform duct, for equal pressure amplitude input at the upstream and downstream ends of the duct, the transmitted power is related by

$$\frac{\Pi_1}{\tilde{\Pi}_1} = \frac{(1 + M)^2}{(1 - M)^2} \tag{53}$$

Here Π_1 is the transmitted power at the downstream end due to a source at the upstream end and $\tilde{\Pi}_1$ is the transmitted power at the upstream end due to a source at the downstream end, both in the nominal flow. Because the result of Davis is for a converging diverging duct, with both ends of the same area, $M_0 = M_L = M$.

By using equations (46) and (47), which define acoustic power in terms of acoustic potential amplitudes, and by modifying them using equations (35)-(37) to relate acoustic pressure amplitude to acoustic potential amplitude, the incident power at $x = 0$ is

$$\Pi_{inc}(x = 0) = \frac{1}{2}|p_0^+|^2 \frac{A_0}{\rho_{r_n} c_{r_n}} (1 + M_0)^2 \tag{54}$$

Similarly, for an acoustic pressure input at $x = L$, the incident power there is

$$\tilde{\Pi}_{inc}(x = L) = \frac{1}{2}|\tilde{p}_L^-|^2 \frac{A_L}{\rho_{r_u} c_{r_u}}(1 - M_L)^2 \tag{55}$$

p_0^+ and $\tilde{p}_L^-$ are pressure mode amplitudes incident at the ends $x = 0$ and $x = L$. Superscripts + and - reinforce the idea that at $x = 0$ the incident mode is a right running wave and at $x = L$ the incident mode is a left running wave. The tilde (~) reminds that the source is at the end $x = L$. By using the fact that the transmitted power in each case is the product of the incident power and the appropriate power transmission coefficient, which is the same for either case ($T_{\pi_\theta} = \tilde{T}_{\pi_\theta}$), and that the incident modal pressure amplitudes are the same for either source ($|p_0^+| = |\tilde{p}_L^-|$) , it follows that

$$\frac{\Pi_{trans}}{\tilde{\Pi}_{trans}} = \frac{A_0}{A_L}\frac{\rho_{r_u}}{\rho_{r_\eta}}\frac{c_{r_u}}{c_{r_\eta}}\frac{(1 + M_0)^2}{(1 - M_L)^2} \tag{56}$$

Equation (56) contains Davis' result [4] in the case of a converging diverging duct when the duct area, flow density, speed of sound and Mach number are the same at both ends. Other results are possible involving acoustic potential and acoustic pressure amplitudes from the core result that the power transmission coefficients are invariant.

CONCLUSION

A reverse flow theorem for acoustic propagation in one dimensional compressible potential flow has been obtained directly from the field equations without recourse to energy conservation arguments. A reciprocity theorem for the scattering coefficients for propagation of acoustic modes has been obtained. Reciprocal relations and power conservation arguments are used to show that scaled power reflection and transmission coefficients are invariant to flow reversal and switching of source location from one end of the duct to the other.

Numerical verification of the reciprocal relationships has been made using a finite element model for duct propagation, and is reported in a companion paper [5].

REFERENCES

1. W. Eversman 2000 Journal of Sound and Vibration (in review). A reverse flow theorem and acoustic reciprocity in compressible potential flows.

2. W. Moehring 1978 Journal of the Acoustical Society of America 64(4), 1186-1189. Acoustic energy flux in nonhomogeneous ducts.

3. W. Moehring 2000 Journal of Fluid Mechanics (in review). Energy conservation, time reversal invariance and reciprocity in ducts with flow. (In review).

4. S. S. Davis 1976 Journal of the Acoustical Society of America 59(2), 264-266. On an invariance property of acoustic waveguides.

5. W. Eversman 2000 Journal of Sound and Vibration (in review). Numerical experiments on acoustic reciprocity in compressible potential flows. (In review).

6. C. L. Morfey 1971 Journal of Sound and Vibration 14, 159-170. Acoustic energy in non-uniform flows.

7. W. Eversman 1979 Journal of Sound and Vibration 62(4), 517-532. Acoustic energy in ducts: further observations.

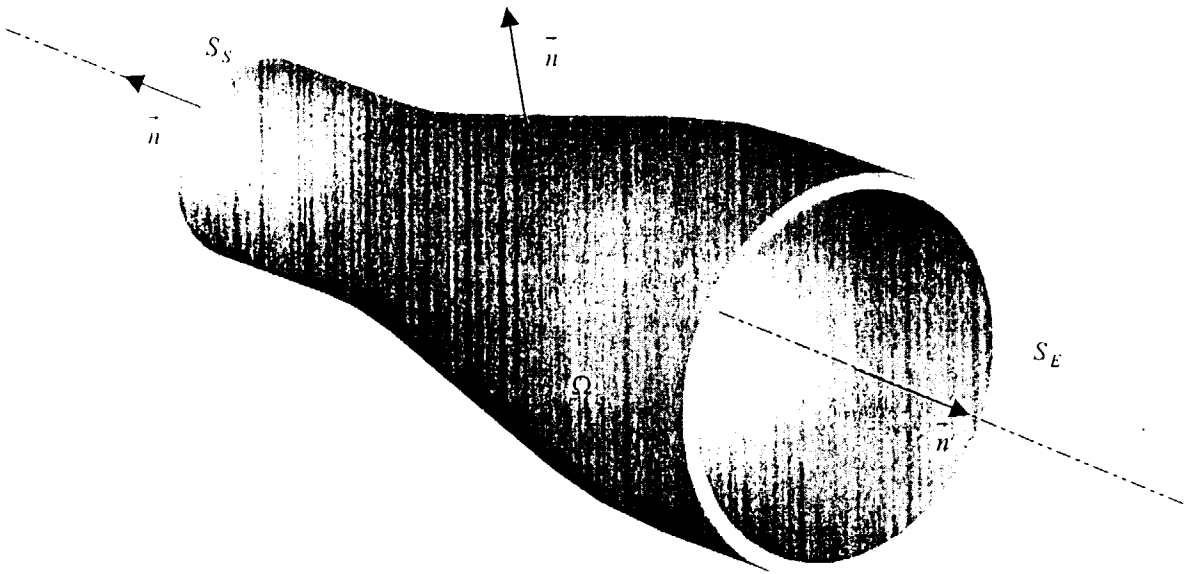

Figure 1. A general duct configuration suitable for one dimensional analysis.

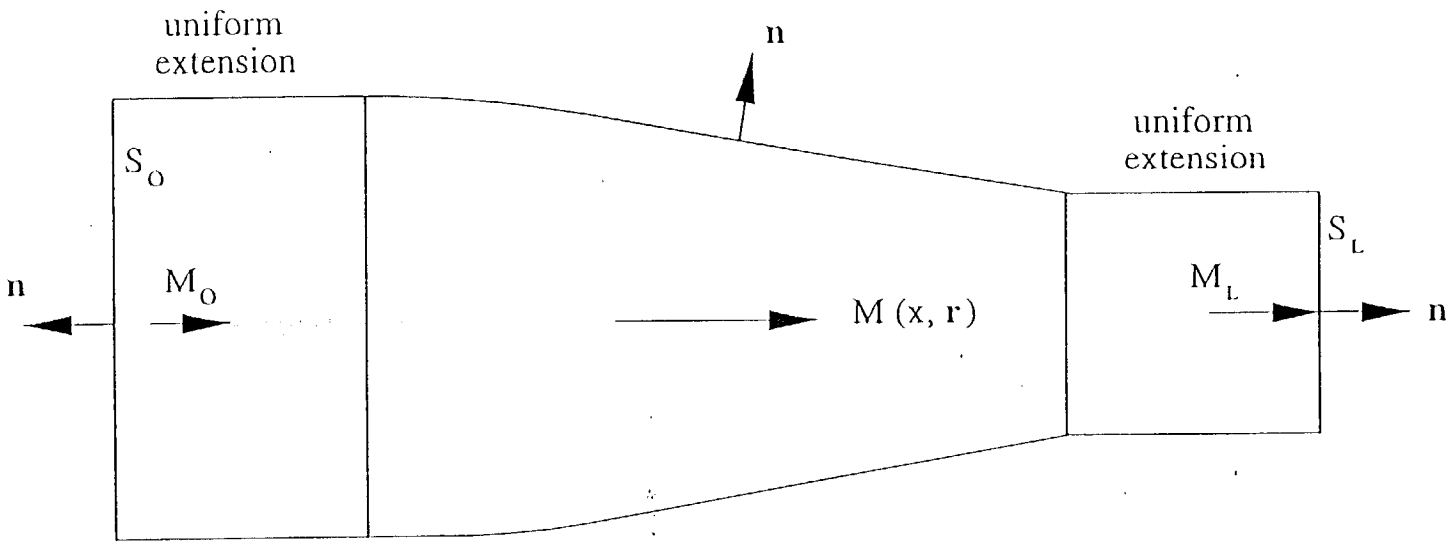

Figure 2. A duct configuration showing uniform extensions. Cross section shape is irrelevant in one dimensional approximation, as is the outward unit normal on the duct walls.

NUMERICAL EXPERIMENTS ON ACOUSTIC RECIPROCITY IN COMPRESSIBLE POTENTIAL FLOWS

Walter Eversman
Mechanical and Aerospace Engineering
and Engineering Mechanics
University of Missouri-Rolla
Rolla, MO 65401

ABSTRACT

A reciprocity theorem for the scattering matrix for propagation of acoustic modes in a duct with acoustically hard walls or with acoustically absorbing walls has been given in a companion publication. It was found that for a source at a specified end of the duct, suitably scaled reflection matrices in direct and reverse flow have a reciprocal relationship. Scaled transmission matrices obtained for direct flow and reversed flow with simultaneous switching of source location from one end to the other also have a reciprocal relationship. A reverse flow theorem for the equivalent one dimensional propagation model, which is a good approximation to the three dimensional model at low frequencies, was also obtained. In this case, using reciprocity and acoustic power conservation arguments it is additionally found that the acoustic power transmission coefficient is the same for a source at either end of the duct for a given flow direction. This result leads to an invariance theorem which relates acoustic power propagated due to sources of equal pressure amplitude at the two ends of the duct. Numerical verification of these reciprocal relationships is given here for propagation in axially symmetric (circular and annular) ducts with multi-modal propagation and at low frequencies when a one dimensional model is appropriate.

INTRODUCTION

In two companion papers [1,2], a reverse flow reciprocity theorem has been developed for acoustic propagation in non-uniform ducts carrying compressible mean flow. In [1] the general case of multi-mode propagation is considered and reciprocity is shown for ducts with either rigid walls or with walls which include a normally reacting, dissipative section. For a source at one

end of the duct, scaled reflection matrices in direct and reverse flow have a reciprocal relationship. Scaled transmission matrices obtained for direct flow and reversed flow with simultaneous switching of source location from one end to the other also have a reciprocal relationship. In [2] reverse flow reciprocity is shown for the long wave length approximation when a one dimensional model is applicable. In this case acoustic treatment is not part of the model. Results similar to the multi-modal case are established for reciprocal relationships for reflection and transmission coefficients. Additional results which are part of a general power transmission invariance principal are also found as a result of reciprocity and energy conservation. This invariance principal contains as a special case a result found by Davis [3].

The reverse flow reciprocity theorem is developed directly from an integral relationship based on the acoustic field equations, using an approach similar to that used in [4] in the case of propagation in a non-uniform duct in the absence of flow. In particular, the development does not begin with an energy principle. This is in distinction to the approach of Moehring [5,6]. The major complication which arises in the present formulation is the case when a portion of the duct wall is acoustically treated with a normally reacting dissipative lining. The boundary condition of Myers [7] is manipulated, using identities of vector calculus suggested by Moehring [6], to make it possible to establish reciprocity in this case.

The reverse flow reciprocity theorem is developed in detail in references [1] and [2] and the results are briefly summarized here. Figure 1 shows a non-uniform duct section bounded on either end by uniform sections (long enough to have essentially uniform flow so that acoustic propagation can be synthesized in terms of duct modes). At the two ends of the duct the acoustic field is the superposition of modes propagating to the right and to the left (including cut off modes which technically do not propagate, but which can be segregated into right and left modes). Amplitudes a_n^+ and a_n^- refer to right and left modes at the end $x = 0$ and b_n^+ and b_n^- refer to right and left modes at $x = L$. a^+, a^-, b^+, b^-, are vectors of modal amplitudes. These modal amplitudes are related by the scattering matrix $[S]$ according to

$$\begin{Bmatrix} a^- \\ b^+ \end{Bmatrix} = [S] \begin{Bmatrix} a^+ \\ b^- \end{Bmatrix} \tag{1}$$

The scattering matrix is defined as

$$[S] = \begin{bmatrix} [R] & [\tilde{T}] \\ [T] & [\tilde{R}] \end{bmatrix} \tag{2}$$

Contained in $[S]$ are the usual reflection matrix $[R]$ and transmission matrix $[T]$ for acoustic modes incident at $x = 0$ and reflection and transmission matrices $[\tilde{R}]$ and $[\tilde{T}]$ for modes incident at $x = L$. In multi-modal propagation the scattering matrix relates all modes which are considered. In the case of one dimensional propagation (the long wave length approximation), the scattering matrix relates only two modal amplitudes at each end. The reflection and transmission matrices are scalars, defined as reflection and transmission coefficients.

In the context of reversed flow reciprocity there is a scattering matrix $[S_1]$ for nominal mean flow and a second one $[S_2]$ for reversed flow. It is the relationship between $[S_1]$ and $[S_2]$ which is considered in [1,2]. Modal amplitudes in the present discussion are in terms of acoustic potential duct modes, because the acoustic field equations are naturally in terms of acoustic potential. Equivalent results are obtained in [1,2] for acoustic pressure modal amplitudes and it is only necessary at this point to refer to the properties of the acoustic potential scattering matrices.

The reverse flow reciprocity principle is

$$[S_1]^T [J] [\alpha] = [J] [\alpha] [S_2] \tag{3}$$

or

$$[J] [\alpha] [S_1] = ([J] [\alpha] [S_2])^T \tag{4}$$

The diagonal matrices $[J]$ and $[\alpha]$ are scaling matrices which have elements depending on the mode considered. The evaluation of these matrices is covered in detail in [1,2].

Equations (3) and (4) show that a weighted version of the nominal flow acoustic potential

scattering matrix and similarly weighted version of the reversed flow acoustic potential scattering matrix are transposes of one another. In terms of the acoustic potential reflection and transmission coefficient matrices the result is

$$[R_1]^T [J_0] [\alpha_0] = [J_0] [\alpha_0] [R_2] \tag{5}$$

$$[\tilde{R}_1]^T [J_L] [\alpha_L] = [J_L] [\alpha_L] [\tilde{R}_2] \tag{6}$$

$$[T_1]^T [J_L] [\alpha_L] = [J_0] [\alpha_0] [\tilde{T}_2] \tag{7}$$

$$[\tilde{T}_1]^T [J_0] [\alpha_0] = [J_L] [\alpha_L] [T_2] \tag{8}$$

Subscripts 0 and L refer to the evaluation of the relevant scaling coefficients at the two ends $x = 0$ and $x = L$. The reciprocal relationships of equations (5)-(8) involve acoustic potential reflection and transmission coefficient matrices, with diagonal elements representing reflection and transmission coefficients in the incident modes (here referred to as direct reflection or transmission) and off diagonal reflection and transmission coefficients from the incident mode to another mode. Equations (5) and (6) show that direct acoustic potential reflection coefficients are invariant in reversed flow. The transmission coefficient matrix pairs $[T_1]$, $[T_2]$ and $[\tilde{T}_1]$, $[\tilde{T}_2]$ are not reciprocally related but the pairs $[T_1]$, $[\tilde{T}_2]$ and $[\tilde{T}_1]$, $[T_2]$ are related by equations (7) and (8). The notation convention uses the subscripts 1 and 2 to denote flow direction (1 being nominal, 2 being reversed). Tilde, or lack thereof denotes source location (tilde denoting source location reversal).

In the one dimensional approximation [2] the same reciprocal relations apply, but in a simplified form. Reflection coefficients in nominal and reversed flow are invariant:

$$R_1 = R_2 \tag{9}$$

$$\tilde{R}_1 = \tilde{R}_2 \tag{10}$$

Scaled transmission coefficients are invariant to simultaneous flow reversal and source plane reversal:

$$T_1 A_L \frac{\rho_{r_L}}{c_{r_L}} = \tilde{T}_2 A_0 \frac{\rho_{r_0}}{c_{r_0}} \tag{11}$$

$$T_2 A_L \frac{\rho_{r_L}}{c_{r_L}} = \tilde{T}_1 A_0 \frac{\rho_{r_0}}{c_{r_0}} \tag{12}$$

In the case of one dimensional propagation there are additional results which can be deduced based on reciprocity and energy conservation. Power transmission coefficients T_π are defined as the ratio of transmitted power to incident power. It is found that

$$T_{\pi_1} = T_{\pi_2} = \tilde{T}_{\pi_1} = \tilde{T}_{\pi_2} \tag{13}$$

Here, as in the previous discussion the subscripts 1 and 2 refer to flow direction and the tilde or lack thereof refers to source location. Power transmission coefficients are invariant to flow reversal and source location reversal. That is, the power transmission coefficient is the same for flow in either direction, for a source at either end of the duct. Power reflection coefficients R_π are defined as the ratio of reflected power to incident power. It is also found that

$$R_{\pi_1} = R_{\pi_2} = \tilde{R}_{\pi_1} = \tilde{R}_{\pi_2} . \tag{14}$$

Power reflection coefficients are invariant to flow reversal and source location reversal.

The results summarized by equations (5)-(14) are interesting theoretically and also provide useful benchmarks which can be used to validate propagation calculations. In the following sections two finite element codes for duct propagation, one multi-modal and the other one dimensional, are used to demonstrate several of these reciprocal relations.

ACOUSTIC PROPAGATION IN A COMPRESSIBLE POTENTIAL FLOW

Reciprocity relations previously described will be verified by computations based on two FEM codes for duct propagation, one for multi-modal propagation and the other specialized for one-dimensional propagation. In this section only a brief description of the multi-modal propagation code will be given. Details of the FEM modeling approach can be found in references [8,9].

A formulation in terms of acoustic potential is used to produce a weak formulation suitable for finite element discretization to reduce the field equations to a single scalar variable. The geometry of the duct in Figure 1, and the steady flow field is axially symmetric. The acoustic field is not axially symmetric but is represented as azimuthally periodic in a cylindrical coordinate system with x being the axis of symmetry, r the cylindrical radius in a circular cross section at $x = 0$, and θ the angular coordinate. Solutions are sought in angular harmonics of a Fourier Series in θ enumerated by the angular mode number m. This reduces the solution domain to a two dimensional x, r plane, shown in Figure 1. The duct shape in a θ = constant plane shows the surface S which defines the duct shape and could include an inner surface for an annular duct. Part of S includes S_w, which is a locally reacting acoustic treatment.

The acoustic field is assumed to be harmonic in time at non-dimensional frequency η_r. Geometry is non-dimensional based on a reference length generally chosen as the radius of the inlet at the source plane, R. Acoustic and steady flow variables are non-dimensional based on reference values of the speed of sound and density of the medium, ρ_∞, c_∞, generally defined at the plane of the acoustic source. The non-dimensional frequency is $\eta_r = \omega R / c_\infty$, with ω the harmonic source frequency.

Field equations for continuity and momentum and the isentropic equation of state are

used in a weighted residual statement to obtain an integral formulation which is then written in discrete form using standard FEM procedures. In terms of acoustic potential the weak formulation is

$$\int\int\int_V \frac{\rho_r}{c_r^2}\{c_r^2 \nabla W\cdot\nabla\phi - (\vec{V}_r\cdot\nabla W)(\vec{V}_r\cdot\nabla\phi) + i\eta_r[W(\vec{V}_r\cdot\nabla\phi) - (\vec{V}_r\cdot\nabla W)\phi] - \eta_r^2 W\phi\}\,dV$$

$$= \int\int_S \frac{\rho_r}{c_r^2}\{c_r^2 W\nabla\phi - \vec{V}_r W(\vec{V}_r\cdot\nabla\phi) - i\eta_r \vec{V}_r W\phi\}\cdot\vec{n}\,dS \qquad (15)$$

where the local non-dimensional steady flow velocity is $\vec{V}_r = \nabla\phi_r$, with ϕ_r the non-dimensional steady flow velocity potential. The local non-dimensional density and speed of sound are ρ_r, c_r. The surface integral on the right hand side introduces the noise source and termination conditions on S_0 or S_L and a possible impedance boundary condition on S inside the duct. In the present investigation it is the impedance boundary condition which is of interest on S_w, a portion of S. In equation (15), the weighted residuals statement, W represents an arbitrary weighting function selected from the class of continuous functions. In this weak formulation the approximation to the solution ϕ is also chosen from the class of continuous functions

At a duct wall the mean flow is tangential to the wall and $\vec{V}_r\cdot\vec{n} = 0$ causing the boundary integral (the contribution to the right hand side of equation (1) related to the impedance condition) to become

$$I_b = \int_{S_w}\int \rho_r W\nabla\phi\cdot\vec{n}\,dS \qquad (16)$$

It is shown in [10] that at a wall of admittance A the weighted residual boundary integral of equation (16) on the duct surface S_w, derived from the Myers boundary condition [7], is

$$I_b = -\int_{S_w}\int A\rho_r^2 \{ i\eta_r W\phi + W\vec{V}_r\cdot\nabla\phi - \phi\vec{V}_r\cdot\nabla W - \frac{1}{i\eta_r}(\vec{V}_r\cdot\nabla W)(\vec{V}_r\cdot\nabla\phi)\} dS \qquad (17)$$

An accurate representation of this impedance boundary condition is essential to obtaining verification of reciprocal relationships when acoustic treatment is inserted in the duct wall [10]. References [8,9] deal with propagation and radiation to the far field from open ended ducts. In the code described here, rather than model radiation to the far field from the open end, imposes non-reflecting boundary condition at the termination. The boundary integral of equation (15) is used to introduce the source (at either end of the duct) as a superposition of acoustic potential duct modes and to implement the non-reflecting boundary condition based on another superposition of duct modes. The one-dimensional code is based on the one-dimensional field equations [2], and therefore has no provision for acoustic treatment. Other details of this code are similar to the multi-modal code. In both cases the steady mean flow field which is required data for propagation calculations is provided by an FEM potential flow code which introduces compressibility by iteration of successive incompressible flow problems. Steady flow is produced on the acoustic FEM mesh for convenience of data transfer.

The FEM duct codes provide solutions for the acoustic potential field which is post-processed to obtain acoustic pressure. Included as part of the solution are the acoustic potential modal amplitudes a^+, a^-, b^+, b^-. These are also converted to acoustic pressure modal amplitudes. Additional post-processing produces computations of acoustic power and power reflection and transmission coefficients.

NUMERICAL EXPERIMENTS ON RECIPROCITY

The first numerical verification of the reciprocal characteristics of the scattering matrix for an axially symmetric duct has been carried out in the case of a duct with a transition from annular to circular, as shown in an x, r slice in Figure 2. The interior contour is that of a typical turbofan inlet and the uniform extensions are added to meet the requirements of the present

analysis (uniform flow and proper definition of acoustic eigenfunctions). The finite element mesh used in the computations is shown on this figure and is typical for examples cited here. The conditions for the "nominal" case are standard atmospheric conditions at the source plane ($x = 0$), Mach number at the source plane $M_0 = 0.27$, directed left to right (opposite to the direction in an inlet). The non-dimensional frequency (based on the source plane) is $\eta_r = 10$. In the nominal case the input plane for scattering is the source plane at $x = 0$. Figure 3 shows iso-potential contours for the steady compressible flow in the duct which varies roughly between $M = 0.27$ and $M = 0.15$. Figure 3 is unaltered in form for reverse flow (right to left and in the direction expected in an inlet). The acoustic analysis is based on input modes with angular dependence $m = 3$, for which there exist two propagating modes at each end of the duct (n=1, n=2).The third mode, n=3, is cut off at both ends of the duct with cut-off ratio $\xi = 0.87$ at $x = 0$ and $\xi = 0.84$ at $x = L$. Two cases of duct wall characteristics are studied. In the first case the duct walls are acoustically hard, that is the impedance is infinite and the admittance vanishes. In the second case the outer duct wall is acoustically treated from $x = 1.0$ through 80 % of the non-uniform section. The impedance is chosen as $Z = 2.0 - 1.0\,i$, which is not optimum for attenuation for the given conditions, but is not untypical for aircraft applications. The acoustic power attenuation with the simplest radial mode incident (m=3, n=1) is about 9 dB, so there is a significant decrease in acoustic power from one end of the duct to the other, attributable to the wall treatment.

To generate the scaled reflection and transmission coefficient matrices in this case input modes $n = 1$, $n = 2$ and $n = 3$ are considered. This produces 3 x 3 matrices which include two propagating modes and one mode which is cut off at both ends. To build the reflection and transmission matrices to verify equations (5) and (7) it is required to consider nine propagation cases: three input modes at $x = 0$ for nominal flow; three input modes at $x = 0$ for reverse flow; and three input modes at $x = L$ for reverse flow.

Reference to contours of equal acoustic pressure provide evidence of the differences induced by varying the source mode number, source location and the flow direction. Figure 4 shows acoustic iso-pressure contours for the duct with acoustic treatment when the input radial mode at $x = 0$ is $n = 1$. There is significant scattering and this is verified by reference to the

scattering coefficients. Figure 5 shows the case of mode $n = 3$ input at $x = L$ in reverse flow. This mode is cut off at both ends, and it should be noted how rapidly the acoustic pressure level is attenuated away from the source plane.

Table 1 shows the scaled acoustic potential reflection coefficient matrix in nominal flow with the scattering plane (acoustic source plane) at $x = 0$, which corresponds to the left hand side of equation (5). Table 2 is the reflection matrix at $x = 0$ in reversed flow, corresponding to the right hand side of equation (5). Equation (5) predicts that these matrices should be reciprocals of one another. Tables 1 and 2 verify this with exceptional accuracy.

mode	1	2	3
1	-0.14380 - 0 .03098 i	-0.13986 + 0.07217 i	-0.153(-4) - 0.549(-5) i
2	-0.13746 + 0.71323 i	-0.04113 + 0.20572 i	0.104(-3) + 0.732(-5) i
3	-0.424(-5) + 0.841(-5) i	-0.144(-4) - 0.903(-4) i	-0.682(-5) + 0.497(-8) i

Table 1. Scaled acoustic potential reflection coefficients for nominal flow and source at $x = 0$ for the transition from an annular to circular hard wall duct. Corresponds to the left hand side of equation (5). $\eta_r = 10$, $m = 3$.

mode	1	2	3
1	-0.14380 - 0 .03098 i	-0.13746 + 0.71323 i	-0.424(-5) + 0.841(-5) i
2	-0.13986 + 0.07217 i	-0.04113 + 0.20572 i	-0.144(-4) - 0.903(-8) i
3	-0.153(-4) - 0.549(-5) i	0.104(-3) + 0.732(-5) i	-0.682(-5) + 0.497(-8) i

Table 2. Scaled acoustic potential reflection coefficients for reverse flow and source at $x = 0$ for the transition from an annular to circular hard wall duct. Corresponds to the right hand side of equation (5). $\eta_r = 10$, $m = 3$.

Tables 3 and 4 verify the prediction of equation (7). Table 3 gives the scaled acoustic potential transmission coefficients in nominal flow with the source at $x = 0$. Table 4 gives the

scaled transmission coefficients in reversed flow with the source shifted to $x = L$. Equation (7) predicts a reciprocal relationship which is accurately substantiated in Tables 3 and 4. A point of interest in the results shown in Tables 1 through 4 is that reciprocity extends to cutoff modes in which case the power transmission is only accounted for by interaction of left and right modes.

mode	1	2	3
1	-4.12246 + 0.00532 i	-0.56880 + 0.23281 i	0.151(-4) - 0.109(-4) i
2	0.58902 + 0.37376 i	-1.74565 - 0.27580 i	0.834(-4) + 0.174(-4) i
3	-0.300(-4) - 0.897(-4) i	-0.169(-3) + 0.105(-3) i	0.808(-8) - 0.488(-8) i

Table 3. Scaled acoustic potential transmission coefficients for nominal flow and source at $x = 0$ for the transition from an annular to circular hard wall duct. Corresponds to the left hand side of equation (7). $\eta_r = 10$, $m = 3$.

mode	1	2	3
1	-4.12246 + 0.00532 i	0.58902 + 0.37376 i	-0.300(-4) - 0.897(-4) i
2	-0.56880 + 0.23821 i	-1.74565 - 0.27580 i	-0.169(-3) - 0.105(-3) i
3	0.151(-4) - 0.109(-4) i	0.834(-4) + 0.174(-4) i	0.808(-8) - 0.488(-8) i

Table 4. Scaled acoustic potential transmission coefficients for reverse flow and source at $x = L$ for the transition from an annular to circular duct. Corresponds to the right hand side of equation (7). $\eta_r = 10$, $m = 3$.

Tables 5 through 8 are for the case with acoustic treatment in place. Table 5 shows the scaled acoustic potential reflection coefficient matrix in nominal flow with the scattering plane (acoustic source plane) at $x = 0$, and with the nonuniform portion of the duct outer wall acoustically treated. This corresponds to the left hand side of equation (5). Table 6 is the reflection matrix at $x = 0$ in reversed flow, corresponding to the right hand side of equation (5) for the same acoustic treatment configuration. Equation (5) predicts that these matrices should

be reciprocals of one another. Tables 5 and 6 verify this, again with exceptional accuracy.

mode	1	2	3
1	0.16904 - 0.23900 i	-0.12975 - 0.18014 i	-0.482(-3) - 0.677(-4) i
2	-0.07368 - 0.10133 i	-0.00984 - 0.03495 i	-0.275(-3) + 0.950(-4) i
3	-0.305(-3) + 0.632(-5) i	-0.283(-3) + 0.556(-5) i	-0.693(-5) + 0.510(-6) i

Table 5. Scaled acoustic potential reflection coefficients for direct flow and source at $x = 0$ for the transition from an annular to circular acoustically treated duct. Corresponds to the left hand side of equation (5). $\eta_r = 10$, $m = 3$.

mode	1	2	3
1	0.16904 - 0.23900 i	-0.07368 - 0.10133 i	-0.305(-3) + 0.632(-5) i
2	-0.12975 - 0.18014 i	-0.00984 - 0.03495 i	-0.283(-3) + 0.556(-5) i
3	-0.482(-3) - 0.677(-4) i	-0.275(-3) + 0.950(-4) i	-0.693(-5) + 0.510(-6) i

Table 6. Scaled acoustic potential reflection coefficients for reverse flow and source at $x = 0$ for the transition from an annular to circular acoustically treated duct. Corresponds to the right hand side of equation (5). $\eta_r = 10$, $m = 3$.

Tables 7 and 8 verify the prediction of equation (7) in the case of an acoustically treated outer wall. Table 7 gives the scaled acoustic potential transmission coefficients in direct flow with the source at $x = 0$. Table 8 gives the scaled transmission coefficients in reversed flow with the source shifted to $x = L$. Equation (7) predicts a reciprocal relationship which is accurately substantiated in Tables 7 and 8. Again, the applicability of the reciprocity principle to cut-off modes is verified.

mode	1	2	3
1	-1.21549 + 0.02495 i	-0.25788 + 0.60030 i	0.780(-4) - 0.227(-3) i
2	0.38577 - 0.37557 i	-0.76395 + 0.24663 i	0.146(-3) - 0 .741(-4) i
3	-0.319(-4) - 0.753(-4) i	-0.532(-4) + 0.849(-4) i	0.109(-7) - 0.205(-7) i

Table 7. Scaled acoustic potential transmission coefficients for direct flow and source at $x = 0$ for the transition from an annular to circular acoustically treated duct. Corresponds to the left hand side of equation (7). $\eta_r = 10$, $m = 3$.

mode	1	2	3
1	-1.21549 + 0.02495 i	0.38577 - 0.37557 i	-0.319(-4) - 0.753(-4) i
2	-0.25788 + 0.60030 i	-0.76395 + 0.24663 i	-0.532(-4) + 0.849(-4) i
3	0.780(-4) - 0227(-3) i	0.146(-3) - 0.741(-4)	0.109(-7) - 0.205(-7) i

Table 8. Scaled acoustic potential transmission coefficients for reverse flow and source at $x = L$ for the transition from an annular to circular acoustically treated duct. Corresponds to the left hand side of equation (7). $\eta_r = 10$, $m = 3$.

The next case considered involves a steady flow in which the Mach number becomes relatively high, emphasizing the dependence of the acoustic treatment boundary condition on Mach number. An additional complication introduced here is the segmenting of the acoustic treatment into two equal length parts with different impedances, spanning the entire transition section. A continuous transition occurs within one element of the FEM mesh. The impedances in this case are $Z_1 = 2.0 - 1.0\,i$, $Z_2 = 3.0 - 2.0\,i$ (numbered left to right) . This satisfies the requirement of the reciprocity theorem and also simulates a near discontinuity of impedance. Here a converging duct with a contraction ratio of $\sigma = 0.5$, as shown in Figure 6, accelerates the flow (iso-potential contours are shown on Figure 6) from a Mach number at the nominal source plane of $M = 0.13$ to $M = 0.71$ at the exit plane. An acoustic propagation analysis has been

carried out for the non-dimensional frequency $\eta_r = 10$ for a source with angular mode $m = 3$. In this geometry and the resulting steady flow there are two propagating modes at $x = 0$ (determined in the hard wall case), but just one propagating mode at $x = L$. Results given here are for scaled potential reflection and transmission matrices. 3 x 3 reflection and transmission matrices are investigated by considering input radial modes $n = 1$, $n = 2$, and $n = 3$. At $x = 0$ the two propagating modes and one cut-off mode have cut-off ratios $\xi = 2.40$, $\xi = 1.26$, $\xi = 0.89$, respectively. At $x = L$ the single propagating mode and two cut off modes have cut-off ratios $\xi = 1.65$, $\xi = 0.87$, $\xi = 0.61$. An interesting feature of this geometry and flow is that mode $n = 2$ makes a transition from cut on to cut off in going from left to right. Mode $n = 3$ is deeply cut off at $x = L$.

Figure 7 shows acoustic iso- pressure contours for the case of nominal flow (left to right) with the mode $n = 1$ input at $x = 0$. The contours are consistent with a well cut on mode and significant scattering. Figure 8 shows contours for the case of reverse flow (right to left) with the source at the end $x = L$, and the input mode $n = 3$. This mode is deeply cut off and it should be noted how rapidly the acoustic pressure levels decay away from the source plane. It can be concluded that this mode effectively produces no acoustic pressure at $x = 0$.

Tables 9 through 12 are presented to verify the predicted reciprocal characteristics of the scaled acoustic potential reflection and transmission coefficients. Tables 9 and 10 show the scaled pressure reflection coefficients for nominal flow (left to right) and reverse flow (right to left) with the source at $x = 0$. These correspond with the left and right hand sides of equation (5). The reflection matrices shown in these two tables are seen to be reciprocals, as predicted.

mode	1	2	3
1	0.16566 + 0.11529 i	0.23310 + 0.05472 i	-0.00056 - 0.00099 i
2	0.20720 + 0.09263 i	-0.02814 + 0.01965 i	0.00035 - 0.00035 i
3	-0.00044 - 0.00067 i	-0.00069 - 0.00111 i	-0.291(-4) + 0.286(-5) i

Table 9. Scaled acoustic potential reflection coefficients for direct flow and source at $x = 0$ for the converging circular acoustically treated duct. Corresponds to the left hand side of equation (5). $\eta_r = 10$, $m = 3$.

mode	1	2	3
1	0.16566 + 0.11529 i	0.20720 + 0.09623 i	-0.00044 - 0.00067 i
2	0.23310 + 0.05472 i	-0.02814 + 0.01965 i	-0.00069 - 0.00111 i
3	-0.00056 - 0.00099 i	0.00035 - 0.00035 i	-0.291(-4) + 0.286(-5) i

Table 10. Scaled acoustic potential reflection coefficients for reverse flow and source at $x = 0$ for the converging circular acoustically treated duct. Corresponds to the right hand side of equation (5). $\eta_r = 10$, $m = 3$.

Tables 11 and 12 show the scaled potential transmission coefficients for nominal flow (left to right) with the source plane at $x = 0$ and reverse flow (right to left) with the source at $x = L$. These correspond with the left and right hand sides of equation (7). The reflection matrices shown in these two tables are seen to be reciprocals for modes $n = 1$, $n = 2$. Reciprocity involving mode $n = 3$ seems to fail. The reason for this can be deduced by referring back to Figure 8 and noting that the deeply cut off mode $n = 3$ creates acoustic pressure levels at $x = 0$ which are probably unresolvable with accuracy by the numerical model. To test this hypothesis, another test of reciprocity with the same geometry, flow, and mode number was carried out, but with the non-dimensional frequency increased to $\eta_r = 12$ (from $\eta_r = 10$). This changes the cut-off ratios for the modes $n = 1$, $n = 2$, $n = 3$ to $\xi = 2.88$, $\xi = 1.51$, $\xi = 1.07$ at $x = 0$ and $\xi = 1.98$, $\xi = 1.04$, $\xi = 0.73$ at $x = L$.

This makes three propagating modes at the left end and two propagating modes at the right end, and retains the interesting feature of the transition from cut on to cut off for mode $n = 3$ in a transition from left to right, or from cut off to cut on in the opposite direction.

mode	1	2	3
1	-0.18538 + 0.24017 i	0.04016 + 0.13443 i	-0.223(-5) - 0.286(-6) i
2	0.374(-4) - 0.570(-4) i	-0.115(-4) - 0.288(-4) i	0.110(-8) - 0.344(-8) i
3	-0.521(-7) + 0.116(-6) i	0.301(-7) - 0.507(-7) i	0.260(-11) + 0.595(-11) i

Table 11. Scaled acoustic potential transmission coefficients for direct flow and source at $x = 0$ for converging circular acoustically treated duct. Corresponds to the left hand side of equation (7). $\eta_r = 10$, $m = 3$.

mode	1	2	3
1	-0.18538 + 0.24017 i	0.374(-4) - 0.570(-4) i	-0.521(-7) + 0.116(-6) i
2	0.04016 + 0.13443 i	-0.115(-4) - 0.288(-4) i	0.301(-7) + 0.507(-7) i
3	0.00014 - 0.00005 i	0.332(-7) + 0.961(-8) i	-0.644(-10) - 0.770(-11) i

Table 12. Scaled acoustic potential transmission coefficients for reverse flow and source at $x = L$ for the converging circular acoustically treated duct. Corresponds to the left hand side of equation (7). $\eta_r = 10$, $m = 3$.

mode	1	2	3
1	-0.08862 + 0.41280 i	0.31074 - 0.05362 i	0.03674 + 0.06580 i
2	-0.02353 - -0.00062 i	0.02811 - 0.03804 i	0.00839 - 0.00304 i
3	0.877(-5) - 0.791(-5) i	0.0255(-5) + 0.237(-4) i	-0.208(-5) + 0.397(-5) i

Table 13. Scaled acoustic potential transmission coefficients for direct flow and source at $x = 0$ for converging circular acoustically treated duct. Corresponds to the left hand side of equation (7). $\eta_r = 12$, $m = 3$.

mode	1	2	3
1	-0.08862 + 0.41280 i	-0.02353 - 0.00062 i	0.877(-5) - 0.791(-5) i
2	0.31074 - 0.05362 i	0.02811 - 0.03804 i	0.255(-5) +0.237(-4) i
3	0.03674 + 0.06580 i	0.00839 - 0.00304 i	-0.208(-5) +0.397(-5) i

Table 14. Scaled acoustic potential transmission coefficients for reverse flow and source at $x = L$ for the converging circular acoustically treated duct. Corresponds to the left hand side of equation (7). $\eta_r = 12$, $m = 3$.

Figure 9 shows acoustic iso-pressure contours for the case of reverse flow, with the source at the right end with $n = 3$ and $\eta_r = 12$. The contour levels show that at the left end the acoustic pressure levels are substantially higher than those shown in Figure 8, and they are more accurately resolved by the modeling scheme.

Tables 13 and 14 show the scaled potential transmission coefficients for nominal flow (left to right) with the source plane at $x = 0$ and reverse flow (right to left) with the source at $x = L$. The non-dimensional frequency is $\eta_r = 12$. Now reciprocity is satisfied (a reciprocal relationship of the scaled transmission matrices) to a high level of accuracy. It is concluded that

accurate resolution of the acoustic field of the deeply cut off mode $n = 3$. This warns that there is a practical limit beyond which reciprocity may not be verifiable for cut off modes.

A final example considers the converging circular duct profile previously shown in Figure 6 with the same steady flow Mach number, but in this case treated as one dimensional. Inlet and exit Mach numbers for the nominal flow are M = 0.13 and M = 0.71. Acoustic propagation is also taken to be one dimensional at non-dimensional frequency $\eta_r = 1.0$ based on a reference length which is the radius (of an assumed circular cross section) of the duct at the nominal source plane $x = 0$. This scaling makes everything consistent with the axially symmetric duct formulation. Propagation at the chosen frequency has been modeled by the axially symmetric formulation using angular mode $m = 0$ and radial mode $n = 1$. Iso-potential contours for the steady flow are shown in Figure 6 and iso-acoustic pressure contours are shown in Figure 10 (with longer uniform extensions at the two ends, as compared to Figure 6). Because of the duct contour and steady flow there is noticeable deviation from true one dimensional propagation, however there is no indication of substantial scattering into higher order modes, which the one dimensional theory necessarily excludes.

Table 15 is a summary of the reciprocity and power invariance benchmark tests which are available in the one dimensional case. The results of (a) and (b) substantiate the reciprocity statement of equation (9) and the results of (c) and (d) substantiate the reciprocity statement of equation (11). The power results (e)-(l) substantiate the observations based on power considerations that power reflection and transmission coefficients are independent of flow direction and source location (equations (13) and (14)). As an indication of the comparison between the axially symmetric (3-Dim) duct model and the one dimensional model, power reflection and transmission coefficients for the axially symmetric model are shown also. The invariance of the power transmission and reflection coefficients to flow direction and source location is true (numerically) at low frequencies in the axially symmetric duct and the one dimensional predictions of reflection and transmission characteristics quite favorably correlate with predictions of the axially symmetric model. The properties of invariance of the power reflection and transmission coefficients is not generally true at higher frequencies in the axially symmetric model when scattering into higher or lower modes occurs.

Coefficient	3-Dim	1-Dim	1-Dim
(a). Reflection coefficient, direct flow, source left			0.430129 + 0.050053 i
(b). Reflection coefficient, reverse flow, source left			0.430129 + 0.050053 i
(c). Scaled transmission coefficient, direct flow, source left			0.384607 + 0.145370 i
(d). Scaled transmission coefficient, reverse flow, source left			0.384607 + 0.145370 i
(e). Power reflection coefficient, direct flow, source left:	0.171105	0.187517	
(f). Power reflection coefficient, reverse flow, source left	0.171105	0.187517	
(g). Power reflection coefficient, direct flow, source right	0.171105	0.187517	
(h). Power reflection coefficient, reverse flow, source right	0.171105	0.187517	
(i). Power transmission coefficient, direct flow, source left	0.828895	0.812483	
(j). Power transmission coefficient, reverse flow, source left	0.828895	0.812483	
(k). Power transmission coefficient, direct flow, source right	0.828895	0.812483	
(l). Power transmission coefficient, reverse flow, source right	0.828895	0.812483	

Table 15. Summary of scattering matrix reciprocity and power invariance benchmark tests for a one dimensional converging duct, with power invariance comparisons for an axially symmetric model. $M_0 = 0.13$, $M_L = 0.71$, $\eta_r = 1.0$ ($m = 0$, $n = 1$ in the axially symmetric case).

CONCLUSION

Numerical verification of the reciprocal relationships derived in References [1,2] has been accomplished using a finite element model for duct propagation. Three cases have been presented for an axially symmetric duct model, one introducing the feature of transition from an annular to a circular duct without and with acoustic treatment, and the second introducing a converging duct with substantial steady flow acceleration and segmented acoustic treatment. A fourth case is presented for the converging duct at low frequency where a one dimensional model of propagation is appropriate. Reciprocal characteristics of the scattering matrices are verified with exceptional accuracy, as are predicted relationships for power reflection and transmission coefficients in the one dimensional case.

REFERENCES

1. W. Eversman 2000 Journal of Sound and Vibration (in preparation). A reverse flow theorem and acoustic reciprocity in compressible potential flows.

2. W. Eversman 2000 Journal of Sound and Vibration (in preparation). Reciprocity and acoustic power in one dimensional compressible potential flows.

3. S. S. Davis 1976 Journal of the Acoustical Society of America 59(2), 264-266. On an invariance property of acoustic waveguides.

4. W. Eversman 1979 Journal of Sound and Vibration 47(4), 515-521. A reciprocity relationship for transmission in non-uniform hard walled ducts without flow.

5. W. Moehring 1978 Journal of the Acoustical Society of America 64(4), 1186-1189. Acoustic energy flux in nonhomogeneous ducts.

6. W. Moehring 2000 Journal of Fluid Mechanics (in review).Energy conservation, time reversal invariance and reciprocity in ducts with flow. (In review).

7. M. K. Myers 1980 Journal of Sound and Vibration 71(3),429-434. On the acoustic boundary condition in the presence of flow.

8. I. Danda Roy and W. Eversman 1995 ASME Journal of Vibration and Acoustics 117(1), January, 1995, 109-115. Improved finite element modeling of the turbofan engine inlet radiation problem.

9. W. Eversman and D. Okunbor 1998 Journal of Sound and Vibration 213(2),235-257. Aft fan duct acoustic radiation.

10. W. Eversman 2000 Journal of Sound and Vibration. (In preparation) The boundary condition at an impedance wall in a nonuniform duct with potential mean flow.

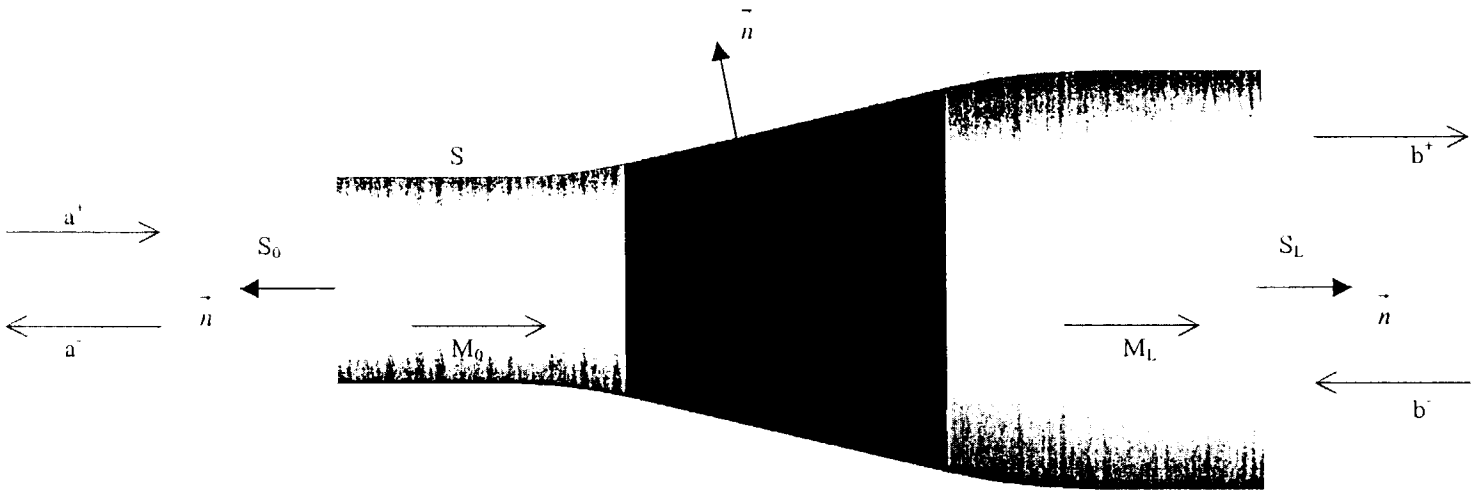

Figure 1. An x, r slice of a non-uniform duct showing acoustic treatment, uniform extensions, acoustic modal amplitudes, and relevant surfaces and surface normals.

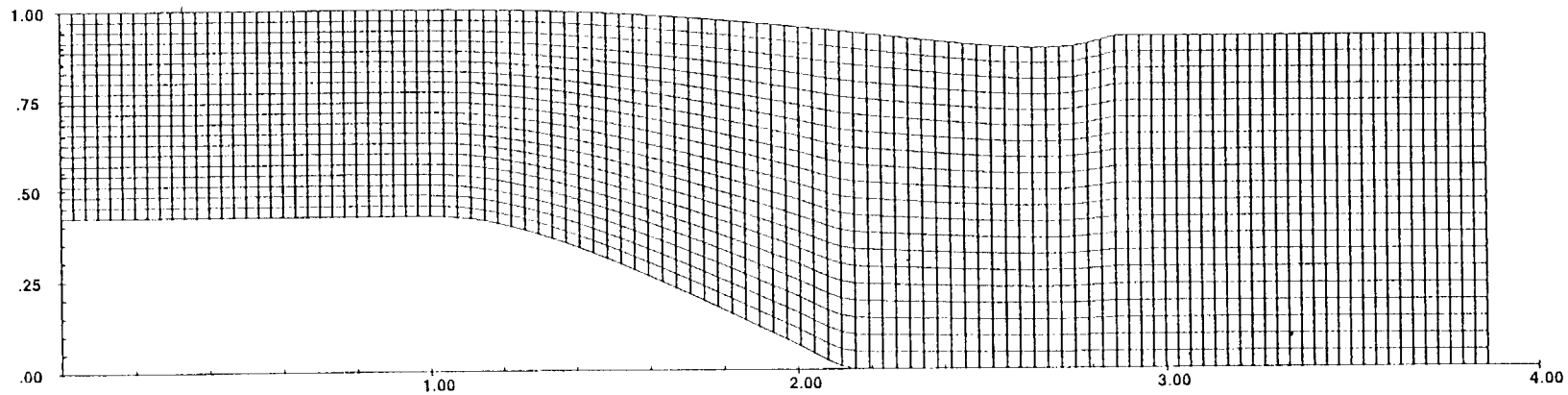

Figure 2. Plane section through the axis of a duct which has a transition from annular to circular, showing the duct profile and a typical finite element mesh.

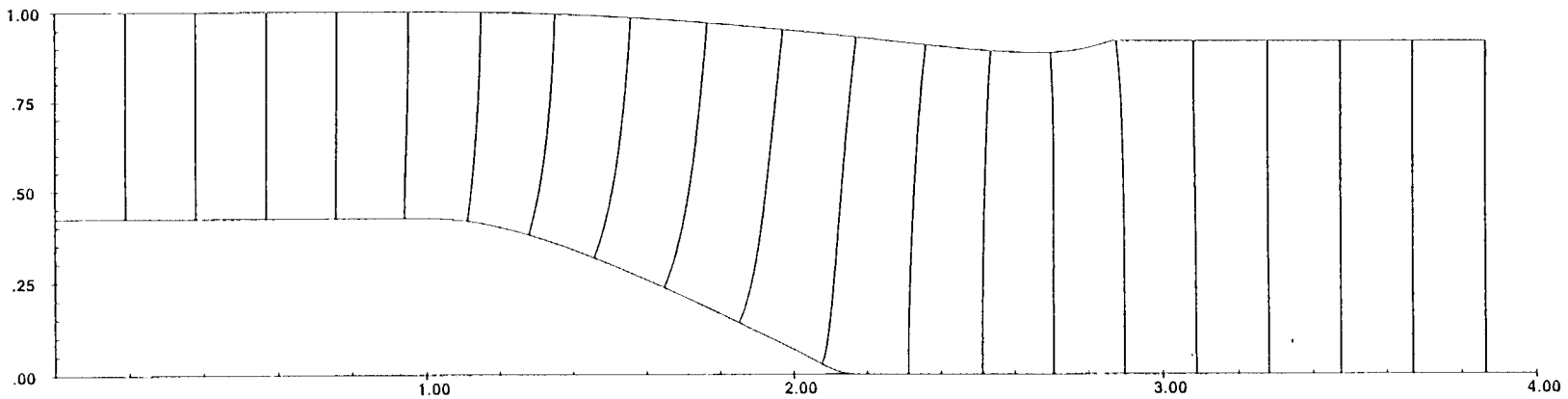

Figure 3. Iso-potential contours for steady flow through the annular/circular duct.

Figure 4. Acoustic iso-pressure contours for acoustically treated annular/circular duct with nominal flow. At $x = 0$ the Mach number is $M_0 = 0.27$, the non-dimensional frequency is $\eta_r = 10.0$, and the input mode at the left is $m = 3$, $n = 1$. Contours are typical for a well cut on input mode.

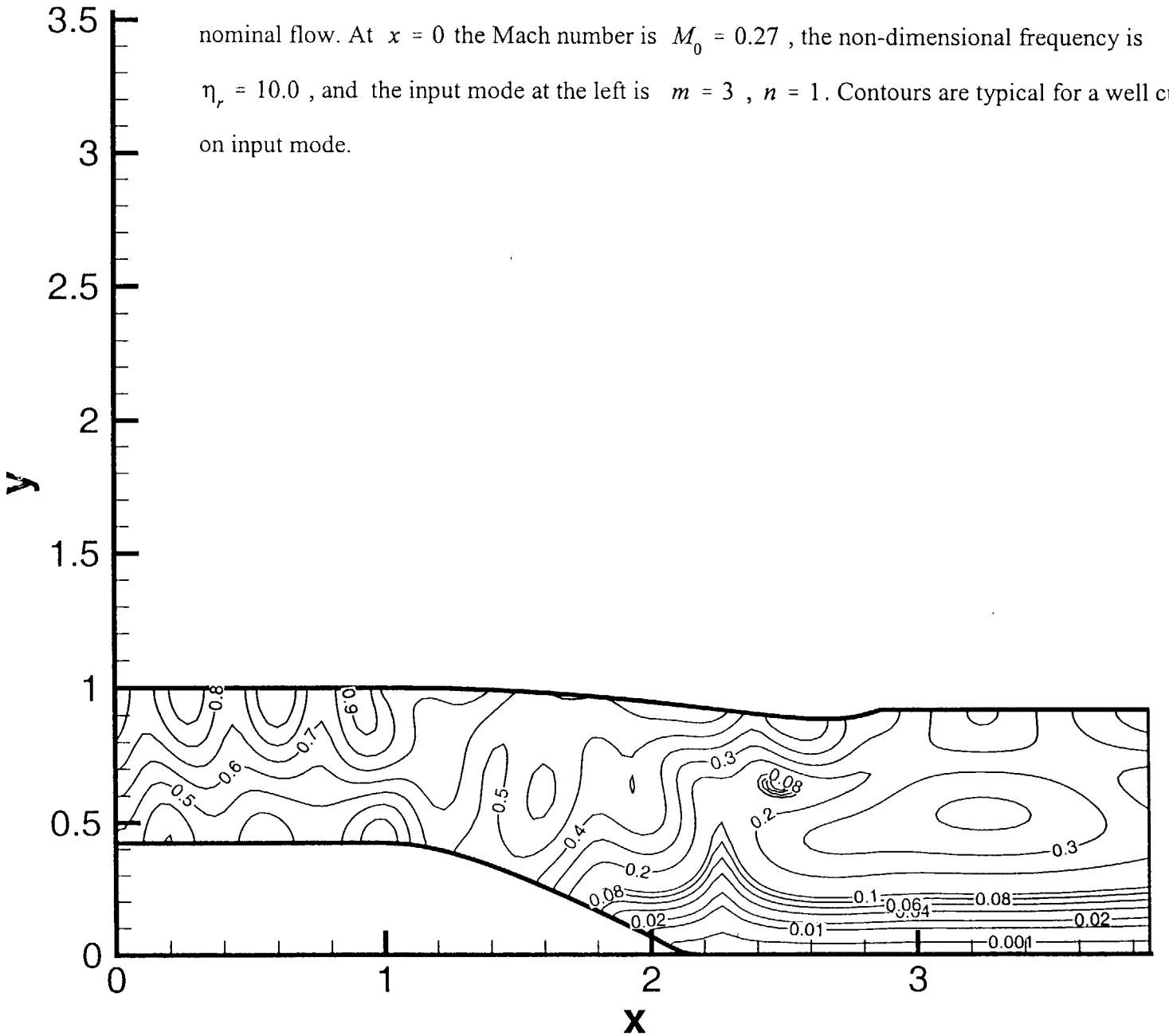

Figure 5. Acoustic iso-pressure contours for acoustically treated annular/circular duct with reverse flow. At $x = 0$ the Mach number is $M_0 = -0.27$, the non-dimensional frequency is $\eta_r = 10.0$, and the input mode at the right is $m = 3$, $n = 3$. Contours are typical for a moderately cut off input mode.

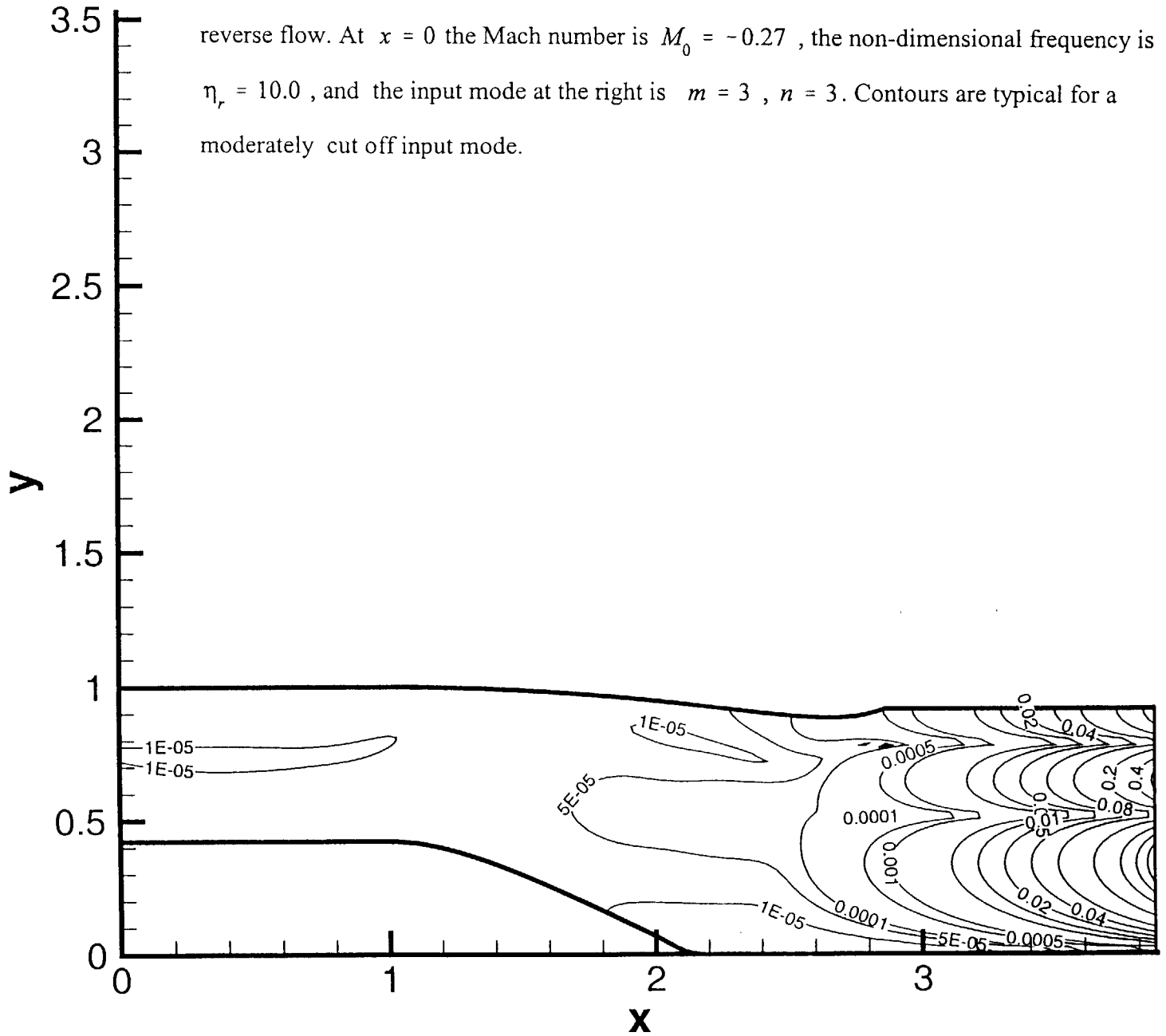

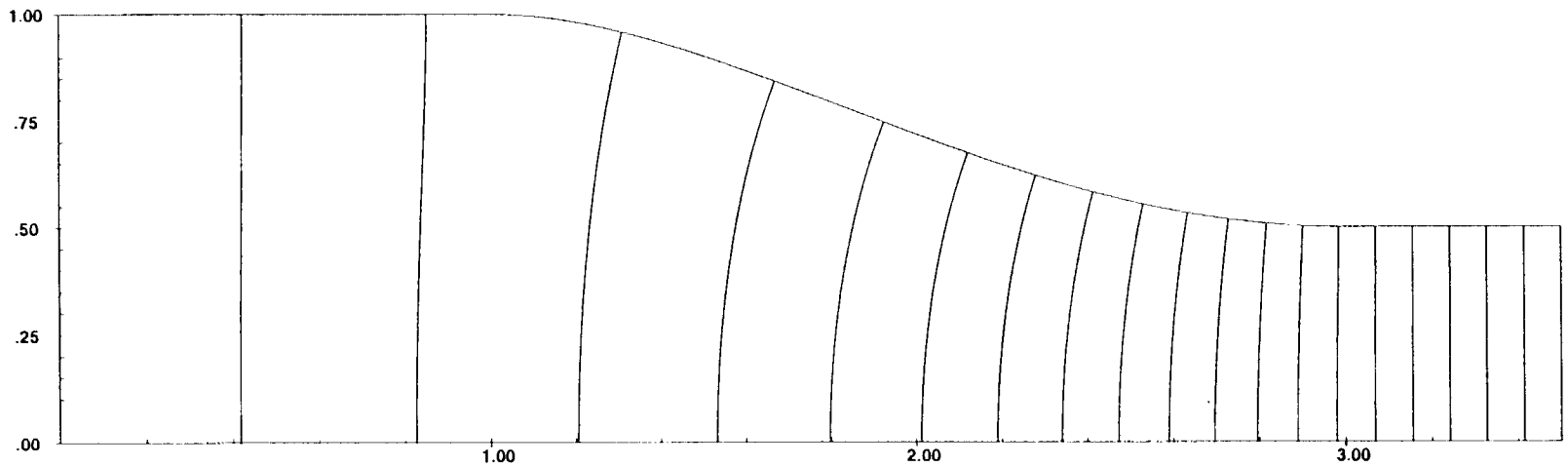

Figure 6. Duct shape and iso-potential contours for steady flow through the converging circular duct

Figure 7. Acoustic iso-pressure contours for acoustically treated converging circular duct with nominal flow. At $x = 0$ the Mach number is $M_0 = -0.13$ and at $x = L$ the Mach number is $M_L = -0.71$. The non-dimensional frequency is $\eta_r = 10.0$, and the input mode at the left is $m = 3$, $n = 1$. Contours are typical for a well cut on input mode.

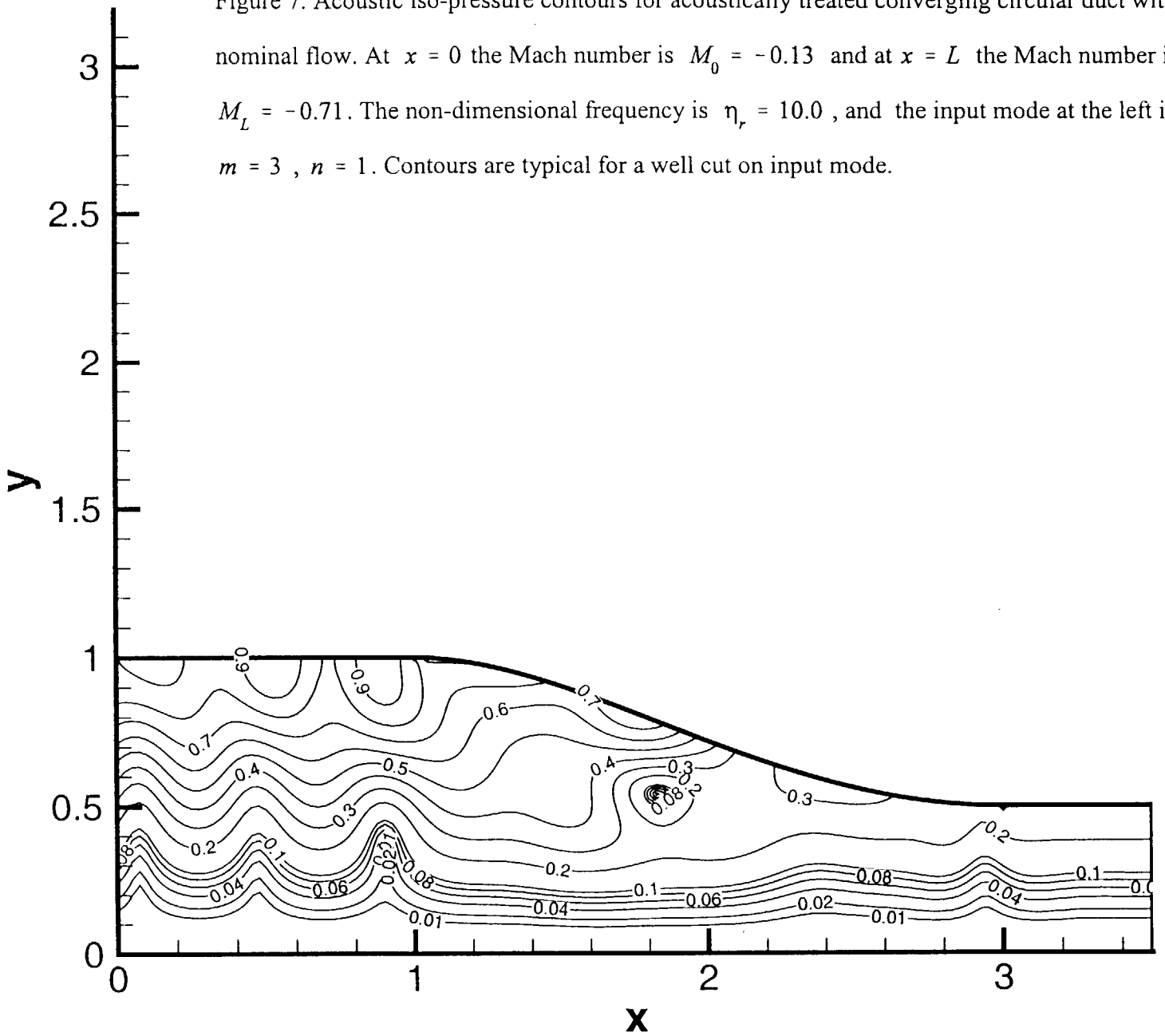

Figure 8. Acoustic iso-pressure contours for acoustically treated converging circular duct with reverse flow. At $x = 0$ the Mach number is $M_0 = -0.13$ and at $x = L$ the Mach number is $M_L = -0.71$. The non-dimensional frequency is $\eta_r = 10.0$, and the input mode at the right is $m = 3$, $n = 3$. Contours are typical for a deeply cut off input mode.

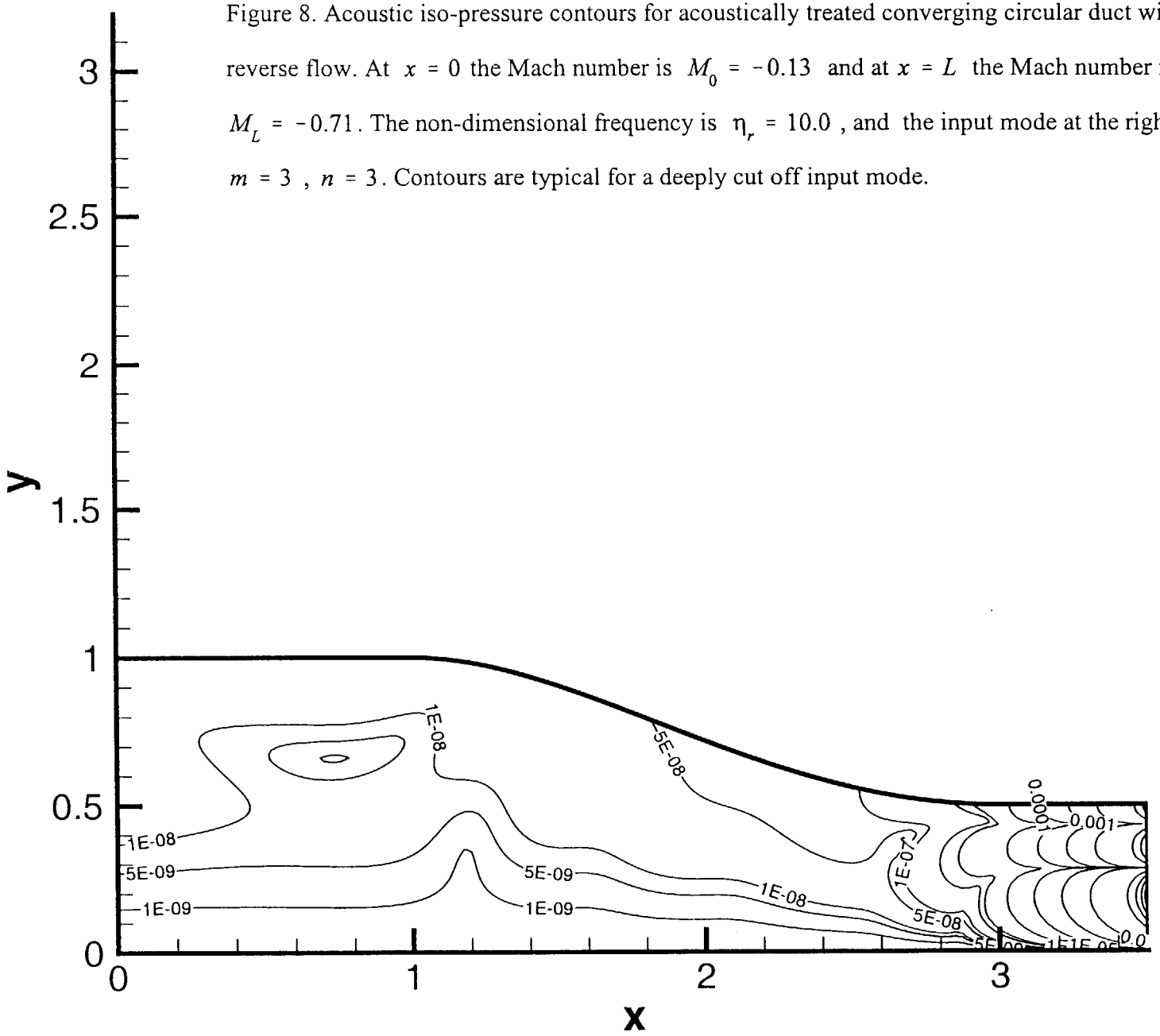

Figure 9. Acoustic iso-pressure contours for acoustically treated converging circular duct with reverse flow. At $x = 0$ the Mach number is $M_0 = -0.13$ and at $x = L$ the Mach number is $M_L = -0.71$. The non-dimensional frequency is $\eta_r = 12.0$, and the input mode at the right is $m = 3$, $n = 3$. Contours are typical for a moderately cut off input mode.

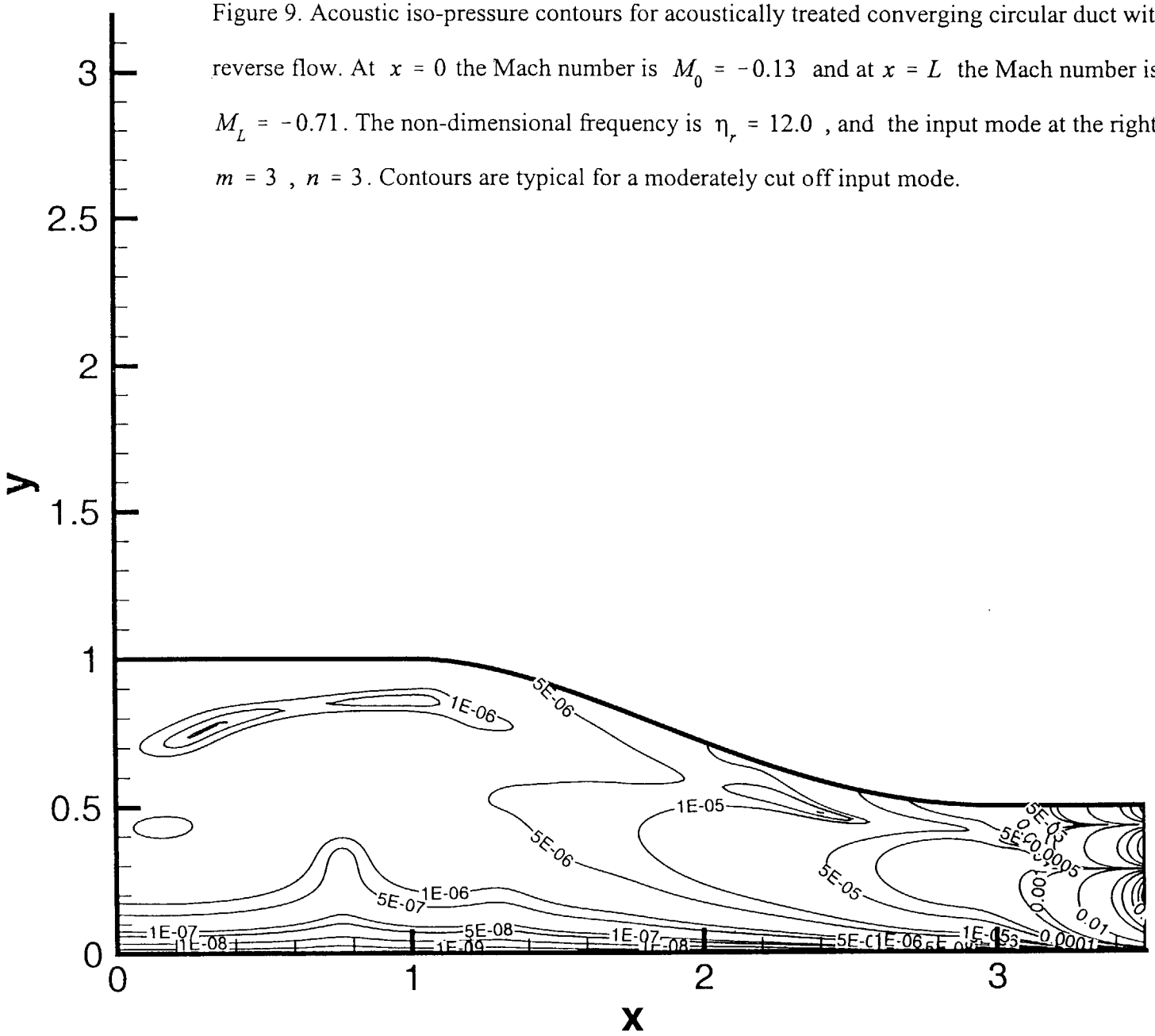

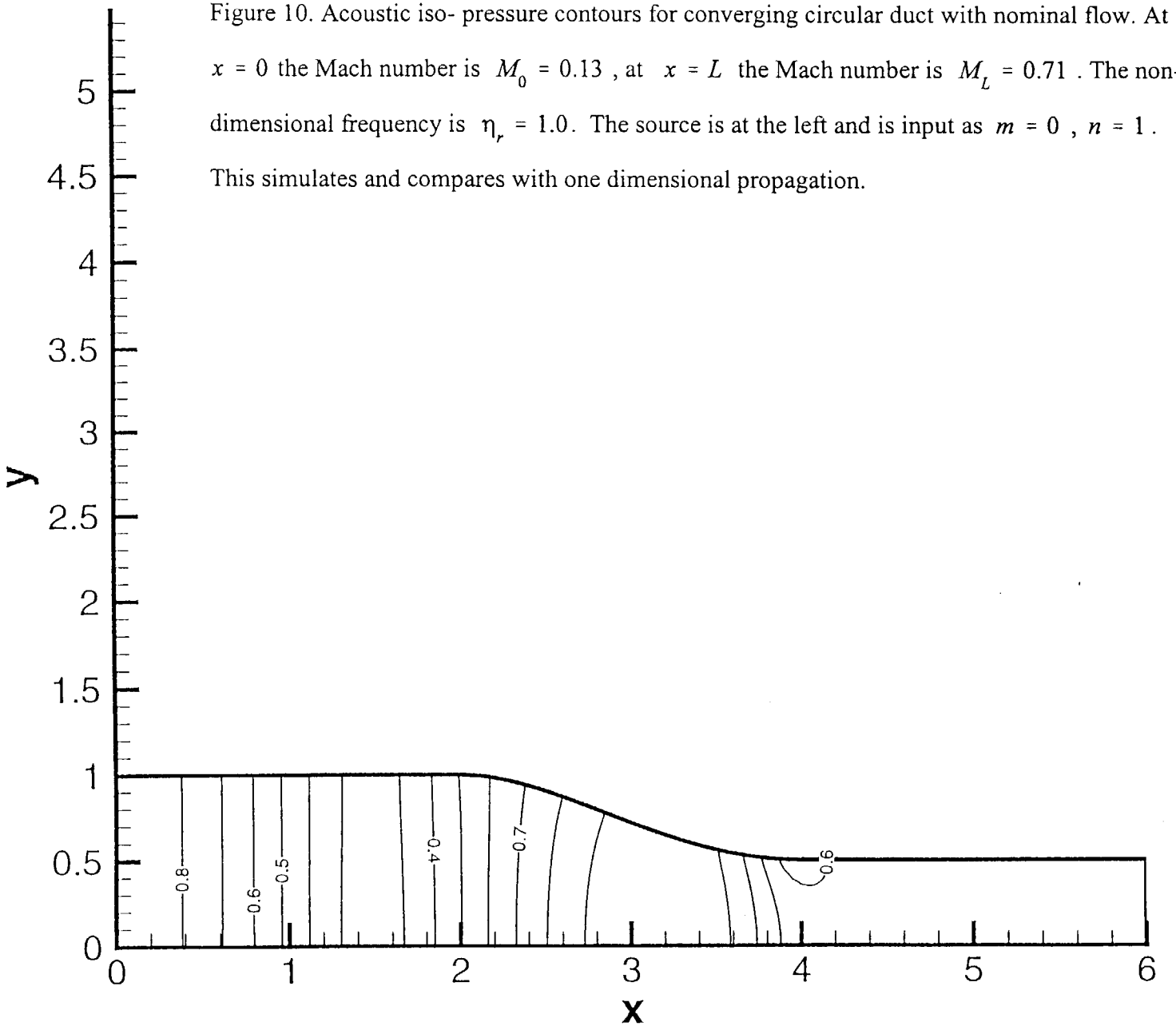

Figure 10. Acoustic iso- pressure contours for converging circular duct with nominal flow. At $x = 0$ the Mach number is $M_0 = 0.13$, at $x = L$ the Mach number is $M_L = 0.71$. The non-dimensional frequency is $\eta_r = 1.0$. The source is at the left and is input as $m = 0$, $n = 1$. This simulates and compares with one dimensional propagation.